Design and Synthesis of Functional Materials for Smart Label Devices

Francesca Stals

A thesis submitted in partial fulfilment of the requirements for the award of

Doctor of Philosophy

School of Natural and Environmental Sciences, Chemistry

Newcastle University

July 2024

Abstract

Maintaining the quality of temperature-sensitive products across the cold-supply chain is critical in preventing food waste and loss. Time temperature indicators (TTIs) are a type of smart label that can offer part of the solution to this complex problem. Unlike conventional "use-by date" labels, TTIs monitor the cumulative effects of time and temperature, and provide a visual indication to the consumer when the product is no longer safe for consumption. Providing the end user with this information can greatly reducing waste by presenting a real-time evaluation of food freshness.

The aim of this project is to identify and develop functional materials that can be integrated into a TTI smart label device as either a) the visible indicator, or b) as a functional component that provides autonomous activation via light-sensitive microfluidic valves.

In the first section of this work, polyoxometalate-polymer hybrids were synthesised for use as redox-active colour indicators. *N*-vinylimidazole and *N*-vinylimidazolium monomers were co-polymerised with poly(ethylene glycol) diacrylate crosslinkers to yield highly crosslinked polymer networks. $[PMo_{12}O_{40}](TBA)_3$ was immobilised onto the polymer supports and reduction of the resulting composite materials with aqueous ascorbic acid resulted in vivid colour changes. The hybrid materials were then integrated into prototype diffusion-based TTIs. Temperature and ascorbic acid concentration was varied, and it was found that the prototype systems exhibited time-temperature dependent colour changes, although there were inconsistencies between repeated device experiments. More elaborate device designs are needed in any future work to address this issue.

In the latter section of this thesis, an array of spiropyran derivatives were synthesised *via* palladium catalysed Suzuki-Miyaura cross coupling reactions between bromo-substituted spiropyrans and arylboronic acids. Conversions of up to 99 % were recorded under mild reaction conditions and with low catalyst loadings. Phenol- (SpOH) and pyridine- (SpPy) substituted spiropyran derivatives were shown to possess photochromic and acidochromic properties. Interestingly, SpPy derivatives also displayed solid-state photochromism. SpOH compounds were further transformed into spiropyran-acrylates (SpA) for covalent incorporation into poly(*N*-isopropylacrylamide)-based hydrogels as light-responsive microfluidic valves. However, light actuation was not observed as smaller-scale testing methods were required.

Acknowledgements

Table of Contents

Appendix   150

List of Abbreviations

AA	Acrylic acid
BuVimBr	1-butyl-3-vinylimidazolium bromide
FTIR	Fourier-transform infrared spectroscopy
MBIS	N,N'-Methylenebis(acrylamide)
Mc	Merocyanine
McH$^+$	Protonated merocyanine
NIPAM	*N*-Isopropylacrylamide
PEG	Poly(ethylene) glycol
PEG400DA	Poly(ethylene) glycol (M_n = 400 g/mol)
PEG700DA	Poly(ethylene) glycol (M_n = 700 g/mol)
PMo$_{12}$	$[PMo_{12}O_{40}](TBA)_3$
POM	Polyoxometalate
POM@Polymer	Polyoxometalate-polymer composites
PW$_{12}$	$[PW_{12}O_{40}](TBA)_3$
SEM	Scanning electron microscopy
SiW$_{12}$	$[SiW_{12}O_{40}](TBA)_4$
Sp	Spiropyran
SpA	Acrylate-substituted spiropyran
SpBr	Bromo-substituted spiropyran
SpOH	Phenol-substituted spiropyran
SpPy	Pyridine-substituted spiropyran
TEM	Transmission electron microscopy

TGA   Thermogravimetric analysis

UV-Vis   Ultraviolet-visible spectroscopy

Vim   *N*-vinylimidazole

TTI   Time-temperature indicator

List of Figures

List of Tables

List of Schemes

Chapter 1 Introduction

1.1 Intelligent and Active Packaging

As worldwide population is estimated to reach 9.7 billion by 2050, the development of new initiatives to improve the sustainability of global food production is of great importance.[1] Recent studies carried out by the Food and Agricultural Organization of the United Nations (FAO) has revealed that an estimated 30 % of all food produced for human consumption is wasted or lost.[2] *Food loss* refers to produce losses across the upstream food supply chain due to factors such as lack of infrastructure, poor handling and pre-harvest insect infestations. *Food waste* results from the retailer or consumer discarding food for reasons such as low quality, poor aesthetics, or over-purchasing. Food loss and waste represent a significant impact both economically and environmentally, giving rise to increases in food prices due to shortage, negatively impacting on farmers' incomes and the waste of natural resources used during the rearing/cultivation of products.[3]

Reliable packaging is essential to prevent the deterioration of food products throughout the supply chain and to the point of consumption by the end-user. Traditional food packaging has four main functions; protection, communication, convenience and containment (Figure 1.1).[4] Recent innovations in packaging technology have aimed to enhance one or more of these basic functions and address issues surrounding sustainability such as recyclability and reuse.[5] To this end, many different functional devices and materials have been developed for integration into food packaging, and are broadly assigned to two main categories, as defined by K. L. Yam *et. al.*[4]:

- **Active packaging (AP)** *actively preserves* perishable products by maintaining the internal environment of the packaging, therefore improving shelf-life and quality (e.g., oxygen scavengers and moisture controllers).
- **Intelligent packaging (IP)** *monitors the product quality in real time* and communicates with the user, thereby reducing waste and improving consumer confidence (e.g., time-temperature indicators).
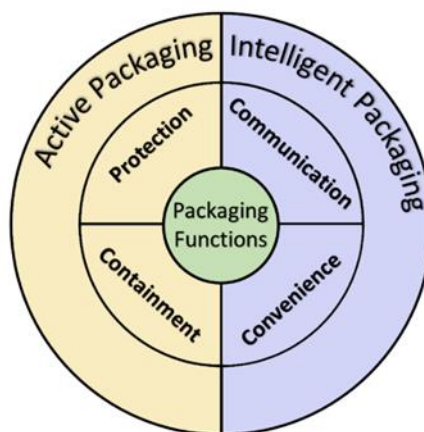
Figure 1.1: Model of packaging functions where AP technology enhances protection and containment of goods and IP enhances communication with and convenience for the consumer. Image recreated from reference 4.

There are many commercially available AP systems including moisture absorbers, antimicrobial packaging, and oxygen scavengers.[6] There are also different types of IP systems, known as "smart labels", which include time-temperature indicators (TTIs) and biosensors. These devices are inherently more complex than conventional use-by labels due to their multi-component nature, which is essential for monitoring and reporting changes in food quality over time. The implementation of such devices into packaging can increase consumer confidence in food safety and hence minimise waste and risk of food-related illness.

1.2   Time Temperature Indicators

Time temperature indicators (TTIs) are a type of smart labelling device that monitor the temperature of a product over time.[7] The TTI reports to the consumer when the product is no longer safe for consumption *via* an irreversible visible signal, i.e., a colour change. TTIs are currently one of the most widely used IP solutions as, unlike other types, the functioning of a TTI does not rely on the nature of the food product itself or the presence of chemical substances (e.g., deteriorative gasses). TTIs are designed to monitor the environment of the product instead of detecting any physical changes in the product itself, making them a relatively simplistic option.[8]

Given that temperature abuse is one of the most dominant contributory factors to the spoilage of fresh food, the development of accurate TTIs is of particular interest as they

can enable suppliers, retailers, and consumers to monitor the quality of their product across the whole cold-chain.[9] For example, a recent study carried out by Göransson *et. al.* investigated the temperature at which smoked ham and fresh cod were kept in Swedish cold food supply chains.[10] The group explored the effect that deviations from safe temperatures across the supply chain had on the shelf life of the perishable products. From their field-test studies, they concluded that temperature abuse mostly took place in retailer displays, and that monitoring the temperature of the products across the whole supply chain was of high importance to ensure appropriate levels of food safety and quality. Additionally, the group highlight the fact that perfectly safe-to-eat products were thrown away as manufacturers state the shelf-life of a product based on whole-lifetime storage at the maximum recommended temperature. However, in practice, most efficient cold food supply chains ensure products are kept at temperatures lower than the allowed maximum. This issue leads to consumers and retailers unknowingly wasting food by following safety protocol according to conventional use-by labels. Overall, the issues discussed in the study highlight the general need for monitoring devices such as TTIs.

1.2.1 Chemical Time Temperature Indicators

TTI types can be divided into three categories based on their working principle; chemical, physical, or biological.[11] A *chemical TTI* is designed to present a colour change to the user *via* a chemical reaction that is initiated through device activation. The onset and extent of the chemical reaction is dependent on the cumulative effects of temperature and time.[12] Colour change of the indicators in commercially available chemical TTIs involve polymerisation or photochromic reactions. Research of redox-based systems has also been investigated, however, toxicity and accuracy issues have prevented such devices from being used commercially.[13]

The Fresh-Check® TTI is based on the polymerisation of a thin layer of colourless acetylenic monomer to a coloured, opaque polymer.[14] As the temperature rises, polymerisation of the monomeric species increases at a rate that is comparable with the deterioration of the product's quality. The visible aspect of the label is made up of an inner circle (the active indicator) and a darker outer oval (Figure 1.2a). Once polymerisation is initiated, the inner circle of the label becomes darker, eventually signaling to the consumer that the product has reached expiry. The chemical changes that bring about this colour

change involve a 1,4-addition polymerisation reaction that yields polydiacetylene (PDA) polymers (Figure 1.2b). The resulting conjugated polymers have alternating ene–yne sequencing and are highly coloured.[15]
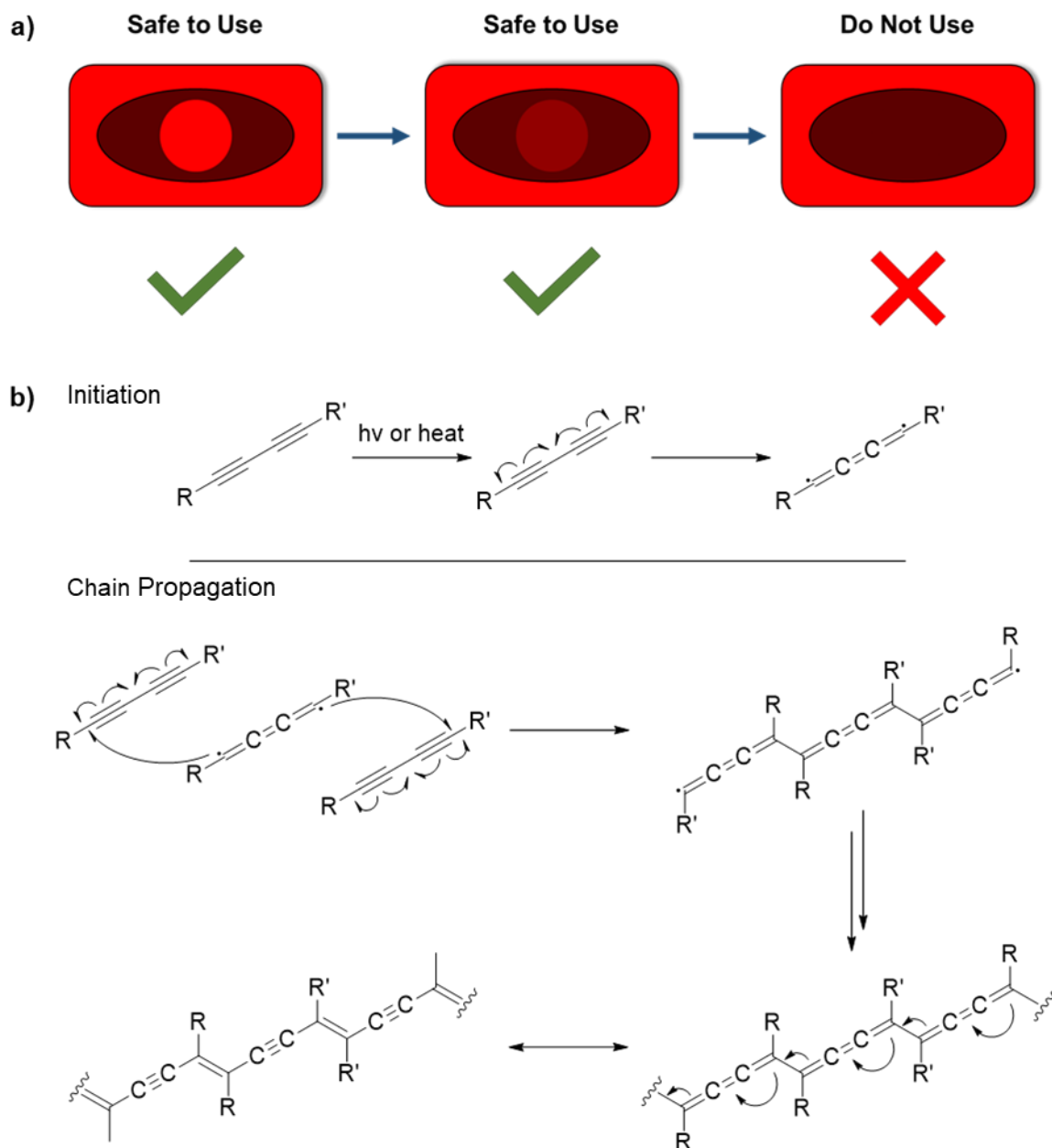
Figure 1.2: a) Schematic of the Fresh-Check® TTI. After activation, the central part of the label containing the colourless monomer gradually begins to change colour until it matches the colour of the surrounding label, indicating food is no longer safe for consumption; b) the 1,4-addition polymerisation mechanism of monomeric diacetylene to polydiacetylene (PDA).[16]

OnVu™ is a non-toxic, printable TTI label that uses a photochromic ink as an indicator (Figure 1.3a).[17] A spiropyran (Sp) chromophore is used as the active colour-changing element in the ink. In the ring-closed stable form, the Sp compound is colourless. Upon exposure to UV light, Sp isomerises to the deeply blue coloured, metastable merocyanine (Mc) isomer (Figure 1.3b). The label is firstly "charged" with UV-light, then a UV-filter film is placed onto the label (to prevent "recharge" of the chromophore *via* UV light). The Mc in the ink then thermally relaxes to the more stable Sp form, which results in fading of the dark-blue ink with time, and the process is accelerated at higher temperatures. Once the dark ink fades to a colour similar to that of the surrounding label, the product is no longer safe for consumption.
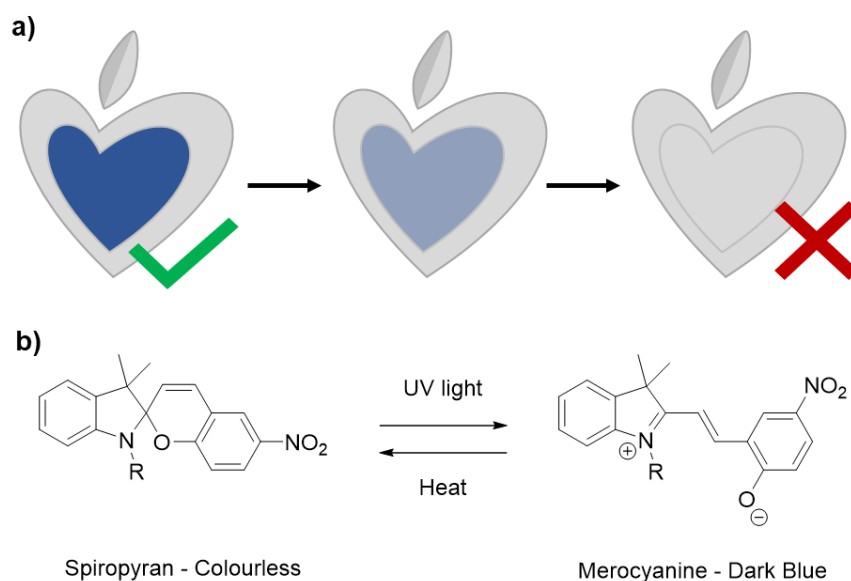
Figure 1.3: a) Schematic of the OnVu™ TTI where the photochromatic indicator in the central part of the label fades in colour over time; b) scheme to show spiropyran (Sp) and merocyanine (Mc) isomers.

A redox-active, fadable ink-based TTI was developed by Y. Galagan and W. F. Su.[13] The red-coloured reduced species of an anthraquinone derivative was used as the active component within the ink, which in the presence of oxygen, fades to a beige colour (Figure 1.4). The TTI was constructed by printing the word "FRESH" onto a substrate using the ink, under oxygen-free conditions. A polyacrylate protective coating was added as a seal to prevent water damage, and to control the rate of oxygen diffusion to the active part of the label. The TTI was then placed in air at 25 °C. Fading of the ink was observed and

after 5 days, the printed text was no longer legible. Although this system shows promise, commercial use is limited due to the toxicity of the components and the need for an oxygen-free atmosphere when synthesising the ink pigment and assembling/storing the device.
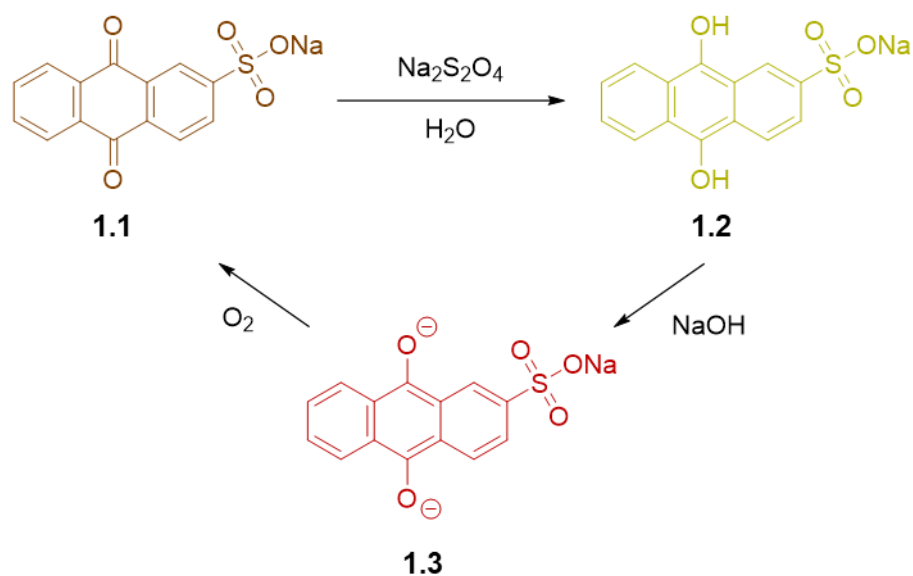
Figure 1.4: Scheme to show the redox processes within the ink. Reduction of beige-coloured sodium anthraquinone β-sulfonate **1.1** yields a yellow dihydroxyanthracene derivative **1.2**. Subsequent deprotonation with NaOH gives the red fadable ink pigment **1.3**. Reoxidation of **1.3** in the presence of O_2 yields **1.1**, which allows for fading of the printed text in the TTI.

1.2.2 Physical Time Temperature Indicators

Physical TTIs use working parameters such as diffusion or electronic control. Many commercially available, inexpensive TTI systems are based on diffusion-controlled devices e.g., MonitorMark™ and Tempix.[18]
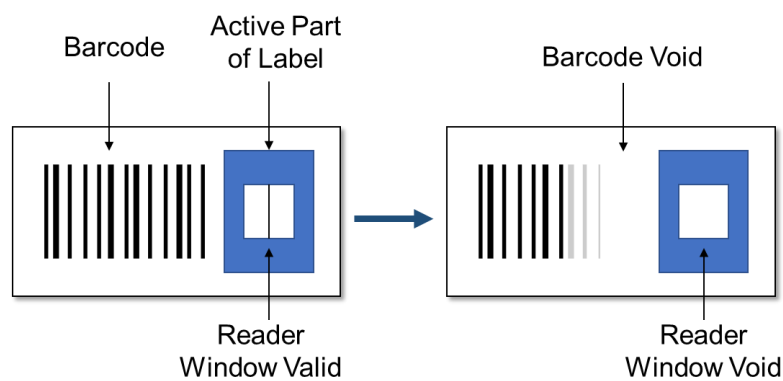
Figure 1.5: A schematic of the Tempix[TM] label, a diffusion-based TTI. Once the temperature has reached an upper threshold limit, the active part of the label obscures the adjacent barcode so that the reader window becomes void.

Tempix is a diffusion based TTI that is designed to inform the consumer whether or not a product has been kept within a specified temperature range (Figure 1.5). The active part of the label is constructed of a porous, capillary-suctioning material and a substance that melts above a specified temperature, which is the activation mechanism of the device. Once activated, the control bar within the reader window disappears, and the adjacent barcode becomes unreadable. This type of label helps to identify the point in the cold chain that temperature abuse took place.[19]

MonitorMark™ is another example of a diffusion based TTI. A coloured fatty acid ester is held in a reservoir by a polyester thin film.[20] The device is activated once the melting point of the thin film is met and the coloured substance travels through a diffusion path. Remaining shelf life is indicated by the diffusion front of the mobile phase.

1.2.3 Biological Time Temperature Indicators

The working principle of biological-based TTI systems are based on enzymatic or microbiological reactions. Biological-based TTIs are designed to mimic food-spoilage by reproducing the microbiological reactions that take place within the food product itself e.g., lactic acid bacteria (LAB) TTIs such as TopCryo®.[21] The TopCryo® label contains an indicator window that is made up of pH indicators, a growth medium, and psychrotrophic LAB. Over time, the bacteria acidify the surrounding growth medium causing the pH to lower, and therefore the pH indicator to change colour from green to purple/red. The process is accelerated with any rise in temperature throughout the cold chain. There is a range of TopCryo® labels covering temperature limits from 2 ºC – 12 ºC.
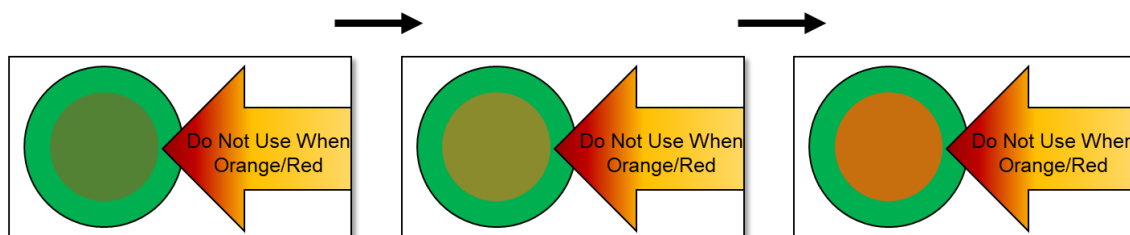
Figure 1.6: A schematic of CheckPoint®, an enzymatic based TTI. Pressure activation initiates the device, and once the indicator window appears orange/red, the consumer is visibly warned against use of the product.

CheckPoint® is an enzymatic-based TTI that changes colour as a lipid substrate is hydrolysed in the presence of lipase. This reaction produces an acid, causing a colour change in the pH indicator in the label (Figure 1.6).[22] The label is activated by pressure, whereby two separate compartments containing the lipid substrate and the enzyme are mixed. The labels can be tuned to fit the time-temperature profile of different products by adjusting substrate concentration and enzyme type.

1.2.4 Future Considerations

Some of the main issues surrounding current and developing TTI technology include:

- *Safety*: many TTIs contain potentially harmful/toxic substances. Devices must be designed so to ensure that no substances are able to leach from the label and contaminate food products.[23]
- *Accuracy*: there are many factors that may affect the accuracy of a given TTI. Firstly, TTIs do not monitor the quality/temperature of a food product directly, rather the surrounding environment. Manufacturers may also test devices under isothermal conditions, which does not reflect the temperature fluctuations that inevitably happen during real-life transport of goods, leading to errors in predicted shelf-life. Other issues include readability and misinterpretation of the indicator, manual activation errors and interference from other environmental factors e.g. light exposure can accelerate polymerisation processes in some chemical TTIs, or the re-oxidation of redox active ink TTIs in the presence of oxygen.[10]
- *Cost*: beyond research, the cost of a TTI becomes crucial for commercial implementation.[24] Manufacturers, retailers, and consumers will be unwilling to accept TTIs if they add significant cost to products.
- *Consumer Confidence*: understanding and willingness of consumers to accept TTI devices is of great importance. K. Pennanen *et. al.* carried out a study to gain insight into the perceptions that consumers had regarding TTI devices.[25] The group surveyed 16 focus groups from 4 European countries (Germany, Greece, Finland and France) and investigated the concerns participants had surrounding the use of TTI devices. Overall, it was found that the majority of participants thought that TTIs offered a sense of safety and security, but most people also had concerns around accuracy, mistrust in manufacturers, increase in the cost of goods and safety.

In the development and commercialisation of any future TTI devices, the issues discussed above must be considered to successfully integrate this emerging technology into everyday food packaging.

1.2.5 Proposed Device Designs

To provide an understanding of the overall aims of this project, two initial label concepts are outlined below. Both label/device concepts rely on specific properties of functional materials to operate effectively, the background chemistry of which will be discussed in the subsequent sections of this chapter.

Concept 1 is a chemical and diffusion based TTI (Figure 1.7). It includes a concealed diffusion matrix and reagent reservoir, as well as an indication window that can be seen by the consumer. After device activation, the liquid reagent travels through the diffusion matrix towards the indicator window. Once the diffusion front reaches the indicator window, a colour change will progress. This concept was based on the idea of a redox-active label, with reaction between a liquid reagent (reductant) and an indicator (oxidant) leading to the colour change that the consumer would see.
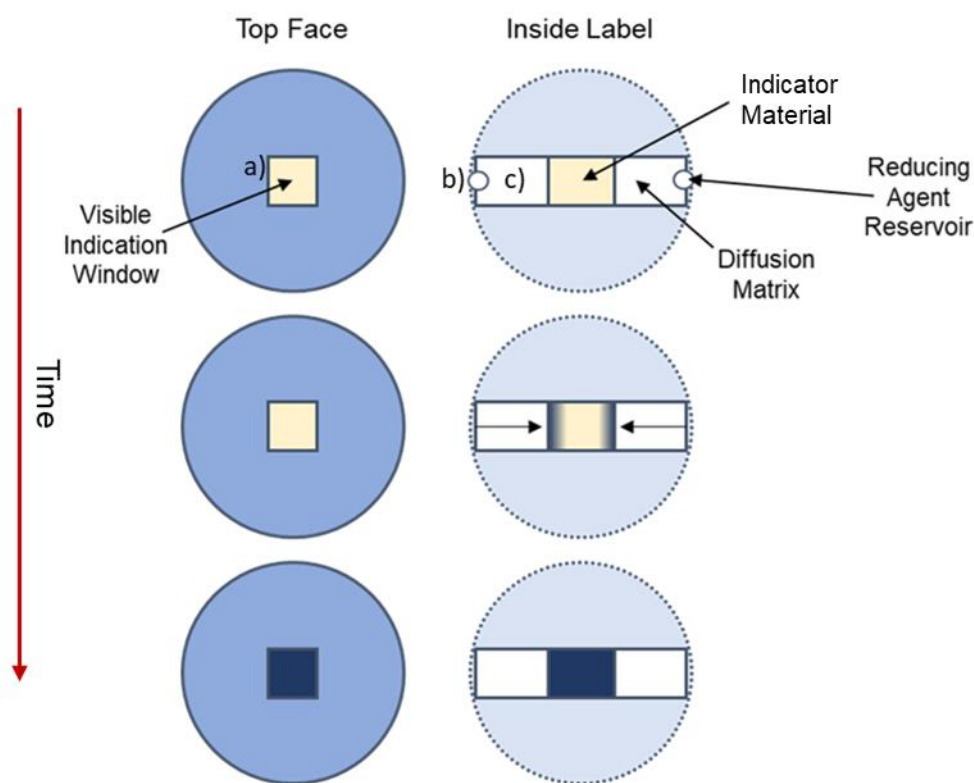
Figure 1.7: Concept 1. Schematic to show an example design principle for a TTI with; a) a visible indicator window, b) reagent reservoirs to hold a liquid component for diffusion, and c) a diffusion matrix. After a given activation mechanism (e.g. pressure), a reducing agent is released from the reservoirs (b). The reducing agent travels through the diffusion

track (c). The time in which it takes to reach the indicator and react to induce colour change is dependent upon temperature.

In order to explore the concept outlined above, Keggin-type polyoxometalates (POMs) were identified potential redox-active indicators, as they are known to undergo vivid colour changes upon reduction. Further details of POM chemistry is given in Section 1.4.

To investigate the prospect of autonomous activation of a TTI, Concept 2 was envisioned (Figure 1.8). In this design, a reagent is held in a reservoir by a light-sensitive material acting as a valve. Upon exposure to visible light, the valve material "opens", allowing the liquid reagent to flow through the diffusion path towards the indicator. To this end, light-responsive hydrogels were identified as potential candidates as valve materials. This concept is discussed further in Section 1.3.
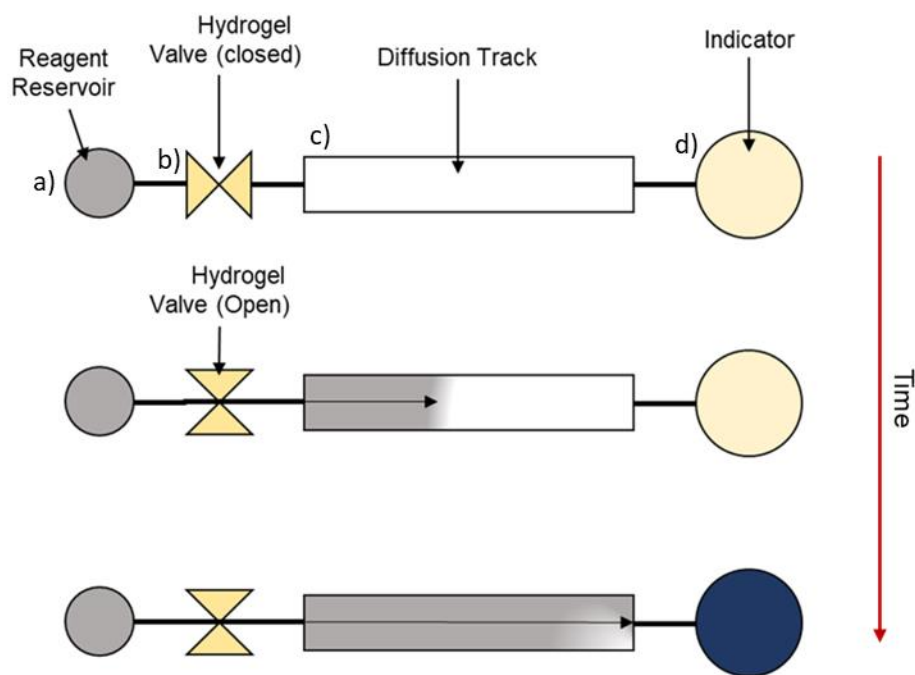
Figure 1.8: Concept 2. A schematic to show a light-actuated diffusion-based TTI design; a) a reagent reservoir, b) light sensitive hydrogel valves, c) a diffusion track and d) an indicator. The device activates upon exposure of the valves (b) to light. After activation, the reagent from the reservoir (a) will travel through a diffusion path (c). The time in which it takes for the reagent to diffuse to the indicator (d) is dependent on the temperature.

1.3   Hydrogels as Light-Activated Valves

1.3.1 Background

Hydrogels are highly crosslinked polymer networks that are capable of retaining large volumes of water in the swollen state.[26] This characteristic arises from hydrophilic functional groups attached to the polymer backbones of hydrogels and the high degree of crosslinking between polymer chains, preventing dissolution in water. The mechanical properties of different hydrogels can vary greatly and can be tuned to suit specific applications by varying properties such as crosslinking density and water content.[27]

Hydrogels have gained considerable research interest over the past few decades due to their versatility and potential as functional materials. The table below summarises a small selection of commercially available hydrogel products and their uses.

Application	Example	Description
Wound dressings	Suprasorb® G [28]	Acrylic, polyethylene and phenoxyethanol based hydrogel film
	Neoheal® Hydrogel [29]	Agar, polyvinylopyrrolidone, and polyethyleneglycol hydrogel film
Cosmetics	Simple® Water Boost™ [30]	A "100 % hydrogel" face mask infused with plant collagen and PENTAVITIN™
	e.l.f Hydrogel Under Eye Mask [31]	An agar-based hydrogel mask infused with water, seaweed extract and licorice
Contact Lenses	Biotrue® ONEday [32]	An *N*-vinyl pyrrolidone/ (hydroxyethyl)methacrylate copolymer with a water content ~ 78 %, which incorporates a UV filter

	ACUVUE® VITA™ [33]	A monthly-disposable *N*-vinyl pyrrolidone-based hydrogel contact lense with silicones.
Cell Cultures	Collagel® Kit [34]	A collagen gel solution with fast gelation at 37 ˚C for 3D cell-seeded bioartificial gel.
	Polyacrylamide [35]	A widely-used material for 2D-cellcultures
Dermal Fillers	Juvéderm™ [36]	A dermal filler based on hyaluronic-acid cross-linked with butanediol diglycidyl ether.
	CosmoDerm® [22]	A collagen-based filler used for reducing the appearance of wrinkles.
Medical Electrodes	TheraGel [37]	The hydrogel acts as an interface between the electrode and the patients skin, delivering dispersed therapeutic electrical current.

Table 1.1 A non-exhaustive list of some of the common applications of hydrogels and commercially available examples.

1.3.2 Classification of Hydrogels
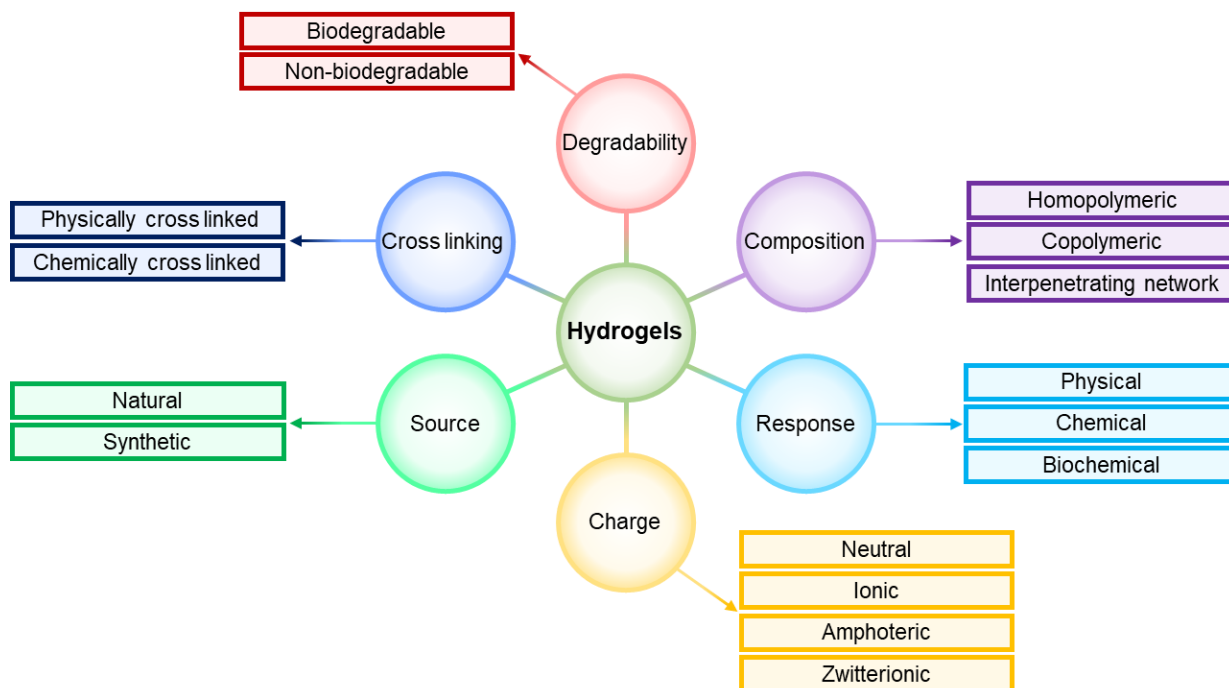
Figure 1.9: Diagram to summarise some of the main ways in which hydrogels are categorised, based on different properties.

There are many ways in which a hydrogel can be classified (Figure 1.9). Each classification method has been outlined in detail below:

Type of Crosslinking

The crosslinks between polymer chains in hydrogels can be physical (e.g., hydrogen bonding, chain entanglement) or chemical (e.g. covalent, ionic).[38]

- *Chemically crosslinked (CC) hydrogels*: CC gels consist of covalently linked polymer chains/networks. Monomers that have more than one polymerisable functionality are incorporated into the polymer backbone, which results in covalent crosslinking. CC gels are also known as permanent hydrogels, as their formation is irreversible due to the strong covalent crosslinks.
- *Physically crosslinked (PC) hydrogels:* PC gels are formed by virtue of physical interactions between polymer chains, including hydrogen bonding, hydrophobic interactions, chain entanglement and crystallite formation. PC gels are sometimes

15

referred to as reversible hydrogels, as the secondary interactions are weaker than covalent bonds. However, the physical interactions are sufficiently strong enough to prevent dissolution of PC gels in water.

Classification based on source

Hydrogels can be classified based on the source material used to synthesise the polymer i.e. *natural* or *synthetic* (Figure 1.10).[39]

- Examples of natural monomers used for hydrogel synthesis include collagen, fibrin, agarose, methylcellulose and chitosan.[40]
- Synthetic hydrogel source examples include poly(vinyl alcohols), poly(ethylene glycols), poly (vinyl ethers), acrylates and synthetic polypeptides.
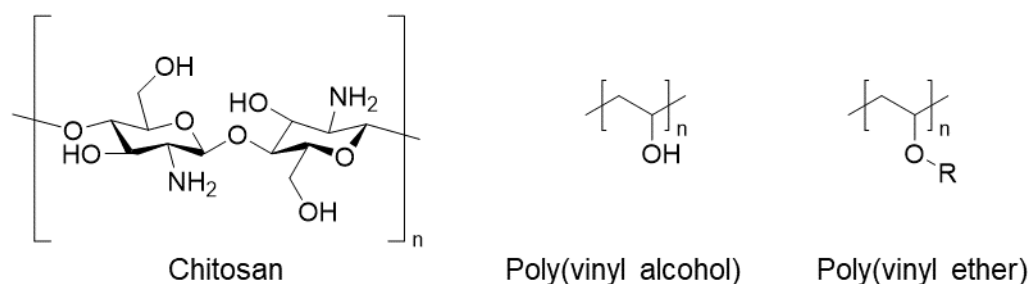
Figure 1.10: Chemical structures of Chitosan (natural hydrogel source), poly(vinyl alcohol) and poly(vinyl ether) (synthetic hydrogel sources).

Natural hydrogels tend to be used for biomedical/biological applications due to their non-toxicity, biodegradability and biocompatibility.[41] Synthetic hydrogels generally have enhanced mechanical strength and water/solvent uptake capacity.[42] *Hybrid hydrogels* are synthesised from a combination of natural and synthetic sources.

Classification based on composition/preparation

The classification type is based on the monomers/polymers used to prepare a hydrogel:[43]

- *Homopolymers:* homopolymeric hydrogels are synthesised with a single monomer species.
- *Copolymers:* copolymeric hydrogels are synthesised using more than one monomer species. At least one of the monomers must be hydrophilic. Depending on the polymerisation technique, the copolymers can be arranged in random, block or alternating configuration.
- *Interpenetrating Polymer Networks (IPNs)*: IPNs are made up from two or more independent polymer networks. At least one polymer is synthesised or crosslinked within the presence of the other, so that no covalent bonds are formed between the two separate components, but neither can be separated from the other without the cleavage of chemical bonds.

Classification based charged groups

Gel type can be categorised according to charged groups:[44]

- *Neutral hydrogels* – neutral (or nonionic) hydrogels have zero charge.
- *Ionic hydrogels -* contain cationic or anionic fragments.
- *Amphoteric hydrogels* – contain both basic and acidic fragments.
- *Zwitterionic hydrogels* – contain both anionic and cationic groups in each polymer unit where number of cationic groups = number of anionic groups.

Classification based on response:

Hydrogels can swell and deswell reversibly in water, resulting in significant volume changes. This feature has led to the design of functional hydrogels that respond (i.e. shrink or expand) to a variety of different stimuli: [45]

- *Physical*: hydrogels that respond to physical stimuli including light, temperature, pressure, electric fields, or magnetic fields.
- *Chemical*: hydrogels that respond to changes in pH, ionic strength, solvent and chemical species.

- *Biochemical*: hydrogels that respond to the presence/absence of biological components such as antigens, enzymes and ligands.

1.3.2 *Spiropyran Functionalised Light-Responsive Hydrogels*

Stimuli-responsive hydrogels are sensitive to external factors such as light, temperature and changes in pH. Exposing a "smart" hydrogel to such stimuli induces changes in their properties such as swelling, porosity and physical structure. Poly(*N*-isopropylacrylamide) based hydrogels are a well-known example; the thermoresponsive polymers undergo a lower critical solution temperature phase transition at ~32 ºC in water, from a hydrated swollen state to a shrunken dehydrated state.[46] Other forms of responsiveness can be introduced by incorporation of functionalised (co)monomers or additives to the hydrogel base material. This particularly advantageous feature has resulted in the implementation of hydrogels in a wide variety of applications; from pH-responsive sustained drug-release systems [47] to light-actuated microfluidic control.[48]

Response to light has previously been achieved by functionalising hydrogels with photosensitive components. The covalent attachment of molecular photoswitches such as azobenzene- [49], diarylethene- [50], stilbene- [51] and spiropyran-derivatives [52] has been widely investigated due to their tunable and reversible reconfiguration upon exposure to light.
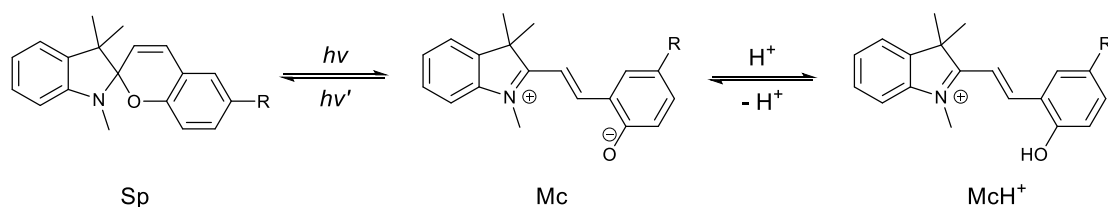
Scheme 1.1**:** Photo-induced isomerisation of spiropyran (Sp) to the ring-opened merocyanine isomer (Mc). Protonation of the Mc isomer increases stability.

Spiropyran derivatives are a particularly interesting class of photoswitch, as isomers possess greatly different properties (Scheme 1.1).[53] In particular, the difference in hydrophilicity between the isomers means that covalent incorporation of spiropyran fragments into the backbone of hydrogels allows for light-mediated control over swelling properties (Figure 1.11). This has led to a significant amount of research focused on the development of spiropyran-hydrogel materials as photo-actuated valves for microfluidic

control in small devices. For example, Sumaru *et. al.* developed Sp-containing hydrogels and explored their use as photoresponsive microvalves for fluid manipulation.[54] The group used poly(*N*-isopropylacrylamide) as the base polymer and modified it with 1.5 mol% *N,N*-methylene-bis(acrylamide) crosslinker and 1 mol% spiropyran monomer. The gels were treated with acid before light stimulation and after 120 s of blue light irradiation at 28 °C, the gels contracted to 68 % of their original size. Shrinking was attributed to the isomerisation of the spiropyran monomer from its protonated ring-opened form to its more hydrophobic ring-closed form, inducing expulsion of water from the hydrogel network. The group then explored how modifications made to spiropyran fragments (e.g. introducing electron-withdrawing/donating groups) effected the kinetics of isomerisation of the chromophore.[55] They found that they could influence the rate of ring opening by selecting specific substituents at different positions of the spiropyran chromene fragment.
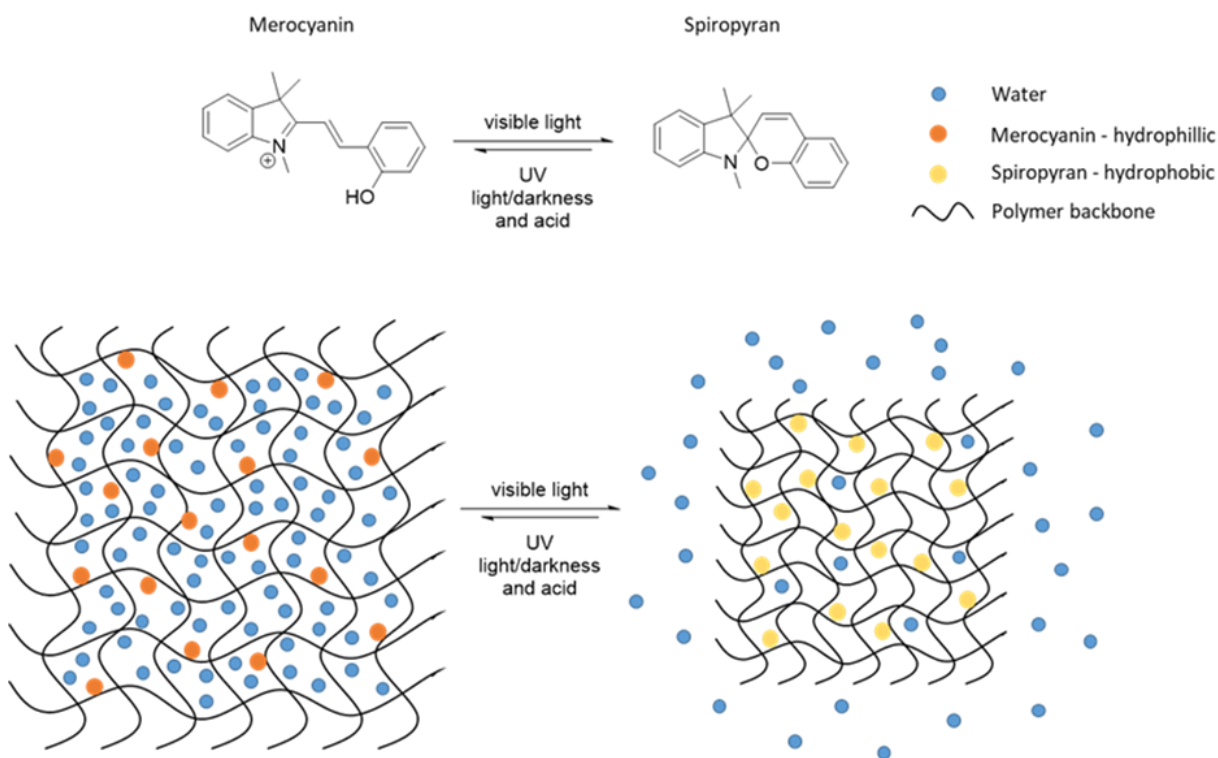
Figure 1.11: Schematic to show the reversible swelling and deswelling of a spiropyran-functionalised hydrogel.

The main disadvantage associated with the system developed by the Sumaru group was the prerequisite of treatment and storage in strongly acidified solutions in order for light stimulated shrinkage to be achieved. Low pH was essential to the reversible swelling

function of the valves, as by virtue of the acidic environment, the hydrophillic McH$^+$ isomer was thermodynamically favorable in the absence of light. This ensured the materials were in a constant "swollen state" prior to light actuation and reverted back to this state once light stimulation ceased.

The Diamond group later addressed the issue surrounding acid treatment by incorporating small amounts of acrylic acid monomer (AA) into Sp-modified poly(NIPAM) gels (Figure 1.12).[56] The group synthesised a series of gels with 1 mol% spiropyran monomer and differing amounts of AA from 0-5 mol% and allowed them to swell in deionised water in the dark. The gels were then exposed to white light for up to 20 mins. It was found that the gel containing the greatest concentration of AA (5 mol%) showed relative shrinkage of ~ 50 % compared to a negligible amount of shrinking for the gel containing no AA. Upon investigating the effect of Sp concentration at 5 mol% AA, the group found that the extent of shrinking increased slightly (to ~46 % of the original size) at 2 mol% Sp monomer. The extent of shrinking decreased dramatically with 3 mol% Sp monomer, as the gel retained ~76 % volume. They also addressed that the amount of AA and Sp had an effect on the kinetics of reswelling after light exposure. Overall, the self-protonation feature improves the activation mechanism of the valve material by removing the need to pre-soak in HCl. More recently, the Diamond-McCaul group further demonstrated the feasibility of their Sp-hydrogel valves by designing a fluidic platform and incorporating the gels into the channels *via in-situ* photopolymerisation. They achieved precise control of flow by using proportional-integral-derivative (PID) control for LED light stimulation.[57]
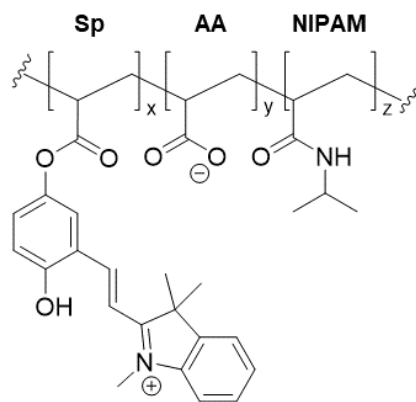
Figure 1.12: Structure of the self-protonating, light-sensitive hydrogel developed by the Diamond group.[56] The ring-opened merocyanine isomer is made more stable *via*

protonation from the acrylic acid. Where x, y and z are the relative molar ratios of Sp, AA, and NIPAM, respectively.

Sp-functionalised hydrogels are attractive candidates for use as light actuators in small devices. With further research and development, soft valves could be incorporated into TTI devices.

1.4   Polyoxometalates as Indicators

Polyoxometalates (POMs) are a class of metal-oxide cluster compounds (Figure 1.13). POMs consist of $\{MO_x\}$ building blocks, where M (known as the addenda atoms) are high oxidation-state metals in group 5 or 6 and x can vary from 4 to 7.[58] POMs are formed in a self-assembly process whereby tetrahedral metal complexes $\{MO_4\}$ expand into octahedra $\{MO_6\}$ and then condense under acidic conditions, resulting in shared oxo-ligands between clusters. The anionic building blocks can also coordinate to cationic heteroatoms (e.g. P(V), As(V), Si (IV)). Heteroatoms can be primary (essential to the structure of the POM) or secondary (filling externally vacant sites on partially decomposed POMs known as Lacunary anions).

Figure 1.13: Example of POM structures; Lindqvist, Keggin and Wells-Dawson from left to right.

POMs are well known for their rich redox chemistry and their ability to accept large numbers of electron without subsequent degradation. There are many different structural types of POMs that have been widely studied and their unique properties have led to their application in areas including catalysis, energy storage, biology and spectroscopy.[59]

Some polyoxometalate species, such as the Keggin anion $[PMo_{12}O_{40}]^{3-}$, undergo dramatic colour changes upon reduction to a highly-coloured mixed-valence species (Figure 1.14).

This feature has been used to develop analytical techniques such as colorimetric detection of P, As, Si and Ge.[60]
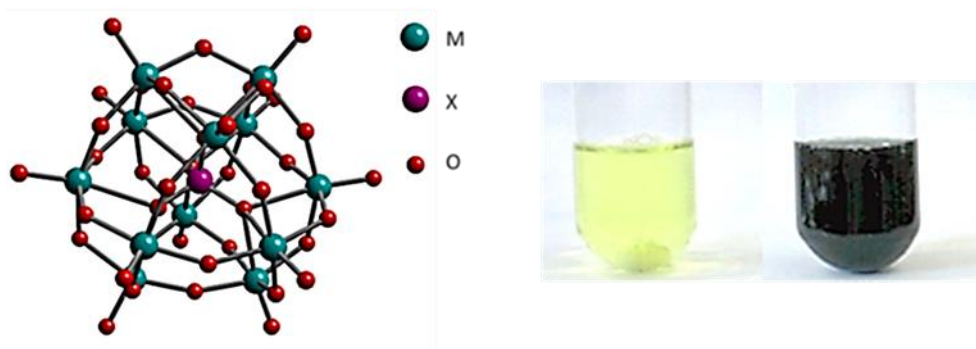
Figure 1.14: The general structure of a Keggin anion $[XM_{12}O_{40}]^{n-}$ where X = the heteroatom such as P or Si, M = the metal such as Mo or W (left) and the colour change from pale yellow to deep blue upon reduction of $[PMo_{12}O_{40}]^{3-}$ (right).

The use of a polyoxometalate-based indicator in a TTI device could help to overcome some of the issues surrounding redox-based TTIs such as toxicity. [61] However, to prevent leaching of any molecular species of POM, a solid support system to immobilise the anions would be necessary.

1.5 Project Aims

The aim of this work is to develop and investigate functional materials for smart label device concepts outlined in Section 1.2.5. The project can be divided into two main sub areas, as outlined below:

1.5.1 Polyoxometalate Composites as Indicators

A previously mentioned, Keggin-type polyoxometalates undergo vibrant colour changes upon chemical reduction, making this group of compounds potential candidates for use as redox-active indicators. However, to utilise this property within a smart label device, there are practical considerations that must be addressed. Firstly, the POM must not leach into other areas of the device when mixed with a chemical reducing agent solution. Further to this, a non-toxic reducing agent is required to mitigate safety concerns. Additionally, time-temperature dependency with respect to colour change must be established in any TTI system. With this in mind, the following research objectives were established:

Preparation of a suitable polyoxometalate support: hydrogel/polymer-based supports will be developed with the purpose of immobilising polyoxometalates to yield hybrid indicator materials. Neutral and ionic polymers will be investigated to establish whether POM-loading onto the support systems can be achieved without subsequent leaching.

Optimisation of the indicator: different Keggin-type POMs will be immobilised onto the polymer supports to ensure sufficient colour change is achieved upon reaction with a reducing agent. Hybrid materials containing both heteropoly acids, and organic salts of the POMs will be considered for reduction by aqueous ascorbic acid (vitamin C) as the non-toxic redox partner.

Testing of TTI Prototype System: prototype TTI devices will be constructed to confirm time-temperature dependent colour changes can be achieved with the use of the POM-polymer composites developed. The devices will be tested with variables such as temperature and reducing agent concentration to explore whether the time in which it takes for colour-change to occur differs.

1.5.2   Light Responsive Hydrogels as Valves

The main aim of this section of the project is to identify an appropriate synthetic route to access spiropyran-derivatives for incorporation into hydrogel base materials as light-actuated microfluidic valves. Additionally, the chromatic properties of Sp compounds will be explored. These aims are summarised through the following objectives:

Establish a synthetic route to access spiropyran derivatives: The synthesis of simple spiropyran compounds is well-established, but further reaction is required to introduce additional functionality such as polymerisable groups. To this end, bromine-substituted Sp compounds will be synthesised for further modification *via* Suzuki cross-coupling reactions. This work will aim to establish optimal reaction conditions between structural isomers of bromo-substituted spiropyran compounds and a variety of arylboronic acids, catalysed by an efficient palladium catalyst.

Explore the chromatic properties of Sp-derivatives: once Sp-derivatives have successfully been synthesised, their acido- and photochromatic properties will be investigated *via* UV-Vis spectroscopy. Comparison of the results will allow for an understanding of the effect that different substituents have on the properties of Sp-derivatives.

23

Incorporate Sp-derivatives into hydrogels for use as light-actuated valves: Sp-derivatives in this work will be incorporated into poly(*N*-isopropylacrylamide) based hydrogels and response to visible light will be compared to a literature benchmark material. These materials will act as microfluidic valves outlined in the TTI design in Section 1.2.5 (Figure 1.8).

1.6   References

[1] United Nations, Department of Economic and Social Affairs, Population Division, 2015 World Population Prospects: The 2015 Revision, Key Findings and Advance Tables, https://population.un.org/wpp/Publications/Files/Key_Findings_WPP_2015.pdf (accessed May 2019)

[2] Food and Agricultural Organisation of the United Nations, Global Initiative on Food Loss and Waste Reduction, 2015, http://www.fao.org/3/a-i4068e.pdf (accessed May 2019)

[3] Food and Agricultural Organisation of the United Nations, Food Loss and Waste in the Food Supply Chain, http://www.fao.org/3/a-bt300e.pdf, (accessed May 2019)

[4] K. L. Yam, P. T. Takhistov, J. Miltz, *Food Sci.*, 2005, **70**, 1-10

[5] M. Vanderroost, P. Ragaert, F. Devlieghere, B. De Meulenaer, *Trends Food Sci. Technol.*, 2014, **39**, 47-62

[6] P. Prasad, A. Kochhar, *J. Environ. Sci., Toxicol. Food Technol.,* 2014, **8**, 1-7

[7] N. Bhargava, V. S. Sharanagat, R. S Mor, K. Kumar, *Trends Food Sci. Technol.*, 2020, **105**, 385-401

[8] E. Poyatos-Racionero, J. V. Ros-Lis, J. L. Vivancos, R. Martínez-Máñez, *J. Clean Prod.*, 2018, **172**, 3398-3409

[9] V. Adiani, S. Gupta, P. S. Variyar, *J. Food. Eng.*, 2021, **311**, 110731

[10] M. Göransson, F. Nilsson, Å. Jevinger, *Food Control*, 2018, **86**, 332-341

[11] Y. Guiavarc'h, A. Van Loey, F. Zuber, M. Hendrickx, 2004, *Innov. Food Sci. Emerg. Technol.*, **5**, 317-325.

[12] S. Wang, X. Liu, M. Yang, Y. Zhang, K. Xiang, R. Tang, *Packag. Technol. Sci.* 2015, **28**, 839–867

[13] Y. Galagan, W. F. Su, *Food Res. Int.*, 2008, **41**, 653-657

[14] M. Nuin, B. Alfaro, Z. Cruz, N. Argarate, S. George, Y. L. Marc, J. Olley, C. Pin, *Int. J. Food Microbiol.*, 2008, **127**, 193-199

[15] H. Y. Lee, K. R. Tiwari, S. R. Raghavan, *Soft Matter*, 2011, **7**, 3273-3276

[16] D. Takajo, K. Sudoh, *Langmuir*, 2019, **35**, 2123-2128

[17] J. Kreyenschmidt, H. Christiansen, A. Hubner, V. Raab, B. Petersen, *J. Food Sci. Tech.*, 2010, **45**, 208-215

[18] D. Y. Choi, S. W. Jung, T. J. Kim, S. J. Lee, *J. Food. Eng.*, 2014, **120**, 118-123

[19] JUSTIA Patents, https://patents.justia.com/assignee/tempix-ab, (accessed June 2021)

[20] M. Biegańska, D. Gwiazdowska, W. Kozak, K. Kluczyńska, presented in part at II Domestic Scientific Conference AGROLOGISTYKA 2014, Poznań, Poland, 2014.

[21] A. Girardeau, V. Biscola, S. Keravec, G. Corrieu, F. Fonseca, in *Lactic Acid Bacteria A Functional Approach,* M. A. C. de Albuquerque, A. de Monreno de LeBlanc, J. G. LeBlanc, R. Bedani, Taylor & Francis Group, Boca Raton, 2020, Ch. 14, 241-260

[22] A. Pavelková, *Acta Univ. Agric. Silvic. Mendel. Brun.*, 2012, **61**, 245-251

[23] P. S Taoukis, T. P. Labuza, in *Novel Food Packaging Techniques*, ed. R. Ahvenainen, Woodhead Publishing Ltd, Cambridge, 2003, 6, 103-122

[24] J. Han, L. Ruiz-Garcia, J. P. Qian, X. T. Yang, *Compr. Rev. Food Sci. Food Saf.*, 2018, **17**, 860-877

[25] K. Pennanen, C. Focas, V. Kumpusalo-Sanna, K. Keskitalo-Vuokko, I. Matullat, M. Ellouze, S. Pentikäinen, M. Smolander, V. Korhonen, M. Ollila, *Packag. Technol. Sci.*, 2015, **28**, 303-323

[26] Y. S. Zhang, A. Khademhosseini, *Science*, 2017, **356**, 1-10

[27] E. M. Ahmed, *J. Adv. Res.*, 2015, **6**, 105-121

[28] Lohmann & Rauscher International, https://www.lohmann-rauscher.com/en/products/wound-care/modern-wound-care/suprasorb-g-gel-dressing/, (accessed June 2021)

[29] Kikgel, https://kikgel.com.pl/en/products/neoheal/#-1, (accessed June 2021)

[30] Simple, https://www.simple.co.uk/products/face-scrubs-and-face-masks/water-boost-5-minute-reset-hydrogel-mask.html#accordion-content-22491785135124-2 (accessed June 2021)

[31] Boots, https://www.boots.com/elf-hydrogel-under-eye-masks-3s-10259617, (accessed June 2021)

[32] A. Lorente-Velázquez, M. García-Montero, F. J. Gómez-Sanz, L. Rico del Viejo, J. L. Hernández-Verdejo, D. Madrid-Costa, *Int. J. Ophthalmol.*, 2019, **4**, 640-646

[33] Johnson and Johnson Vision, https://www.jnjvisioncare.co.uk/contact-lenses/all-acuvue-brand-contact-lenses/spherical/acuvue-vita, (accessed June 2021)

[34] Flexcell International Corporation, http://store.flexcellint.com/collagel.html, (accessed June 2021)

[35] S. R Caliari, J. A Burdick, *Nature Methods*, 2016, **13**, 405-414

[36] S. Cascone G. Lamberti, *Int. J. Pharm.*, 2020, **573**, 1-19

37 TheraSigma, http://www.therasigma.com/wp-content/uploads/Hydrogel-Electrodes-White-Paper.pdf, (accessed June 2021)

38 J. Maitra, V. K. Shukla, *Am. J. Polym. Sci.*, 2014, **4**, 25-31

39 A. S. Hoffman, *Adv. Drug Deliv. Rev.*, 2012, **64**, 18-23

40 Jabran Saroia, W. Yanen, Q. Wei, K. Zhang, T. Lu, B. Zhang, *Bio. Des. Manuf.*, 2018, **1**, 265–279

41 Zhijun Shi, X. Gao, M. W. Ullah, S. Li, Q. Wang, G. Yang, *Biomaterials*, 2016, **111**, 40-45

42 S. Bashir, M, Hina, J. Iqbal, A. H. Rajpar, M. A. Mujtaba, N. A. Alghamdi, S. Wageh, K. Ramesh, S. Ramesh, *Polymers*, 2020, **12**, 2702

43 N. Das, *Int. J. Pharm. Pharm. Sci.*, 2013, **5**, 112-117

44 S. Garg, A. Garg, *Asian J. Biomater. Res.*, 2016, **2**, 163-170

45 F. Ullah, M. B. H. Othman, F. Javed, Z. Ahmad, H. Md. Akil, *Mater. Sci. Eng. C*, 2015, **57**, 414-433

46 R. Pelton, *J. Colloid Interf. Sci.*, 2010, **348**, 673-674

47 P. Patel, A. Mandal, V. Gote, D. Pal, A. K. Mitra, *J. Polym. Res.*, 2019, **26**, 1-11

48 D. J. Beebe, J. S. Moore, J. M. Bauer, Q. Yu, R. H. Liu, C. Devadoss, B. H. Jo, *Nature*, 2000, **404**, 588–590

49 K. G. Yager, C. J. Barrett, *J. Photoch., Photobio., A*, 2006, **182**, 250-261

50 Z. Li, H. Chen, B. Li, Y. Xie, X. Gong, X. Liu, H. Li, Y. Zhao, *Adv. Sci.*, 2019, **6**, 1901529

51 I. G. Ivanova, D. Kuckling, H. J. P. Adler, T. Wolff, K. F. Arndt, *Des. Monomers Polym.*, 2012, **3**, 447-462

52 C. Li, A. Iscen, L. C. Palmer, G. C. Schatz, S. I. Stupp, *J. Am. Chem. Soc.*, 2020, **142**, 8447−8453

53 R. Klajn, *Chem. Soc. Rev.*, 2014, **43**, 148-184

54 a) K. Sumaru, M. Kameda, T. Kanamori, T. Shinbo, *Macromolecules*, 2004, **37**, 4949-495; b) K. Sumaru, K. Ohi, T. Takagi, T. Kanamori, T. Shinbo, *Langmuir*, 2006, **22**, 4353-4356; c) K. Sumaru, S. Sugiura, K. Ohi, K. Hiroki, T. Takagi, T. Kanamori, *Sens. Actuators A*, 2007, **140**, 176–184

55 K. Sumaru, T. Satoh, T. Takagi, T. Kanamori, *Soft Matter*, 2011, **7**, 8030-8034

56 B. Ziołkowski, L. Florea, J. Theobald, F. Benito-Lopez, D. Diamond, *Soft Matter*, 2013, **9**, 8754–8760

[57] K. Pandurangan, R. Barrett, D. Diamond, M. McCaul, *Front. Mater*, 2021, **7**, 466-477

[58] M. Hutin, M. H. Rosnes, D.-L.Long, L.Cronin, in *Comprehensive Inorganic Chemistry II (Second Edition)*, ed. J. Reedijk, K. Poeppelmeier, Elsevier, Amsterdam, 2nd edn, 2013, vol. 2, ch. 2, pp. 241-269

[59] W. Liu, X. L. Wang, Y. Q. Lan in *Polyoxometalate-Based Assemblies and Functional Materials*, ed. Y. F. Song, Springer International Publishing, Switzerland, 1st edn, 2017, vol. 176, ch. 5, pp. 89-119

[60] S. Ganesh, F. Khan, M. K. Ahmed, P. Velavendan, N. K. Pandey, U. Kamachi Mudali, *Water Sci. Technol.*, 2012, **66**, 2653-2658

[61] S. Omwoma, C. T. Gore, Y. Ji, C. Hu Y.-F. Song, *Coord. Chem. Rev.*, 2015, **286**, 17-29

Chapter 2 Polyoxometalate Polymer Composite Materials

2.1 Introduction

Polyoxometalates are well known for their rich redox chemistry and their ability to accept large numbers of electrons without subsequent degradation.[1] They have been widely studied, and their unique properties have led to their utilisation in areas including catalysis, energy storage, biology and spectroscopy.[2] A distinguishable characteristic associated with certain groups of POMs is the colour change they undergo upon reduction (i.e. POMs with metal atoms bearing single terminal M=O). This phenomenon is discussed in further detail below, with particular emphasis on the chemistry of Keggin-type polyoxometalates.

2.1.1 Chemical Reduction of Polyoxometalates

One of the earliest practical applications of Keggin-typ POMs, specifically molybdates, was adopted in the field of analytical chemistry for the quantitative and qualitative detection of orthophosphates.[3]
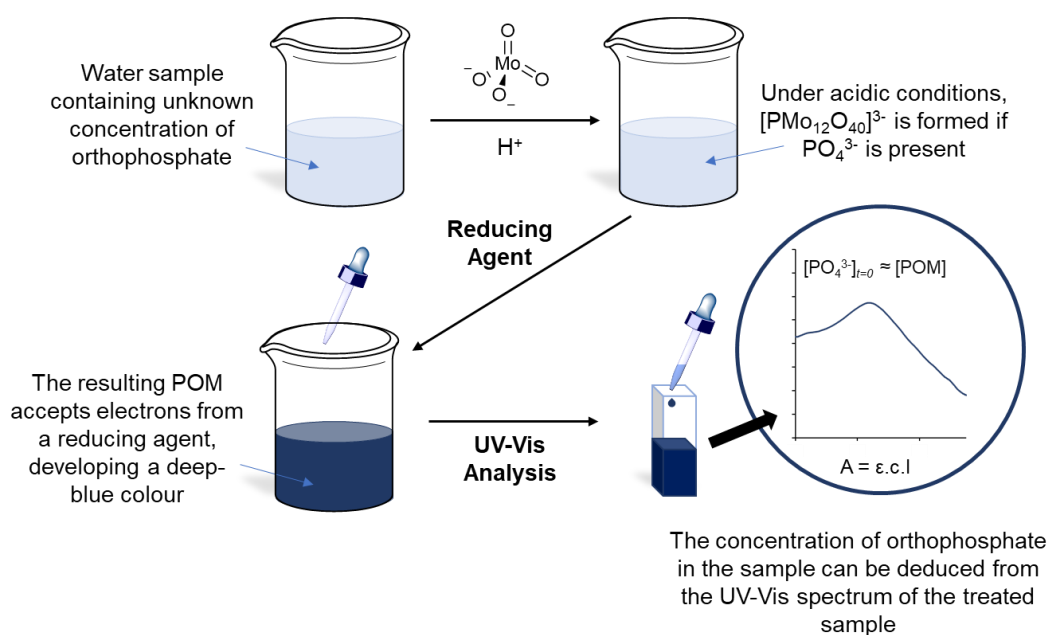
Figure 2.1: Schematic showing the steps involved in the molybdenum blue method for orthophosphate determination.

$$PO_4^{3-} + 12\ MoO_4^{2-} + 27\ H^+ \longrightarrow H_3[PMo_{12}O_{40}] + 12\ H_2O \qquad \textbf{(2.1)}$$

$$H_3[PMo(VI)_{12}O_{40}] + ne^- \longrightarrow [H_3PMo(VI)_{12-n}Mo(V)_nO_{40}]^{n-} \qquad \textbf{(2.2)}$$
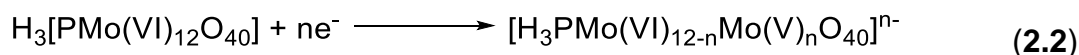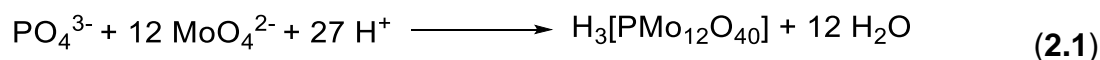
The analytical method involves mixing water samples containing an unknown concentration of PO^{4-} with a molybdenum oxide precursor. Acidification of the solution yields the heteropoly anion, $[PMo_{12}O_{40}]^{3-}$ (Equation **2.1**). The pale yellow Keggin ion becomes intensely blue upon reaction with chemical reducing agents (Equation **2.2**), a property of which was the foundation for its use as an indicator in the detection method. Due to the intense blue colour of the reduced POM species, this method allowed for confirmation of phosphate presence in the water sample with the naked eye. In addition, heteroatom concentration could be determined quantitatively by spectroscopic analysis (Figure 2.1). Entitled the "molybdenum blue method", the technique was developed further throughout the 20th century and has also been employed for the detection of silicates, arsenates and germanates.[4]

The intense colour and stability of the reduced species can be rationalised by examining the electronic structure of Keggin type POMs. The properties of $[PMo_{12}O_{40}]^{3-}$ (which will subsequently be abbreviated as PMo_{12}) will be discussed as an example, but the principles considered can be applied to other Keggin-type POMs (e.g. PW_{12}). Metal oxide units within the POM structure can be thought of as occupying *approximately* octahedral sites, and their electronic properties are comparable to that of the corresponding single-metal complexes where each metal centre is bonded to one terminal oxygen atom and five shared oxygen atoms $[MOL_5]$, and can be assigned with C_{4v} symmetry, giving rise to the molecular orbitals outlined in Figure 2.2.[5]

2a₁* + e*

$2a_1^* + e^*$

np

$a_1^*\ (xy)$

ns

$b_1^*\ (x^2 - y^2)$
$e^*\ (xz,\ yz)$

(n-1)d

$b_2\ (xy)$

$\pi\ (z)$

e

$\sigma\ (xy)$

$3a_1 + b_1 + e$

$\sigma\ (z)$

Metal Orbitals (M)   **Ligand Orbitals (O)**
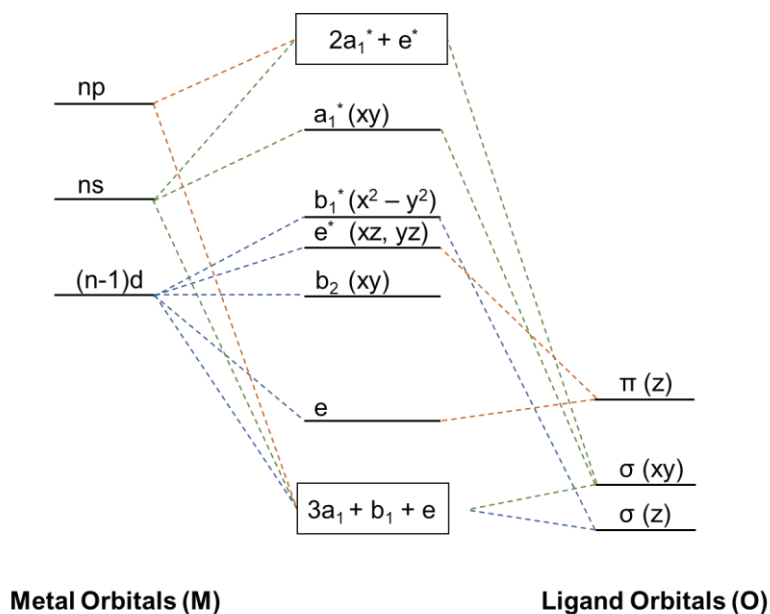
Figure 2.2: Molecular orbital diagram of an MOL_5 complex with C_{4v} symmetry.

Electrons are accepted into the d_{xy} (b_2) orbitals of the Mo centres of the POM. Given their non-bonding nature, reduction does not have a profound effect upon on metal-oxygen bond order, hence PMo_{12} and other Keggin POMs can accept multiple electrons while retaining structural integrity. Although Mo(V) d-d electronic transitions occur within reduced PMo_{12}, it is in fact the intervalence charge transfer (IVCT) between Mo(V) and Mo(VI) that is predominantly responsible for the deep blue colour, with strong molar absorptivities around 700 nm.[6]

2.1.2 Photochemical Reduction of Polyoxometalates

Heteropoly tungstates, vanadates and molybdates are well-established as photochemically active compounds, and colour change can be induced *via* UV-light.[7] These POMs exhibit strong absorption bands in the UV region due to ligand to metal charge transfer (LMCT) transitions from the terminal oxygen atoms to the M centres. Using PW_{12} as an example, UV-light absorption excites an electron from the HOMO of the ligand (O 2p-orbital) to the LUMO (metal d-orbital), resulting in the formation of a reactive oxo-radical (Figure 2.3).[8] In the presence of a protic organic substrate (e.g. an alcohol), the electron is trapped *via* hydrogen abstraction.[9]

This property has been exploited in various sensing applications, for example, M.Sánchez *et. al.* recently developed a sensor for the real-time naked-eye detection of ethanol in

saliva and sweat using PW_{12} as the active colour-indicator component.[10] The group impregnated a non-woven material with PW_{12} and placed artificial sweat/saliva samples containing various concentrations of ethanol onto the device, before irradiating with UV-light for 10 min (Figure 2.4). The study showed that the intensity of the blue colouration correlated with the concentration of ethanol in the samples, and therefore using this technique, alcohol concentrations could be judged with the naked eye and digital colour analysis.
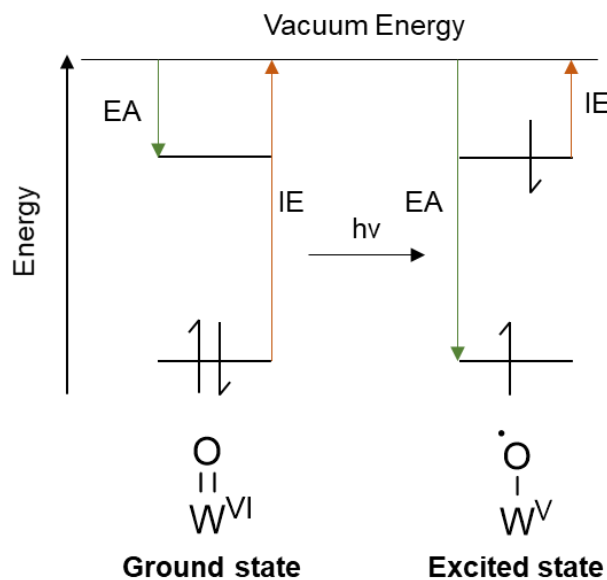
Figure 2.3: Simplified energy diagram showing the differences in electron affinity (EA) and IE ionization energy (IE) between the ground and photoexcited state of the POM. The excited state is both a better oxidant and reductant ($EA_{GS} < EA_{ES}$ AND $IE_{GS} > IE_{ES}$). Recreated from reference 8.
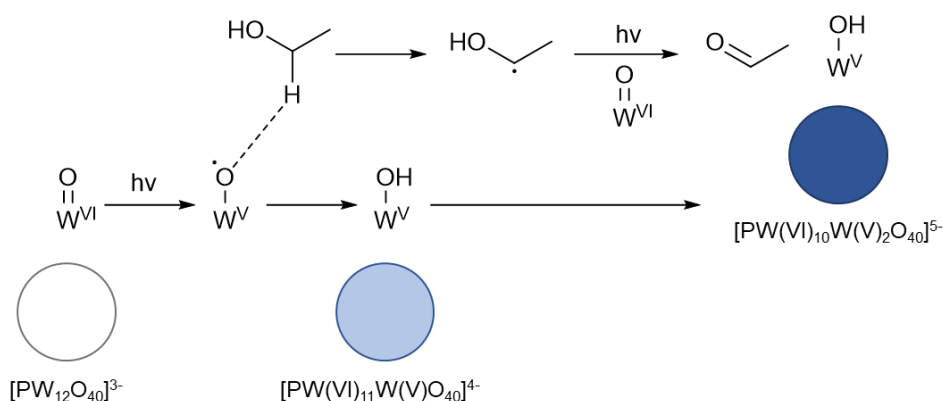
Figure 2.4: Schematic to show the photochemical reaction between PW_{12} and ethanol. Irradiation of UV light into the LMCT bands results in a photoexcited state. α-H abstraction from the alcohol leads to electron trapping and reduction of the POM. The POM is further reduced upon oxidation of the radical alcohol species to acetaldehyde.

2.1.3 Electrochemical Reduction of Polyoxometalates

The field of POM electrochemistry is vast, and new research into POM-based fuel cells, supercapacitors, batteries and electrocatalysts is quickly expanding.[11] It is a well-established fact that POMs undergo reversible, electrochemically induced redox processes, and POM reduction/oxidation potentials can be tuned with many variables such as pH, counter-ion, solvent, and of course, careful design of the POM itself (e.g. *via* substitution of addenda atoms with redox-active heteroatoms).[12]

An interesting application that combines the electrochemistry and colour change associated with reduction of POMs can be found in some electrochromic devices. For example, Wang and coworkers developed electrochromic devices for use as smart windows with two Preyssler-type POMs, $[NaP_5W_{30}O_{110}]^{14-}$ and $[NaS_5W_{30}O_{110}]^{9-}$ (abbreviated to P_5W_{30} and S_5W_{30}, respectively).[13] The group screenprinted TiO_2 onto a fluorine-doped tin oxide (FTO) electrode, then electrodeposited the POMs onto the titania *via* cyclic voltammetry. The devices were constructed by heat-sealing the POM@TiO_2/FTO working electrode together with an FTO counter electrode, before vacuum injecting 0.1 M LiI in propylene carbonate between the layers to act as the electrolyte in the system (Figure 2.5). Under an applied potential of – 1.5 V, the P_5W_{30} smart-window exhibited a deep-blue colour, whereas the S_5W_{30} smart window developed a deep-grey colour at – 2.0 V.
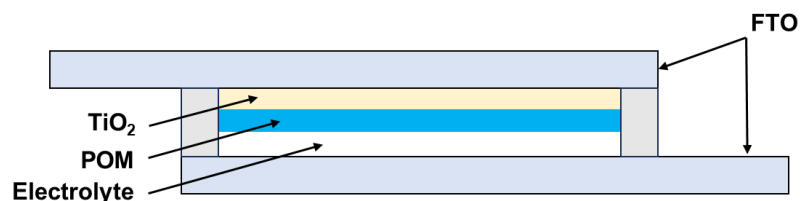
Figure 2.5: Schematic to show the construction of the Preyssler Pom-based electrochromic device.

2.2 Polyoxometalate, Polymer and Composite Synthesis

2.2.1 Polyoxometalate Synthesis

The counter cation can be selected to control the solubility of POMs in different solvents. Tetrabutylammonium (TBA) POM salts were identified as suitable candidates to prevent leaching from the polymer support into aqueous solution. This approach has previously been employed to prevent leaching of POMs from proton exchange membranes.[14]

Keggin-Type polyoxometalates were synthesised for further use in POM-polymer indicator materials using previously reported literature methods.[15] $[PMo_{12}O_{40}](TBA)_3$ **2.1** was synthesised from the sodium molybdate precursor (Scheme 2.1). Compounds $[PW_{12}O_{40}](TBA)_3$, **2.2** and $[SiW_{12}O_{40}](TBA)_4$ **2.3** were synthesised *via* ion exchange between the corresponding heteropoly acids and tetrabutylammonium bromide.

$$12\ Na_2MoO_4 \cdot 2H_2O + H_3PO_4 + 21\ HNO_3 + 3\ (TBA)Br \xrightarrow{1,4 - dioxane/H_2O} [PMo_{12}O_{40}](TBA)_3 + 3\ NaBr + 21\ NaNO_3 + 12\ H_2O$$
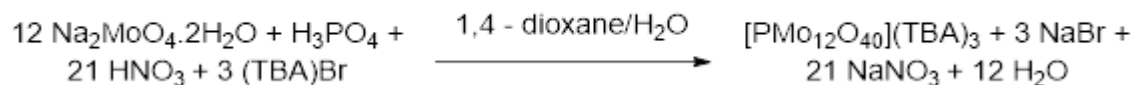
Scheme 2.1: The synthesis of $[PMo_{12}O_{40}](TBA)_3$ **2.1**

TBA salts **2.1**, **2.2**, and **2.3** were confirmed by FTIR and phosphorus-containing POMs **2.1** and **2.2** were further characterised by ^{31}P NMR.

2.2.2 Preliminary Polymer and Composite Review

The Doherty group have previously investigated the use of photopolymerisable *N*-vinylimidazolium-*co*-poly(ethylene glycol) diacrylate polymers as support systems for sulphonated pH-responsive dyes to produce reusable pH-indicator materials.[16] The commercially available dyes were immobilised onto the polymer networks *via* post-polymerisation wet-impregnation. This approach was identified as a feasible method for the fabrication of POM@polymer composites. To this end, the monomer *N*-vinylimidazole (Vim) and crosslinker poly(ethylene glycol diacrylate) (PEGDA) were selected to produce the preliminary support material for POMs. Vim was chosen in the first instance to investigate if a non-ionic polymer could act as a POM support, as donor – acceptor interactions between imidazole-based ligands and POMs have previously been reported.[17]

For polymer synthesis, equimolar quantities of *N*-vinylimidazole **2.4** and poly(ethylene glycol) diacrylate (Mn_{av} = 400 g/mol) **2.5** were added to a glass vial. A sulfonium salt of tetrakis(pentafluoroborate), commercially known as Irgacure 290 (2.0 wt. %), was employed as the photoinitiator, and the prepolymer mixture was dissolved in THF (2 mL per total g monomer and crosslinker). The glass vial was sealed to prevent evaporation of the solvent then sonicated for 3 min to ensure even dissolution of all components. The pre-polymer resin was then injected into a circular PTFE mold (diameter = 20.0 mm, depth = 1.0 mm) and exposed to an LED UV-light source (395 nm) for 10 min to ensure full curing. The resulting polymer gels **2.6** were washed thoroughly with THF and water to remove any unreacted monomer. Prior to FTIR analysis, the polymers were dried in a vacuum oven at 50 °C for one day to remove any residual solvent. Polymers intended for subsequent POM impregnation were stored in MeCN.
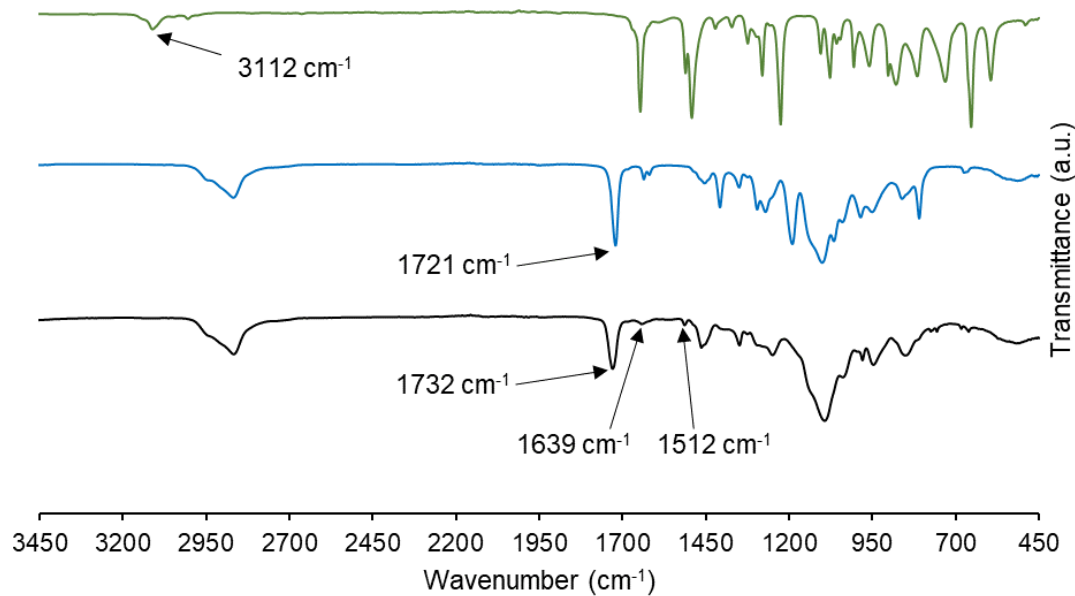
Figure 2.6: FTIR spectra of *N*-vinylimidazole **2.4** (green), PEG-400-DA **2.5** (blue) and Vim:PEG-400-DA 1:1 **2.6** (black).

The peak at 1732 cm^{-1} in the FTIR spectrum of the polymer **2.6** is characteristic of C=O stretching and can be attributed to the incorporation of PEG400DA **2.5** into the polymer (Figure 2.6, black). The weak N-H stretching band at 3112 cm^{-1} in the spectrum of Vim **2.4** (green) is not present in the spectrum of the polymer (black) due to the small relative mass of Vim to crosslinker, however, the small peaks around 1639 cm^{-1} and 1512 cm^{-1} can be attributed to C=N and C=C stretching of the imidazole ring respectively.[18]

Immobilisation of the TBA salts **2.1, 2.2** and **2.3** onto the polymer samples was carried out. The polymer samples of **2.6** were submerged into a saturated solution of POM in MeCN and left overnight. The resulting materials were then washed with MeCN to remove any excess POM from the polymer surface. The POM@Polymer composites SiW$_{12}$@Vim:PEG400DA **2.7a**, PMo$_{12}$@Vim:PEG400DA **2.7b** and PW$_{12}$@Vim:PEG400DA **2.7c** were then submerged into a saturated aqueous solution of ascorbic acid at room temperature, and colour change was monitored (Figure 2.7).
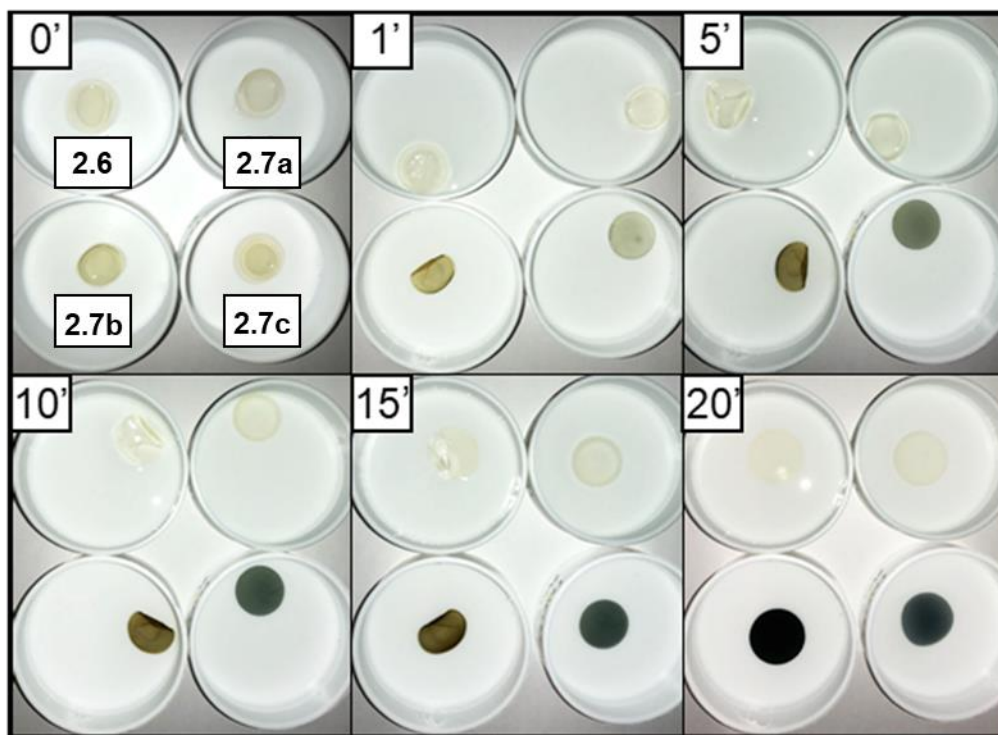
Figure 2.7: Colour change of the POM@polymers in ascorbic acid solution at T = 0, 1, 5, 10, 15 and 20 min.

The 2e$^-$ donating chemical reducing agent (ascorbic acid) was chosen due to its non-toxic nature. Both polymer composites **2.7b** and **2.7c** underwent a considerable colour change, but ultimately the PMo$_{12}$ based composite **2.7b** gave the greatest optical contrast (Figure 2.7). An attempt to synthesise analogous heteropoly acid-based composites was also made using H$_3$[PW$_{12}$O$_{40}$] and H$_3$[PMo$_{12}$O$_{40}$]. However, the materials suffered from considerable leaching of the POM into the surrounding aqueous solution, so were not carried forward for further investigation (Figure 2.8).

Figure 2.8: Leaching of H$_3$[PMo$_{12}$O$_{40}$] from **2.6** into an aqueous ascorbic acid solution.

Poly(ethylene glycol)-type polymers have been shown to immobilise POMs in the absence of any other functionalised *co*-monomer.[19] To establish the effect that the imidazole group had on the amount of immobilised POM, a series of polymers with varying ratios of Vim:PEG400DA were synthesised using the procedure outlined above. The polymers were allowed to dry in a vacuum oven for 3 days and their dry weights were recorded. Impregnation of PMo_{12} was carried out using the procedure previously outlined and the composites were allowed to dry for a further 3 days. The weight of the POM@polymer composites was then recorded (Figure 2.9).
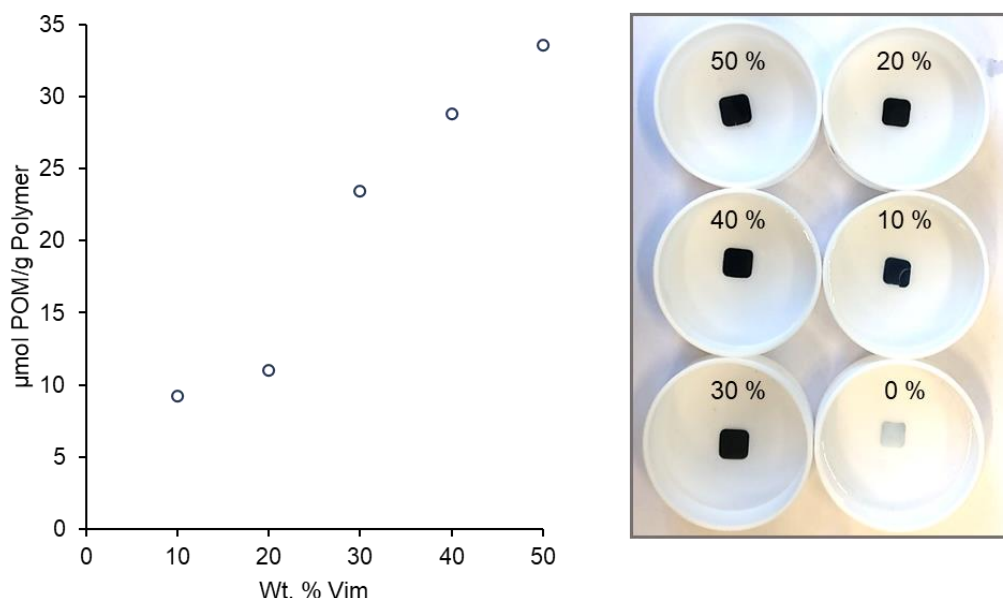
Figure 2.9: Graph to show the measured values of POM loaded onto polymers as a function of Wt. % Vim (left) and an image of POM@polymer samples with varying Wt. % Vim after treatment with ascorbic acid (right).

The loading of POM increased with increasing weight % of Vim from 9.2 µmol/g polymer at 10 wt. % to 33.6 µmol/g polymer at 50 wt. %. Although the amount of POM per g of each polymer is within the order of just micromoles, the visibility of the POM after reduction is marked (Figure 2.9, right). In addition, the difference in POM loading between polymers containing different amounts of Vim was not obvious to the naked eye. The PEGDA homopolymer (0% Vim) displayed no such obvious colour change. This suggests that a) there may be a direct interaction between the vinylimidazole fragments of the polymer and the POM, and/or b) a greater wt % of Vim alters the macromolecular properties of the polymer (e.g. porosity), allowing for a greater amount of POM to impregnate the network

of the material. The result demonstrates that POM loading can be tuned by adjusting the prepolymer formula, and that the neutral Vim monomer plays a crucial role in obtaining a deeply-coloured composite.

Solvent uptake was also measured as a function of Vim content within the polymer, as this is an important property to consider when designing materials for use in devices for the following reasons:

- The materials must allow for mobility of solvent through the polymer network to facilitate diffusion of a reducing agent solution.
- Absorption/uptake of solvents results in an increase in the volume of the material and can have an effect on its mechanical properties.[20] This can lead to undesired deformities (e.g. surface fractures) and the swollen material may exert pressure onto its surroundings (i.e. other components of a device).

Given the issues mentioned above, it is vital to strike a balance between sufficient solvent mobility and limited swelling of the polymer gels. The effect of varying Vim content on solvent uptake is outlined in Figure 2.10. The polymer samples were dried before their weight (Wt_{dry}) was recorded. The polymers were then allowed to equilibrate in 10 mL of solvent at 20 $^\circ$C for 24 hours. Excess solvent was removed from the surface of the polymers before the wet weight (Wt_{wet}) was measured. Solvent uptake was calculated as weight-percent increase (Figure 2.10, left) and molar solvent uptake (Figure 2.10, right) according to the following equations:

$$Wt\ \%\ increase = 100 - \left[\frac{Wt_{wet} - Wt_{dry}}{Wt_{dry}} \times 100 \right]$$

(**2.3**)

$$Molar\ Uptake\ = \left[\frac{1000 \times (Wt_{wet} - Wt_{dry})}{Mr_{solvent}} \right] \div Wt_{dry}$$

(**2.4**)
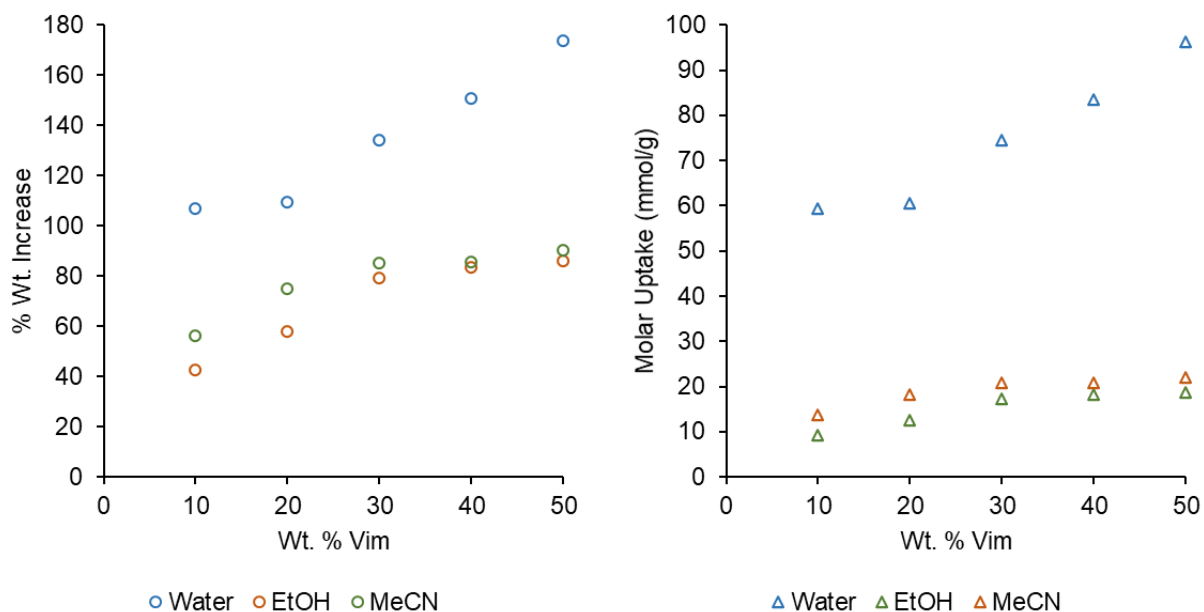
Figure 2.10: Solvent uptake by weight % increase (left) and molar solvent uptake (right) of polymers with varying weight % of vinylimidazole. Measured at 20 ºC.

Uptake of water, ethanol and acetonitrile was measured. For all solvents, uptake increased with increasing Vim content. This observation can be attributed to an increase in polymer free volume due to the lesser degree of chemical and physical crosslinking of the polymer network.[21] Water uptake was greater and increased more significantly with increasing wt % Vim than for that of ethanol and acetonitrile. This was unsurprising given the inherent hydrophilic nature of PEGDA. Uptake of EtOH and MeCN began to plateau at 30 wt % Vim. The results of the solvent uptake investigation together with POM loading experiments show that adjusting the Vim:PEGDA ratio can alter the properties of the polymer. Lower Vim content inhibits the degree of swelling, without completely hindering solvent uptake which is a desirable characteristic, as previously mentioned. Although increasing Vim content leads to an increase in POM loading, images of the composites show that this is inconsequential in terms of visual colour change. A lower Vim content is therefore advantageous in terms of polymer properties.

2.2.3 Expanding the Scope of the Polymer Support

Additional polymer formulas were explored for comparison and optimization (Figure 2.11). Two variables were implemented:

1) *Chain length of the crosslinker:* previous studies have shown that chain length of PEGDA crosslinkers can influence polymer properties e.g. mechanical strength, pore size and solvent uptake.[22]

2) *Incorporation of an ionic monomer:* a cationic monomer would allow for a strong electrostatic interaction with the POM.

n = 6, **2.5**
n = 14, **2.8**

2.9   **2.10**   **2.11**
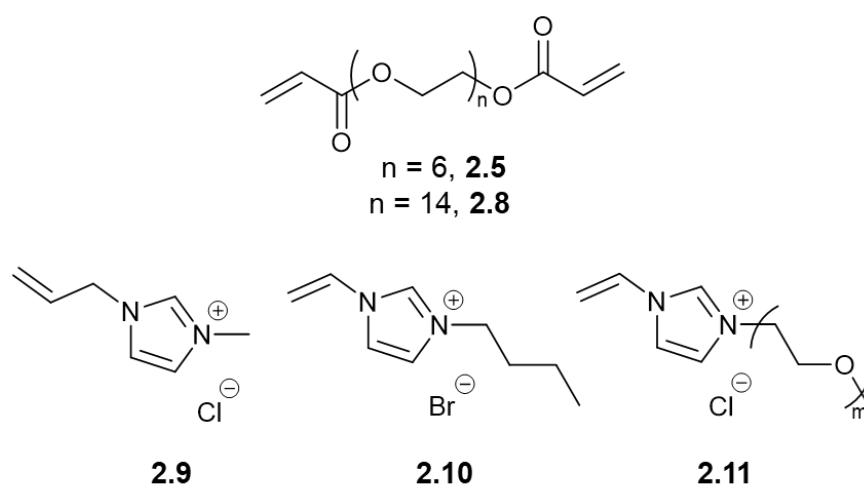
Figure 2.11: Structure of the crosslinker (top row) and potential ionic monomers (bottom row)

PEGDA crosslinkers and 1-allyl-3-methylimidazolium chloride **2.9** were purchased without further purification. The synthesis of 1-butyl-3-vinylimidazolium bromide **2.10**, and the attempted synthesis of 1-PEG-3-vinylimidazolium **2.11** are outlined below:

2.4   **2.10**

60 °C
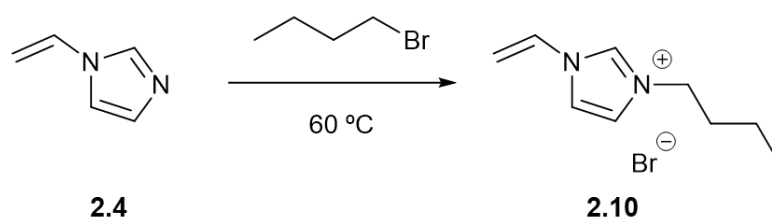
Scheme 2.2: The *N*-alkylation of Vim **2.4** with n-butyl bromide to yield BuVimBr **2.10**.

1-butyl-3-imidazolium bromide (BuVimBr) **2.10** was prepared by heating equimolar quantities of *N*-vinylimidazole **2.4** and n-butyl bromide at 60 ºC for 3 h (Scheme 2.2). The product BuVimBr **2.10** was then washed with Et₂O and confirmed by ¹H NMR (Figure 2.12).
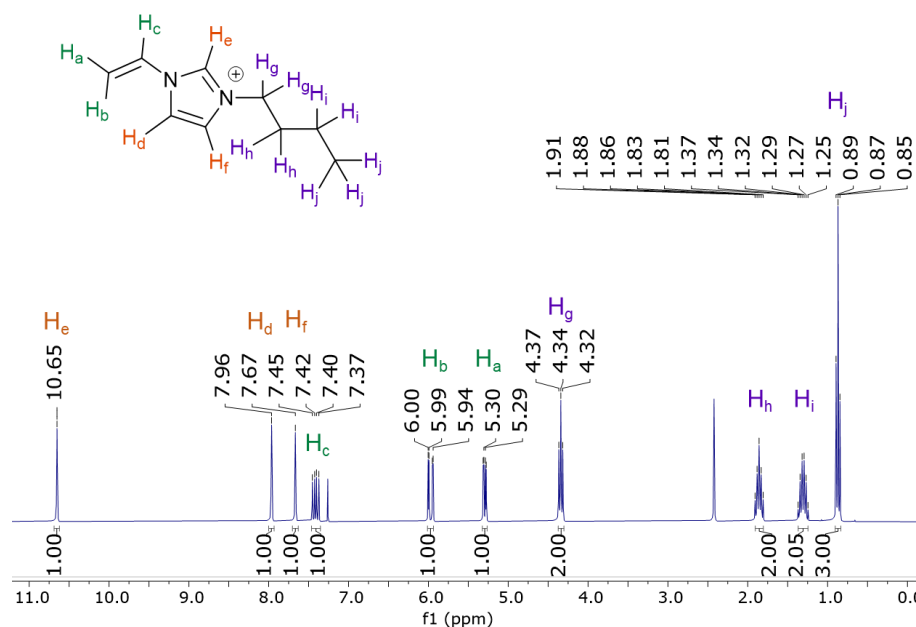
Figure 2.12: Annotated proton NMR spectrum of BuVimBr **2.10**.

For the synthesis of **2.11**, a chloro-substituted PEG precursor **2.13** was made (Figure 2.13): under N₂, poly(ethylene glycol) monomethyl ether **2.12** was dissolved in dry THF and deprotonated with pyridine. The colourless solution was heated to 80 ºC and two equivalents of thionyl chloride was added dropwise, which resulted in immediate effervescence of HCl gas, while the solution became turbid. The reaction was allowed to heat for 3 days before the brown suspension was cooled to room temperature and water was added dropwise to quench excess SOCl₂ prior to extraction of **2.13**.

43
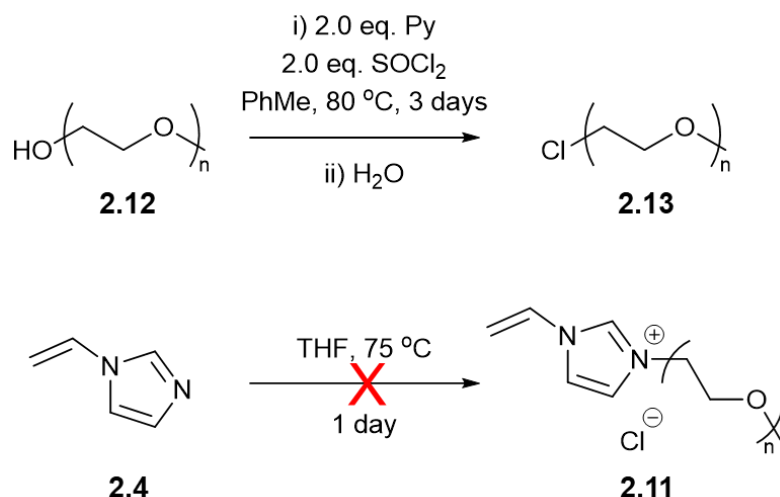
Figure 2.13: The attempted synthesis of PEGVimCl **2.11**.

Attempts to synthesise compound **2.11** following the previously reported procedure was unsuccessful.[16] *N*-vinylimidazole **2.4** and 1.1 molar equivalents of **2.13** were dissolved in THF and heated to reflux for 1 day. Quaternisation of the N atom of *N*-vinylimidazole was not evident in the ^{1}H NMR spectrum of the reaction product. The reaction was repeated with toluene to increase the reflux temperature, however, this also proved unsuccessful. Although a similar method was adopted by the Doherty group to synthesise an ionic PEGylated derivative of 2-methyl-imidazole, the nucleophilicity of the N lone pair of **2.4** was not sufficient to facilitate the S_N2 reaction.

Vim **2.4,** AllyVimCl **2.9** and BuVimBr **2.10**, were then taken forward for polymerisation with PEGDA crosslinkers **2.5** and **2.8**. All polymers were synthesised under the same conditions: in equimolar amounts of monomer:crosslinker, with 5 wt. % Irgacure 290 as the photoinitator, dissolved in water:THF (1:4) (2 mL per total g monomer and crosslinker). Prepolymer mixtures were added to a PTFE mold (1.0 mm x 1.0 mm x 0.5 mm) and allowed to cure under a UV light source (395 nm) for 10 min.

The Vim and BuVimBr based formulas photopolymerised to give robust, uniform polymers (Figure 2.14). However, copolymers of **2.9** exhibited macropores and large surface deformities, a problem of which was not remedied by altering the water:THF ratio of pre-polymer solvent. As a result, **2.9** based polymers were not carried forward for POM immobilisation.

n = 6; Vim:PEG400DA **2.6**   n = 6; BuVimBr:PEG400DA **2.15a**
n = 14; Vim:PEG700DA **2.14**   n = 14, BuVimBr:PEG700DA **2.15b**
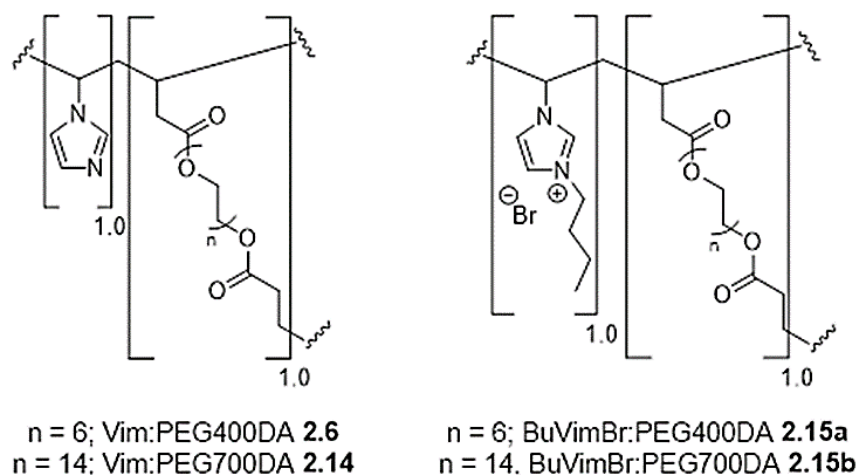
Figure 2.14: The structure of neutral Vim-based polymers **2.6** and **2.14**, and ionic BuVimBr-based polymers **2.15a** and **2.15b**. Where n = 6 corresponds to PEG400DA and n = 14 corresponds to PEG700DA.

2.2.4 Solvent, Polyoxometalate and Ascorbic Acid Uptake

Solvent, polyoxometalate and ascorbic acid uptake capacity of each polymer **2.6**, **2.14**, **2.15a** and **2.15b** was measured. Solvent uptake experiments were carried out under the same conditions as outlined in section 2.2.2. Polyoxometalate and ascorbic acid uptake was determined by placing a dry sample of each polymer into 10 mL of 0.01 M solution of POM in MeCN, or 0.1 M solution of ascorbic acid in water. The polymers were allowed to equilibrate in solution for 24 hours then dried in a vacuum oven for 3 days. POM and ascorbic acid loadings were determined by calculating the difference in weight of the dried polymer samples before and after immobilisation of the respective compound.
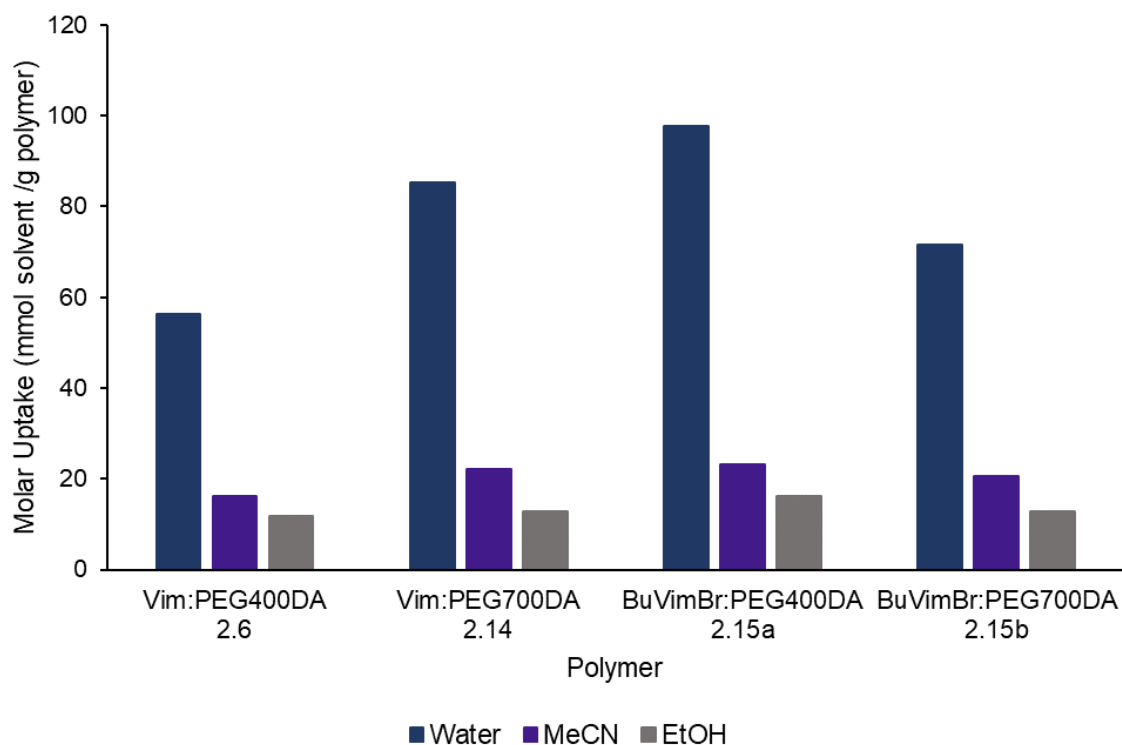
Figure 2.15: Solvent uptake of polymers reported as mmol of solvent per g of polymer.

For all polymers, the order of solvent uptake was water > MeCN > EtOH (Figure 2.15). Unsurprisingly, each material absorbed a much greater amount of water owing to the highly hydrophilic nature of the PEG chains within each polymer network. There was no clear pattern between solvent uptake and the varying properties of the polymers (i.e. neutral/ionic or PEGDA chain length). The order of solvent uptake capacity was BuVimBr:PEG400DA **2.15a** > Vim:PEG700DA **2.14** > BuVimBr:PEG700DA **2.15b** > Vim:PEG400DA **2.6**.

The exact amount of $[PMo_{12}O_{40}]^{3-}$ immobilised onto the ionic polymer networks cannot be accurately deduced from gravimetric measurements alone. This is because the extent of counterion exchange between the TBA cations associated with the POM and the vinylimidazolium groups of the polymers is unknown (Figure 2.16). For this reason, gravimetric loading measurements were reported as mass % increase and not as molar uptake (Figure 2.17). Although it is a reasonable assumption that ion exchange does not take place between the neutral polymers and the POM, loading measurements were reported in the same way for continuity and comparison.
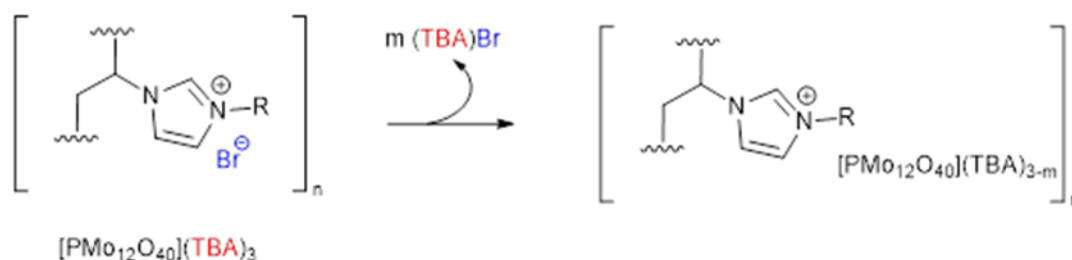
Figure 2.16 schematic illustrating ion exchange between the POM and the ionic polymer, where m = 1 to 3.

Mass increase after loading of $[PMo_{12}O_{40}](TBA)_3$ **2.1** and ascorbic acid onto the polymers was recorded (Figure 2.17). As expected, a greater amount of POM was immobilised onto the ionic polymers than the neutral polymers with mass increases of 36.2 % and 34.1 % for **2.15a** and **2.15b** respectively, and mass increase of only 2.8 % and 2.3 % for **2.6** and **2.14** respectively. The reverse pattern is true for uptake of ascorbic acid, where the neutral polymers' mass increase was recorded at 27.3 % for **2.6** and 19.1 % for **2.14** compared to 6.4 % and 4.1 % for **2.15a** and **2.15b**, respectively. The neutral polymers immobilised a greater amount of ascorbic acid due to the basic Vim groups. Overall, polymer **2.15a** immobilised the greatest amount of POM, whereas **2.6** displayed the greatest uptake capacity for ascorbic acid.
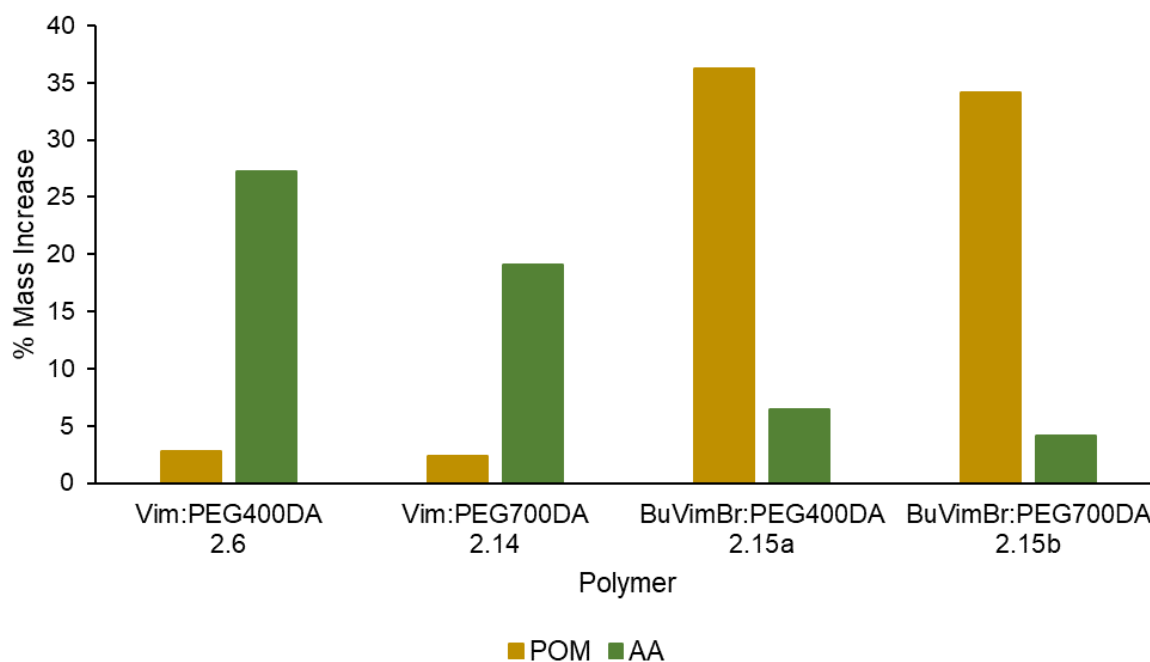
Figure 2.17: Mass % increase of polymers after immobilisation of POM (yellow) and ascorbic acid (green).

Due to the limitations associated with gravimetric experiments discussed above, ICP analysis was identified as the most accurate technique to determine the amount of POM present within each composite. However, despite multiple attempts to digest the POM@polymer composites in aqua regia and piranha solution, residual solid material remained, even with prolonged reaction time, elevated temperatures and increased ratio of composite:acid.

2.3 Polyoxometalate-Polymer Composite Characterisation

For subsequent characterisation, unless stated otherwise, polymers **2.6**, **2.14**, **2.15a** and **2.15b** were loaded with POM by placing the 1 mm x 1 mm x 0.5 mm polymer samples separately into an excess of a 0.01 M solution of PMo_{12} **2.1** in MeCN for 24 h. All POM@polymer composites were then washed with MeCN to remove excess POM, and are subsequently denoted as PMo_{12}@VimPEG400DA **2.16a**, PMo_{12}@VimPEG700DA **2.16b**, PMo_{12}@BuVimBr:PEG400DA **2.17a** and PMo_{12}@BuVimBr:PEG400DA **2.17b**.

2.3.1 FT-IR Characterisation

The FTIR spectra of each polymer was compared with PMo_{12} **2.1** and the corresponding POM@polymer composite pre- and post-reduction with ascorbic acid (Figures 2.18 – 2.21).
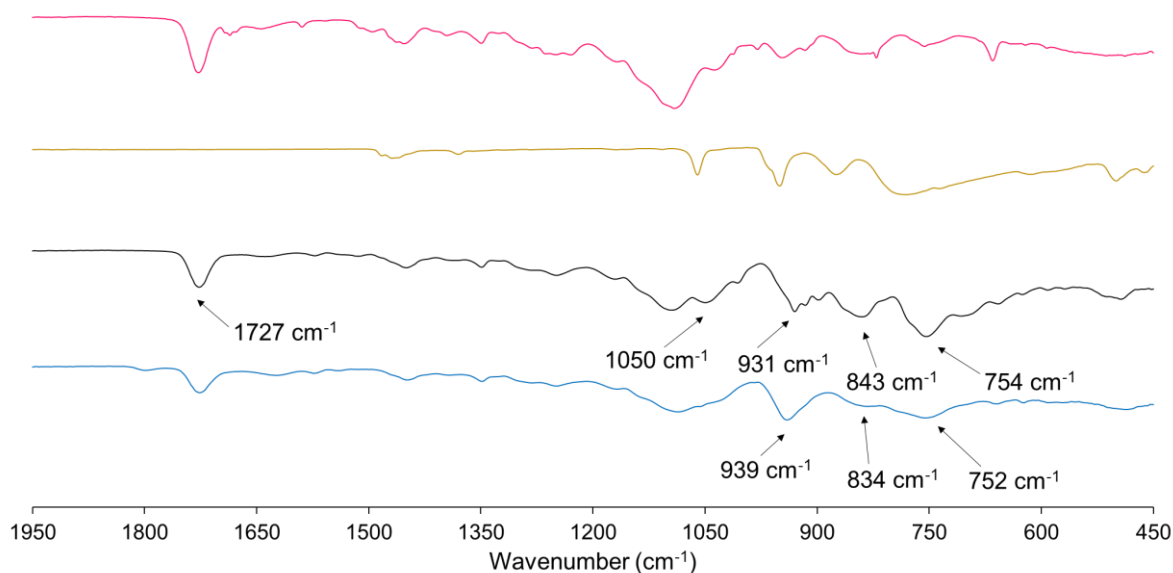
Figure 2.18: Stacked FTIR spectra of Vim:PEG400DA **2.6** (pink), PMo_{12} **2.1** (yellow), PMo_{12}@Vim:PEG400DA **2.16a** (black) and ascorbic acid reduced PMo_{12}@Vim:PEG400DA **2.16a** (blue)

The spectrum of PMo_{12}@Vim:PEG400DA **2.16a** (Figure 2.18, black) is closer in character to that of the blank polymer **2.6** (Figure 2.18, pink) than that of the POM **2.1** (Figure 2.18, yellow). Generally, the intensity of peaks associated with the polymer decreased after POM immobilisation, as is evident with the carbonyl peak at 1727 cm^{-1} associated with

49

PEGDA chains. Peaks in the spectrum of the composite material at 1050 cm^{-1} v(P-O), 931 cm^{-1} v(Mo-O$_t$), 843 cm^{-1} v(Mo-O$_c$-Mo) and 754cm^{-1} v(Mo-O$_e$-Mo) were assigned to PMo$_{12}$. Metal-oxygen peaks of the POM shift towards lower wavelengths after polymer immoblisation (Table 2.1). All peaks in the spectrum of the material become less well-defined after treatment with ascorbic acid (Figure 2.18, blue). This weakening and broadening of peaks is to be expected, given the loss of symmetry associated with the reduction of Keggin POMs.[23]

Peaks associated with Vim:PEG700DA **2.14** remain intense after POM immobilisation in the spectrum of composite **2.16b** (Figure 2.19, black). Due to overlap, the only distinguishable POM stretching frequency in the spectrum of the neutral PEG700DA-based POM@Polymer composite is v(Mo-O$_t$) at 940 cm^{-1}. There were no significant changes to the spectrum of the composite after exposure to ascorbic acid (Figure 2.19, blue).
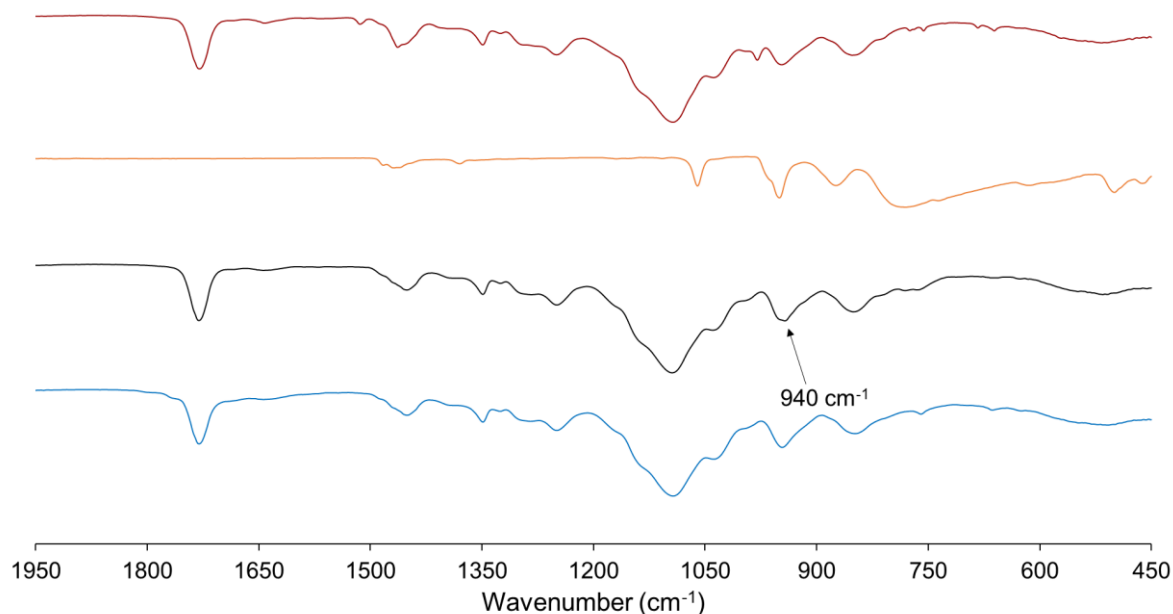
Figure 2.19: Stacked FTIR spectra of Vim:PEG700DA **2.14** (red), PMo$_{12}$ **2.1** (yellow), PMo$_{12}$@Vim:PEG700DA **2.16b** (black), ascorbic acid reduced PMo$_{12}$@Vim:PEG700DA **2.16b** (blue).

In contrast to the spectrum of neutral-polymer composites **2.16a** and **2.16b**, the spectrum of the ionic-polymer composite PMo_{12}@BuVimBr:PEG400DA **2.17a** is more comparable to that of PMo_{12} **2.1** than BuVimBr:PEG400DA **2.15a** (Figure 2.20). Peaks corresponding to the POM in the spectrum of **2.17a** were recorded at 1059 cm^{-1} v(P-O), 953 cm^{-1} v(Mo-O_t), 872 cm^{-1} v(Mo-O_c-Mo) and 786cm^{-1} v(Mo-O_e-Mo) (Figure 2.20, black). After treatment with ascorbic acid, the v(P-O) peak was no longer distinguishable and v(Mo-O_t), v(Mo-O_c-Mo) and v(Mo-O_e-Mo) peaks shift to lower wavenumbers of 938 cm^{-1}, 834 cm^{-1} and 754 cm^{-1} respectively (Figure 2.20, blue).
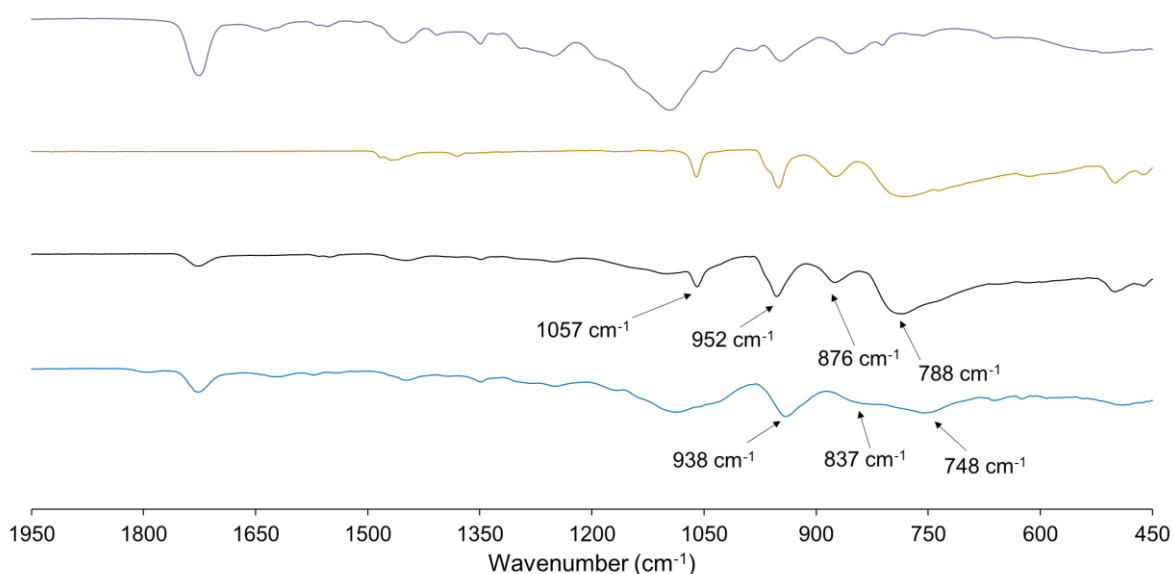
Figure 2.20: Stacked FTIR spectra of BuVimBr:PEG400DA **2.15a** (pink), PMo_{12} **2.1** (yellow), PMo_{12}@BuVimBr:PEG400DA **2.17a** (black), ascorbic acid reduced PMo_{12}@BuVimBr:PEG400DA **2.17a** (blue).

Of the four POM@polymer composites examined, the spectrum of the ionic PEG700DA-based material **2.17b** exhibits the most well-defined features of both the POM **2.1** and the original polymer **2.15b**, without the characteristic peaks of either component obscuring the other (Figure 2.21, black). The vibrational modes associated with the POM are prominent in the spectrum of the composite: 1061 cm^{-1} v(P-O), 955 cm^{-1} v(Mo-O_t), 877 cm^{-1} v(Mo-O_c-Mo) and 803 cm^{-1} v(Mo-O_e-Mo). Peaks corresponding to v(P-O) and v(Mo-O_e-Mo) appeared much more intense than in the spectrum of the free-POM. All peaks

associated with the POM shift to lower frequencies and broaden after treatment with ascorbic acid (Figure 2.21, blue).
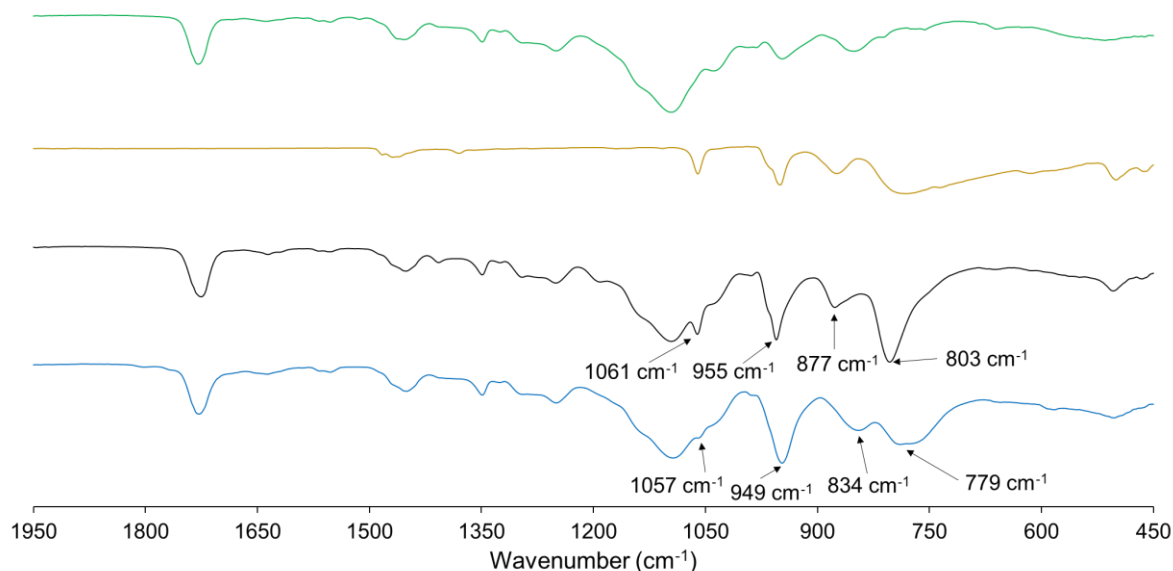
Figure 2.21: Stacked FTIR spectra of BuVimBr:PEG700DA **2.15b** (green), PMo$_{12}$ **2.1** (yellow), PMo$_{12}$@BuVimBr:PEG700DA **2.17b** (black), ascorbic acid reduced PMo$_{12}$@BuVimBr:PEG700DA **2.17b** (blue).

The FTIR spectra of all composite materials show to some degree that the POM is incorporated into- and interacts with the polymer network. Peaks corresponding to vibrational modes associated with the POM are more apparent in the spectra of ionic polymer composites **2.17a** and **2.17b** than neutral polymer composites **2.16a** and **2.16b**. Table 2.1 summaries peaks associated with the POM in each material.

Compound	Wavenumber (cm^{-1})			
	v(P-O)	v(Mo-O$_t$)	v(Mo-O$_c$-Mo)	v(Mo-O$_e$-Mo)
PMo$_{12}$@VimPEG400DA **2.16a**	1050	931	843	754
PMo$_{12}$@Vim:PEG700DA **2.16b**	-	940	-	-
PMo$_{12}$@ BuVimBr:PEG400DA **2.17a**	1057	952	876	788
PMo$_{12}$@BuVimBr:PEG700DA **2.17b**	1061	955	877	803
[PMo$_{12}$O$_{40}$](TBA)$_3$ **2.1**	1059	950	874	786 (br)

Table 2.1: A summary of frequencies associated with vibrational modes corresponding to [PMo$_{12}$O$_{40}$]$^{3-}$ in the polymer composites

2.3.2 Polymer and Composite Surface Morphology

Scanning electron microscopy (SEM) was carried out to evaluate the morphology of the polymers and the POM@polymer composites before and after reduction with ascorbic acid. All materials were dried in a vacuum oven at 50 ºC for at least 24 hours before analysis (Figure 2.22)
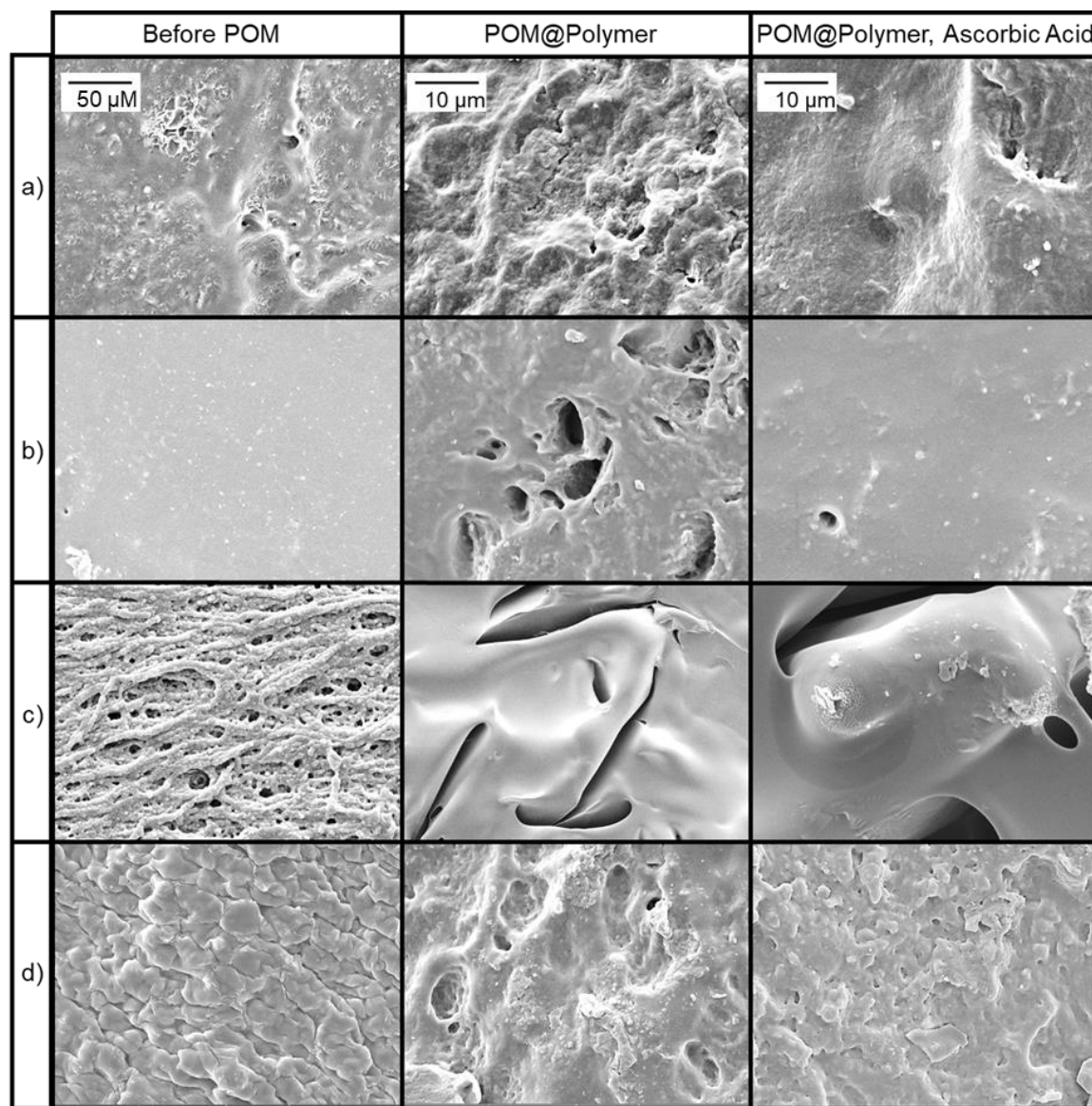
Figure 2.22: SEM images of each polymer, POM@polymer composite and POM@polymer composite after reduction with ascorbic acid: a) Vim:PEG400DA **2.6**, PMo$_{12}$@ Vim:PEG400DA **2.16a** b) Vim:PEG700DA **2.14,** PMo$_{12}$@Vim:PEG700DA **2.16b** c) BuVimBr:PEG400DA **2.15a,** PMo$_{12}$@BuVimBr:PEG400DA **2.17a** d) BuVimBr:PEG700DA **2.15b,** PMo$_{12}$@BuVimBr:PEG700DA **2.17b**.

The surface of polymer **2.6** appears coarse with unevenly distributed pores ranging from 1 – 2 µM in diameter (Figure 2.22a). Images taken after POM immobilisation and subsequent treatment with ascorbic acid show that the surface of **2.16a** exhibits a rougher, ridge-and-valley-type texture with globular protrusions. Polymer **2.14** is smooth and almost pore-free (Figure 2.22b). There is an obvious change in the morphology after POM immobilisation, whereby an array of pores with varying sizes were distributed across the surface of **2.16b**. Treatment of the composite **2.16b** with ascorbic acid appeared to reduce the number of pores.

The surface morphologies of the ionic polymers are appreciably different to those of the neutral polymers. The surface of polymer **2.15a** (Figure 2.22c) is fibrous with a high density of micropores, where fractures emerged upon impregnation of the POM. Polymer **2.15b** features were nodular and compact (Figure 2.22d). A rough, uneven surface with hollow pores arises after POM immobilisation to composite **2.17b**. Pores become less pronounced after treatment of **2.17b** with ascorbic acid.

An attempt was made to determine the size and distribution of POM clusters throughout the polymers *via* TEM analysis (Figure 2.23). However, difficulties were encountered upon attaining good-quality micrographs.
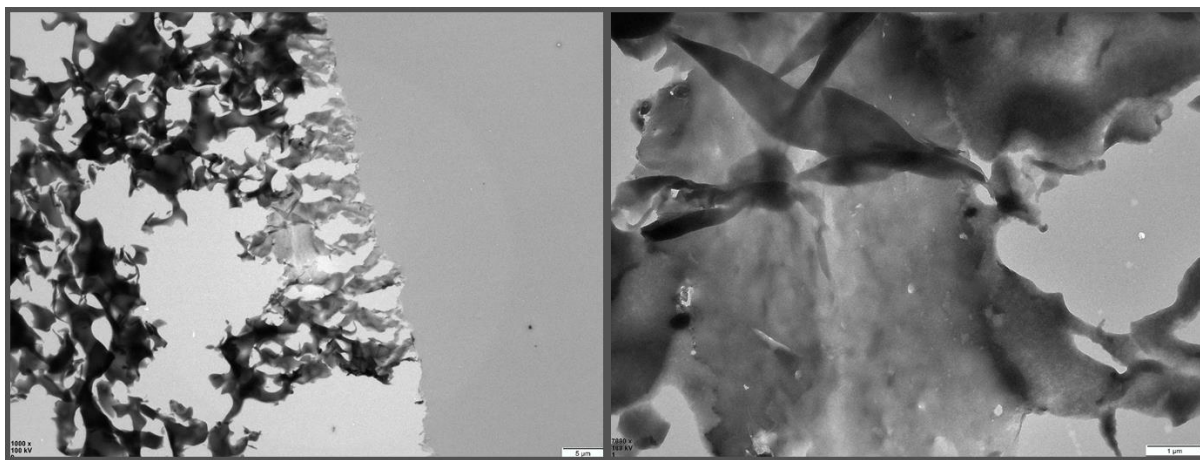
Figure 2.23: Example TEM images of a cross section of PMo_{12}@BuVimBrPEG700DA **2.17a**

2.3.3 Mass Analysis – CHN and TGA

The composition of the polymers and POM@polymer composites were investigated *via* CHN microanalysis. Prior to analysis, all materials were ground and dried in a vacuum oven at 50 ºC for 2 days to ensure removal of any residual solvent.

Sample	C (%)	H (%)	N (%)	Other (%)	Difference in % Other
Vim:PEG400DA **2.6**	56.22	7.99	4.93	30.85	**3.39**
PMo$_{12}$@VimPEG400DA **2.16a**	53.15	7.91	4.70	34.24	
Vim:PEG700DA **2.14**	55.67	7.86	3.08	33.39	**3.09**
PMo$_{12}$@VimPEG700DA **2.16b**	52.38	8.12	3.03	36.48	
BuVimBr:PEG400DA **2.15a**	52.80	8.29	2.67	36.23	**21.86**
PMo$_{12}$@BuVimBrPEG400DA **2.17a**	34.49	5.55	1.87	58.09	
BuVimBr:PEG700DA **2.15b**	53.00	8.55	2.23	36.22	**19.29**
PMo$_{12}$@BuVimBrPEG700DA **2.17b**	36.73	6.13	1.63	55.51	

Table 2.2: CHN data for each polymer and POM@polymer composite.

Comparison of the elemental compositions of the polymers and the corresponding POM@polymer composites are given in Table 2.2. The increase in weight % of elements other than C, H and N (% other) after POM immobilisation can be attributed to the presence of $[PMo_{12}O_{40}]^{3-}$. This difference was significantly higher for ionic polymer-based materials, with the value increasing by 21.86 % from **2.15a** to **2.17a** and 19.29 % from **2.15b** to **2.17b**. Contrastingly, the differences in weight % other between **2.6** and **2.16a**, and **2.14** and **2.16b** were calculated as 3.39 % and 3.09 %, respectively. This observation supports the conclusion drawn from POM uptake experiments detailed in section 2.2.4, where it was determined that the ionic polymers are capable of immobilising a greater amount of POM than the neutral polymers.

Thermogravimetric analysis profiles of each polymer and the corresponding POM@polymer composite were also compared (Figure 2.24). The materials were heated from 30 ºC to 900 ºC with a heating rate of 10 ºC/min under an N_2 atmosphere with a flow rate of 20 mL/min.
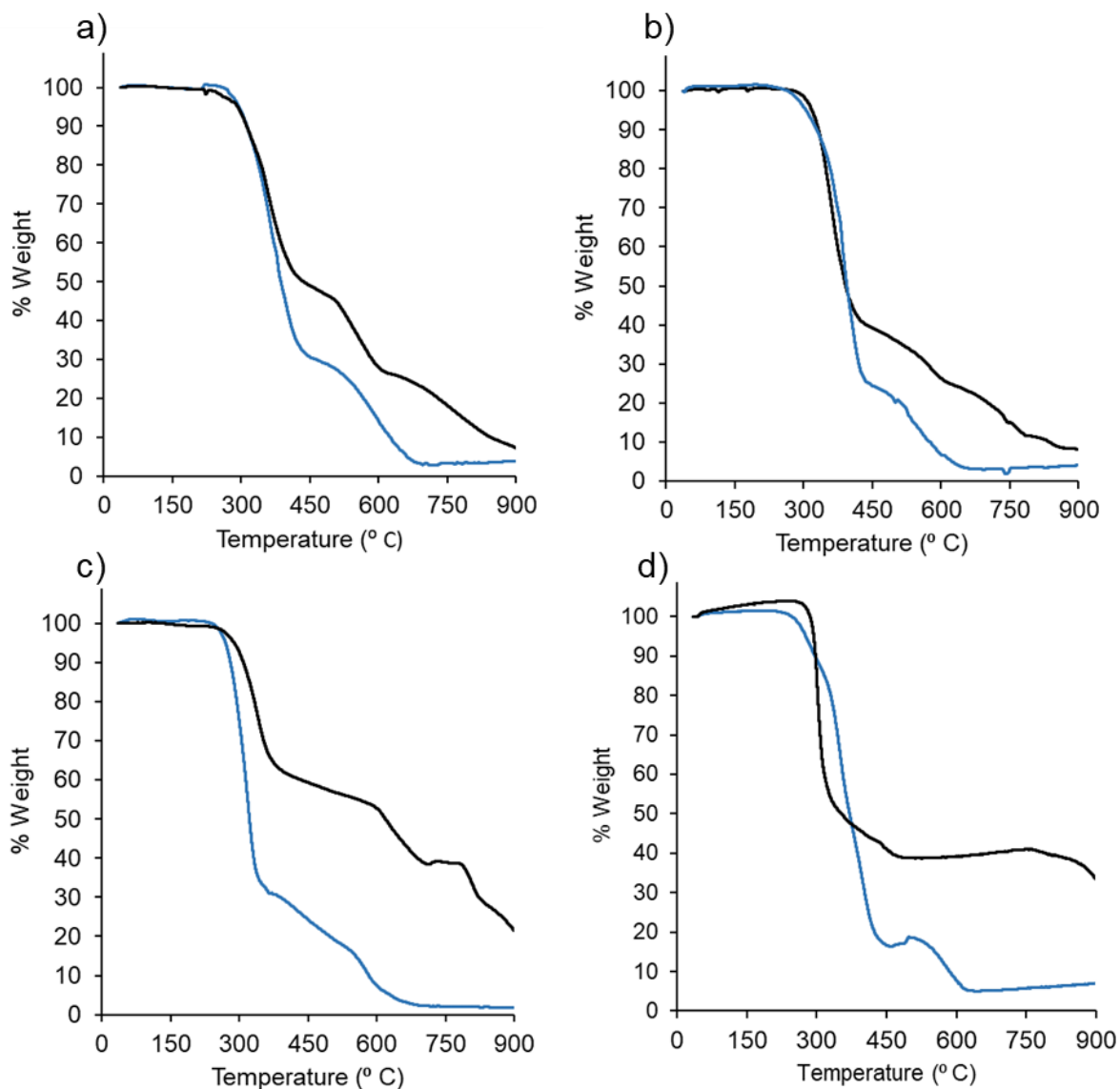
Figure 2.24: TGA profiles of polymers (blue) and POM@polymer composites (black) where a) Vim:PEG400DA **2.6** and PMo_{12}@Vim:PEG400DA **2.16a**; b) Vim:PEG700DA **2.14** and PMo_{12}@VimPEG700DA **2.16b**; c) BuVimBr:PEG400DA **2.15a** and PMo_{12}@VimPEG400DA **2.17a**; d) BuVimBr:PEG700DA **2.15b** and PMo_{12}@BuVimBr:PEG700DA **2.17b**.

The TG weight loss curve of material **2.6** (Figure 2.24a) shows that the polymer is thermally stable up to 240 ºC (T_1), at which point weight loss occurs rapidly with increasing

temperature. A second rapid weight loss region is observed between 488 ºC (T_2) and 696 ºC. The corresponding composite material **2.16a** displays onset of degradation at a lower temperature (219 ºC) than the polymer **2.6**, although **2.16a** retains a greater mass percentage at higher temperatures. Total mass of **2.6** fell to 32 % after the initial degradation event, whereas mass of **2.16a** fell to 51 %. The TG profile of **2.16a** has three distinct degradation points, one more than that of **2.6**. A very similar pattern is observed in the TG graphs of neutral polymer **2.14** and composite **2.16b** (Figure 2.24b). It is clear that presence of the POM enhances the thermal stability of the neutral polymers.

The ionic polymers **2.15a** and **2.15b** produced similar TG profiles to their neutral counterparts (Figure 2.24c and 2.24d). Onset of thermal degradation (T_1) began at 230 ºC and 238 ºC, for polymers **2.15a** and **2.15b** respectively. POM immobilisation gave rise to a stabilising effect where T_1 was recorded at 259 ºC for composite **2.17a** and at 280 ºC for material **2.16b**. 65.1 wt. % of the composite **2.17a** was retained after the first degradation event, compared to 34.0 wt. % for the blank polymer **2.15a**. Initially, composite **2.17b** lost a greater proportion of mass at lower temperatures than polymer **2.15b**, but then retained a relatively greater mass % at temperatures in excess of 365 ºC.

At 950 ºC, remaining mass of the ionic composites **2.17a** (21 %) and **2.17b** (33%) was significantly higher than that of the neutral-polymer composites **2.16a** (7 %) and **2.16b** (9%). The finding is again reflective of the ionic polymers immobilisng a relatively greater mass of POM. A summary of decomposition onset temperatures and residual mass % after degradations steps is given in Table 2.3.

Material	Decomposition Temperature (°C)			Residual Mass (%)		
	T_1	T_2	T_3	m_1	m_2	m_3
Vim:PEG400DA **2.6**	280	510	-	32	3	-
PMo$_{12}$@VimPEG400DA **2.16a**	219	509	634	51	27	7
Vim:PEG700DA **2.14**	264	513	-	26	3	-
PMo$_{12}$@VimPEG700DA **2.16b**	283	550	738	42	25	9
BuVimBr:PEG400DA **2.15a**	230	533	-	33	3	-
PMo$_{12}$@BuVimBr:PEG400DA **2.17a**	259	604	789	63	39	21
BuVimBr:PEG700DA **2.15b**	238	530	-	17	5	-
PMo$_{12}$@BuVimBr:PEG700DA **2.16b**	280	801	-	53	33	-

Table 2.3: A summary of degradation onset temperatures (T_{onset}) and % weight loss after each significant degradation step

2.3.4 UV-Vis Spectroscopy

To investigate the optical properties of the composite materials, thin films with a thickness in the order of ~ 100 μm were fabricated to allow for transmission of light. Initially, attempts to polymerise thin films were carried out by employing the same prepolymer formulas as outlined in section 2.2.2. In general, the monomer mixture (0.5 mL) was injected onto a clean, oven-dried PTFE surface and a glass slide was placed on top of the liquid to obtain a thin, uniform layer of monomer solution. The monomer mixture was then exposed to UV-light (395 nm) for 10 min to allow adequate curing time. Attempts to synthesise thin films in this way were unsuccessful, even with prolonged exposure to UV light (20 min). Unlike the photopolymerisation process described in section 2.2.2 where there is an open air-resin interface, the solvent was trapped in this system. This inhibited the polymerisation

process as the effective concentration of monomers was decreased and the growing polymer chains were spatially separated to a greater extent.[24] For this reason, the amount of solvent added to the prepolymer resin was reduced. The process was repeated, and thin films were successfully obtained. Once cured, the PTFE-polymer-glass units were submerged into deionised water to minimise friction upon removal of the films from the mold.

The films were washed with excess THF and water, then submerged into a 0.01 M solution of PMo_{12} in MeCN (20 mL) and left overnight. The composites were removed from the POM solution and washed with MeCN, then dried in air. PEG400DA-based thin films of **2.16a** and **2.17a** exhibited severely poor structural integrity upon transfer between solvents and during the drying process. For this reason, only PEG700DA based thin film composites **2.16b** and **2.17b** were analysed.
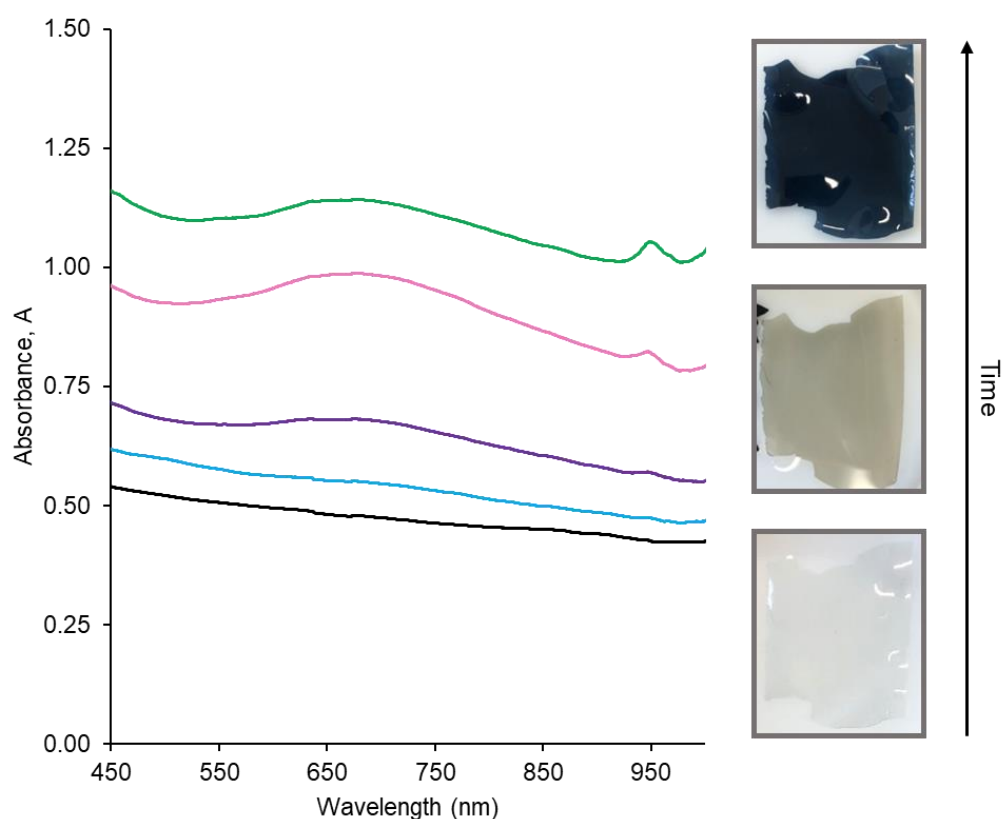
Figure 2.25: UV-Vis absorbance spectra (left) of PMo_{12}@Vim:PEG700DA **2.16b** before reduction (black) and at different time intervals after exposure to ascorbic acid: 10 min (blue) 20 min (purple) 40 min (pink) 60 min (green). Images of the thin film colour developing (right). Film thickness = 97 ± 0.1 μm.

Absorption profiles of the neutral-polymer composite **2.16b** were recorded (Figure 2.25). The material was submerged into a 0.1 M aqueous solution of ascorbic acid at room temperature. Excess liquid was removed from the film and UV-Vis spectra were recorded at different time intervals over a period of one hour. The film was returned to the reducing solution in between readings.

The film appears completely transparent before reduction (Figure 2.25, right). After a few minutes of exposure to the reducing solution, a green-brown colour had developed. The film slowly became blue after approximately 30 min. The fully oxidised material does not display any spectral features in the visible region (Figure 2.26, left). A very broad absorption peak around ~ 660 nm (λ_{max} = 664 nm) appears at T = 20 min. This peak can be attributed to intervalence charge transfer (IVCT) bands from electron exchange between Mo(V)-Mo(VI) centres of the reduced POM species.[6] There is also a sharp, but weak peak at 941 nm that increases in intensity over time. Absorption peaks corresponding to IVCTs in the near-IR region have previously been reported for reduced PMo$_{12}$ species, although peaks are generally broader and are found at longer wavelengths (~1050 nm).[25] The source of this absorption peak is therefore unknown.

The fully oxidized PMo$_{12}$@BuVimBr:PEG700DA **2.17b** thin film was vibrantly coloured (Figure 2.26, right). Initially yellow after POM immobilisation, the composite became yellow-green upon washing and air-drying. The material also suffered from considerable curling when dry, although retained its flexibility and was easily handled without breakage. Once placed in ascorbic acid solution, the material expanded and became brittle causing fractures, and immediately developed a dark-blue colour. Within minutes of submerging in the aqueous reducing solution the material had become completely opaque. At T = 1 min, a very broad band (λ_{max} = 780 nm) is present as a result of Mo(V)-Mo(VI) IVCT in the reduced POM species (Figure 2.26, left). A sharper peak (λ_{max} = 944 nm) is also present, much like that observed in the absorption spectra of the neutral composite PMo$_{12}$@Vim:PEG700DA **2.16b** (Figure 2.25). At T = 2 min this peak sharpens and is slightly blue-shifted (λ_{max} = 944 nm to 952 nm).
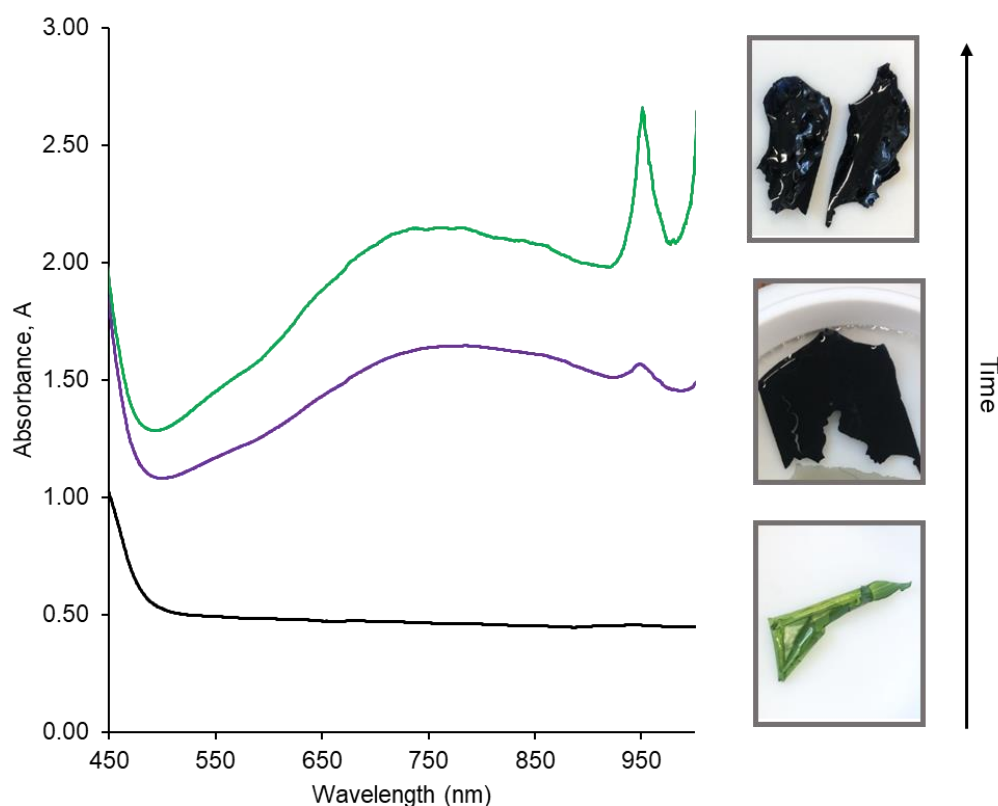
Figure 2.26: UV-Vis absorbance spectra (left) of PMo_{12}@BuVimBr:PEG700DA **2.16b** before reduction (black) and at different time intervals after exposure to aqueous ascorbic acid: 1 min (purple) 2 min (green). Images of the thin film colour developing (right). Film thickness = 112 ± 0.1 μm.

Overall, the spectral features of both reduced composites are similar to those previously reported of electrochemically two-electron-reduced $PMo_{12}O_{40}(TBA)_3$ in MeCN[25], and that of $[PMo_{12}O_{40}](TBA)_3$ chemically reduced with ascorbic acid in MeCN (Figure 2.27).

The ionic composite **2.17b** displayed a more profound colour contrast in a much shorter period of time than **2.16b**, owing to the difference in the amount of POM immobilised onto each polymer composite. From a processing/handling perspective, **2.17b** exhibited undesirable physical properties (i.e. curling and fracturing). Both materials underwent naked-eye-detectable colour change as thin films of ~ 100 μm in thickness.
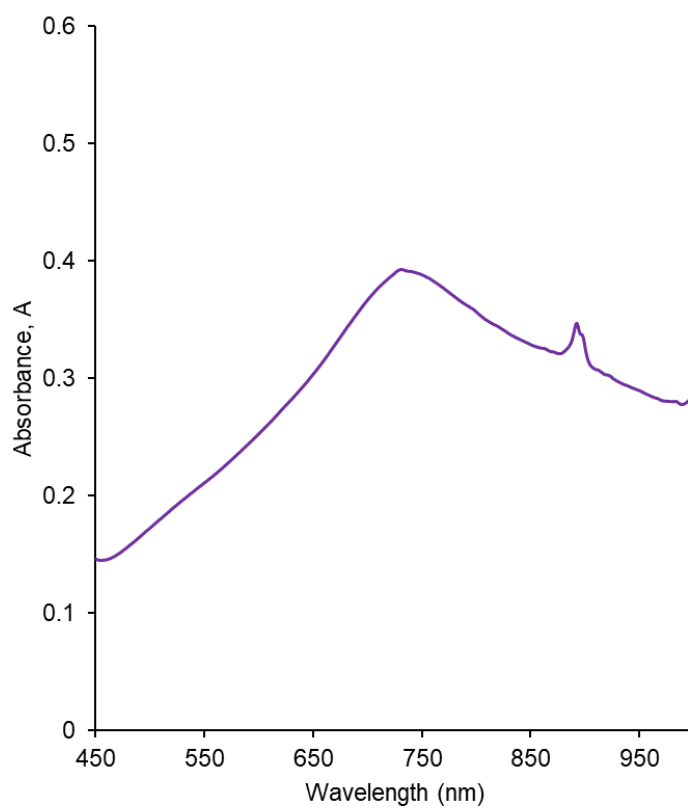
Figure 2.27: UV-Vis absorption spectrum of 0.1 mM $[PMo_{12}O_{40}](TBA)_3$ **2.1** in MeCN after reaction with one molar equivalent of ascorbic acid. λ_{max} = 733.5 nm, 896 nm

2.3.5 Solid State NMR

The polymers and composites were insoluble in deuterated solvents owing to their highly cross-linked polymer networks. Solid state (SS) ^{13}C NMR analysis of the PEG700DA polymers before and after POM immobilisation was carried out to provide a comparison between the neutral and an ionic polymer systems. NMR samples were prepared by allowing the composites to dry in a vacuum oven for 3 days before grinding them to a free-flowing powder and diluted with MgO prior to analysis.
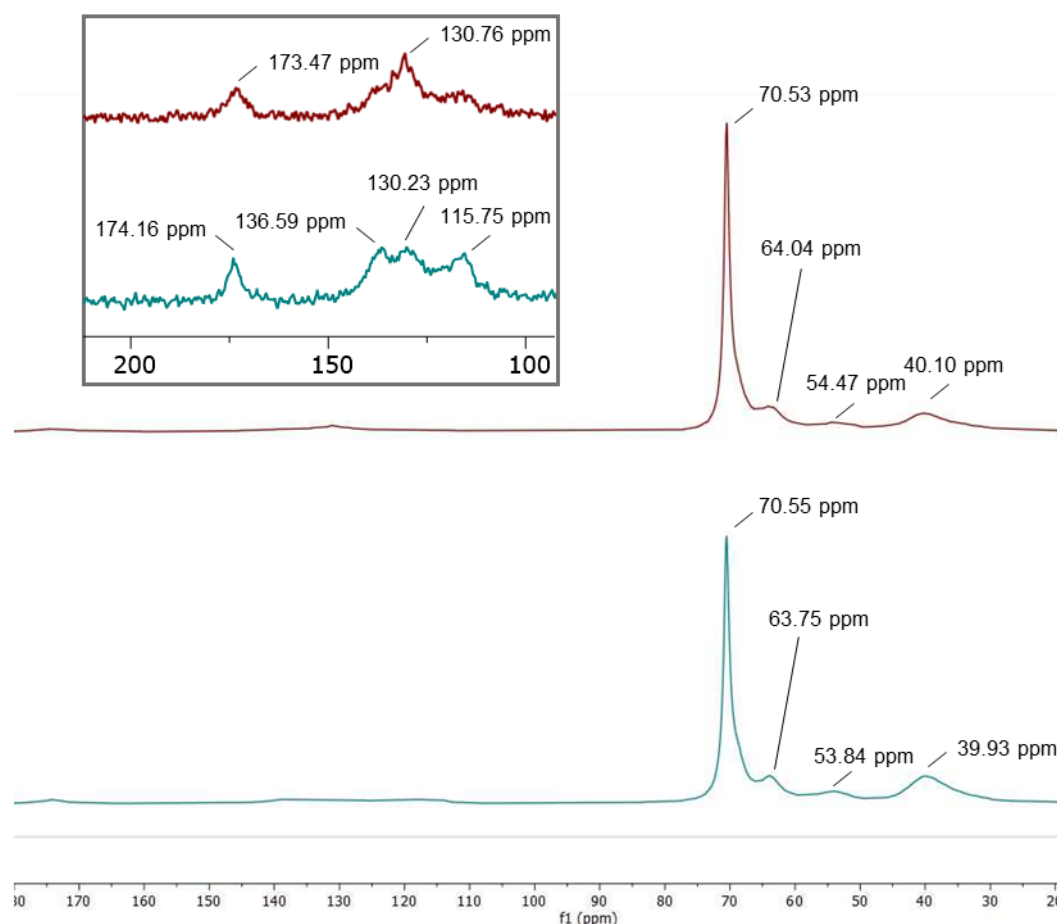
Figure 2.28: Solid state ^{13}C spectra of Vim:PEG700DA **2.14** (maroon) and PMo$_{12}$@Vim:PEG700DA **2.16b** (teal).

There is very little difference between the ^{13}C spectra of the neutral polymer **2.14** and the corresponding composite **2.16b** (Figure 2.28). The peak corresponding to the carbon atoms adjacent to O atoms in the ethylene glycol chains of the crosslinker (**2.14**: δ = 70.53

ppm, **2.16b**: δ = 70.55 ppm) are the most prominent in each spectrum. In both spectra, the broad peaks at ~ 64 ppm, 54 ppm and 40 ppm are associated with other C atoms of the PEGDA fragments. Poorly resolved resonances between 110 ppm – 180 ppm correspond to carbonyl and aromatic C atoms associated with PEGDA and Vim fragments, respectively.
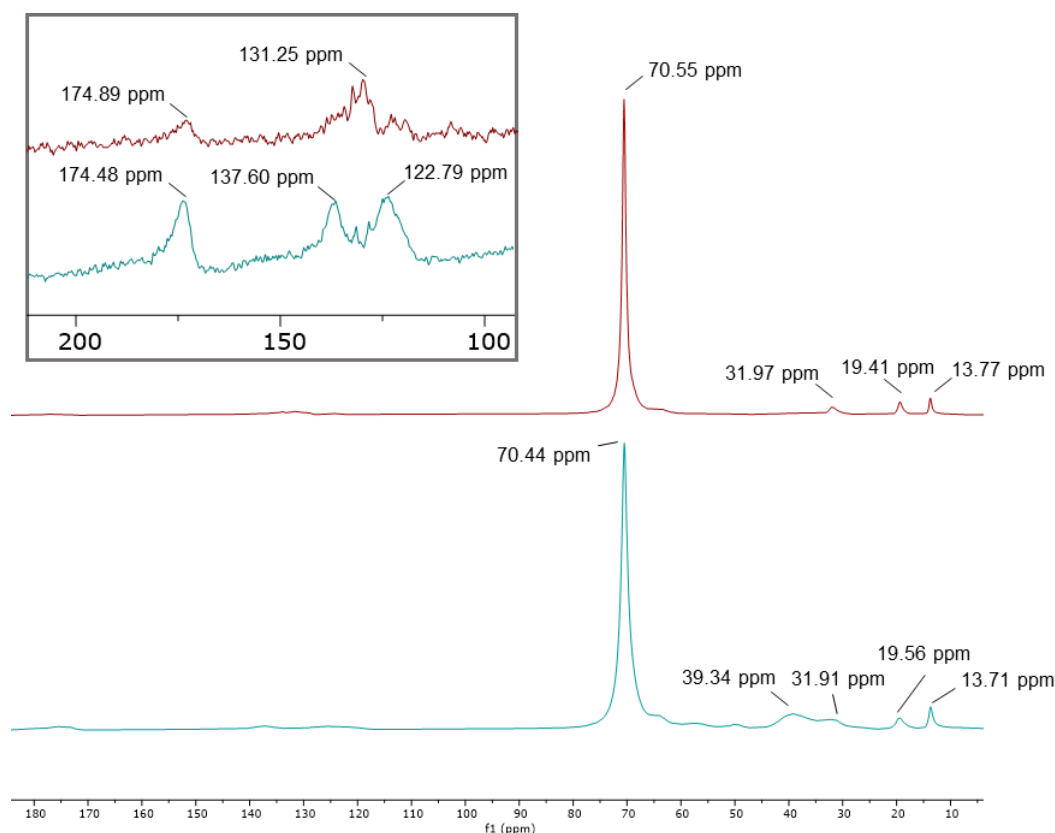
Figure 2.29: Solid state ^{13}C NMR spectra of BuVimBr:PEG700DA **2.15b** (maroon) and PMo$_{12}$@BuVimBr:PEG700DA **2.17b** (teal).

The stacked ^{13}C SS NMR spectra of BuVimBr:PEG700DA **2.15b** and PMo$_{12}$@BuVimBr:PEG700DA **2.17b** is given in Figure 2.29. The peak corresponding to the C atoms adjacent to oxygen in the PEG chains of **2.15b** at 70.55 ppm (maroon) remains prominent in the spectrum of the composite **2.17b** (teal), shifting slightly to 70.44 ppm. A new, broad peak centred around 39.9 ppm in the spectrum of **2.17b** may be attributed to presence of TBA. In both spectra, poorly resolved peaks resonate between the region of 120 ppm – 175 ppm, corresponding to aromatic C atoms of the imidazole fragments and carbonyl carbons.

To provide a comparison with solid-state ^{31}P NMR spectra of POM@polymer composites, solution ^{31}P NMR of PMo$_{12}$ reacted with different equivalents of ascorbic acid was recorded (Figure 2.30).
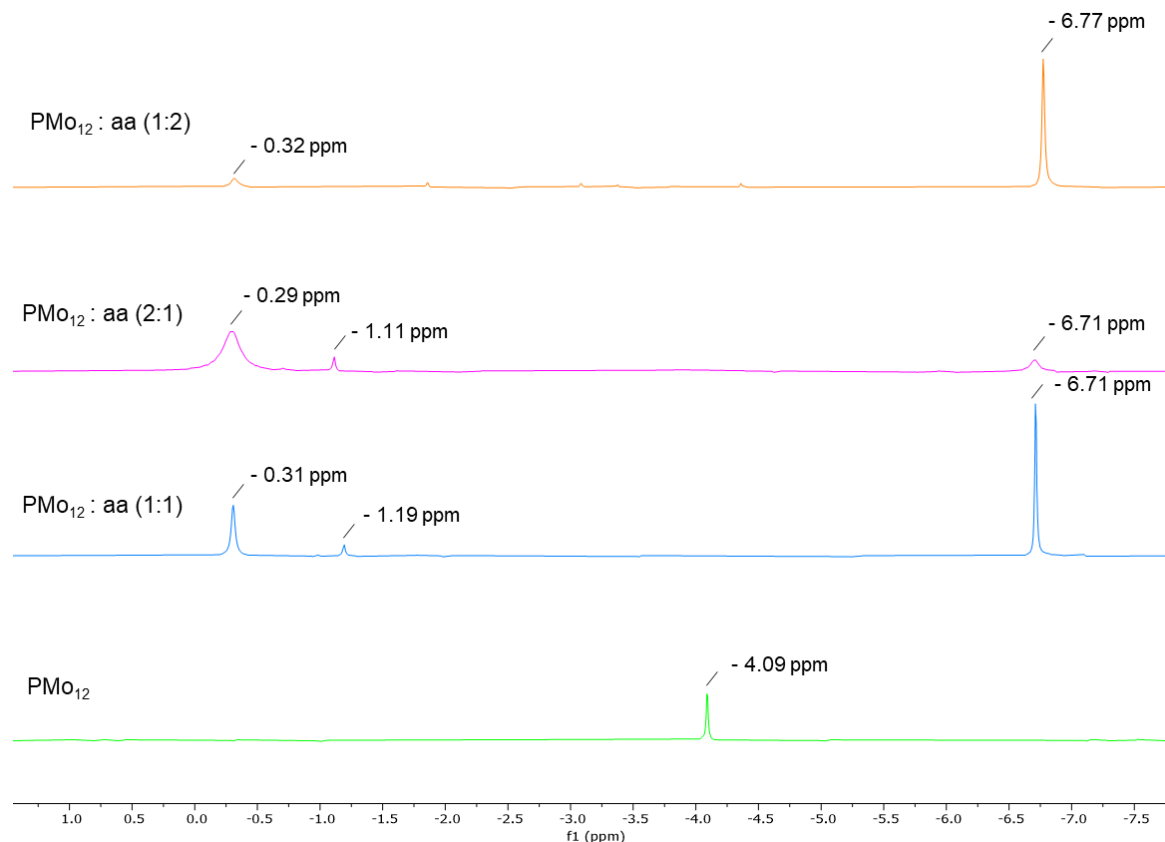
Figure 2.30: $^{31}P\{^{1}H\}$ NMR spectra of **2.1** (PMo$_{12}$) reacted with different equivalents of ascorbic acid (aa): green = 0 eq. aa, blue = 1.0 eq. aa, pink = 0.5 eq. aa, orange = 2.0 eq. aa in DMSO.

One resonance at – 4.09 ppm was present in the spectrum of fully-oxidised PMo$_{12}$ (Figure 2.30, green).[26] Reaction with 1 molar equivalent of ascorbic acid (aa) results in a mixture of two major POM species (Figure 2.30, blue). The downfield peak at δ – 0.31 corresponds to [PMo$_{12}$O$_{40}$]$^{4-}$ (one-electron reduced) and the upfield major peak at δ - 6.71 corresponds to [PMo$_{12}$O$_{40}$]$^{5-}$ (two-electron reduced). The impurity resonance at -1.19 ppm is attributed to an unknown species. When the ratio of POM:aa was 2:1, [PMo$_{12}$O$_{40}$]$^{4-}$ was detected as the predominant species, and when there was excess reducing agent (POM:aa 1:2), [PMo$_{12}$O$_{40}$]$^{5-}$ was found to be the major species (Figure 2.30, pink and orange, respectively). Although the ^{31}P shifts of the POM are sensitive to the environment (i.e.

solvent, solid-state vs solution-state) the relative positions of peaks can be used as a guide towards identifying species in solid-state spectra of the composites.

Solid state ^{31}P {^1H} NMR of the composites PMo$_{12}$@Vim:PEG700DA **2.16b** and PMo$_{12}$@BuVimBr:PEG700DA **2.17b** were taken before and after reduction with ascorbic acid. Due to low levels of POM-loading associated with neutral-polymer composite **2.16b**, the ^{31}P NMR spectra suffered from a low signal-to-noise ratio (Figure 2.31). One species of POM was detected in each spectrum: between -1.17 and 1.46 ppm in the spectrum of the pre-reduced sample (yellow) and at 1.59 ppm for ascorbic acid treated **2.16b** (blue). It is likely that the species detected in both samples was [PMo$_{12}$O$_{40}$]$^{4-}$. Exposure of the composite to light may have allowed for photo-reduction of PMo$_{12}$ prior to treatment with ascorbic acid. Unexpectedly, the major-species present in the ascorbic acid-treated sample was one-electron reduced PMo$_{12}$, although it was noted that between sample preparation and analysis (~ 2 days), the reduced-blue composite slowly turned green in colour, indicative of reoxidation.
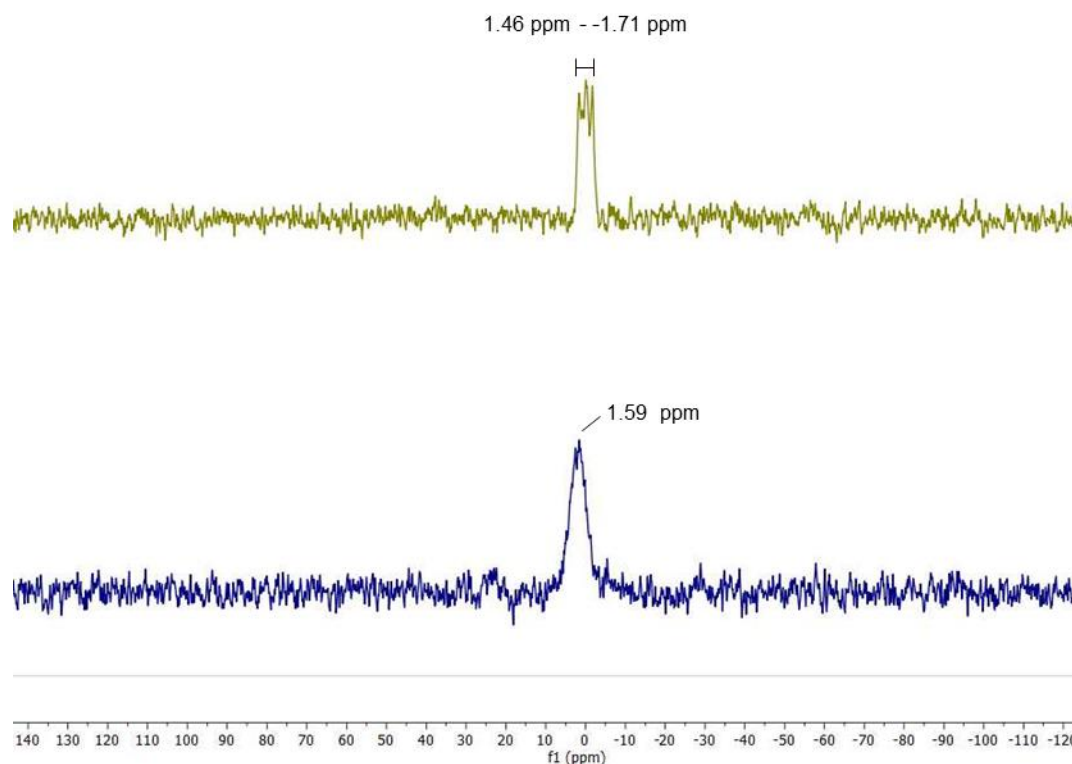
Figure 2.31: Solid state ^{31}P {^1H} NMR spectra of PMo$_{12}$@Vim:PEG700DA **2.16b** before (yellow) and after (blue) treatment with ascorbic acid.

^{31}P SS-NMR spectra of composite **2.17b** before and after reduction with ascorbic acid was compared (Figure 2.32). The single resonance at $\delta - 3.96$ in the spectrum of the pre-reduced composite sample falls within the region expected for the fully-oxidised species of $[PMo_{12}O_{40}]^{3-}$.[27] After reduction with ascorbic acid, two peaks were detected; one downfield at $- 0.13$ ppm and another upfield at $- 6.54$ ppm, corresponding to $[PMo_{12}O_{40}]^{4-}$ and $[PMo_{12}O_{40}]^{5-}$ respectively. The pattern and relative position of peaks was also observed with solution-state spectra (Figure 2.32). Relative integrals of the peaks showed that 90 % of POM in the sample was 2-electron reduced.
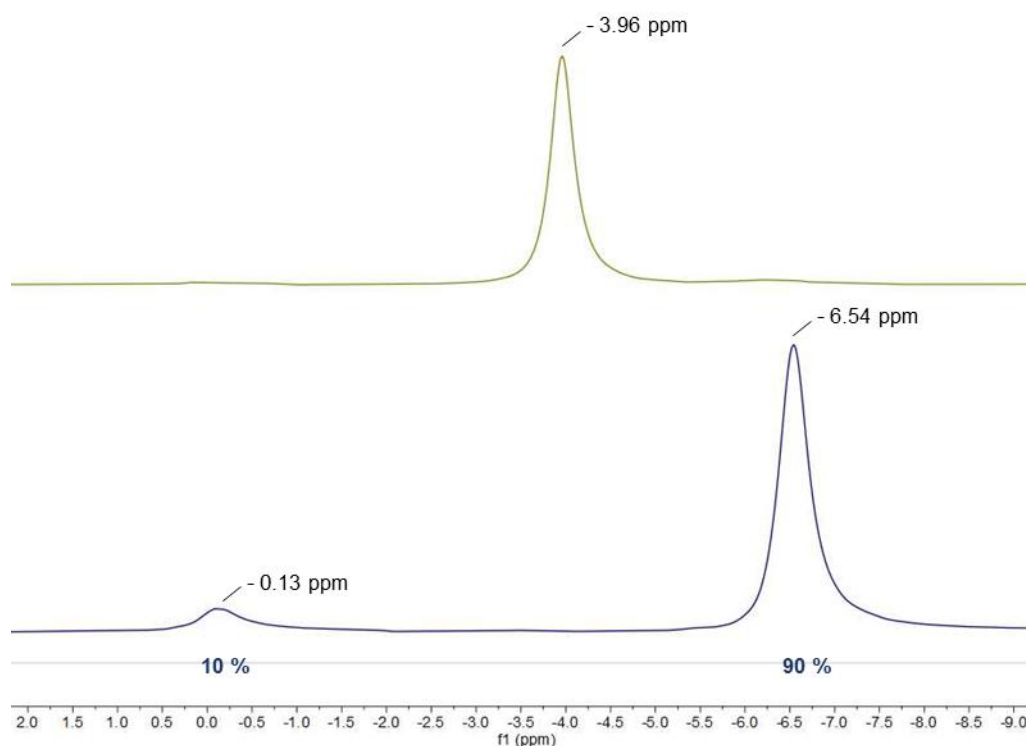
Figure 2.32: Solid state ^{31}P{^{1}H} NMR spectra of PMo$_{12}$@BuVimBr:PEG700DA **2.17b** before (yellow) and after treatment with ascorbic acid (blue).

2.4   Alternative Polymer Applications in Catalysis

This work has predominantly focused on the development of support materials for use as indicators in smart label devices, but the polymers formulated are not limited to anchoring POMs. A preliminary investigation was carried out to determine if the materials could be applied as heterogenous supports for transition metal nanoparticles in catalysis.

The Doherty group have explored a vast range of polymer-supported metal nanoparticle (NP) catalysts for a multitude of different reactions, most recently for the hydrolysis of sodium borohydride.[28] As an extension of this work, platinum nanoparticles were immobilised onto a photopolymerised polymer support **2.18** (Figure 2.33).
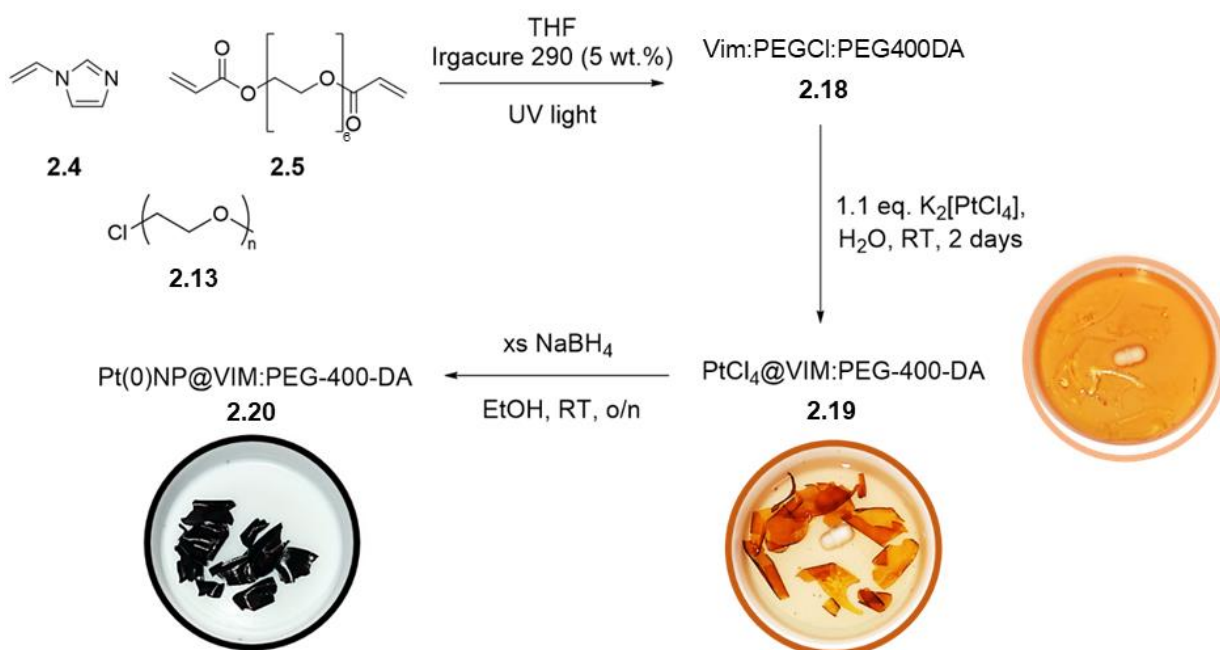
Figure 2.33: Reaction scheme for the curing polymer support **2.18**, immobilisation of a palladium precursor salt to **2.19**, then subsequent reduction to PdNP@polymer **2.20** with NaBH$_4$,

A batch of prepolymer solution containing *N*-vinylimidazole **2.4**, PEGCl **2.13** and PEG400DA **2.5** (molar ratio 2:2:3, respectively) in THF (0.8 mL) was prepared and placed into a PTFE mold. Irgacure 290 was added as the photoinitiator (5 wt. %) and the mixture was exposed to UV light (395 nm) for 20 min. The resulting polymer was thoroughly washed with THF and water to remove any unreacted monomer. K$_2$[PtCl$_4$] was then dissolved in water and the polymer was added to the solution, broken into smaller sections. The suspension was left overnight to allow time for immobilisation of the Pt(II) salt onto the polymer. The next day, the resulting PtCl$_4$@Vim:PEGCl:PEG400DA

composite **2.19** was washed with water then reduced with excess NaBH₄ in EtOH overnight. The material became black in colour, indicative of the Pt(II) precursor's reduction to Pt(0)NPs. The catalyst **2.20** was washed with EtOH then dried under vacuum before use. To determine the amount of Pt embedded into the polymer network ICP-OES was employed, which revealed that Pt loading was 0.75 mmol Pt/ g catalyst.

Initial catalyst testing was carried out for the hydrolysis of sodium borohydride (Scheme 2.3). The evolution of hydrogen from a reaction flask containing NaBH₄ (21.0 mg, 37.8 mmol) in water (2 mL) in the presence of the catalyst (0.5 mol% PtNP) was monitored over time at various temperatures (Figure 2.34). Evolution of H_2 due to self-hydrolysis of NaBH₄ was subtracted from catalyst testing results by taking control readings of hydrogen evolution under the same conditions in the absence of the catalyst. All experiments were repeated in duplicate and average readings were taken.

$$NaBH_4 + 4H_2O \longrightarrow NaB(OH)_4 + 4H_2$$

Scheme 2.3: The hydrolysis of NaBH₄

Temperature (ºC)	TOF (molH$_2$.molPt$^{(0)-1}$.min^{-1})
20	7.15
30	15.63
40	28.01
50	41.69
60	66.71

○ 60 ºC   ○ 50 ºC   ○ 40 ºC   ○ 30 ºC   ○ 20 ºC
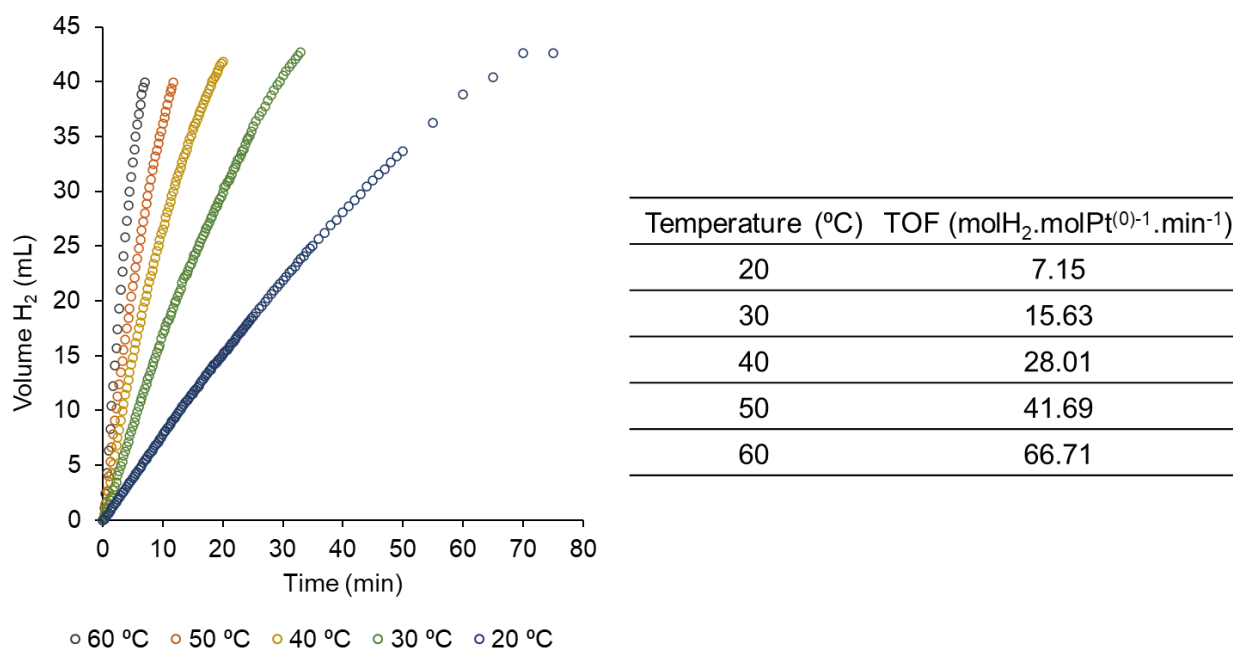
Figure 2.34: Graph to show volume of hydrogen evolved as a function of temperature (left) and table to show the calculated turn over frequency TOF (moles of H_2 evolved per mole Pt(0) per minute) at different temperatures.

Initial first order rates (k) were calculated from the linear part of each plot at different temperatures. An Arrhenius plot was then used to calculate the activation energy (E_a) for the reaction, which was determined to be 43.11 kJ mol^{-1}, according to equations 2.5 and 2.6 (Figure 2.35).

$$\ln(k) = - E_a/RT + \ln A \qquad \textbf{(2.5)}$$

$$m = - E_a/RT \qquad \textbf{(2.6)}$$

Where k = calculated rate constant; R = 8.31 J K^{-1} mol^{-1}; T = temperature (K)
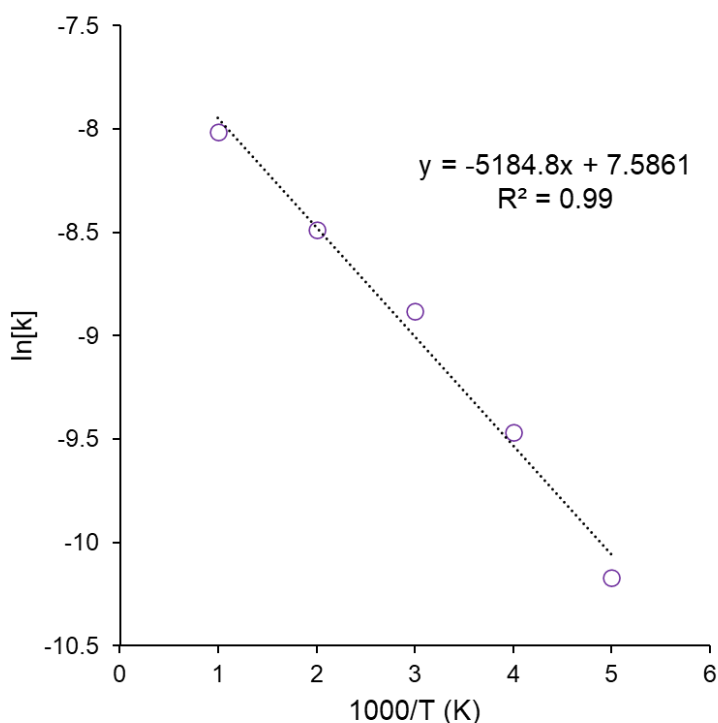
Figure 2.35: Plot of the natural log of rate k as a function of (1000/T). The linear equation is given in the form y = 1000mx + c, to account for scaling of the x axis.

The activation energy associated with the catalyst was found to be higher than that of other polymer immobilised ionic liquid support-based PtNP catalysts developed by the Doherty group. However, this preliminary study has shown that Vim – PEGDA based materials are feasible NP catalyst supports, and with further experimentation and development, catalytic efficiency could be improved.

2.5 Conclusion and Future Work

Four POM@polymer composites were identified as potential indicators for use in smart label devices. Polymer supports are uncomplicated and cheap, which is commercially desirable. It has been demonstrated that the polymer supports are capable of immobilising $[PMo_{12}O_{40}](TBA)_3$ in different quantities, depending on the formula. Neutral polymers immobilised less POM than ionic polymers, illustrating that the amount of POM immboilised within composite materials can be altered by choice of imidazole-based monomer.

Further characterisation is needed to elaborate on the exact properties of POM@Polymer materials. Firstly, a suitable digestion method would allow for ICP analysis of the composites, which would accurately establish the POM content. Long-term experiments are needed to determine the effective "shelf-life" of the composites by ensuring the structural integrity of the POM is not compromised over long time periods. Physical property measurements of the composite materials would provide quantitative information about their mechanical strength (e.g. tensile strength, % elongation at break). Once the gaps in analysis have been closed, polymer/composite optimisation could begin. There are many possible combinations of monomers, crosslinkers, photoinitiators, plasticisers, polyoxometalates and more that could be explored to further improve the quality and performance of the composites. This work has established a small foundation for future research. Prototype devices using materials described in this work will now be discussed in Chapter 3.

2.6   Experimental

2.6.1 Synthesis of [PMo$_{12}$O$_{40}$](TBA)$_3$ **2.1**

Na$_2$MoO$_4$.2H$_2$O (29.06 g, 120.0 mmol) was dissolved in deionised water (120 mL) before addition of 1 M H$_3$PO$_4$ (10.0 mL, 10.0 mmol) to give a colourless solution. 1,4-dioxane (100 mL) was then added, which resulted in slight clouding of the reaction solution. Concentrated HNO$_3$ (15.0 mL) was added dropwise, which resulted in an immediate colour change of the solution to clouded yellow. Clouding subsided after ca. 5 min stirring at room temperature. TBA(Br) (10.2 g, 31.6 mmol) was dissolved in deionised water (10 mL) with heating and added to the reaction solution, which resulted in precipitation of a yellow solid. The suspension was then stirred at room temperature for 30 min. The precipitate was isolated *via* vacuum filtration and allowed to air-dry overnight. The next day, the crude yellow solid was added to water (100 mL) and the suspension was boiled for 10 min to remove any water-soluble starting materials. Once the suspension cooled to room temperature, the yellow powder was isolated by vacuum filtration and washed with water (3 x 25 mL), IMS (3 x 25 mL) and diethyl ether (3 x 25 mL). The yellow solid was then dissolved in the minimum amount of MeCN (ca. 500 mL), then cooled and allowed to recrystallize overnight. The yellow crystals were isolated via vacuum filtration, then transferred to a Schlenk line and dried under high vacuum to remove any residual solvent, which gave a yield of 25.49 g (> 99 %).

FT-IR (cm^{-1}): 2961.81 (m), 2933.19 (w), 2873.95 (w), 1482.93 (w), 1469.43 (m), 1380.33 (w), 1060.57 (s), 950.38 (s), 874.60 (s), 784.64 (s, br), 615.98 (m), 500.76 (s), 463.69 (s)

^{31}P{^{1}H} NMR: DMSO-d_6: - 4.09 ppm

2.6.2   Synthesis of [PW$_{12}$O$_{40}$](TBA)$_3$ **2.2**

H$_3$[PW$_{12}$O$_{40}$](TBA)$_3$.26H$_2$O (4.99 g, 1.49 mmol) was dissolved in water (15 mL). Spearately, TBA(Br) (1.45 g, 4.47 mmol) was dissolved in water (50 mL) then added dropwise to the heteropoly acid solution. The mixture quickly became viscous, and was diluted with a further 50 mL water to aid stirring for 30 min. A white powder was isolated upon filtration of the suspension. The crude product was added to water (50 mL) and heated to 100 ºC with stirring to remove any excess starting material. Once cooled, the white solid was isolated by filtration and washed with IMS (3 x 25 mL) and Et$_2$O (3 x 25

mL). The crude product was recrysallised from hot MeCN (40 mL) and retrieved *via* filtration. The white crystalline product was allowed to dry in a vacuum oven for 24 h. Yield 88 %

FT-IR (cm^{-1}): 2962.21 (m), 2873.63 (w), 1469.32 (m), 1379.73 (w), 1077.1 (s), 971.71 (s), 891.24 (s), 795.24 (s), 735.77 (s), 594.4 (m), 507.63 (s).

2.6.3   Synthesis of [SiW$_{12}$O$_{40}$](TBA)$_4$ **2.3**

H$_4$[SiW$_{12}$O$_{40}$].26H$_2$O (4.99 g, 1.50 mmol) was dissolved in water (5 mL). Separately, TBA(Br) (2.13 g, 6.60 mmol) was dissolved in water (4 mL) then added dropwise to the heteropoly acid solution. The mixture quickly became viscous, and was diluted with a further 10 mL water to aid stirring for 30 min. A white powder was isolated upon filtration of the suspension. The crude product was added to water (50 mL) and heated to 100 ºC with stirring to remove any excess starting material. Once cooled, the white solid was isolated by filtration and washed with IMS (3 x 25 mL) and Et$_2$O (3 x 25 mL). The crude product was recrystallised from hot MeCN (80 mL) and retrieved *via* filtration. The white powdered product was allowed to dry in a vacuum oven for 24 h. Yield 74 %

FT-IR (cm^{-1}): 2959.52 (s), 2935.10 (m), 2872.95 (m), 1482.90 (m), 1425.90 (m), 1009.17 (m), 964.16 (s), 915.86 (s), 882.41 (s), 786.80 (s), 528.87 (s), 482.05 (m)

2.6.4   Synthesis of Poly(ethylene glycol) Chloride **2.13**

Polyethylene glycol monomethyl ether 350 (10.5 g, 30.0 mmol), pyridine (4.85 mL, 60.0 mmol) and dry toluene were added to an oven-dried Schlenk flask under an inert atmosphere. The colourless solution was heated to 70 ºC before drop-wise addition of thionyl chloride (4.35 mL, 60.0 mmol), which resulted in immediate formation of a white gas and the reaction mixture became turbid. As more thionyl chloride was added, the suspension became yellow and darkened gradually over time to form a red/brown oil phase and an orange/brown organic phase. The mixture was left to stir at 80 ºC for 2 days. Once cooled, water (5 mL) was added slowly to the reaction mixture. The organic layer was separated and the dark brown aqueous layer was extracted with toluene (3 x 25 mL). The clear yellow organic extracts were combined and evaporated under reduced pressure to give a clear orange oil. The crude oil was dissolved in DCM and drawn through a plug of silica to remove any impurities (8.47 g, 81.0 %).

^{1}H NMR (300 MHz, CDCl$_3$) δ 3.28 (3H, s), 3.44 – 3.46 (2H, t), 3.51 – 3.56 (27 H, m), 3.65 – 3.67 (2H, t). ^{13}C NMR (400 MHz, CDCl$_3$) δ 72.55, 71.91, 70.60, 70.58, 70.55, 70.53, 70.48, 70.32, 61.66, 59.00.

2.6.5 Synthesis of 1-butyl-3-vinylimidazolium bromide **2.10**

N-vinylimidazole (1.88 g, 20.0 mmol) and bromobutane (2.74 g, 20.0 mmol) were added to a reaction flask and heated to 60 ºC. After 3 h, the viscous crude product was washed with Et$_2$O (3 x 50 mL) then dried under vacuum to yield the puridied product. Yield 95 %

^{1}H NMR (300 MHz, CDCl$_3$) δ 0.85 – 0.89 (3H, s), 1.27 -1.34 (2H, sx), 1.81 – 1.91 (2H, sx), 2.42 (1H, s), 4.34 (2H, t), 5.28 – 5.31 (1H, dd, J = 9 Hz, 3 Hz), 5.94 – 6.00 (1H, dd, J = 15 Hz, 3 Hz), 7.37 – 7.45 (1H, dd, J = 15 Hz, 9Hz), 7.69 (1H, t), 7.96 (1H, t), 10.65 (1H, t).

3.6.6 General Polymer Synthesis

Monomer and crosslinker were mixed in equimolar quantities. Photoinitiator (5 wt. %) was added and the mixture was dissolved in water:THF (1:4) (2 mL per g total monomer and crosslinker). The prepolymer mixture was allowed to sonicate for 5 min, then 0.5 mL of the resulting solution was injected into custom PTFE molds and allowed to cure under a UV-light source (395 nm) at a distance of 2 cm for 10 min. Polymer samples were removed from the mold and then washed with THF and water. Polymer samples were stored in MeCN. For thin films, the volume of solvent used to dissolve the prepolymer formula was halved.

2.6.7 General Polyoxometalate-Polymer Composite Synthesis

Polymer samples were placed into an excess of a saturated solution of [PMo$_{12}$O$_{40}$](TBA)$_3$ in MeCN and left overnight. The resulting composites were then washed with MeCN (3 x 30 mL) and then stored in MeCN for analysis.

2.6.8 PtNP Catalyst Synthesis

N-vinylimidazole (38.0 mg, 0.4 mmol), PEGCl (367.9 mg, 0.4 mmol) and PEG400DA (400.0 mg, 0.6 mmol) were dissolved in THF (0.8 mL). Irgacure 290 (5 wt. %) was added to the prepolymer formula then cured under UV light for 10 min. The resulting polymer was washed with THF (3 x 30 mL) and allowed to dry in air for 24 h. The polymer was then placed into a solution of K$_2$[PtCl$_4$] (104 mg, 0.25 mmol) in water (20 mL) and

immobilization was allowed to take place overnight. The resulting orange/pink precatalyst composite was then washed with water (3 x 10 mL) and then EtOH (3 x 10 mL). The precatalyst was then added to a solution of $NaBH_4$ (60.6 mg, 1.60 mmol) in EtOH (20 mL) and reduction was allowed to continue overnight. The resulting active catalyst PtNP composite was then washed with EtOH (3 x 10 mL) and allowed to dry in a vacuum oven at 50 ^{o}C overnight.

2.6.9 *General Procedure for the Catalytic Hydrolysis of NaBH$_4$*

$NaBH_4$ (21.0 mg, 0.56 mmol) was added to a 50 mL round bottom flask. PtNP@Vim:PEGCl:PEG400DA (0.5 mol% Pt) was added and the reaction flask was allowed to equilibrate to the corresponding temperature. At T = 0 min, water (2 mL) was added to the reaction flask before it was immediately connected to tubing, which was connected to a water-filled burette. H_2 evolution was monitored *via* water displacement.

2.7   References

[1] Y. Zhang, J. Liu, S. L. Li, Z. M. Su, Y. Q. Lan, *EnergyChem*, 2019, **1**, 1 – 58.

[2] a) S. S. Wang, G. Y. Yang, *Chem. Rev.*, 2015, **115**, 4893–4962; b) Y. Ji, L. Huang, J. Hu, C. Streb, Y. F. Song, *Energy Environ. Sci.*, 2015, **8**, 776-789; c) N. I. Gumerova, A. Rompel, *Inorg. Chem.*, 2021, **60**, 6109–6114.

[3] S. R. Crouch, H. V. Malmstadt, *Anal. Chem.*, 1967, **39**, 1084–1089.

[4] P. Jones, R. Stanley, N. Barnett, *Anal. Chim. Acta.*, 1991, **249**, 539-544.

[5] M. T. Pope, in Polyoxometalate Molecular Science, eds. J. J. Borras-Almenar, E. Coronado, A. Muller, M. T. Pope, Kluwer Academic Publishers, Dordrecht, Netherlands, First edn., 2003, ch. 1, pp. 3-31.

[6] E. A. Nagul, I. D. McKelvie, P. Worsfold, S. D. Kolev, *Anal. Chim. Acta,* 2015, **890**, 60 – 82.

[7] a) D. Dimotikali, E. Papaconstantinou, *Inorg. Chim. Acta*, 1984, **87**, 177 – 180; b) T. Yamase, R. Sasaki, T. Ikawa, *J. Chem. Soc. Dalton Trans.*, 1981, 628-634; d) P. Argitis, E. Papaconstantinou, *Inorg. Chem.* 1986, **25**, 4386 – 4389.

[8] E. Papaconstantinou, *Chem. Soc. Rev.*, 1989, **18**, 1 – 13.

[9] J. J. Walsh, A. M. Bond, R. J. Forster, T. E. Keyes, *Coord. Chem. Rev.*, 2016, **306**, 217 – 334.

[10] C. Streb, *Dalton Trans.*, 2012, **41**, 1651-1659.

[11] a) Y. Shen, X. Yan, L. An, S.Shen, L. An, J. Zhang, *Applied Energy*, 2022, **313**, 118781; b) J. Suárez-Guevara, V. Ruiz, P. Gómez-Romero, *Phys. Chem. Chem. Phys.,* 2014, **16**, 20411-20414.; d) J. Lei, X. X. Fan, T. Liu, P. Xu, Q. Hou, K. Li, R. M. Yuan, M. S. Zheng, Q. F. Dong, J. J. Chen, *Nat. Commun.*, 2022, **13**, 1- 10.

[12] a) S. S. Wang, G. Y. Yang, *Chem. Rev.*, 2015, **115**, 4893 – 4962; b) V. Prabhakaran, Z. Lang, A. Clotet, J. M. Poblet, G. E. Johnson, J. Laskin, *ACS Nano*, 2019, **13**, 458 – 466

[13] S. M. Wang, L. Liu, W. L. Chen, Z. M. Zhang, Z. M. Su, E. B. Wang, *J. Mater. Chem. A*, 2013, **1**, 216 – 220.

[14] V. Ramani, H. R. Kunz J. M. Fenton, *Electrochim. Acta*, 2005, **50**, 1181-1187

[15] a) C. Sanchez, J. Livage, J. P. Launay, M. Fournier, Y. Jeannin, *J. Am. Chem. Soc.*, 1982, **104**, 3194 – 3202; b) R. Meenakshi, K. Shakeela, S. Kutti Rani, G. Ranga Rao, *Catal. Lett.*, 2018, **148**, 246 – 257

[16] P. Layford, PhD Thesis, Newcastle University, 2021.

[17] a) P. Le Magueres, S. M. Hubig, S. V. Lindeman, P. Veya, J. K. Kochi, *J. Am. Chem. Soc.*, 2000, **122**, 10073-10082; b) X. Wang, X. Pan, X. Wang, G. Liu, H. Lin, S. Zhang, *Transit. Met. Chem.*, 2019, **44**, 207 – 217.

[18] W. Hou, F. Ma, J. Li, H. Tian, G. Chen, G. Li, L. Jing, P. Yang, *J. Polym. Environ.*, 2023, **31**, 1656–1667.

[19] J. J. Zhu, T. Gotoh, S. Nakai, N. Tsunoji, M. Sadakane, *Mater. Adv.*, 2021, **2**, 3556–3559.

[20] A. Sienkiewicz, P. Krasucka, B. Charmas, W. Stefaniak, J. Goworek, *J. Therm. Anal. Calorim.,* 2017, **130**, 85-93.

[21] J. Maitra, V. K. Shukla, *Am. J. Polym. Sci.*, 2014, **4**, 25- 31.

[22] M. Jamadi, P. Shokrollahi, B. Houshmand, M. D. Joupari, F. Mashhadiabbas, A. Khademhosseini, N. Annabi, *Macromol. Biosci.*, 2017, **17**, 1600479

[23] a) J. P. Tessonnier, S. Goubert-Renaudin, S. Alia, Y. Yan, M. A. Barteau, *Langmuir*, 2013, **29**, 393 – 402; b) X. Lopez, J. M. Maestre, C. Bo, J. M. Poblet, *J. Am. Chem. Soc.* 2001, **39**, 9571–9576

[24] R. G. Holmes, F. A. Rueggeberg, R. S. Callan, F. Caughman, D. C. N. Chan, D. H. Pashley, S. W. Looney, *Dent. Mater.*, 2017, **12**, 1506-1512.

[25] H. R. Sun, S. Y. Zhang, J. Q. Xu, G. Y. Yang, T. S. Shi, *J. Electroanal. Chem.*, 1998, 455, 57-68.

[26] a) V. Artero, A. Proust, *Eur. J. Inorg. Chem.*, 2000, **2000**, 2393-2400; b) K. A. Phipps, PhD Thesis, Newcastle University, 2020.

[27] a) G. Rao, T. Rajkumar, B. Varghese, *Solid State Sci.*, 2009, **11**, 36-42; b) V. Artero, A. Proust, 2000, *Eur. J. Inorg. Chem.*, **2000**, 2393-2400.

[28] S. Doherty, J. G. Knight, H. Y. Alharbi, R. Paterson, C. Wills, C. Dixon, L. Šiller, T. W. Chamberlain, A. Griffiths, S. M. Collins, K. Wu, M. D. Simmons, R. A. Bourne, K. R. J. Lovelock, J. Seymour, *ChemCatChem*, 2022, **14**, 2021017.

Chapter 3 Prototype Devices

3.1 Introduction

There are many examples whereby polyoxometalates have been utilised for detection and sensing purposes, two examples of which were discussed within the introduction section of Chapter 2 (i.e., electrochromic windows and the detection of alcohol in sweat/saliva). Other examples include UV radiation dosimetry indication *via* a POM-based photochromic ink[1], naked-eye detection of the drug acetaminophen with gold nanoparticle-POM hybrids[2], and the optical detection of $ZnCl_2.H_2O$ by a silicomolybdic organic salt[3], to name a few. However, there is no current literature example of a POM-based TTI.

The polyoxometalate-polymer hybrid materials that were synthesised and characterised in Chapter 2 were designed for use as indicator materials in smart label devices. It was established that vinylimidazole or vinylimidazolium-*co*-poly(ethylene glycol) diacrylate polymers were capable of immobilising $[PMo_{12}O_{40}](TBA)_3$, and the resulting POM@Polymer composites underwent vivid colour changes upon contact with aqueous solutions of ascorbic acid.

3.1.1 Background

Up until now, the colour change of POM@Polymers has been evaluated based solely on submerging composites directly into excess reducing agent solution. However, in order to assess the feasibility of integrating the materials within a smart label, it is important to investigate a multicomponent system that can more authentically represent a commercial device. Additionally, the fundamental working principle of TTI smart labels is that the time in which it takes for colour change to occur is dependent upon temperature, and therefore this is an essential investigation parameter. To this end, paper-based microfluidic devices have gained much attention over the last decade due to the inherent advantages associated with such systems, including low cost and simple design.[4] As the diffusion matrix, paper enables the capillary flow of fluids through devices while retaining its flexibility and possesses a good shelf life.[5] For these reasons, multilayer POM@polymer-paper based assemblies were identified as suitable prototype devices to explore essential TTI criteria.

3.1.2 Approach to Prototype Device Testing

The work in this chapter aims to integrate POM@Polymer materials into paper-based diffusion devices to qualitatively monitor colour change with flow of aqueous ascorbic acid through the diffusion matrix over time. Specifically, the time in which it takes for POM@Polymer indicators within the devices to change colour will be assessed by varying:

- *Temperature:* temperature-dependent colour change is a critical specification for any prospective TTI device.
- *Concentration of the reducing solution:* if differing concentration of the reducing agent in solution can be used to control time-temperature dependent colour change of POM@Polymers, this would establish an aspect of tunability without the need to change the chemical or physical properties of the indicator material itself (e.g. POM loading).
- *Ionic vs Neutral POM@Polymer indicators:* the two types of indicator materials were shown to have different properties including POM loading, which could drastically change the kinetics and appearance of colour change under the same environmental conditions.

3.2 Prototype Devices

For prototype devices, PEG700DA-based POM@Polymer materials PMo$_{12}$@VimPEG700DA **2.16b**, and PMo$_{12}$@BuVimBr:PEG700DA **2.17b** were selected for comparison.

3.2.1 Device Assembly

Polymer and composite materials were synthesised as consistently-shaped samples. For the neutral polymer **2.13**, batches were made up by mixing Vim **2.4** and PEG700DA **2.8** in equimolar quantities. Photoinitiator (5 wt. %) was added and the mixture was dissolved in water:THF (1:4) (2 mL per g total monomer and crosslinker). The prepolymer mixture was allowed to sonicate for 5 min, then 0.5 mL of the resulting solution was injected into PTFE moulds (1.0 mm x 1.0 mm x 0.5 mm) and allowed to cure under a UV-light source at a distance of 2 cm for 10 min. Polymer samples were removed from the mold and then

washed with THF and water. The process was repeated with BuVimBr **2.10** as the monomer to yield samples of the ionic polymer **2.15b**. Separately, each batch of polymer was added to an excess of a 5.0 mM PMo$_{12}$ **2.1** solution in MeCN and the POM was allowed to immobilise overnight to yield composite samples of **2.16b** and **2.17b**. The composites were washed with MeCN, then stored in fresh MeCN before subsequent use in devices. Paper-based prototype diffusion devices were constructed as outlined in the schematic below (Figure 3.1).
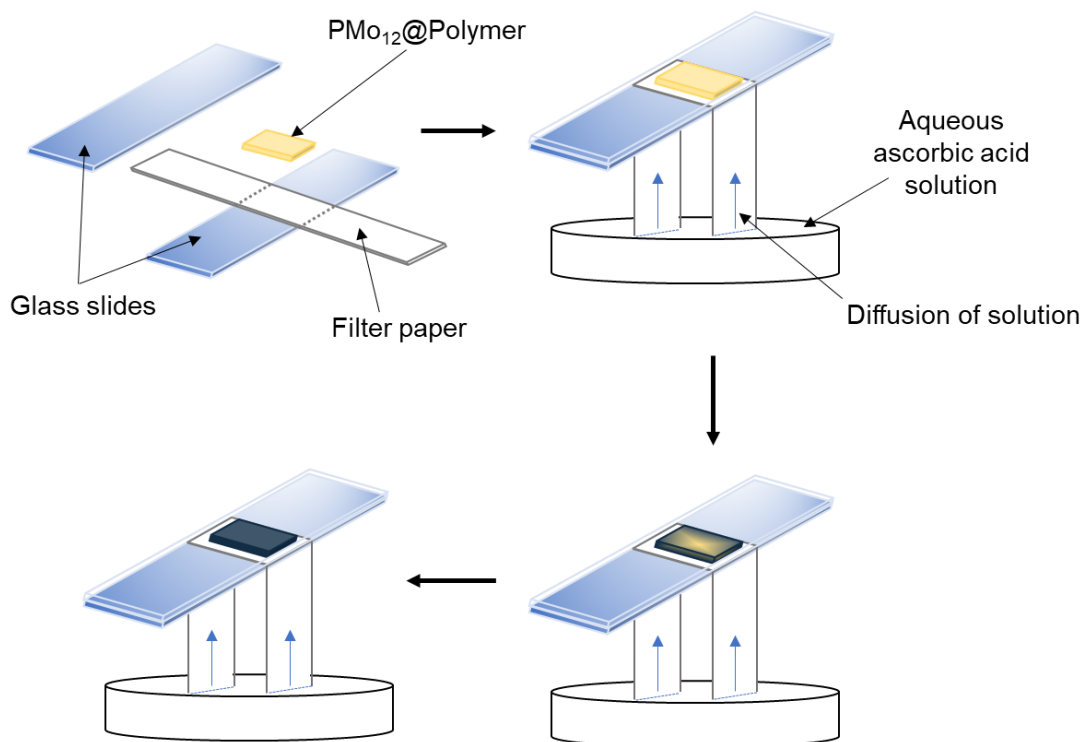
Figure 3.1: Schematic to show the assembly of the paper-based devices.

For the assembly of each device, excess solvent was removed from a 1 mm x 1 mm x 0.5 mm POM@polymer segment, which was then placed upon a filter paper strip of length = 65.0 mm and width = 2.0 mm (Whatman^{TM} Grade 1) and secured between two glass slides by a self-sealing film. The primary stationary phase (paper strip) was submerged into an aqueous solution of ascorbic acid (10 mL) at T= 0 (device activation). The composite, acting the active indicator, was monitored for colour change as time progressed.

Initial device tests began with composite material **2.16b** at room temperature with an ascorbic acid concentration of 0.1 M. However, using the method described above resulted in significant fracturing of the composite upon contact with the reducing solution

in the device (Figure 3.2). Although no-such issue had been encountered when transferring the composite from MeCN into ascorbic acid solution prior to this, physical constraints of the device did not allow for volume changes upon uptake of the aqueous solution. To mitigate this effect, composite indicator materials were instead stored in deionised water to allow for equilibration and therefore prevent significant volume changes after device test initiation.
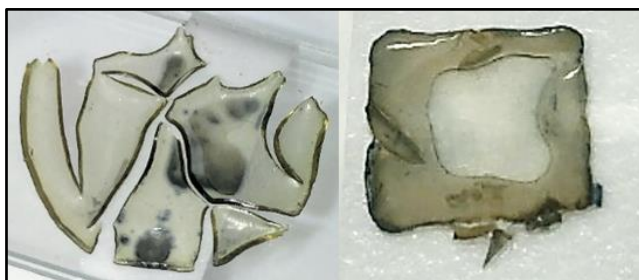
Figure 3.2: Images of composite material **2.16b** taken in device tests after contact with 0.1 M ascorbic acid solution at room temperature.

Changing the storage solvent resolved the preliminary issue, and systematic testing of the TTI prototypes began. Different variables in conditions were investigated, and device tests were ran either: at room temperature (20 ± 2 ºC) or under refrigeration (4.0 ± 1.0 ºC); with an ascorbic acid concentration of 0.1 M or 0.5 M (10 mL); with **2.15b** or **2.16b** as the indicator (Table 3.1). Time of device initiation (T_0) was recorded, and images were taken of the POM@Polymer composites at different time intervals for the first 3 h, and every 24 h thereafter (Figures 3.3 – 3.10). During experiments, the assemblies were kept in a secondary container to avoid contamination and evaporation of water from the ascorbic acid reservoir. Tests were carried out in duplicate.

Indicator Material	Ascorbic Acid Concentration (M)	Temperature (ºC)	Device Test
PMo$_{12}$@VimPEG700DA **2.16b**	0.1	20	**3.1a**
		4	**3.1b**
	0.5	20	**3.2a**
		4	**3.2b**
PMo$_{12}$@BuVimBrPEG700DA **2.17b**	0.1	20	**3.3a**
		4	**3.3b**
	0.5	20	**3.4a**
		4	**3.4b**

Table 3.1: numerical assignment of device test experiments based on indicator material, aqueous ascorbic acid concentration and temperature

3.2.1 Neutral Polymer Support Device Tests

Figure 3.3: Device run **3.1a**; images of PMo$_{12}$@VimPEG700DA **2.16b** during prototype TTI testing at room temperature with 0.1 M ascorbic acid in water, at various time intervals.
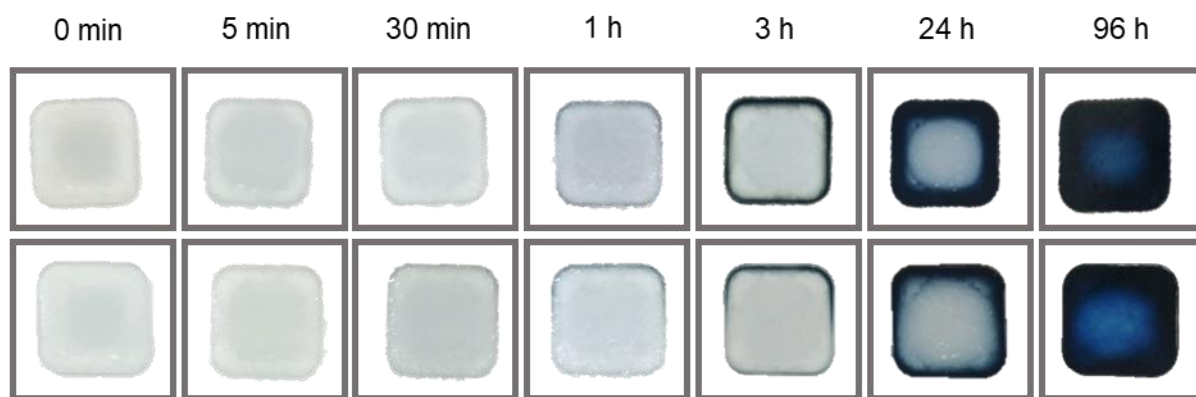
Figure 3.4: Device run **3.1b**; images of PMo$_{12}$@VimPEG700DA **2.16b** during prototype TTI testing at refrigeration temperature with 0.1 M ascorbic acid in water, at various time intervals.

2.16b was translucent at T$_0$ (device test **3.1a**, Figure 3.3, 0 min). 1 h after device initiation, onset of colour change (i.e. POM reduction) was observed around the outer edges of the materials. After 3 h, the diffusion front of the ascorbic acid solution progressed further from the outer-edges towards the centre of the indicator materials. After 24 h, the entire surface of the indicator appeared deep-blue. Similarly, during device run **3.1b**, reduction of the POM became obvious around the edges of the materials 3 h after T$_0$ (Figure 3.4). Unlike observations in experiment **3.1a**, after 24 h the centre-point of the indicator was still colourless. Four days after test initiation, POM embedded within the centre of each indicator had undergone reduction, although colour was less intense towards the centre (Figure 3.4, 96 h). Additionally, there was disparity between the diffusion patterns observed during the two repeat tests.
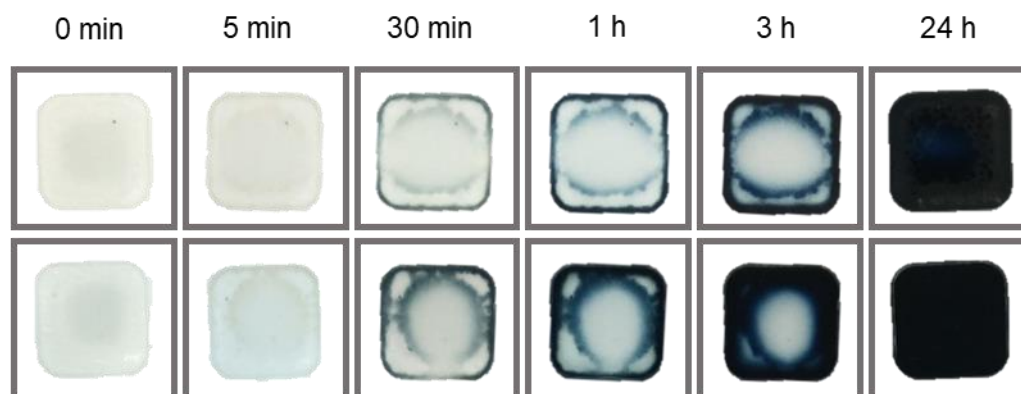
Figure 3.5 Device run **3.2a**; images of PMo$_{12}$@VimPEG700DA **2.16b** during prototype TTI testing at room temperature with 0.5 M ascorbic acid in water, at various time intervals.

85
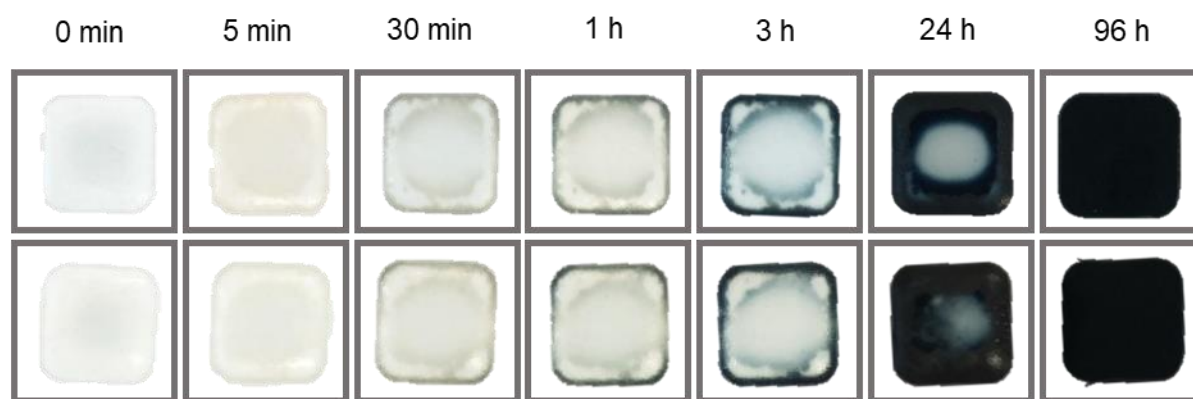
Figure 3.6 Device run **3.2b**; images of PMo$_{12}$@VimPEG700DA **2.16b** during prototype TTI testing at refrigeration temperature with 0.5 M ascorbic acid in water, at various time intervals.

Ascobic acid concentration was increased and test **3.2a** was ran at room temperature (Figure 3.5). After 30 min, the indicators began to change colour around the outer edges, but also around the contact points between the polymer composites and the top glass slide. Between 1 – 3 h, ascorbic acid solution diffused from the contact points towards the outer edges of the materials. Both repeats underwent full colour change after 24 h, with composites appearing dark blue/black to the naked eye. However, colour change patterns were not consistent between repeats.

Diffusion patterns observed during device test **3.2b** were also similar (Figure 3.6). After 24 h, there was a clear difference in the extent of which the reducing solution had travelled towards the centre of the indicators in repeat tests of **3.2b**. After 4 days, materials underwent full, uniform colour change.

3.2.2 Ionic Polymer Support Device Tests
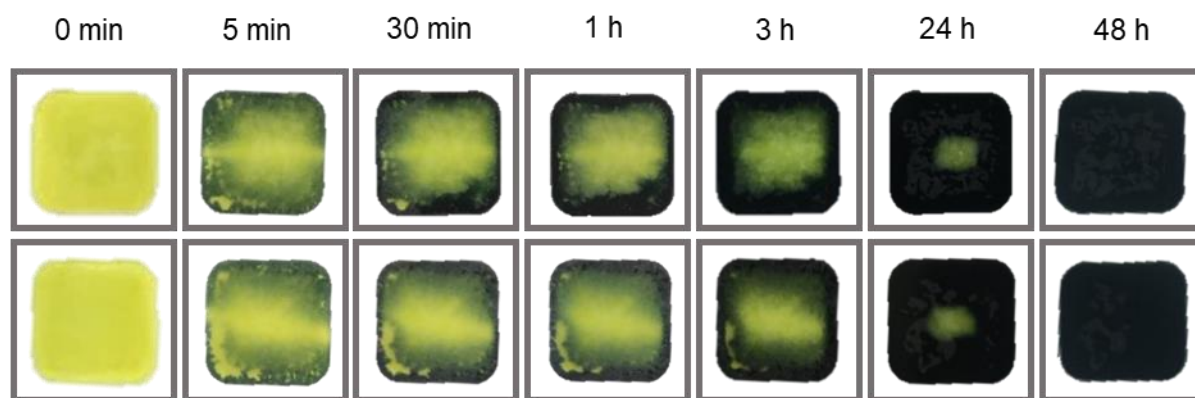
Figure 3.7 Device run **3.3a**; images of PMo_{12}@VimPEG700DA **2.17b** during prototype TTI testing at room temperature with 0.1 M ascorbic acid in water, at various time intervals.
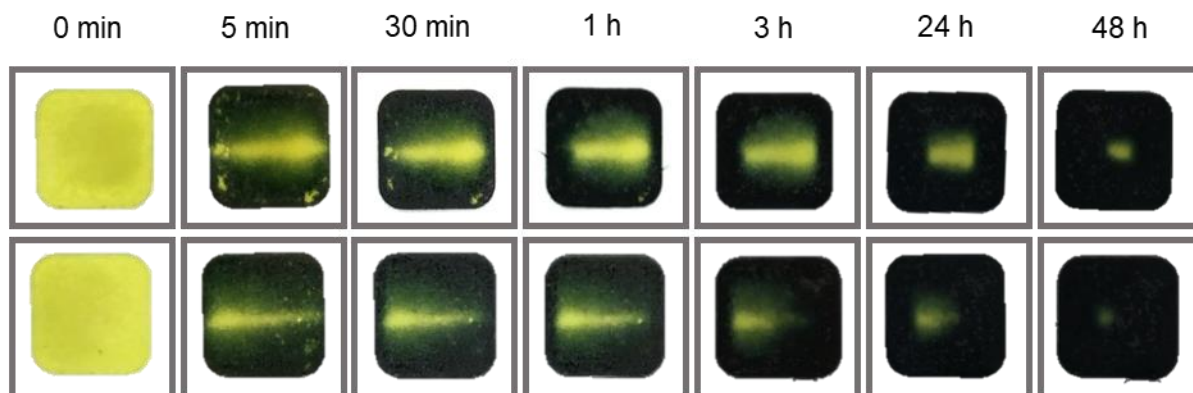
Figure 3.8 Device run **3.3b**; images of PMo_{12}@BuVimBrPEG700DA **2.17b** during prototype TTI testing at refridgeration temperature with 0.1 M ascorbic acid in water, at various time intervals.

The ionic based indicator material **2.17b** was vibrantly yellow at T_0 (Figure 3.7 and 3.8, 0 min). During device test **3.3a** colour change of indicator materials occurred from the outer perimeter of the composites towards the centre; from yellow, to green, to black/blue (5 min – 3 h). After 24 h, the diffusion patterns between repeat tests were consistent, and after 48 h both materials had undergone a uniform colour change.

During test **3.3b** at a lower temperature, composite materials underwent fast colour change, with all but an unsymmetrical yellow band remaining at the centre of indicators after only 5 min. Reducing diffusion patterns were offset from the centre and after 48 h, only a very small portion of the materials were still yellow.
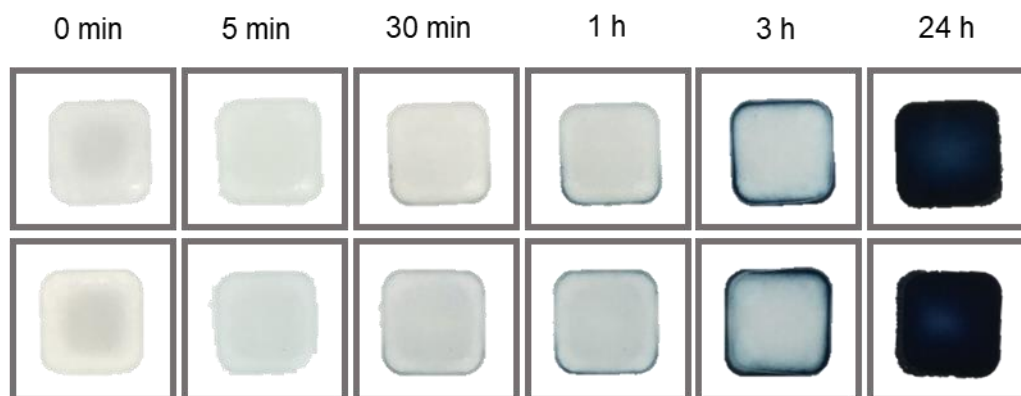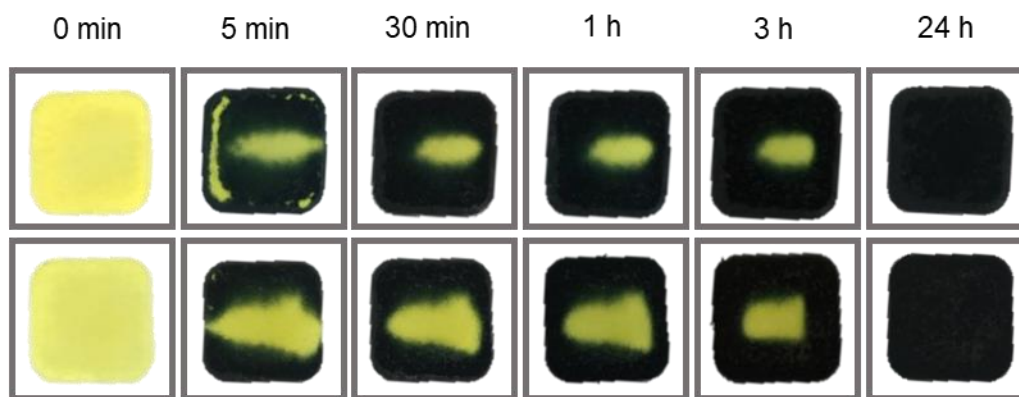
Figure 3.9: Device run **3.4a**; images of PMo$_{12}$@BuVimBrPEG700DA **2.17b** during prototype TTI testing at room temperature with 0.5 M ascorbic acid in water, at various time intervals.
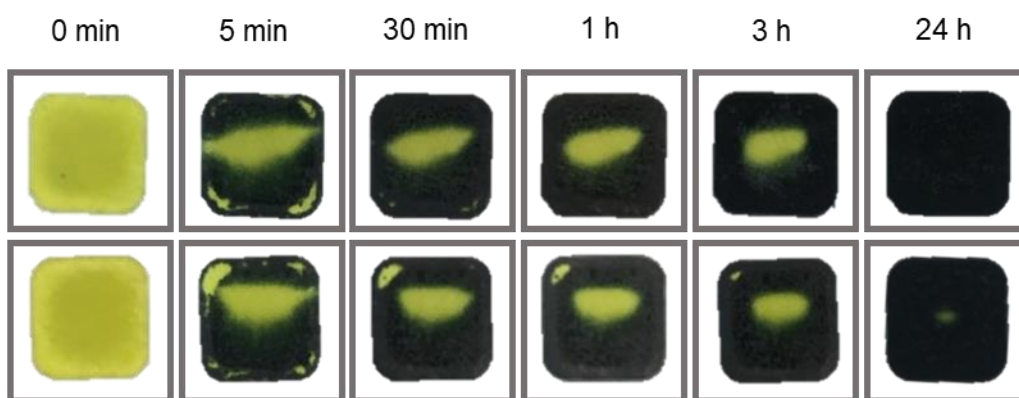
Figure 3.10: Device run **3.4b**; images of PMo$_{12}$@BuVimBrPEG700DA **2.17b** during prototype TTI testing at refrigeration temperature with 0.5 M ascorbic acid in water, at various time intervals.

Upon increasing the concentration of ascorbic acid to 0.5 M during device tests **3.4a** and **3.4b**, temperature dependence became less obvious. At both room temperature and under refrigeration, diffusion of the ascorbic acid throughout indicator materials was rapid. After 3 h, only small central sections of the composites were still yellow in colour, and after 24 h, all materials had undergone complete colour change.

3.2.3 Device Test and Indicator Comparison

In the fully oxidised state, indicator material **2.17b** is vividly yellow, whereas **2.16b** is translucent. Upon reduction, both materials undergo drastic colour changes due to PMo_{12} anchored within each polymer network. Fully reduced **2.17b** appears black to the naked eye, whereas **2.16b** appears deep-blue (Figure 3.11). The observations are a result of the relatively higher loading of POM onto the ionic polymer support.
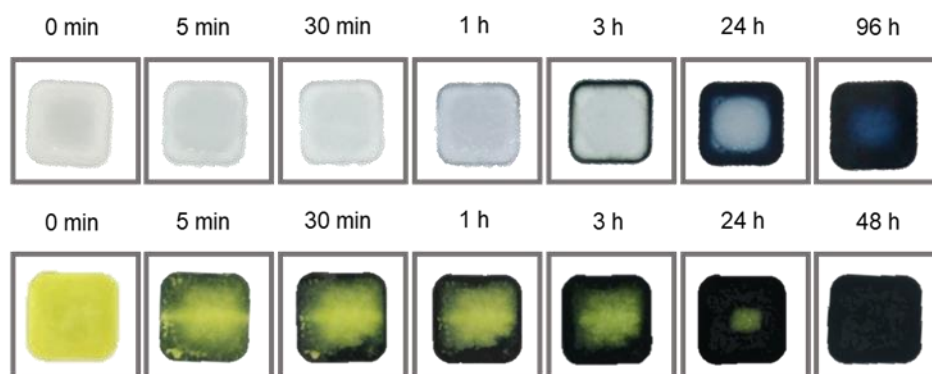
Figure 3.11: A comparison of the appearance and colour change of indicator materials PMo_{12}@Vim:PEG700DA **2.16b** (top row) and PMo_{12}@BuVimBr:PEG700DA **2.17b** (bottom row).

Generally, during device tests (**3.1** - **3.4**) diffusion of the ascorbic acid solution (monitored *via* colour change) progressed from the outer edges of indicators towards the centre. However, when two repeats were carried out for each experiment, there was little consistency between diffusion patterns and the time in which it took for indicators to undergo complete colour change. Part of this issue may be due to inconsistencies in the construct of devices, as the pressure points between the glass and composites could have an influence on diffusion patterns (Figure 3.12).
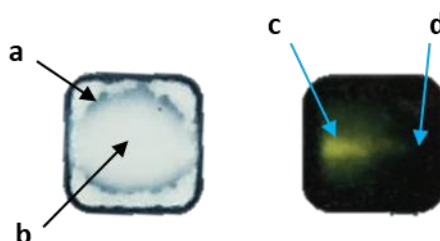
Figure 3.12: Images of PMo_{12}@Vim:PEG700DA **2.16b** (left) and PMo_{12}@BuVimBr:PEG700DA **2.17b** (right) within a device; a) contact limit between the composite material and glass slide; b)

central area of high contact pressure between the indicator and the glass slide; c) an area of high contact pressure between the indicator and glass slide; d) an area of low contact pressure between the indicator and the glass slide.

Despite the irregularities discussed above, the POM@Polymer devices displayed time-temperature sensitivity. For example, during device test **3.1a** (room temperature) the composite had undergone complete colour change 24 h after device initiation, whereas at a lower temperature (device test **3.1b**), full colour change was relatively slower. Ascorbic acid concentration also had an effect on the time in which it took for full colour change to occur e.g. during device test **3.4a**, the indicators (**2.16b**) appeared uniformly black in colour after 24 h, whereas at the same time interval during device tests **3.3a**, materials had not undergone reduction towards the centre point.

3.3   Conclusion and Future Work

A series of POM@Polymer prototype devices were constructed, and time-temperature dependance of colour change was monitored qualitatively. The simple devices used were a rudimentary method of assessing if composites **2.16b** and **2.17b** were suitable indicator materials for the potential use in commercial TTI devices, but the observations from device tests carried out in this work were not consistent, nor accurate enough to give a robust answer to this question. Albeit there was some evidence of time-temperature dependent colour change of the materials tested, and an element of tuneability within the device systems *via* varying ascorbic acid concentration and the indicator material used (i.e. neutral vs ionic polymer support).

3.5 References

[1] W. Zou, A. González, D. Jampaiah, R. Ramanathan, M. Taha, S. Walia, S. Sriram, M.Bhaskaran, J. M. Dominguez-Vera, V. Bansal, *Nat. Commun.*, 2018, **9**, 1 – 10.

[2] T. R. Bastami, A. Ghaedi, S. G. Mitchell, A. Javadian-Saraf, M. Karimi, *RSC Adv.*, 2020, **10**, 16805-16816.

[3] C. Sabarinathan, M. Karthikeyan, R. Murugappan, S. P. Anthony, B. Shankar, K. Parthasarathy, T. Arumuganathan, *New J. Chem.*, 2021, **45**, 5576–5588

[4] Y. Zhang, P. Zuo, B. C. Ye, *Biosens. Bioelectron.*, 2015, **68**, 14 – 19.

[5] Ali T. Jafry, H. Lim, W. K. Sung, J. Lee, *Microfluid. Nanofluid.*, 2017, **21**, 1 – 13.

Chapter 4 Synthesis and Application of Spiropyran Derivatives

4.1   Introduction

Spiropyran-functionalised hydrogels for microfluidic control in TTIs have previously been discussed (Chapter 1), but the photoswitching compounds also exhibit various forms of chromism, making them suitable candidates for indicators within smart labels.

4.1.1 Fundamental Chemistry of Spiropyrans

The basic structure of spiropyrans (Sp) consist of an indoline and a chromene moiety that are joined at a chiral spiro junction (Figure 4.1). They are commonly synthesised *via* a condensation reaction between a methylene-indoline base and a salicaldehyde derivative.[1] Upon cleavage of the spiro C-O bond of the colourless ring-closed isomer (Sp), *cis*-merocyanine (Mc) is formed and, in most cases, bond rotation quickly yields the more stable *trans*-Mc isomer.[2] As the molecule planarises to the Mc form, the previously orthogonal ring systems become fully conjugated. This results in absorption of light in the visible region, accounting for the characteristically vibrant colours associated with Mc isomers.[3] Mc exists in resonance between the zwitterionic and quinoidal states, although the zwitterion is energetically favored.[4] Protonation of the phenolate O atom affords McH+, which is often yellow/orange in colour and is associated with a blue shift in the absorption spectrum relative to Mc.[5]
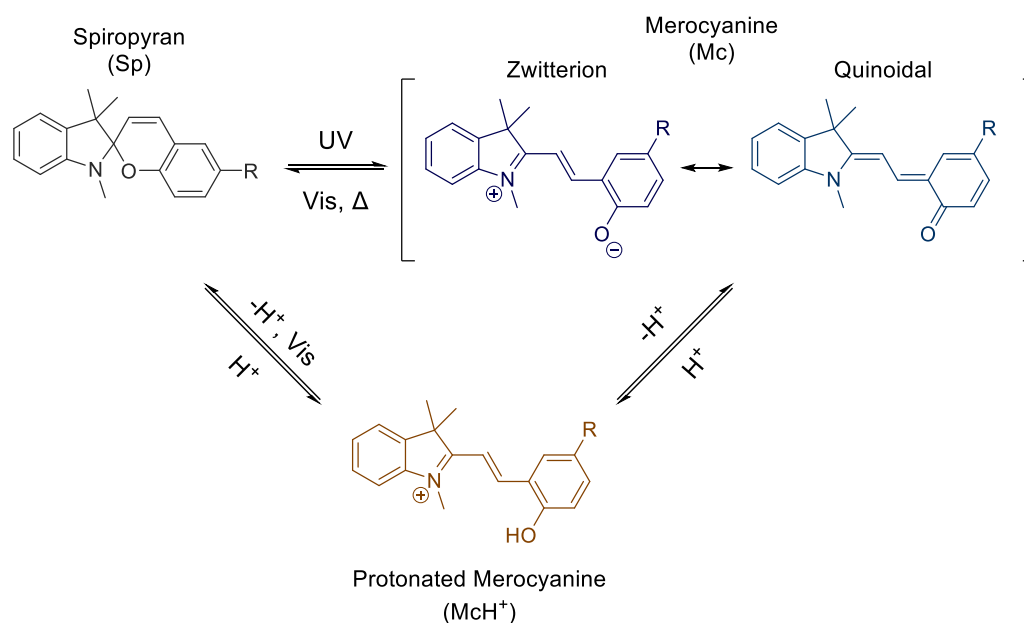
Figure 4.1: different species of spiropyrans including: Sp, the ring closed isomer; Mc, the ring-opened isomer that exists in two resonance forms; McH+, the protonated form of Mc.

The chemical and physical properties of Sp and Mc are vastly different and therefore the position of equilibrium between the two species depends on many factors including pH, solvent polarity, temperature, ionic strength and light exposure.[6] In addition to environmental factors, structural modification of spiropyrans can influence the kinetics and thermodynamics of ring opening/closing.[7] These phenomena can be utilised to tune the characteristic photo-, acido-, solvato-chromic properties of spiropyrans, which are discussed below.

4.1.2 Photochromism
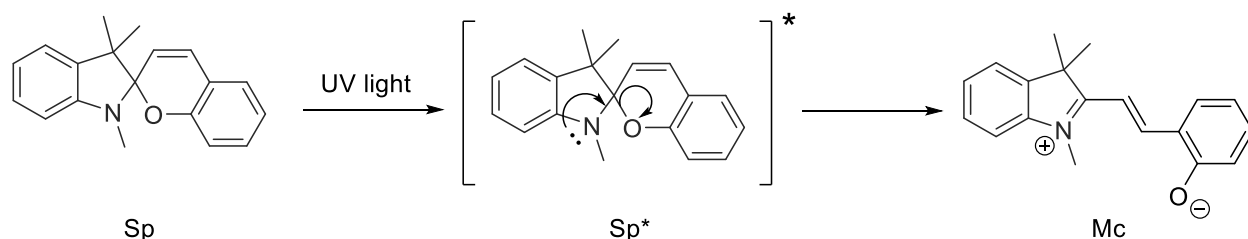
Figure 4.2: Photoexcitation of Sp to Sp* with subsequent ring-opening to Mc.

Photochromism describes the process whereby a photoswitch absorbs incident light and reversibly transforms into a species with different chemical and structural properties, resulting in inequivalent absorption spectra of the two forms.[8] For spiropyran compounds, positive photochromism occurs upon absorption of UV light by Sp, resulting in an excited state (Sp*) that undergoes heterolytic bond cleavage at the C-O spiro junction to yield the highly-coloured Mc isomer (Figure 4.2).[9] Negative photochromism takes place upon the reverse reaction in the presence of visible light or *via* thermal ring-closing. Photoisomerisation to Mc can be greatly enhanced by incorporation of stabilizing electron-withdrawing groups into the chromene ring (such as $-NO_2$), which increases the delocalisation of charge associated with the phenolate moiety of the ring-opened form.[10]

4.1.3 Solvatochromism

Solvent polarity can also have a significant effect on Sp – Mc equilibrium.[11] Solvatochromism occurs because the energy difference between Sp and Mc changes depending on the dielectric constant of the solvent (Figure 4.3). The charge separated Mc isomer is better solvated in more polar solvents, whereas neutral Sp is relatively destabilized (and *vice versa* for non-polar solvents). Increased solvent polarity also

induces bathochromic shifts in the absorption profile of the Mc isomer. This is because the energy gap between the ground state (polar, closely represented by the Mc zwitterionic form) and excited state (non-polar, closely represented by the Mc quinoidal form) is increased.[12]
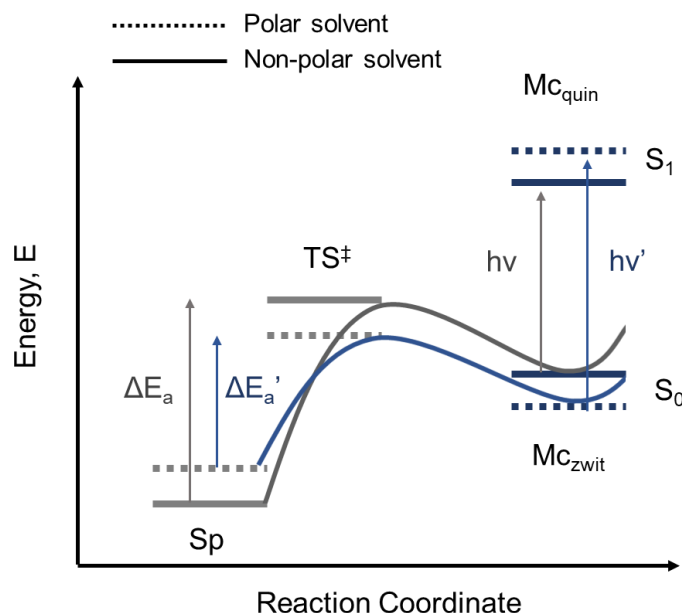
Figure 4.3: Reaction coordinate diagram to show the difference in activation energy (E_a) upon Sp→Mc isomerisation and the difference in energy between the Mc excited (S_1) and ground state (S_0) in solvents with different polarities. $\Delta E_a > \Delta E_a'$ and $h\nu < h\nu'$. Recreated from reference 6.

4.1.4 Acidochromism

pH-mediated ring-opening of spiropyran compounds is observed as a result of the stabilising effect upon protonation of the polar merocyanine isomer.[13] Protonation-driven isomerisation is inhibited by increased steric congestion about the C-O$_{spiro}$ bond, which impedes planarisation.[14] In addition, pK_a of the acid employed must be lower than that of the Mc phenolate for spontaneous ring-opening from the Sp form to occur. The stabilisation effect of protonation can be exploited to inhibit thermal ring-closing at ambient temperatures, which has facilitated the development of spiropyran-based functional materials such as the microfluidic valves discussed in Chapter 1.[15]

There are many other interesting properties associated with spiropyrans including mechanochromism[16], thermochromism[17], electrochromism[18], fluorescence[19] and

photoacidity[20]. Research has shown that each variety of chromism is accessible by careful consideration of the physiochemical differences between Sp and Mc isomers in the design of new spiropyran derivatives.

4.1.5 Modification of Spiropyrans: Suzuki Coupling Reactions

Functionality can be introduced into the structure of Sps *via* modification of the parent indoline and salicaldehyde prior to condensation, allowing for further synthetic transformation of the resulting Sp compound. By adopting this method, Suzuki cross coupling reactions have previously been employed as a convenient synthetic strategy used to access a range of Sp compounds. C. M. Yoon *et. al.* prepared 6-iodo-spiropyran and 6,8-diiodo-spiropyran for subsequent coupling with a series of aryl-boronic acids, employing Pd(OAc)$_2$ as the catalyst (Scheme 4.1).[21]
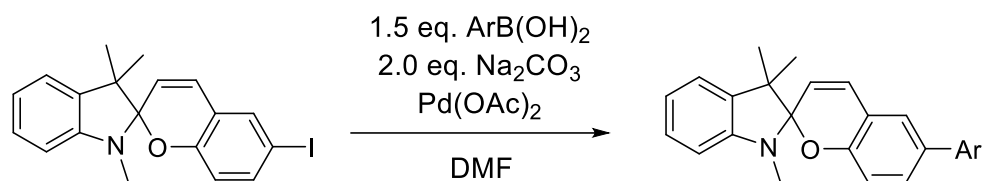
Scheme 4.1: conversion of 6-iodo-spiropyran to 6-aryl-spiropyran *via* Pd-catalysed Suzuki cross-coupling reaction with phenyl-boronic acid derivatives.
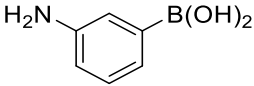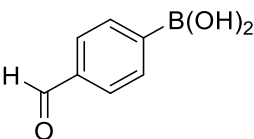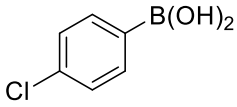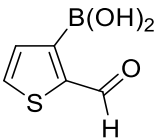
Boronic Acid	Reaction Time (h)	Yield (%)
H_2N — $B(OH)_2$ (aniline structure)	1.0	95
$B(OH)_2$ with aldehyde (4-formylphenyl)	1.5	86
$B(OH)_2$ with Cl (4-chlorophenyl)	1.5	79
$B(OH)_2$ thiophene carbaldehyde	1.5	86

Table 4.1: selected examples of Suzuki coupling products from the Yoon group's study.

The group successfully attained a number of Sp derivatives in moderate to good yields (Table 4.1). It was noted that the group had originally embarked to modify iodo-salicaldehydes prior to spiropyran synthesis, but reaction between this substrate and arylboronic acids was unsuccessful.

To the best of our knowledge, no other recent systematic study of Suzuki-coupling mediated spiropyran transformations has emerged in the literature. Nevertheless, there are examples of the reaction used as part of wider synthetic routes. For example, D. L. Officer *et. al.* synthesized a dithiophenespiropyran monomer from a dibromo-substituted spiropyran parent compound in 47 % yield using 4 mol% Pd(0) catalyst.[22] The Mukherjee-Stang group developed a synthetic pathway to a dipyridylspiropyran compound in 58 % yield *via* reaction of the dibrominated Sp parent compound with 4-pyridlybornic acid in the presence of 10 mol% Pd(0) catalyst.[23]

The Suzuki coupling method is a feasible technique that allows for access to novel Sp compounds with extended conjugation. However, poor yields reported in some syntheses could be greatly improved with the utilisation of more efficient Pd catalysts.

4.2 Starting Material Synthesis

Bromo-substituted (SpBr) Sp compounds were identified as suitable Suzuki coupling substrates to access to a wider range of other Sp derivatives. Two structural isomers were targeted with substitution at *para-* and *meta-* position to the O atom of the chromene moiety to investigate the potential difference in reactivity and properties of the subsequent Suzuki products.

In general, Sp compounds were obtained *via* a condensation reaction between 1,3,3-trimethyl-2-methyleneindoline (**4.1**) and the corresponding bromo-salicaldehyde (**4.2a-b**) (Scheme 4.2, Table 4.2). The reactants were dissolved in EtOH and the mixture was heated at reflux under an N_2 atmosphere for 3.5 hours.

4.1

4.2a: X = Br, X' = H
4.2b: X = H, X' = Br

4.3a: X = Br, X' = H
4.3b: X = H, X' = Br
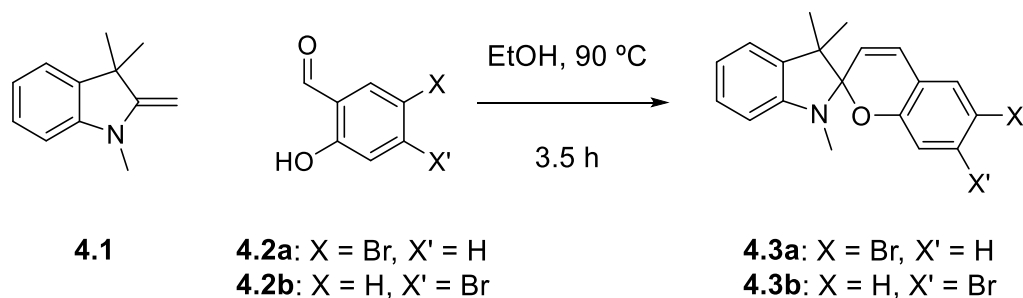
Scheme 4.2: The reaction between indoline **4.1** and salicaldehyde derivatives **4.2a** and **4.2b** to yield Sp compounds **4.3a** and **4.3b.**

Compound	Structure	Yield (%)
4.3a		93
4.3b		89

Table 4.2: Structure and yield of SpBr compounds **4.3a** and **4.3b**.

Purification of SpBr compounds **4.3a** and **4.3b** was achieved with recrystallisation from hot MeOH to give pale-pink powders with yields of 93 % and 89 %, respectively. Structures were confirmed by ^{1}H NMR and X-ray crystallography (Figures 4.4 and 4.5).
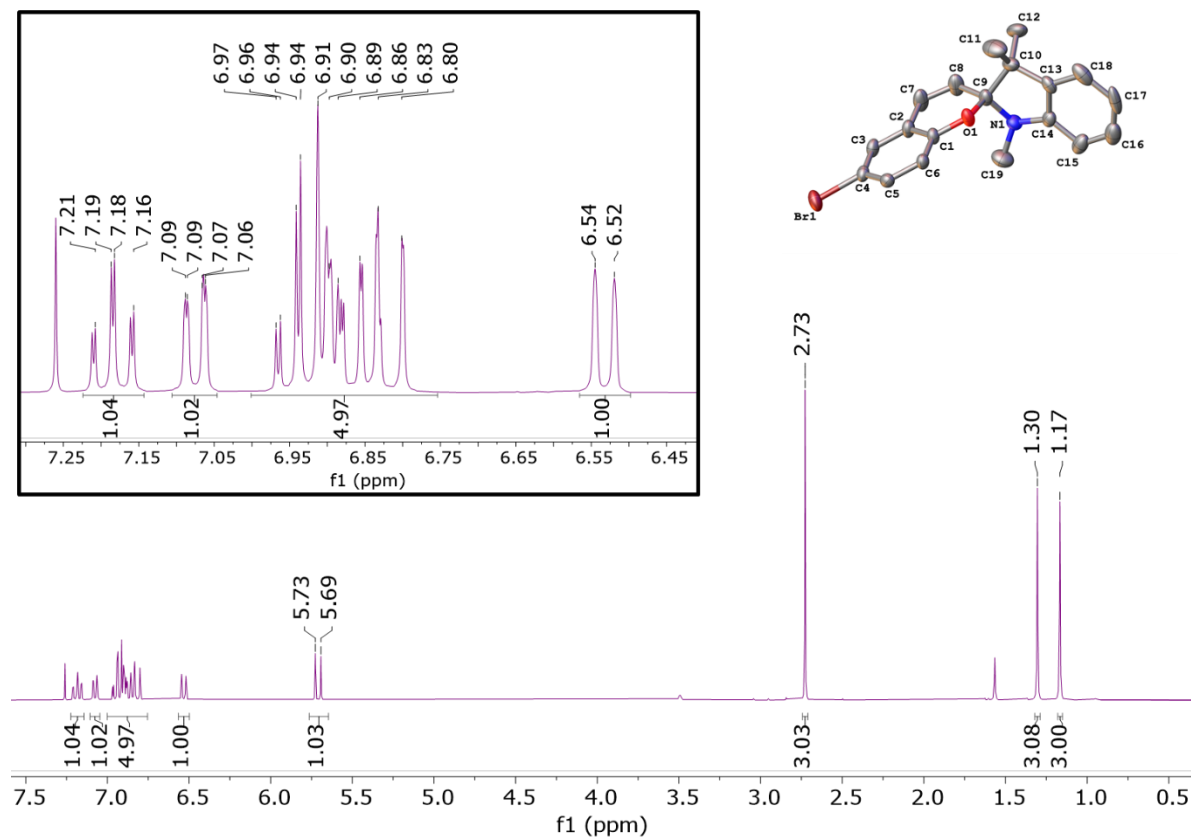
Figure 4.4: ^{1}H NMR spectrum of p-SpBr (**4.3a**) [300 MHz, CDCl₃] and corresponding crystal structure.
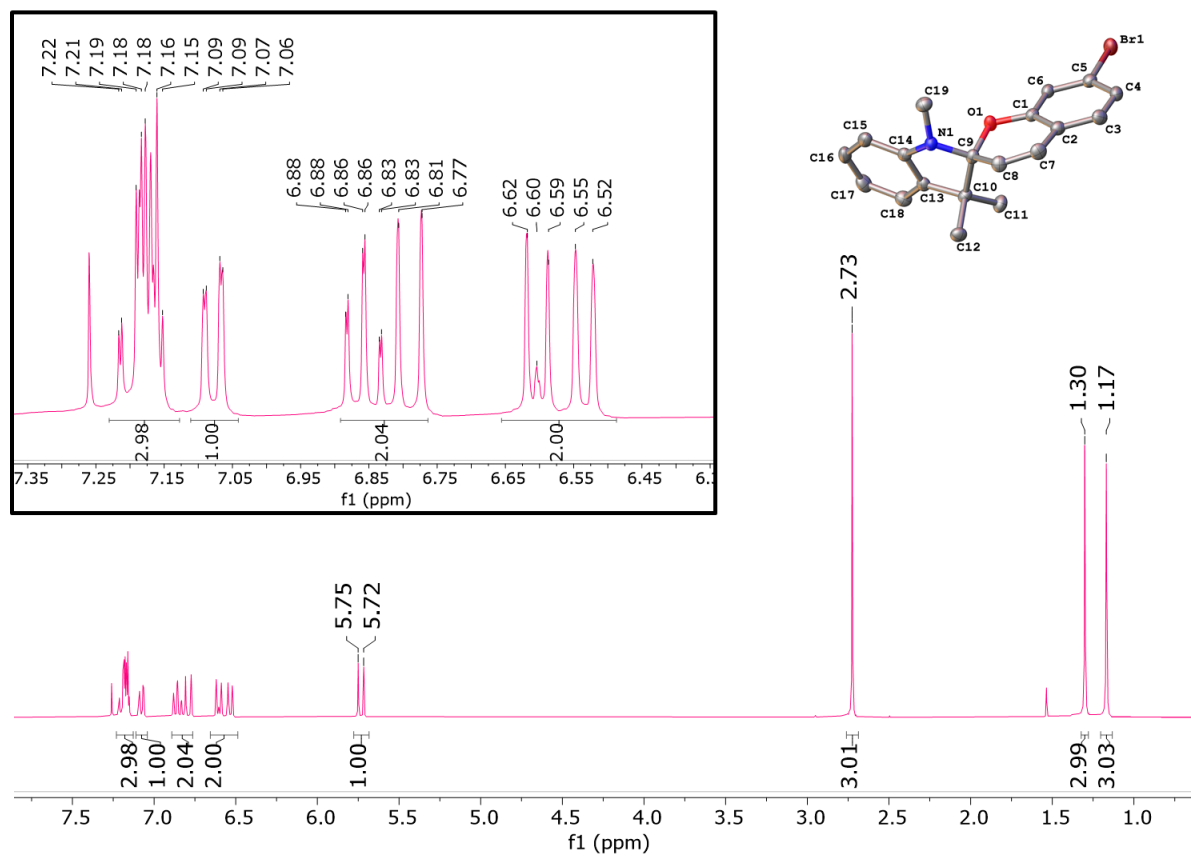
Figure 4.5: ^{1}H NMR spectrum of mSpBr (**4.3b**) [300 MHz, CDCl$_3$] and corresponding crystal structure.

4.3 Suzuki Coupling Reactions

4.3.1 Catalyst Synthesis

A palladium precatalyst **4.8** developed by Buchwald *et. al.* was selected for subsequent Suzuki coupling reactions with SpBr compounds **4.3a** and **4.3b** due to enhanced performance and ease of handling (Scheme 4.3).[24]
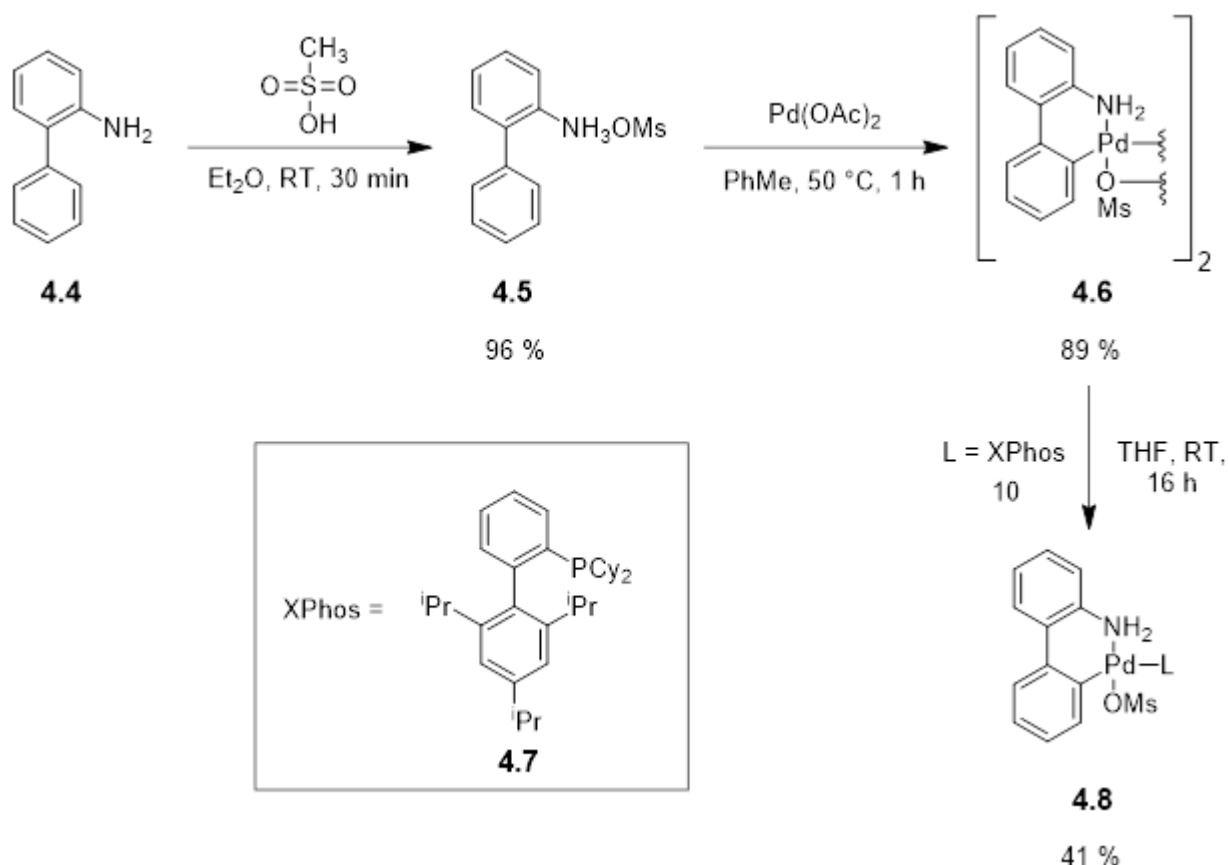
Scheme 4.3: Synthesis of Pd(II) precatalyst **4.8**.

2-aminobiphenyl **4.4** was transformed into 2-amoniumbiphenyl mesylate **4.5** *via* reaction with methane sulfonic acid at room temperature. **4.5** was then reacted with palladium acetate to yield the bridged µ-OMs dimeric species **4.6**. Addition of the phosphine ligand XPhos (**4.7**) yielded the monomeric precatalyst (**4.8**) in 41 % yield, as confirmed by ^{31}P NMR. The active Pd(0) catalyst was later generated *in situ* upon reductive elimination of the deprotonated amine group bound to the Pd centre under basic conditions (Scheme 4.4).

4.8
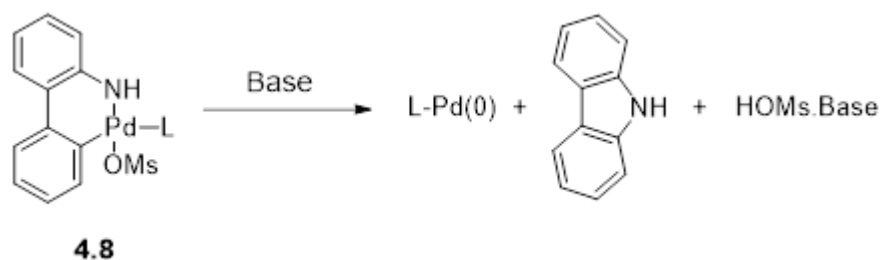
Scheme 4.4: Reaction scheme to show the generation of the active Pd(0) catalyst in the presence of base. The amine group of the biphenyl ligand is deprotonated and subsequently reductively eliminated to give carbazole, L-Pd(0) and a mesylate-base adduct. L = **4.7**.

4.3.2 Reaction Condition Optimisation

To establish suitable reaction conditions for SpBr transformations, a brief preliminary catalyst survey was carried out with **4.3a** and phenylboronic acid as a benchmark substrate (Scheme 4.5). Time, temperature, and catalyst loading was varied to find optimal reaction conditions (Table 4.3). In addition, the effect of generating **4.8** from **4.6** and XPhos *in situ* versus employing the isolated precatalyst was investigated due to the poor yield associated with isolating **4.8**.

4.3a   **4.9**
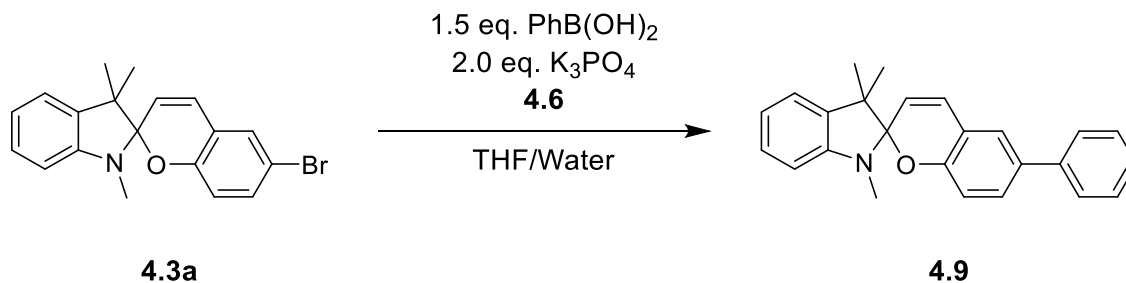
Scheme 4.5: Suzuki coupling reaction between **4.3a** and phenyl boronic acid to yield **4.9**.

Conversion of **4.3a** to **4.9** was calculated *via* ^{1}H NMR based on relative integrals of the *N*-methyl 3H peaks of the starting material and product at *δ* 2.72 ppm and *δ* 2.77 ppm respectively (Figure 4.6).

Time (min)	Temperature (ºC)	(pre) Catalyst [b]	Catalyst Loading [c] (mol%)	Conversion [d] (%)
140	20	*ex situ*	1.0	11
140	20	*in situ*	1.0	14
960	20	*in situ*	1.0	45
165	55	*in situ*	2.0	89
215	55	*in situ*	2.0	> 99

Table 4.3: [a] Reaction conditions: 1.0 mmol **4.3a**, 1.5 mmol PhB(OH)$_2$ 2.0 mmol K$_3$PO$_4$.H$_2$O in 4.5 mL THF and 4.0 mL water; [b] *in situ* precatalyst generation: µ-OMs dimer (**4.6**) and XPhos (**4.7**) added in corresponding amounts according cat. loading, allowed to pre-stir in 1.0 mL THF at room temperature for 20 min; [c] Catalyst loading quoted as mol % of **4.3a**; [d] Conversion (%) determined by ^{1}H NMR.
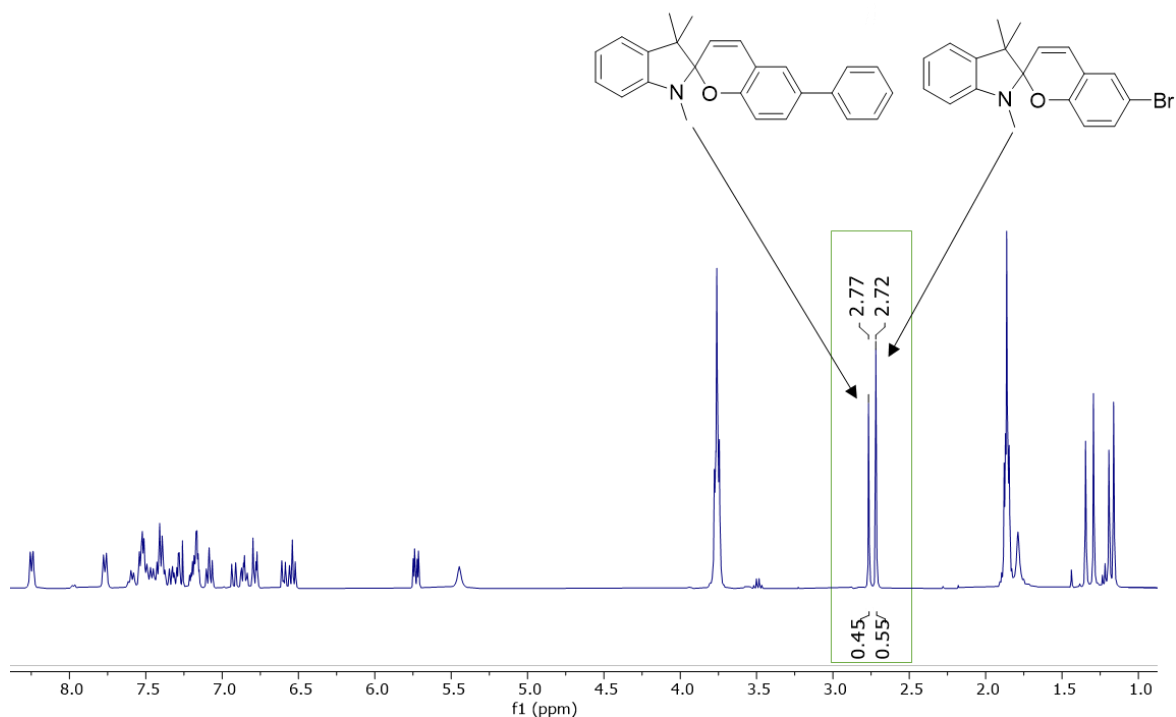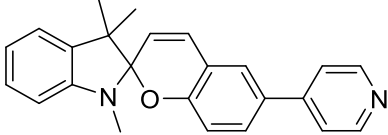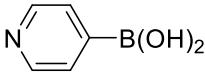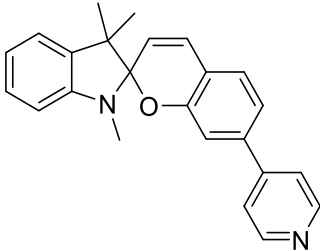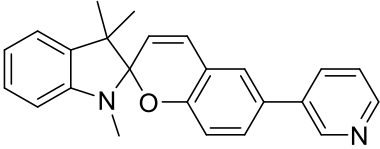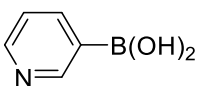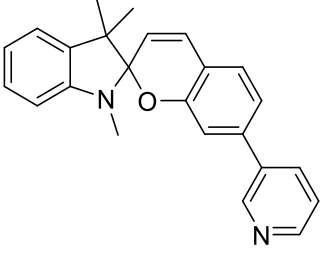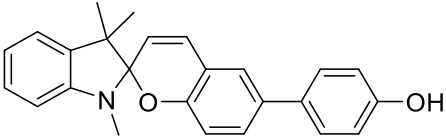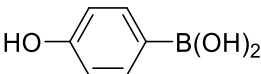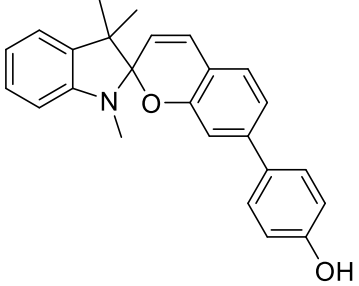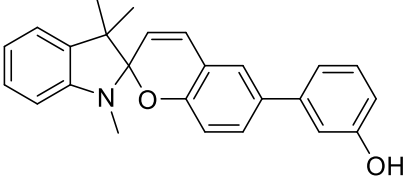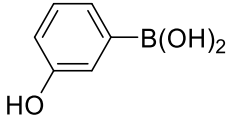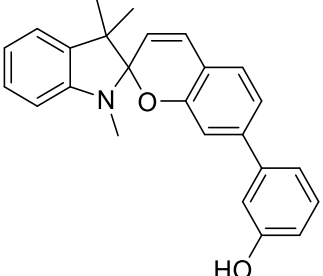
Figure 4.6: Example ^{1}H NMR spectrum of a reaction mixture highlighting resonances associated with *N*-methyl protons of the starting material **4.3a** and product **4.9** used for calculating conversion (Table 4.3) [400 MHz, CDCl$_3$].

Generating pre-catalyst **4.8** *in situ* resulted a marginally higher conversions to the product **4.9**. Although this did not significantly affect conversion, *in situ* generation of **4.8** was carried forward to mitigate loss of the precatalyst during workup, as previously discussed (Table 4.3, entries 1 and 2). However, 14 % conversion to **4.9** was poor under initial conditions, so catalyst loading was increased to 2 mol% and the reaction mixture was allowed to stir at room temperature overnight (Table 4.3, entry 3). This improved the conversion of **4.3a** to **4.9** up to 46 % (Table 4.3, entry 4). The temperature was raised to 55 °C and the reagents were allowed to react for 165 min, which lead to a considerable increase in conversion, reaching 89 % (Table 4.3, entry 5). Optimal reaction conditions were achieved at > 99 % conversion with a reaction time of 215 min at 55 °C with 2 mol% precatalyst, generated *in situ* (Table 4.3, entry 6).

4.3.3 Suzuki Coupling Profile

Conditions established from the survey were applied in subsequent transformations and a series of Sp derivatives were synthesized from SpBr parent compounds (**4.3a** and **4.3b**) with boronic acid substrates (Table 4.4). Sp-phenolic (SpOH) and Sp-pyridyl (SpPy) products were the primary synthetic targets. Four structural isomers of SpOH and SpPy were selected to later examine any effect on physiochemical properties as a result of varying substituent position.

Parent Compound	Substrate	Product	Conversion (%)
4.3a		**4.15a**	40[a]
4.3b	**4.10a**	**4.15b**	49[a]

4.3a		**4.16a**	74[a]
	4.10b		
4.3b		**4.16b**	51[a]
4.3a		**4.17a**	91[a]
	4.11a		
4.3b		**4.17b**	>99[b]
4.3a		**4.18a**	95[a]
	4.11b		
4.3b		**4.18b**	> 99[b]
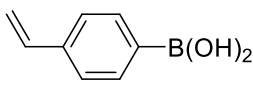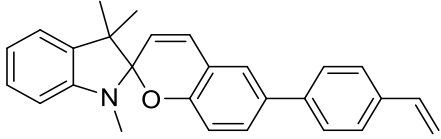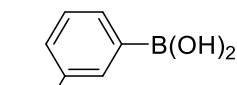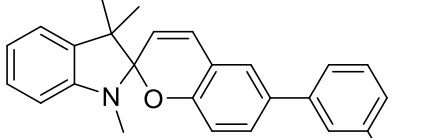
| 4.3a | 4.13 | 4.19 | 98[a] |
| 4.3a | 4.14 | 4.20 | 52[a] |

Table 4.4: Structures of boronic acid substrates and Suzuki coupling products with the respective conversion yields from SpBr compounds, as determined by ^{1}H NMR. [a] Reaction conditions: 1.0 mmol **4.3a** or **4.3b**, 1.5 mmol ArB(OH)$_2$, 2.0 mmol K$_3$PO$_4$.H$_2$O in 4.5 mL THF and 4.0 mL water for 215 min at 55 ºC with 2 mol% catalyst, [b] All reaction conditions the same as [a], except after 215 min, reactants were allowed to stir at room temperature overnight.

Conversion from SpBr **4.3a** and **4.3b** to SpPy derivatives **4.15a, 4.15b, 4.16a** and **4.16b** was poor with a range of conversions from 40 % to 74 % (Table 4.4). Whereas under the same conditions, conversion to SpOH derivatives **4.17a** and **4.18a** was good at 91 % and 95 %, respectively. Boronic acids bearing nitrogen-containing heterocycles and amines are known to be challenging substrates in Pd-catalysed coupling reactions due to their ability to deactivate the catalyst *via* N-metal bonding, and electron rich Py-compounds have a tendency to coordinate Pd.[25] This phenomenon explains the comparatively poor conversion to SpPy compounds and is further demonstrated with the low conversion of **4.3a** to **4.20** (52 %) in the presence of the amine-containing substrate **4.14**.

SpOH compounds **4.17b** and **4.18b** from mSpBr **4.3b** were both obtained with excellent conversion (> 99 %) by allowing for a prolonged reaction time.

A styrene group was also successfully incorporated *via* reaction between parent compound **4.3a** and boronic acid **4.13** to give **4.19** with 98 % conversion. This demonstrates that this method can be used to directly add polymerisable functionality, without the need for further modifications.

4.4 Pyridine Substituted Spiropyrans

4.4.1 Proton NMR

For further synthesis of SpPy compounds, catalyst loading was increased to 10 mol% to reduce reaction time. All crude SpPy compounds were purified over a silica column with an eluent mixture of EtOAc:Petrol (1:3). As SpPy compounds were loaded onto the stationary phase they became deep-red in colour, then immediately colourless when eluted from the column. This observation can be attributed to the ring-opened and ring-closed isomers of each compound in relatively polar (silica column) and non-polar (eluent) environments, respectively.
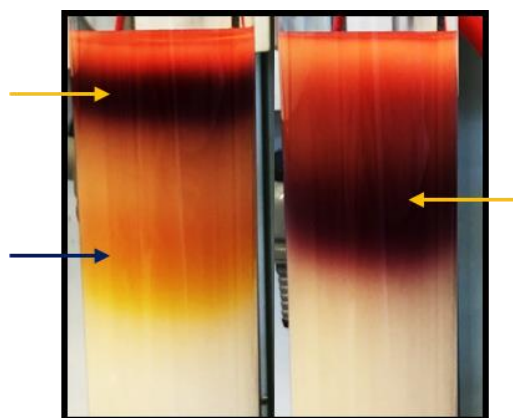
Figure 4.7: Strong purple/red colour of the merocyanine isomer of SpPy **4.15a** (yellow arrows) and the yellow/orange Mc isomer of the SpBr starting material **4.3a** (blue arrow).

Once purified, the aromatic region in the ^{1}H NMR spectrum of each structural isomer was compared (Figures 4.8 – 4.11). Successful incorporation of the pyridine fragments from Suzuki coupling reactions was confirmed with each SpPy compound exhibiting resonances in the region expected for that of Py-protons (Table 4.5).

Compound	Shift (ppm)			
	H_k	H_j	H_l	H_m
4.15a	8.61	7.45	-	-
4.16a	8.80	8.54	7.33	7.81
4.15b	8.60	7.43	-	-
4.16b	8.79	8.54	7.30	7.80

Table 4.5: Pyridyl proton chemical shifts associated with SpPy compounds.
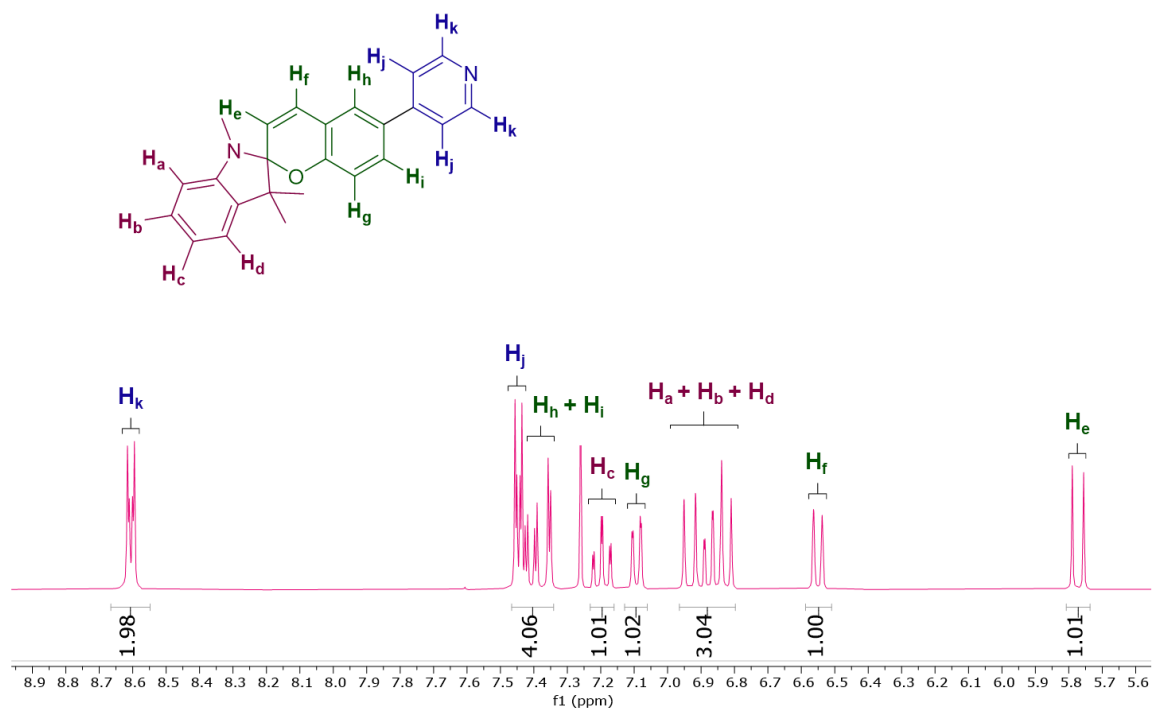
Figure 4.8: Annotated ^{1}H NMR spectrum of **4.15a**. [300 MHz, CDCl$_3$]
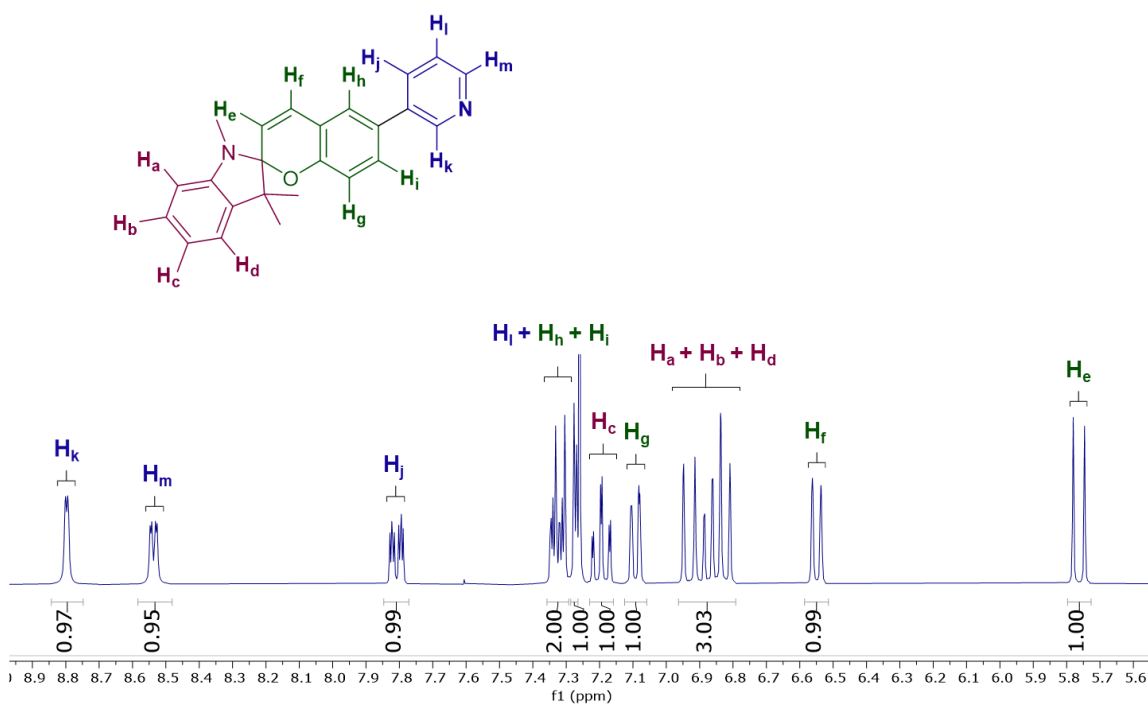
Figure 4.9: Annotated ^{1}H NMR spectrum of **4.16a** [300 MHz, CDCl$_3$].
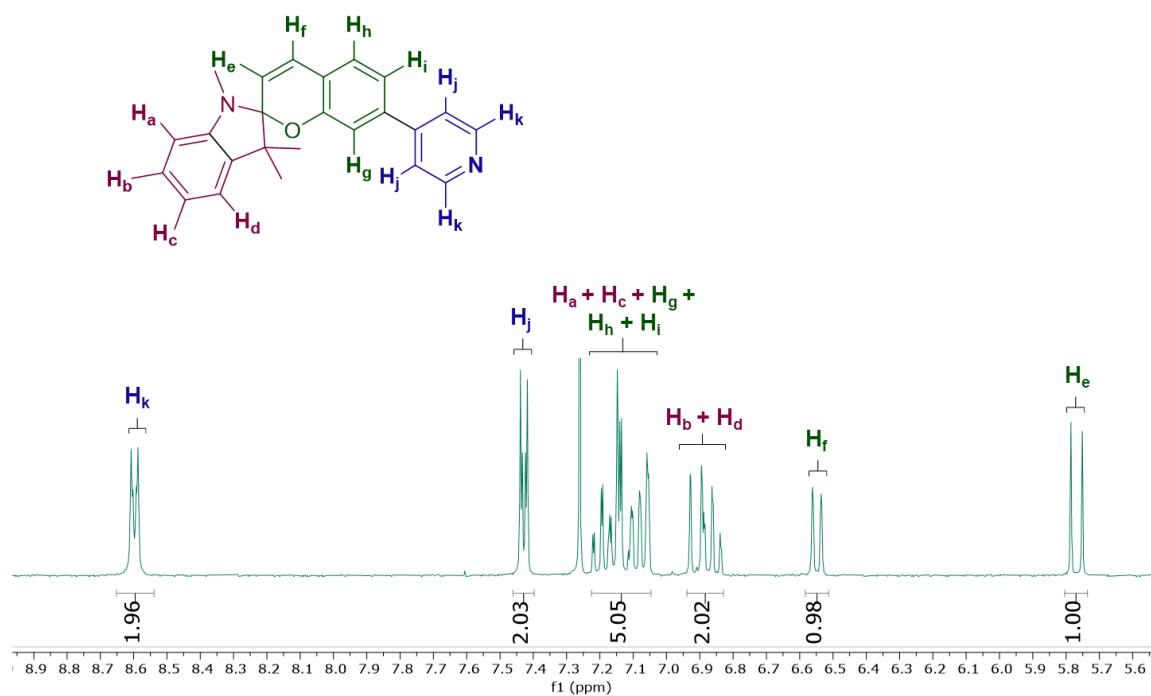
Figure 4.10: Annotated ^{1}H NMR spectrum of **4.15b**. [300 MHz, CDCl$_3$].
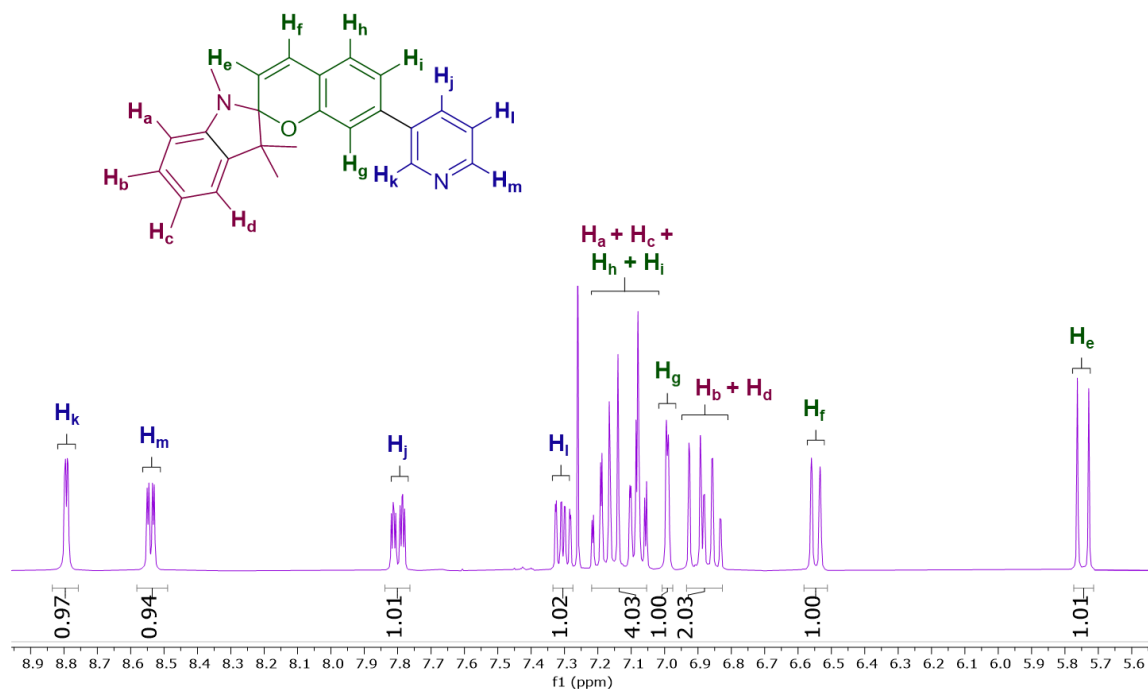
Figure 4.11: Annotated ^{1}H NMR spectrum of **4.16b**. [300 MHz, CDCl$_3$].

Both compounds **4.15a** and **4.16a** are *para*-substituted with respect to the O-atom of the chromene fragment (Figure 4.8 and Figure 4.9, respectively). The spectrum of **4.15a** exhibits two, 2H peaks corresponding to pyridyl protons at 8.61 ppm (H$_k$) and 7.45 ppm (H$_j$), whereas peaks associated with the four protons of the pyridine moiety in compound **4.16a** resonate as separate 1H peaks at 8.80 ppm (H$_k$), 8.54 ppm (H$_m$), 7.33 ppm (H$_j$) and 7.81 ppm (H$_l$).

There was generally a greater degree of overlap between proton resonance peaks in the spectra of *meta*-substituted compounds **4.15b** and **4.16b** (Figure 4.10 and Figure 4.11, respectively). Downfield of 7.40 ppm, each *m*-SpPy spectrum is comparable to that of the corresponding *p*-SpPy analogue bearing the equivalent pyridine substituent. Two, 2H pyridyl-proton resonances were assigned in the spectrum of **4.15b** at 8.60 ppm (H$_k$) and 7.43 ppm (H$_j$). Four distinct 1H peaks were assigned to Py protons in the spectrum of **4.16b** at 8.79 ppm (H$_k$), 8.54 ppm (H$_m$), 7.30 ppm (H$_j$) and 7.80 ppm (H$_l$).

The assignment of pyridyl protons can be rationalised by considering the inductive and mesomeric effects exerted by the N atom of each Py-fragment. Protons at the C2 and C4 positions (with respect to the Py N atom) are deshielded as they are subjected to negative

110

mesomeric effects (Figure 4.12).[26] Moreover, protons at the C2 position are deshielded most strongly as they are adjacent to the negatively inductive nitrogen atom. Protons at the C3 positions are not as strongly affected and resonate further upfield relative to other protons in the Py ring. The negative mesomeric effects (- M) are confined to the Py ring for 3-pyridyl derivatives **4.15b** and **4.16b** (Figure 4.12b), whereas conjugation extends the effect to the adjoined aromatic ring of 4-pyridyl derivatives **4.15a** and **4.16a** (Figure 4.12a).

Overall, the proton NMR spectra of all SpPy compounds confirm the successful coupling of the respective Py fragments to each Sp scaffold. Spectra of SpPy compounds with the same Py moiety (i.e. 3-pyridyl or 4-pyridyl) are almost identical in the region downfield of 7.25 ppm.

a)
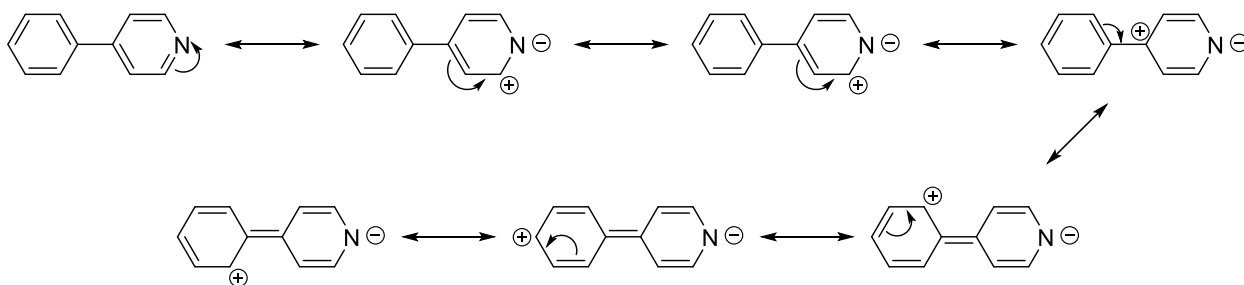
b)
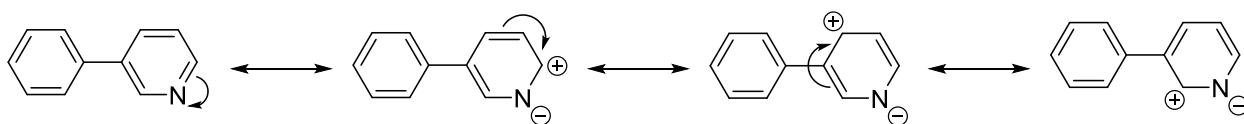
Figure 4.12: Resonance structures of a) 4-phenyl pyridine and b) 3-phenyl pyridine to demonstrate the negative mesomeric effects within the structures of 4-pyridyl Sp derivatives (**4.15a**, **4.15b**) and 3-pyridyl Sp derivatives (**4.16a**, **4.16b**), respectively.

4.4.2 Acidochromism and Photochromism Study

UV-Vis spectroscopy was carried out to investigate the acido- and photochromic properties of SpPy compounds. A 50 µM solution of each SpPy derivative was made by serial dilution in MeOH, which was chosen as a polar, protic solvent capable of stabilising the ring-opened isomer (McH⁺). 3.0 mL of the SpPy solution was added to a cuvette and was exposed to UV light (365 nm) for 5 minutes. No photophysical response to UV-light was recorded for any SpPy compound. For acidochromism experiments, 0.1 mL of 0.1 M HCl (aq) was added to a cuvette containing 3.0 mL 50 µM SpPy solution in MeOH. The analyte was kept in the dark as data was recorded at intervals between 0 – 60 min (Figures 4.13 – 4.16).
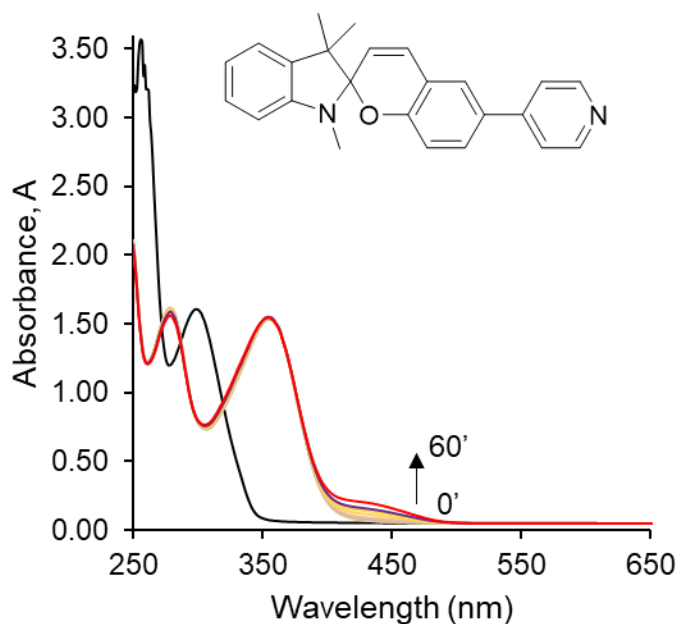
Figure 4.13: Overlayed UV-Vis spectra of a 50 µM solution of **4.15a** in MeOH after the addition of 0.1 mL 0.1M HCl at various time intervals (coloured lines). T = 0, black line; T = 60 min, red line.
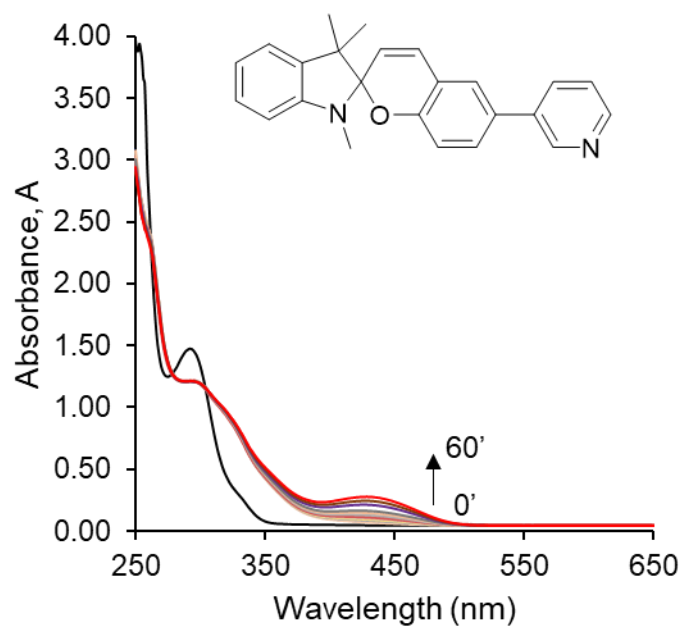
Figure 4.14: Overlayed UV-Vis spectra of a 50 µM solution of **4.16a** in MeOH after the addition of 0.1 mL 0.1M HCl at various time intervals (coloured lines). T = 0, black line; T = 60 min, red line.
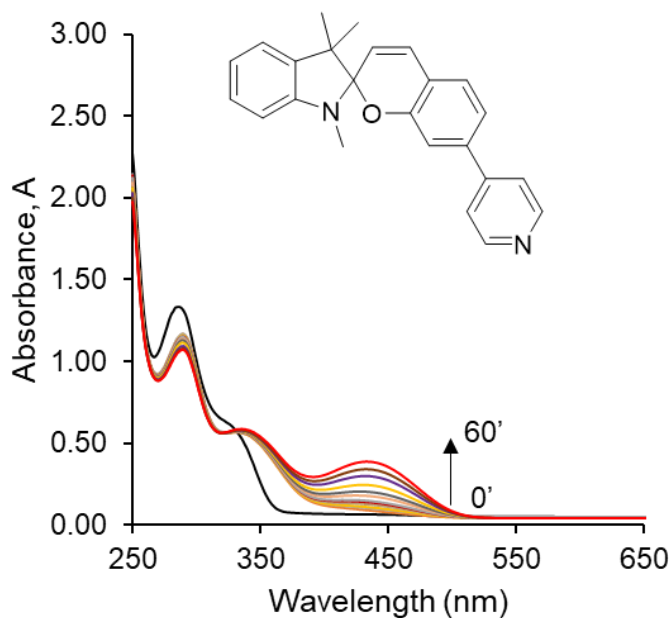
Figure 4.15: Overlayed UV-Vis spectra of a 50 µM solution of **4.15b** in MeOH after the addition of 0.1 mL 0.1M HCl at various time intervals (coloured lines). T = 0, black line; T = 60 min, red line.
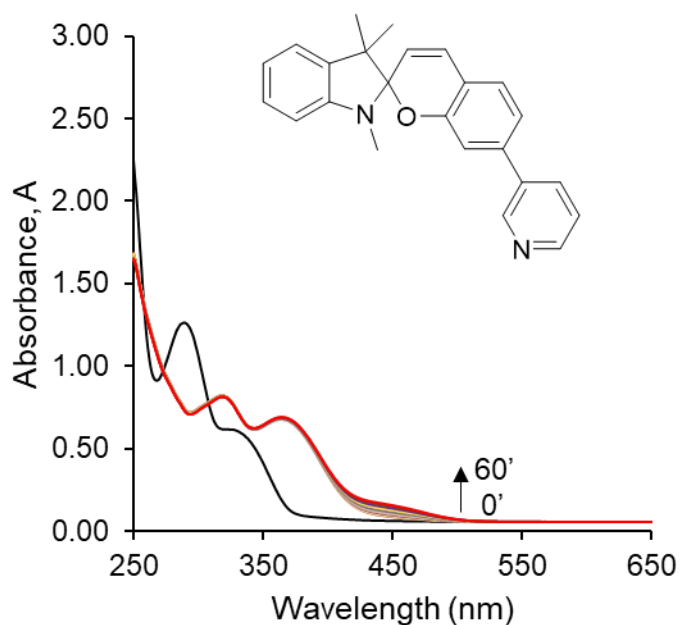
Figure 4.16: Overlayed UV-Vis spectra of a 50 µM solution of **4.16b** in MeOH after the addition of 0.1 mL 0.1M HCl at various time intervals (coloured lines). T = 0, black line; T = 60 min, red line.

Prior to addition of acid at T = 0 min, two absorption bands at 255 nm and 295 nm were observed in the spectrum of **4.15a**, corresponding to $\pi - \pi^*$ electronic transitions of the indoline and chromene rings, respectively (Figure 4.13, black line). Addition of HCl resulted in a bathochromic shift of absorption bands to 279 nm and 354 nm (Figure 4.13, coloured lines). A broad absorption peak began to increase in intensity over time between the region of 400 – 485 nm (red line, T = 60 min).

Absorption maxima were observed at 254 nm and 296 nm in the UV-Vis spectrum of compound **4.16a** (Figure 4.14, black, T=0). Addition of acid resulted in a slight red shift of the peaks to 261 nm and 301 nm respectively, with another broad absorption peak centered around 434 nm developing over-time (Figure 4.14, coloured lines).

Similar patterns were observed in the spectra of compounds **4.15b** (Figure 4.15) and **4.16b** (Figure 4.16). At T = 0, two absorption maxima were recorded for each compound: at 284 nm and 327 nm in the spectrum of **4.15b** (Figure 4.15, black line) and at 293 nm and 329 nm in the spectrum of **4.16b** (Figure 4.16, black line). As with the other SpPy derivatives, addition of acid induced a bathochromic shift of peaks in the spectra (to 291 nm, 344 nm for **4.15b**, and to 325 nm, 371 nm for **4.16b**), as well as the appearance and development of peaks at 440 nm (Figure 4.15, red line) and 453 nm (Figure 4.16, red line)

114

for compounds **4.15b** and **4.16b**, respectively. A summary of key spectral features associated with SpPy isomers are given in Table 4.6.

Each SpPy solution was colourless prior to addition of acid, which is characteristic of ring-closed Sp isomers. Upon mixing with HCl, a subtle colour change to pale yellow was observed and after 60 min, all acid-treated SpPy solutions had become intensely yellow/orange in colour, indicative of McH$^+$. The observed colour changes and the broad absorption peaks that developed from T = 1 min to T = 60 min at ~ 450 nm in the spectra of each compound suggests the slow generation of the ring-opened, protonated McH$^+$ species at a lower pH during analysis.

Bathochromic shifts in each SpPy spectra immediately upon addition of HCl suggest the presence of another species, other than Sp or McH$^+$. With this in mind, T. Halbritter *et. al.* investigated the properties of an Sp derivative bearing a Py ring fused into the chromene fragment of the chromophore and found that at pH 4.8 protonation of the ring-closed form at the Py N-atom (SpH$^+$) resulted in a bathochromic shift of λ_{max} relative to that of the unprotonated Sp form.[27] At pH < 3, a diprotonated species (McH$_2$$^+$) with an absorption band at 420 nm was the dominant species. The phenomena that the Halbritter group reported may explain observations in this work. It is possible that SpPy derivates are first protonated at the Py N-atom upon addition of acid, then thermal ring-opening occurs slowly in the dark, leading the gradual increase of absorption bands attributed to McH$_2$$^+$ (Figure 4.17).
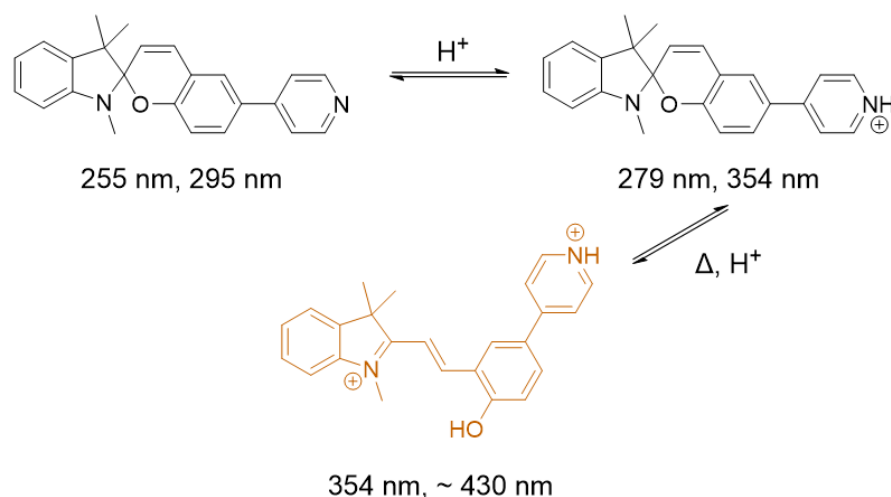
Figure 4.17: **4.15a** as Sp, SpH$^+$ and McH$_2$$^+$ forms and the corresponding λ_{max} attributed to each species.

Compound	Absorption Maxima (nm)		
	Sp	SpH$^+$	McH$_2^+$
4.15a	255, 295	279, 354	~ 430
4.16a	254, 296	261, 301	~ 434
4.15b	284, 327	291, 344	~ 440
4.16b	293, 329	325, 371	~ 453

Table 4.6: the absorption manxima associated with Sp, SpH$^+$ and McH$_2^+$ of each SpPy compound.

Equivalent isomers of *m*-substituted SpPy compounds **4.15b** and **4.16b** absorbed light at longer wavelengths than *p*-substituted **4.15a** and **4.16a**. Compound **4.15b** developed the most intense absorption peak associated with McH$_2^+$ over the 60 min period that was measured. Otherwise, all compounds showed the same general acidochromic response to HCl. Longer experiment times are needed in future work to determine the kinetics associated with Sp→McH$_2^+$ isomerisation.

Interestingly, despite no measurable or visual response to UV-light illumination in solution, all SpPy compounds displayed reversible solid-state photochromism. Images were taken of each compound at intervals during and after exposure to 365 nm UV-light (Figure 4.18).

Figure 4.18: Images of SpPy compounds a) **4.15a** b) **4.16a** c) **4.15b** d) **4.16b** in the solid state after exposure to 365 nm UV-light at time intervals up to 5 min, then at time intervals after removal of the UV light source up to 60 min. Samples were left in ambient light after UV light exposure.

Visually, the most striking photochromic response was that of compound **4.16a** (Figure 4.18b). The white crystalline powder became vibrantly blue after only 30 s of UV light exposure, and the intensity of colour developed further with time. 60 min after withdrawal of UV light, the sample had nearly reverted to its original colour. Compounds **4.15a**, **4.15b** and **4.16b** also exhibited reversible blue colouration after stimulation with UV light, although not as vividly (Figure 4.18a, c and d, respectively). The colour changes observed

were suggestive of isomerism from Sp to the respective Mc isomers. This is not an inherent trait of all Sp compounds, as the ability to isomerise in the solid-state is dependent upon intermolecular packing density and stability of the ring-opened isomer (Mc).[28] The Py fragments give rise to adequate free-volume in the solid state, accommodating for structural changes upon ring opening. In addition, the electron deficient Py rings stabilise the negatively charged O atom of the Mc isomers *via* conjugation. It is unclear as to why SpPy derivatives show no such response to UV light in solution. Furthermore, UV-Vis reflectance spectroscopy is needed to further elaborate on this solid-state transformation.

4.4.3 Pyridine Substituted Spiropyran and Polyoxometalate Complexes

SpPy-POM compounds were targeted as Sp-POMs have previously been shown to have vibrant photochromic properties that could potentially be exploited for the design of smart label devices.[29] N-heterocycles are known to act as ligands and coordinate to transition metals to form complexes and **appertaining** to this work, mixed transition-metal substituted POMs.[30] The Errington group have previously demonstrated the coordination of pyridine to the cobalt atom in a hexametalate POM species, $[(py)CoW_5O_{18}H]^{3-}$ and are currently researching to expand the library of monosubstituted tungstate Lindqvists. To build on more recent work, an Mn-substituted POM was synthesised to explore if POM-SpPy complexes could be formed.

The dimeric species $[(MnW_5O_{18}H)_2](TBA)_6$ **4.22** was synthesized from $[W_6O_{19}](TBA)_2$ **4.21** using a procedure previously developed by a member of the Errington research group (Scheme 4.6).[31] A solution of sodium tungstate in DMF/Ac_2O was acidified with HCl to generate the POM structure before ion exchange with TBA(Br) to yield $[W_6O_{19}](TBA)_2$ **4.21**, which was then purified *via* recrystallisation to yield a white crystalline powder (Scheme 4.6a).

Four equivalents of (TBA)OH were added to a suspension of **4.21** in MeCN under an atmosphere of Ar to partially degrade the POM, allowing for subsequent incorporation of Mn(II) into the structure. A slight excess of $Mn(NO_3).6H_2O$ was added to the pale-yellow reaction suspension, which immediately became intense yellow upon reaction. The reaction solution was allowed to stir overnight and gradually became purple/red, suggesting oxidation of Mn(II) to Mn(III). Removal of solvent under reduced pressure

gave a viscous, deep-purple crude product. The product was redissolved in a small amount of MeCN then added to vigorously stirring EtOAc. A fine purple powder was retrieved upon filtration and dried in a vacuum oven at 50 °C overnight (85 %).

a) $6\ Na_2WO_4 + 10\ HCl + 2\ (TBA)Br \xrightarrow[100\ °C,\ 3\ h]{DMF,\ Ac_2O}$ **4.21** $[W_6O_{19}](TBA)_2 + 2\ NaBr + 2H_2O$

b) $5\ [W_6O_{19}](TBA)_2 \xrightarrow[ii)\ 1.1\ eq.\ Mn(NO_3)_2.6\ H_2O]{i)\ 4.0\ eq.\ (TBA)OH\ \ MeCN,\ RT,\ 45\ min}$ **4.22** $(TBA)_6[(W_5MnO_{18}H)_2] + 7\ H_2O + 2\ (TBA)NO_3$

Scheme 4.6: a) synthesis of Linqvist POM **4.21** and b) synthesis of Mn-containing POM **4.22**

The Mn-substituted hexametalate **4.22** was then reacted with SpPy compounds in an attempt to generate a series of SpPy-Mn-POM derivatives (Scheme 4.7). In general, **4.22** and two molar equivalents of SpPy were dissolved in MeCN and allowed to react at room temperature overnight. Upon addition of each SpPy to **4.22**, all reaction solutions turned from purple to deep red. In each case, once solvent was removed a deep-red sticky product was obtained. SpPy-POM compounds were retrieved as red/brown powders upon trituration with Et$_2$O. The products were allowed to dry in a vacuum oven and then analysed *via* FT-IR (Figure 4.19). Key spectral features of SpPy-POM hybrids are outlined in table 4.7.

$(TBA)_6[(W_5Mn^{III}O_{18})_2] \xrightarrow[MeCN,\ RT]{2.0\ eq.\ SpPy} (TBA)_3[W_5Mn^{III}(SpPy)O_{18}]$

4.22   **4.23a-d**

Scheme 4.7: Synthesis of POM-SpPy hybrid compounds **4.23a-d**

The FTIR spectra of SpPy compounds in the region of 450 cm^{-1} – 1700 cm^{-1} are complex due to the multiple aromatic rings within each molecule. A shift to higher wavenumbers of Py ring vibrational modes upon coordination of the Py N-atom of SpPy compounds to the

119

Mn(III) atom of **4.22** was expected.[32] For uncoordinated SpPy compounds, the expected regions for v_{Py} are approximately 1580 – 1650 cm^{-1} and 1440 – 1510 cm^{-1}.

The strong peak at 940 cm^{-1} present in the spectrum of **4.22** is attributed to v(W=O) and the vibrational mode is not significantly affected after reaction with any SpPy compound (Figure 4.19).[30] The most obvious difference in the spectrum of **4.22** and any **4.23** derivative is found upon inspection of the region between 1590-1660 cm^{-1}, whereby vibrational modes associated with C=C and C=N stretching frequencies are absent in the spectrum of **4.22** and present in the spectra of SpPy-POM compounds. In addition, the corresponding vibrational modes associated with free SpPys were shifted to higher wavenumbers after reaction with **4.22** (Table 4.7). For example, v(C=C/C=N) associated with **4.15a** at 1611 cm^{-1} and 1596cm^{-1} are shifted to 1644 cm^{-1} and 1603cm^{-1}, respectively (Table 4.7, entries 1 and 2). Although the findings are indicative of SpPy-Mn coordination, they are not conclusive, and further investigation is needed to confirm success of the reaction. Attempts to crystalize compounds **4.23a-d** for structural determination via X-ray crystallography were unsuccessful.

Compound	v(C=C/C=N)		v(W=O)
4.15a	1611	1596	-
4.23a	1644	1603	940
4.16b	1648	1596	-
4.23b	1653	1606	939
4.15b	1644	1596	-
4.23c	1653	1604	938
4.16b	1642	1607	-
4.23d	1648	1607	939

Table 4.7: A summary of stretching frequencies associated with C=C/C=N in SpPy derivatives and SpPy-POM compounds, and W=O stretching frequencies in SpPy-POM compounds.

Figure 4.19: Stacked FT-IR spectra of the corresponding SpPy (navy), **4.22** (purple) and a) **4.23a** (green), b) **4.23b** (yellow), c) **4.23c** (pink), d) **4.23d** (blue).

4.5   Phenol Substituted Spiropyrans

For scaled up synthesis of SpOH derivatives, Pd catalyst loading was increased to 10 mol% to reduce reaction times. The products were purified over a silica plug in EtOAc and dried under vacuum prior to analysis.

4.5.1 Proton NMR

In contrast to SpPy compounds, there was a greater degree of overlap between resonances in the aromatic region of the ^{1}H NMR spectra of SpOH (Figure 4.20). For this reason, assignments other than peaks associated with the phenolic protons were omitted.

Figure 4.20: Stacked ^{1}H NMR spectra of SpOH compounds: 4.17a (pink), 4.18a (navy), 4.17b (green), 4.18b (purple)

The 2H proton peak at 7.42 ppm in the spectrum of **4.17a** is assigned to protons at the *meta*-position to the -OH group of the phenol ring (Figure 4.20, pink, H_j). Protons in the *ortho*-position resonate around 7.22 pm and overlap with other aromatic proton peaks. Each proton within the phenol ring of **4.18a** possess different chemical shifts, with H_l and H_j peaks assigned at δ 7.25 – 7.32 and H_m and H_k peaks at δ 7.09 and δ 7.00, respectively (Figure 4.20, navy)

Much like **4.17a**, protons at *meta*-positions to the -OH group of the phenol ring in compound **4.17b** resonate furthermost downfield at 7.41 ppm (Figure 4.20, green, H_j) and H_k (*ortho*- to -OH) resonate at 7.08 ppm. Peaks between δ 7.21 – 7.27 are assigned to H_l and H_j and overlapping peaks at 6.98 ppm correspond to H_k and H_m in the spectrum of **4.18b**. A summary of all peaks associated with the phenol fragments of SpOH compounds is given in Table 4.8.

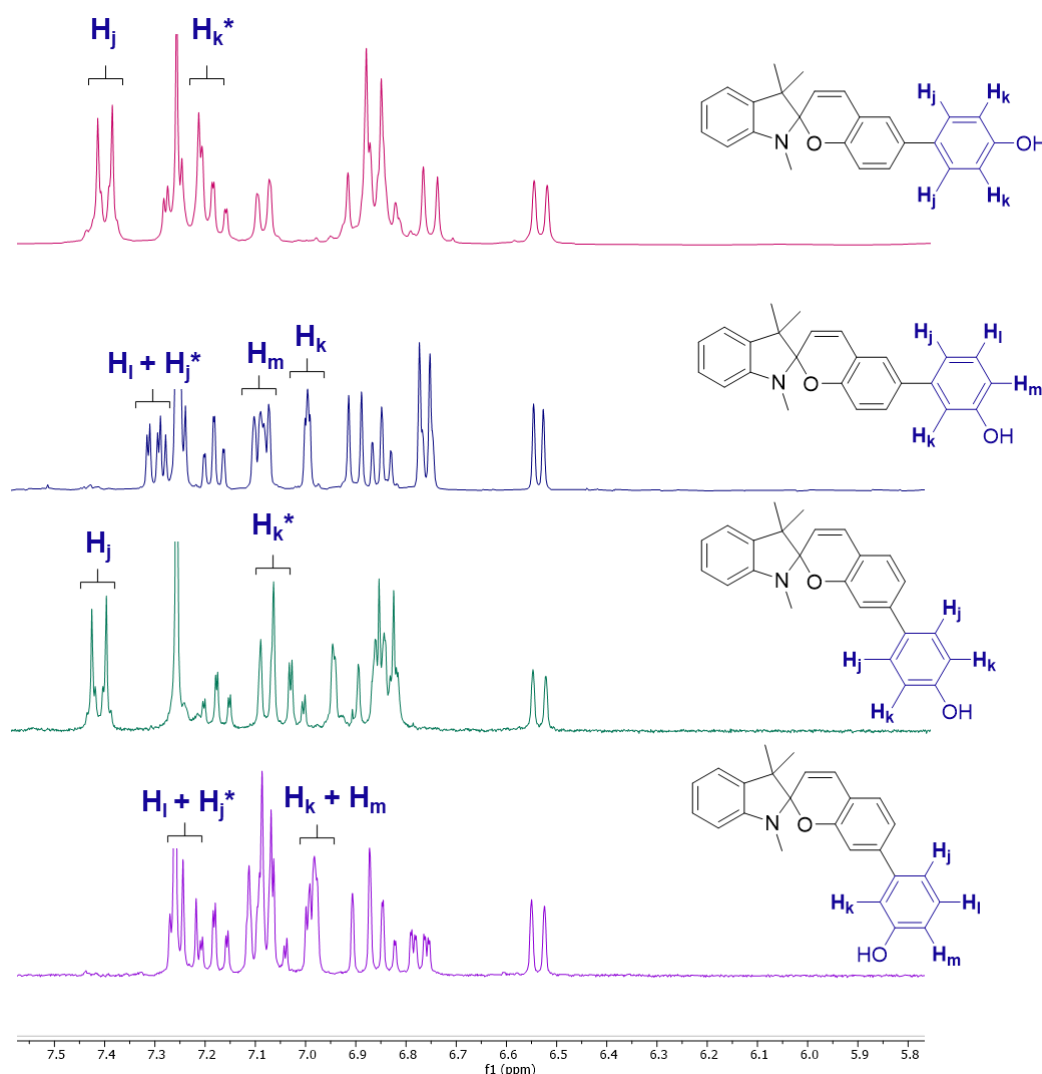In section 4.4.1, mesomeric and inductive effects and how they influence the chemical shifts of protons were discussed. Unlike pyridine substituents that are electron withdrawing, the -OH group of the phenol substituents in SpOH compounds are electron donating. This gives rise to a positive mesomeric effect where protons at the C2 and C4 positions of the phenol moiety are more shielded, which is why phenolic SpOH protons resonate further upfield with respect to SpPy pyridyl protons .*ortho*- protons of the phenol groups in SpOH compounds are still subjected to negative inductive effects from the electronegative O atom. Although phenolic protons were not detected in the ^{1}H NMR spectra of any SpOH derivative (due to rapid exchange), shift patterns of other protons affirm the groups presence.

Compound	Shift (ppm)			
	H_j	H_k	H_l	H_m
4.17a	7.42	7.22	-	-
4.18a	7.25 – 7.32	7.00	7.25 – 7.32	7.09
4.17b	7.41	7.08	-	-
4.18b	7.21 – 7.27	6.98	7.21 – 7.27	6.98

Table 4.8: Phenol proton chemical shifts associated with SpOH compounds.

4.5.2 Acidochromism and Photochromism Study

The response of SpOH compounds to UV light stimulation and exposure to acid was investigated *via* UV-Vis spectroscopy. The same procedure as outlined in section 4.4.2 for analogous SpPy experiments was employed. Unlike SpPy compounds, some SpOH derivatives showed a measurable response to UV-light exposure in solution and the resulting spectra have been included in this section (Figure 4.21 – 4.24). Although SpOH compounds were highly-coloured as powders in the solid state, all four derivatives became colourless upon dissolution in MeOH.

Figure 4.21: a) overlayed absorption spectra of a 50 µM solution of **4.17a** in MeOH at different time intervals after addition of 0.1 mL 0.1M HCl over a 60 min period (coloured lines); b) absorption spectra of a 50 µM solution of **4.17a** in MeOH before exposure to UV light (black) and after 5 min exposure to 365 nm UV light (blue).

The spectrum of **4.17a** was recorded at T = 0 and two absorption peaks were observed at 252 nm and 282 nm, corresponding to $\pi - \pi^*$ transitions of the indoline and chromene ring systems respectively (Figure 4.21). Upon addition of acid, the intensity of both absorption bands decreased with concurrent development of absorption maxima at 383 nm and 472 nm over time. An isosbestic point was recorded at 310 nm. Additionally, the

compound responded to 365 nm UV light exposure (Figure 4.21b). The absorption profile recorded after UV-light illumination was comparable to that of the spectrum recorded at T= 60 min after exposure to acid, suggesting that the two stimuli result in formation of the same species, McH$^+$.

Patterns in the absorption spectra of compound **4.18a** after addition of acid followed the same general trend as that of **4.17a**. At T= 0, two absorption maxima were present at 250 nm and 291 nm (Figure 4.22, black line). Addition of acid resulted in the gradual decline in intensity of those peaks with simultaneous growth of absorption bands at 377 nm and 460 nm (Figure 4.22a, coloured lines). An isosbestic point was present at 317 nm. Unlike **4.17a** however, **4.18a** did not exhibit a photophysical response to UV light (Figure 4.22b).
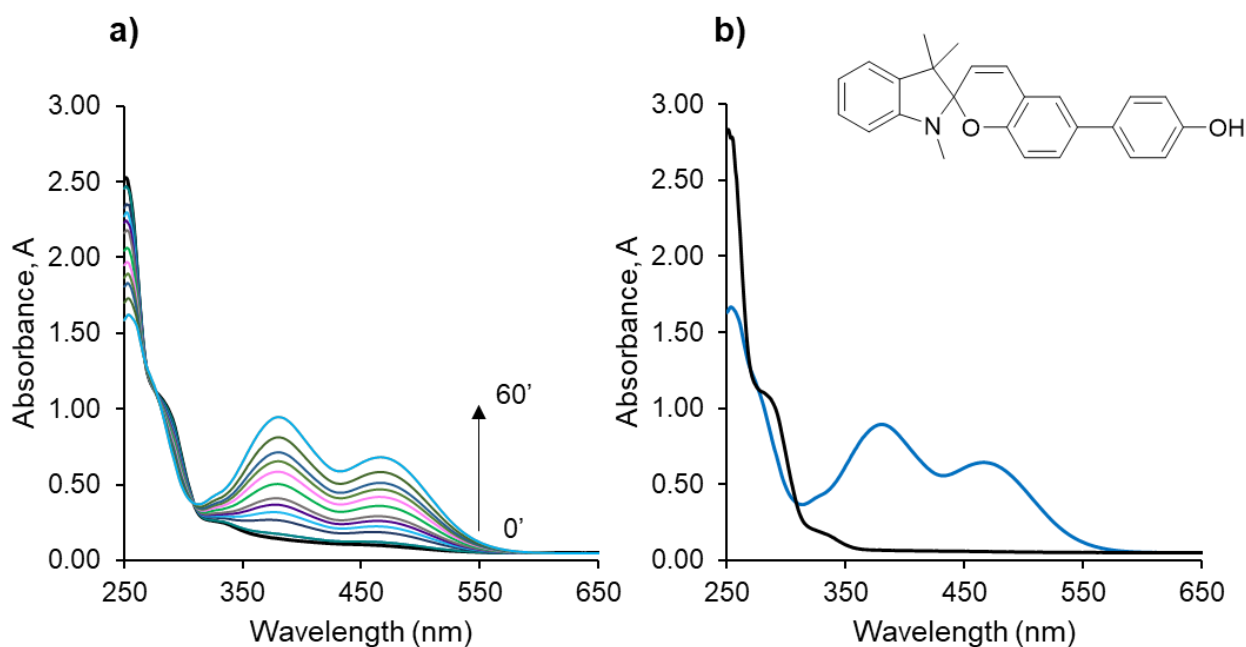

Figure 4.22: a) overlayed absorption spectra of a 50 µM solution of **4.18a** in MeOH at different time intervals after addition of 0.1 mL 0.1M HCl over a 60 min period; b) absorption spectra of a 50 µM solution of **4.18a** in MeOH before exposure to UV light (black) and after 5 min exposure to 365 nm UV light (no change in spectrum).

Untreated **4.17b** exhibited absorption maxima at 293 nm and shouldered peak at 332 nm (Figure 4.23b, black line). The peaks decreased in intensity over time after exposure to HCl, with increasing intensity of a peak at 486 nm (Figure 4.23a, coloured lines). The isosbestic point was recorded at 340 nm. **4.17b** did not respond to UV-light (Figure 4.23b), unlike **4.18b** which demonstrated both acidochromic and photochromic properties (Figure

125

24b). Prior to mixing with HCl, an absorption peak at 284 nm and a shouldered peak at 324 nm were present (Figure 4.24, black line). Upon mixing with HCl, intensity of both initial absorption peaks decreased as a new peak at 460 nm increased in intensity over the data collection period. An isosbestic point was recorded at 353 nm. The spectrum of **4.18b** after exposure to UV-light was comparable to that of the spectra recorded after acid-exposure (Figure 4.24b, 4.24a, respectively).
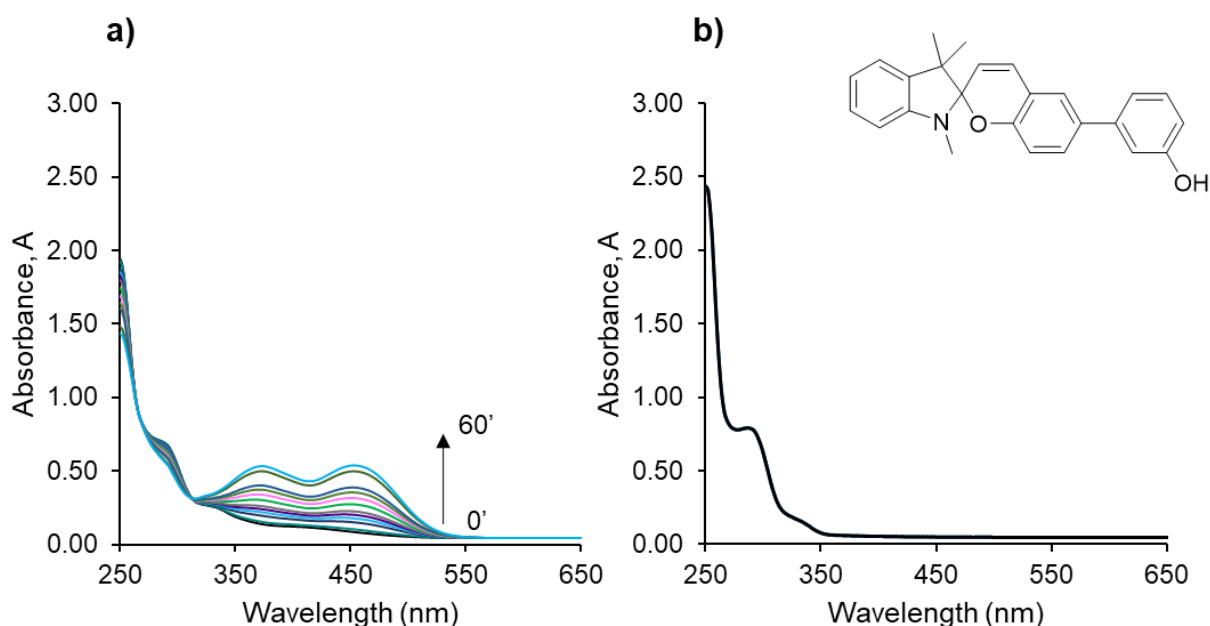

Figure 4.23: a) overlayed absorption spectra of a 50 µM solution of **4.17b** in MeOH at different time intervals after addition of 0.1 mL 0.1M HCl over a 60 min period; b) absorption spectra of a 50 µM solution of **4.17b** in MeOH before exposure to UV light (black) and after 5 min exposure to 365 nm UV light (no change in spectrum).
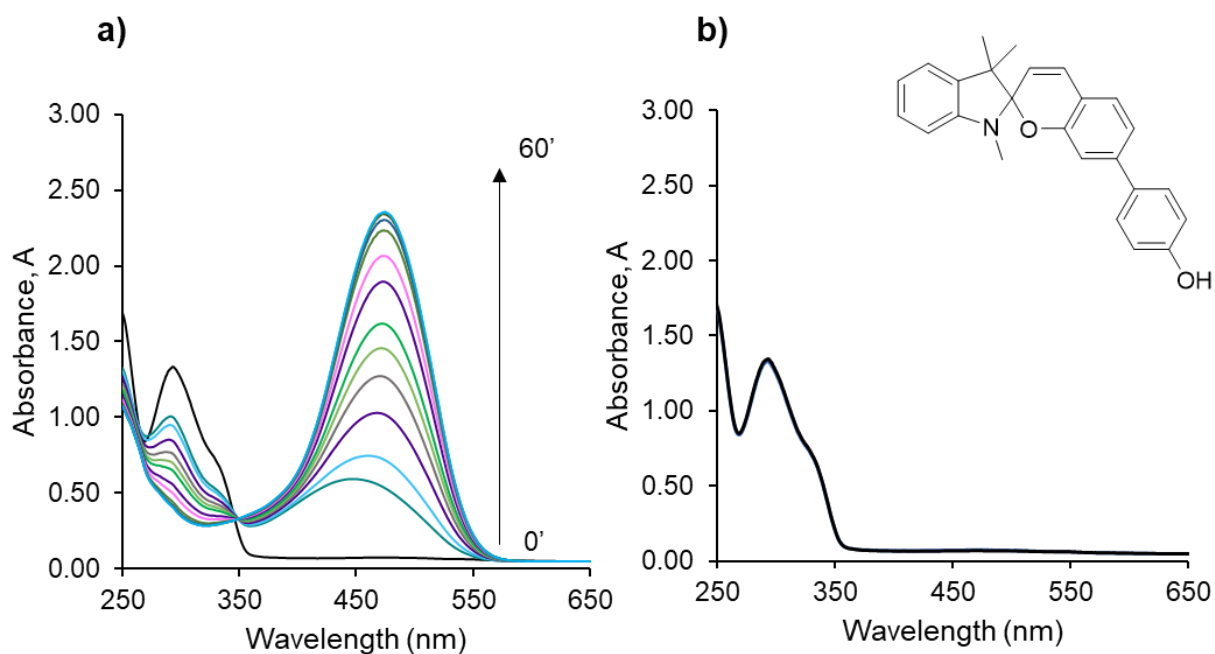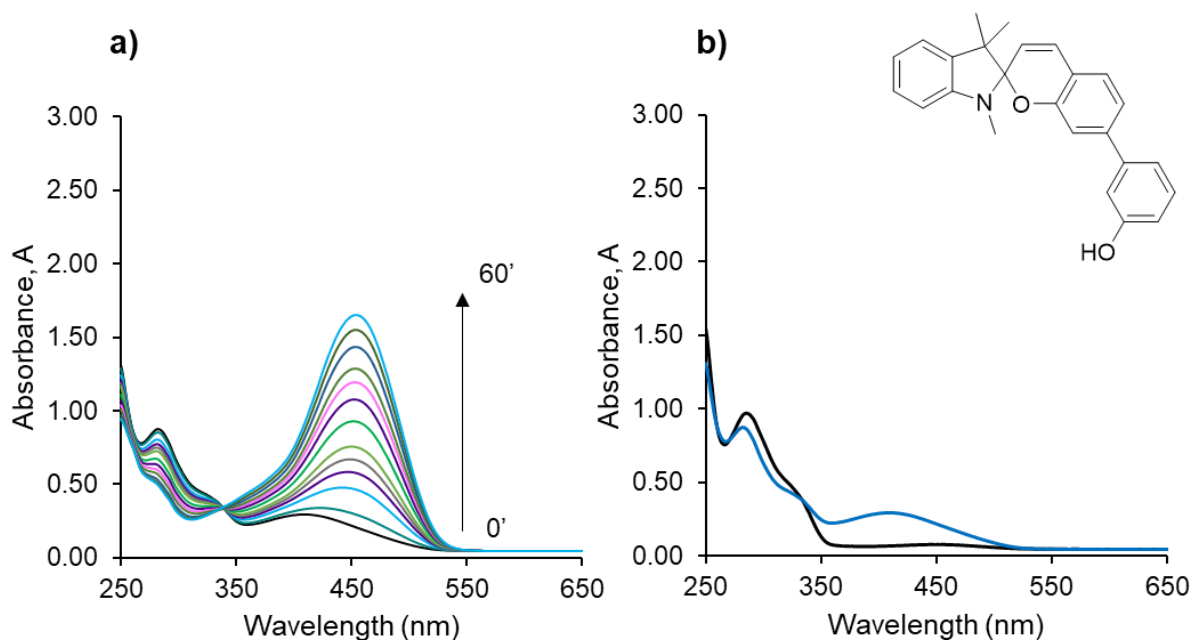
Figure 4.24: a) overlayed absorption spectra of a 50 µM solution of **4.18b** in MeOH at different time intervals after addition of 0.1 mL 0.1 M HCl over a 60 min period; b) absorption spectra of a 50 µM solution of **4.18b** in MeOH before exposure to UV light (black) and after 5 min exposure to 365 nm UV light (blue).

All SpOH compounds isomerised from their respective ring-closed Sp form to McH$^+$ upon addition of acid. There were two absorption maxima associated with McH$^+$ in the absorption profiles of *p*-substituted SpOHs **4.17a** and **4.18a** and one λ_{max} associated with McH$^+$ of each of the *m*-substituted compounds, **4.17b** and **4.18b**. Only compounds **4.17a** and **4.18b** converted to McH$^+$ in the presence of UV-light.

SpOH acid-induced ring opening mechanisms followed first order kinetics (Figure 4.25). Given that absorbance is directly proportional to concentration, ln[A] at λ_{Sp} (λ_{max} associated with each Sp isomer) was plotted against time to calculate rate. Rate constants were calculated from the slope of each graph, according to the integrated first order rate law (Equation 4.1). λ_{max} associated with McH$^+$ was not plotted as the fixed wavelength for rate calculations as absorption peaks were broader and maxima wavelengths shifted during initial measurements.

$$\ln[A] = -kt + \ln[A]_0 \qquad\qquad (\mathbf{4.1})$$
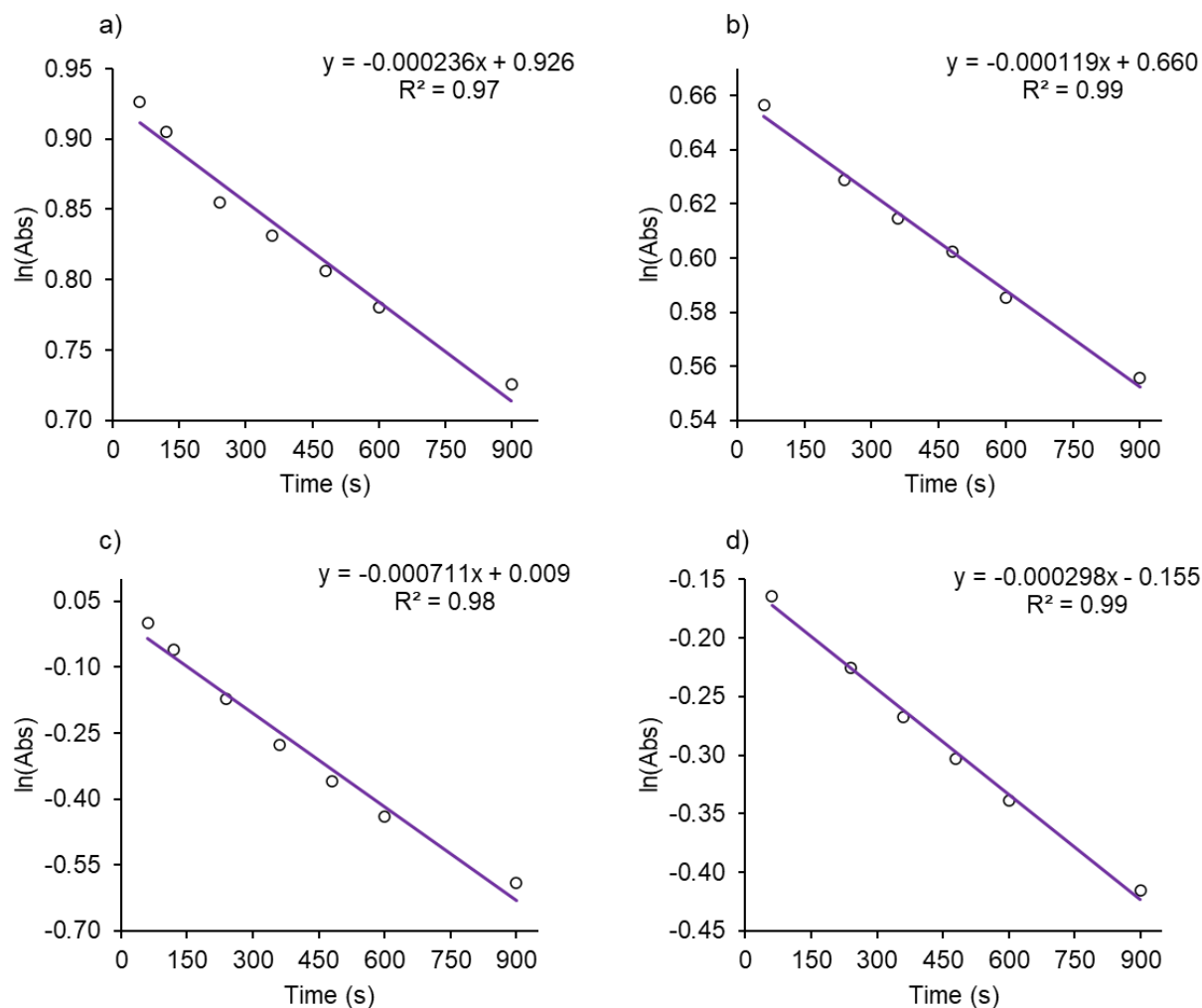
Figure 4.25: Plots of the natural logarithm of absorbance at a fixed wavelength (λ_{Sp}) against time where: a) **4.17a**, $\lambda_{Sp} = 252$ nm b) **4.18a**, $\lambda_{Sp} = 250$ nm c) **4.17b**, $\lambda_{Sp} = 293$ nm d) **4.18b**, $\lambda_{Sp} = 284$.

Kinetics of acid-induced ring opening were determined to be in the order of **4.17b** > **4.18b** > **4.17a** > **4.18b** from fastest to slowest (Table 4.9). *m*-SpOH acid mediated isomerisation was faster than that of *p*-SpOH compounds. Sp and McH$^+$ species associated with *m*-substituted SpOH compounds **4.17b** and **4.18b** absorbed at longer wavelengths than analogues of *p*-substituted **4.17a** and **4.18a**, a trend also observed between SpPy derivatives.

Compound	Absorption Maxima, λ_{max} (nm)		Rate: Sp $\rightarrow$ McH$^+$
	Sp	McH$^+$	$k \cdot 10^4$ (s^{-1})
4.17a	252, 282	383, 472	2.36
4.18a	250, 291	377, 460	1.19
4.17b	293, 332 (sh)	486	7.11
4.18b	284, 324 (sh)	460	2.98

Table 4.9: Summary of absorption peaks associated with Sp and McH$^+$ isomers of SpOH compounds and the rate of conversion from Sp to McH$^+$ upon addition of acid to SpOH compounds. (sh) = shouldered peak.

4.5.3   Spiropyan Hydrogels

Integrating acrylate functional groups within the structure of spiropyrans allows for covalent attachment of the photoswitches into polymer backbones, as discussed in Chapter 1. To this end, acrylated Sp derivatives (SpA) were synthesized from SpOH compounds **4.17a**, **4.18a** and **4.18b**. Additionally, **4.23** was synthesized from **4.22** as a literature benchmark (Scheme 4.8, Table 4.10). In general, SpOH compounds were dissolved in dry THF and deprotonated with freshly distilled NEt$_3$ under an inert atmosphere. A slight excess of acryloyl chloride was added to the reaction solution at 0 ºC, then warmed to room temperature once exotherm had subsided and allowed to react overnight. Excess acryloyl chloride was quenched during workup as the reaction mixture was washed with a saturated aqueous NaHCO$_3$ solution. SpA products were obtained *via* removal of solvent under reduced pressure and confirmed by ^{1}H NMR.
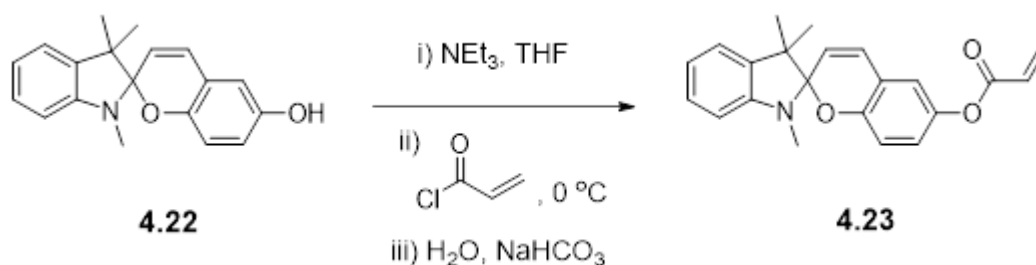
Scheme 4.8: Reaction scheme to show the synthesis of SpA **4.23** from SpOH **4.22**.

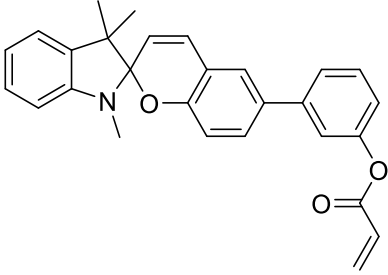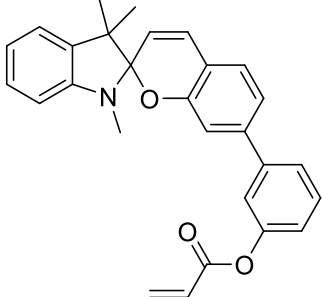| Parent Compound	SpA	Yield
4.22	**4.23**	94
4.17a	**4.24a**	91

4.18a	**4.24b**	89
4.18b	**4.24c**	94

Table 4.10: structure of spiropyran-acrylate (SpA) derivatives **4.23**, **4.24a-c** and their respective yields

Hydrogels were cast using a similar method outlined by the Diamond group.[15] 200 mg *N*-isopropylacrylamide (NIPAM) **4.25** was used as the base hydrogel material with 3.0 mol% *N,N'*-methylenebisacrylamide (MBIS) **4.26** as a cross-linker to add structural robustness to the gels, 5.0 mol% acrylic acid (AA) **4.27** to stabilise the more hydrophilic ring-opened McH+ isomer of the SpA fragments, and 2.0 mol% of SpA. The monomers were then agitated in 0.6 mL of a 1:4 water:dioxane mixture until all solid had dissolved. Photoinitiator was added to the mixture in 5.0 wt% (based on weight of NIPAM) and half of the solution was deposited onto a glass slide.

A UV-LED mounted system with a wavelength of 395 nm was employed for radical initiated photopolymerisation. Samples were held at 2 cm from the light source and allowed to cure for 10 min to ensure polymerisation of all monomers (Scheme 4.9). Once cured, the yellow/orange hydrogels were rinsed thoroughly with deionised water, then stored in fresh deionised water (10 mL) and allowed to equilibrate in the dark overnight.
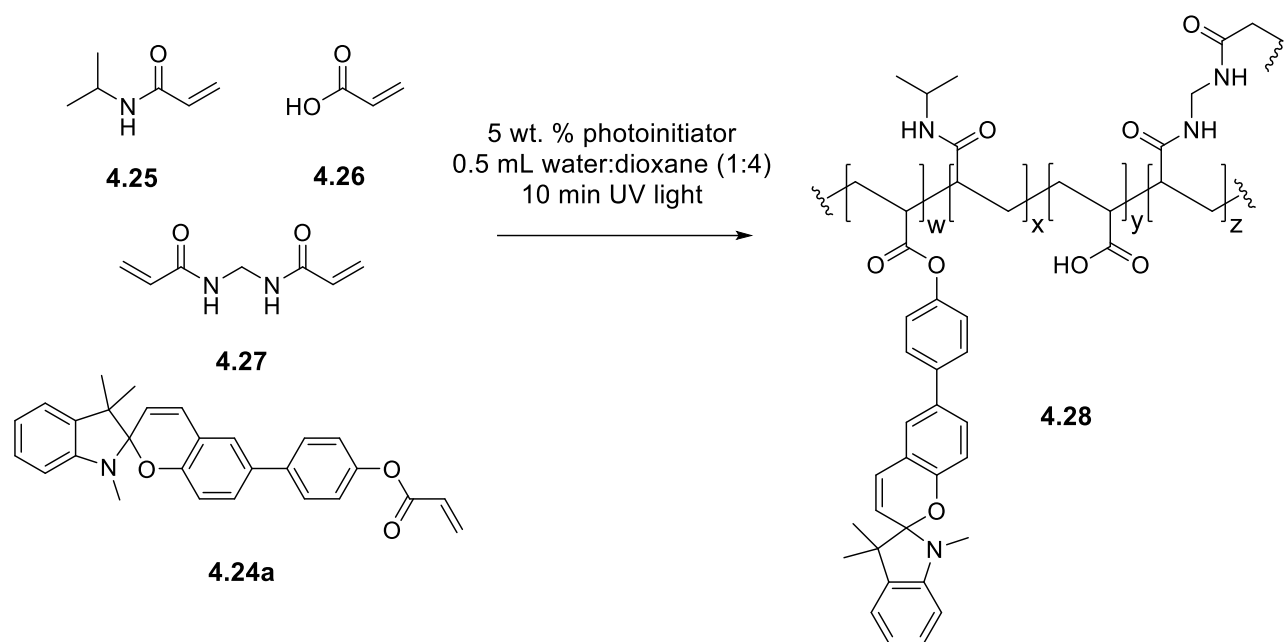
Scheme 4.9: Synthesis of SpA containing hydrogel **4.28** via the UV-light initiated free radical polymerization of monomers **4.24a**, **4.25**, **4.26** and crosslinker **4.27**.

It was noted that there was visible leaching of the original SpA compound **4.23** from the polymer into solution (Figure 4.26a). This was not observed with SpA monomers **4.24a** and **4.24b**, which were incorporated into hydrogels (Figure 4.26b and c). This may be explained by the more hydrophobic nature of the modified SpA compounds due to the additional aromatic ring within their structures.
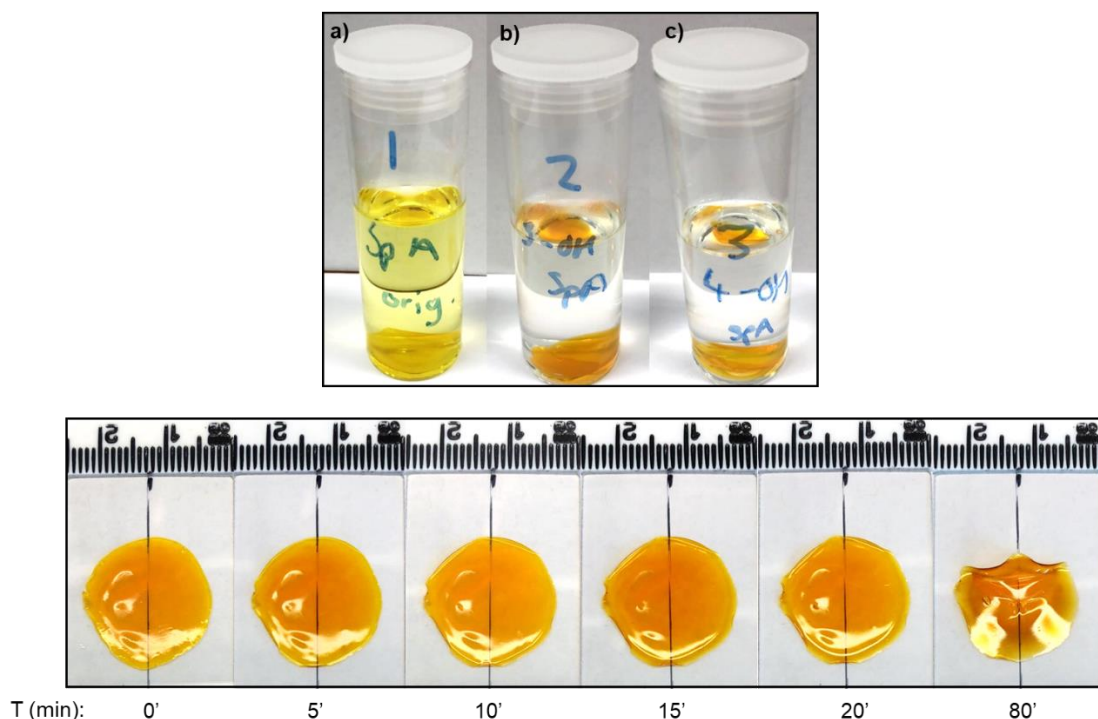
Figure 4.26: Images of hydrogels with SpA a) **4.23**, b) **4.24a** and c) **4.24b** (top) and images of hydrogel **4.28** upon exposure to visible light at different time intervals after equilibrating in water in the dark for 24 h (bottom).

Attempts were then made to quantitatively determine the response (i.e. degree of shrinking) of gels containing SpA monomers upon exposure to visible light, however, issues surrounding reproducibility (i.e. thickness of gels, light exposure) proved to be problematic. A more consistent method is needed in future work to accurately determine swelling kinetics of the hydrogel compounds, in addition to more specialised equipment and software to measure the physical degree of swelling/deswelling. Due to these issues, it was not possible to determine whether the deswelling of the hydrogels in this work was attributed to a photophysical response, or simply evaporation of water from the hydrogel structure over time (Figure 4.26).

4.6 Conclusion and Future Work

Structural isomers of phenol-substituted and pyridyl-substituted siporpyran compounds were successfully synthesised *via* Pd-catalysed Suzuki cross coupling reactions from bromospiropyran parent compounds with good-to-excellent conversion. The acido- and photochromic properties of SpOH and SpPy derivatives were investigated, and further transformations/applications of each type of Sp derivative were briefly explored.

Further work is needed to establish the interaction between SpPy compounds and the Mn(III)-substituted polyoxometalate. Attempts to crystalise the SpPy-POM compounds were unsuccessful, so other methods of structural investigation such as XPS or powder X-ray diffraction may help establish if reactions were successful. SpOH compounds were successfully converted to SpA compounds in good yields, but investigation of their application as the light-sensitive actuator component of NIPAM-based hydrogels was limited. A more accurate method of monitoring deswelling of gels must be developed in future work.

4.6 Experimental

*4.6.1 Synthesis of 6-bromo-1',3',3'-trimethylspiro[chromene-2,2'-indoline] **4.3a***

1,3,3-trimethyl-2-methyleneindoline **4.1** (2.43 g, 14.00 mmol) and 5-bromosalicylaldehyde **4.2a** (2.81 g, 14.00 mmol) were dissolved in warm EtOH (50 mL) under an inert atmosphere and allowed to reflux for 3 h. The deep purple solution was allowed to cool to room temperature, resulting in precipitation of some product. Solvent was removed under reduced pressure to afford a sticky purple crude product. The product was redissolved in the minimum amount of boiling MeOH (~ 15 mL) and a pale pink precipitate was formed upon cooling. The purified product was retrieved upon filtration and was dried in a vacuum oven at 50 °C overnight (4.64 g, 12.70 mmol, 93 %).

^{1}H NMR (300 MHz, CDCl$_3$) δ 1.17 (3H, s), 1.30 (3H, s), 2.73 (3H,s), 5.69 – 5.73 (1H, d, J = 12 Hz), 6.52 – 6.54 (1H, d, J = 12 Hz), 6.80 – 6.97 (5 H, m), 7.06 – 7.09 (1H, dd, J = 9 Hz, 1.5 Hz), 7.16 – 7.21 (1H, dt, J = 6 Hz, 1.5 Hz).

^{13}C NMR (300 MHz, CDCl$_3$) δ 157.31, 148.12, 134.30, 127.63, 123.13, 122.78, 120.36, 117.97, 116.57, 104.81, 51.89, 28.84, 25.71, 20.32.

*4.6.2 Synthesis of 7-bromo-1',3',3'-trimethylspiro[chromene-2,2'-indoline] **4.3b***

1,3,3-trimethyl-2-methyleneindoline **4.1** (2.43 g, 14.00 mmol) and 4-bromosalicylaldehyde **4.2b** (2.81 g, 14.00 mmol) were dissolved in warm EtOH (50 mL) under an inert atmosphere and allowed to reflux for 3 h. The deep red/purple solution was allowed to cool to room temperature. Solvent was removed under reduced pressure to afford a sticky red/purple crude product. The product was redissolved in the minimum amount of boiling MeOH (~ 15 mL) and a pale pink precipitate was formed upon cooling. The purified product was retrieved upon filtration and was dried in a vacuum oven at 50 °C overnight (4.44 g, 12.46 mmol, 89 %).

^{1}H NMR (400 MHz, CDCl$_3$) δ 1.17 (3H, s), 1.30 (3H, s), 2.73 (3H,s), 5.72 – 5.75 (1H, d, J = 12 Hz), 6.52 – 6.55 (1H, d, J = 12 Hz), 6.77 – 6.88 (2H, m), 7.06 – 7.09 (1H, d, J = 12 Hz), 7.06 – 7.02 (3H, m)

^{13}C NMR (400 MHz, CDCl$_3$) δ 155.13, 148.02, 136.53, 127.66, 123.13, 121.51, 119.34, 118.29, 106.89, 51.87, 28.89, 25.86, 20.12.

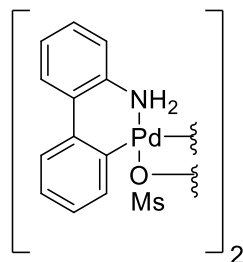### 4.6.3 Synthesis of 2-ammoniumbiphenyl mesylate *4.5*
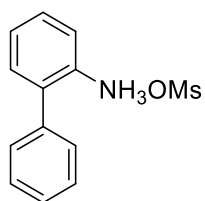
2-amminobiphenyl (2.54 g, 15.00 mmol) was dissolved in Et_2O (50 mL). The clear brown solution was allowed to stir while a separately, methane sulfonic acid (0.97 mL, 15.00 mmol) was dissolved in Et_2O (10 mL). The acid solution was added to the reaction flask slowly, which resulted in the immediate formation of an off-white precipitate, which gradually became pale pink. The suspension was allowed to stir at room temperature for 30 min. The crude pink solid was isolated upon Büchner filtration and washed with Et_2O (3 x 25 mL). The product was dried in a vacuum oven at 45 ℃ overnight. (3.80 g, 14.33 mmol, 96 %).

^{1}H NMR (300 MHz, CDCl₃) δ 2.37 (3H, s), 7.25 – 7.51 (11 H, m), 9.16 (1H, br, s).

4.6.4 Synthesis of Palladium Methanesulfonate Dimer *4.6*

An oven-dried Schlenk flask was charged with 2-ammoniumbiphenyl mesylate 4.4 (2.93 g, 11.00 mmol) and Pd(OAc)₂ (2.50 g, 11.10 mmol). The reaction flask was evacuated and backfilled with N₂ (x 3) before anhydrous toluene (40 mL) was added. The dark red/brown suspension was allowed to stir at 50 ℃ for 1 h 30 min, during which time the reaction solution became clouded and pale in colour. The mixture was allowed to cool to room temperature and a tan-coloured fine powder was isolated *via* filtration through a sintered glass filter. The product was washed with toluene (30 mL) and Et_2O (30 mL) before drying under vacuum (3.64 g, 4.92 mmol, 89 %).

^{1}H NMR (300 MHz, *d*-MeCN) δ 2.57 (6H, s), 6.31 (2H, br, s), 7.03 – 7.61 (16H, m)

4.6.5 Synthesis of XPhos Palladium Precatalyst *4.8*
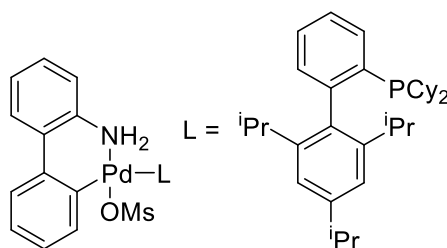
Pd species **4.6** (0.51 g, 0.70 mmol) and XPhos **4.7** was added to an oven dried Schlenk flask under an N_2 atmosphere and dissolved in dry THF (12 mL). The solution was allowed to stir overnight at room temperature. Et_2O (20 mL) was then added to the dark green/brown solution which resulted in the formation of a fine off-white precipitate. The product was isolated *via* filtration through a sintered glass frit and dried under vacuum (0.47 g, 0.55 mmol, 41 %).

^{1}H NMR (400 MHz, CDCl$_3$) δ 0.87 – 2.74 (43H, m), 3.73 (3H, s), 6.76 – 7.71 (13H, m)

^{31}P NMR (400 MHz, *d*-MeCN) δ 35.23

4.6.6 General Method for Conversion Measurements Suzuki-Miyaura Coupling Reaction

All optimisation reactions were carried out twice, and conversion is given as an average of the results. At times specified in Tables 4.x and 4.x, a small aliquot of the reaction solution was taken and immediately worked-up before further reaction could take place. Solvent was removed from the samples under vacuum and without further purification, ^{1}H NMR was used to determine conversion % to the corresponding substrate. General synthetic procedures for corresponding scale-up reactions are given below.

4.6.7 General Procedure for Suzuki-Miyaura Coupling Reactions with Pyridylboronic Acids and Bromospiropyrans

An oven-dried Schlenk flask was charged with Pd-mesylate dimer **4.6** (7.36 mg, 0.05 mmol mmol) and XPhos **4.7** (9.53 mg, 0.1 mmol) and was allowed to stir in dry THF (3.0 mL) at room temperature for 30 min. The reaction flask was heated to 55 °C and once the temperature had stabilised, SpBr (0.713 g, 2.00 mmol), PyB(OH)$_2$ (0.369 g, 3.00 mmol) and K$_2$.PO$_4$.H$_2$O (0.921 g, 4.00 mmol) was added and dissolved in a further portion of THF (6.0 mL) and water (8.0 mL). The suspension was allowed to stir at 55 °C for 180

min. Once cooled, the solution was diluted with water (40 mL) and extracted with Et_2O (3 x 25 mL). Organic extracts were combined and the solvent was removed under reduced pressure. The crude product purified over a silica comlumn using 3:1 EtOAc:petrol 40-60 as the eluent and SpPy compounds were retrieved upon removal of solvent.
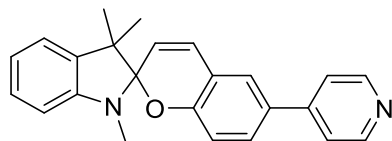

4.15a: ^{1}H NMR (300 MHz,CDCl3) δ 1.19 (3H, s), 1.33, (3H, s), 2.76 (3H, s), 5.76 − 5.79 (1H, d, J = 9 Hz), 6.54 − 6.57 (1H, dd, J = 9 Hz, 3 Hz), 6.81 − 6.94 (3H, m), 7.08 − 7.11 (1H, dd, J = 9 Hz, 1.5 Hz), 7.17 − 7.22, (1H, td, J = 6hz, 1.5 Hz), 8.59 − 8.62 (2H, dd, J = 6 Hz, 3Hz). Yield 71 %
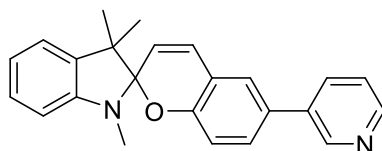
4.16a ^{1}H NMR (300 MHz,CDCl3) δ 1.19 (3H, s), 1.34, (3H, s), 2.77 (3H, s), 5.75 − 5.78 (1H, d, J = 9 Hz), 6.55 − 6.56 (1H, d, J = 3 Hz), 6.81 − 6.95 (3H, m), 7.08 − 7.11 (1H, dd, J = 6hz, 1.5 Hz), 7.17 - 7.22 (1H, td, J = 6 Hz, 1.5 Hz), 7.27 − 7.35 (2H, m), 7.79 − 7.83 (1H, dt, J = 6 Hz, 1.5 Hz), 8.53 − 8.55 (1H, dd, J = 3 Hz, 1.5 Hz) 8.79 − 8.80 (1H, d, J = 3 Hz). Yield 78 %
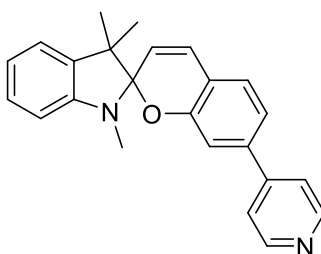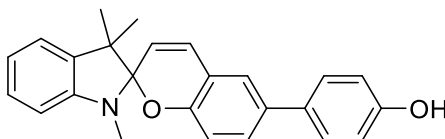

4.15b ^{1}H NMR (300 MHz,CDCl3) δ 1.19 (3H, s), 1.34, (3H, s), 2.76 (3H, s), 5.75 − 5.79 (1H, d, J = 12 Hz), 6.54 − 6.56 (1H, d, J = 6 Hz), 6.84 − 6.93 (2H, m), 7.05 − 7.22 (5H, m), 7.42 − 7.44 (2H, dd, J = 6 Hz, 3 Hz), 8.59 − 8.61 (2H, dd, J = 3 Hz, 1.5 Hz). Yield 69 %
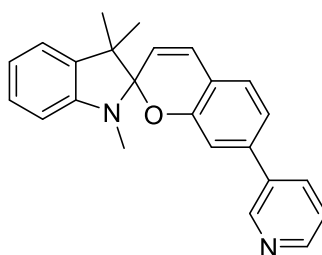
4.16b ^{1}H NMR (300 MHz,CDCl$_3$) δ 1.19 (3H, s), 1.35, (3H, s), 2.77 (3H, s), 5.73 – 5.76 (1H, d, J = 9 Hz), 6.53 – 6.56 (1H, d, J = 9 Hz), 6.83 – 6.88 (1H, td, J = 6 Hz, 1.5 Hz), 6.89 – 6.93 (1H, d, J = 12 Hz), 6.99 (1H, d, J = 1.5 Hz), 7.05 – 7.22 (4H, m), 7.28 – 7.33 (1H, ddd, J = 12 Hz, 6 Hz, 1.5 Hz) 7.78 – 7.82 (1H, dt, J = 6 Hz, 1.5 Hz), 8.53 – 8.55 (1H, dd, J = 6 Hz, 1.5 Hz), 8.79 – 8.80 (1H, d J = 3 Hz). Yield 78 %

4.6.8 General Procedure for Suzuki-Miyaura Coupling Reactions with Phenolboronic Acids and Bromospiropyrans

An oven-dried Schlenk flask was charged with Pd-mesylate dimer **4.6** (7.36 mg, 0.05 mmol mmol) and XPhos **4.7** (9.53 mg, 0.1 mmol) and was allowed to stir in dry THF (3.0 mL) at room temperature for 30 min. The reaction flask was heated to 55 °C and once the temperature had stabilised, SpBr (0.713 g, 2.00 mmol), PhOHB(OH)$_2$ (0.414 g, 3.00 mmol) and K$_2$.PO$_4$.H$_2$O (0.921 g, 4.00 mmol) was added and dissolved in a further portion of THF (6.0 mL) and water (8.0 mL). The suspension was allowed to stir at 55 °C for 180 min. Once cooled, the solution was diluted with water (40 mL) and extracted with Et$_2$O (3 x 25 mL). Organic extracts were combined and the solvent was removed under reduced pressure. The crude product purified over a silica plug with EtOAc as the eluent.
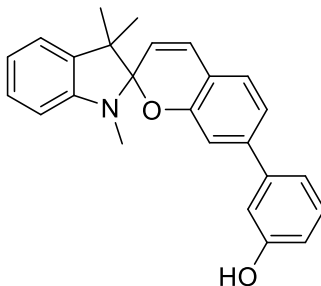

4.17a: ^{1}H NMR (300 MHz,CDCl$_3$) δ 1.19 (3H, s), 1.34, (3H, s), 2.76 (3H, s), 5.71 – 5.74 (1H, d, J = 9 Hz), 6.53 – 6.55 (1H, d, J = 9 Hz), 6.74 – 6.92, (6H, m), 7.07 – 7.10 (1H, d, J = 6 Hz), 7.07 – 7.22 (2H, m), 7.39 – 7.42 (2H, d, J = 9 Hz). ^{13}C NMR (300 MHz, CDCl$_3$) δ 154.70, 153.67, 148.25, 136.82, 133.53, 132.90, 129.67, 129.50, 128.01, 127.83, 127.63, 124.85, 121.55, 119.79, 119.16, 118.92, 115.63, 115.32, 115.28, 106.85, 104.40, 51.79, 28.99, 25.91, 20.23. Yield 81 %
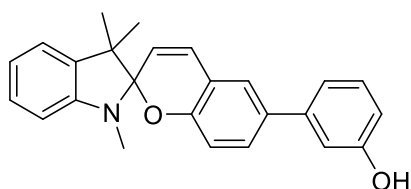
4.18a ^{1}H NMR (300 MHz,CDCl$_3$) δ 1.19 (3H, s), 1.33, (3H, s), 2.76 (3H, s), 5.72 – 5.74 (1H, d, *J* = 6 Hz), 6.53 – 6.55 (1H, d, *J* = 6 Hz), 6.75 – 6.78 (2H, d, *J* = 9 Hz), 6.83 – 6.87 (1H, t, *J* = 6 Hz), 6.89 – 6.92 (1H, d, *J* = 9 Hz), 7.00 – 7.01 (1H, t, 3 Hz), 7.08 – 7.11 (2H, m), 7.17 – 7.21 (1H, td, *J* = 6 Hz, 1.5 Hz), 7.29 – 7.32 (1H, dd, *J* = 9 Hz, 3 Hz). ^{13}C NMR (300 MHz, CDCl$_3$) δ 155.89, 154.27, 148.21, 142.50, 136.77, 132.70, 129.91, 129.42, 128.37, 127.63, 125.26, 121.54, 119.87, 119.18, 118.93, 115.32, 113.59, 113.53, 106.85, 104.50, 51.81, 28.98, 25.90, 20.20. Yield 74 %
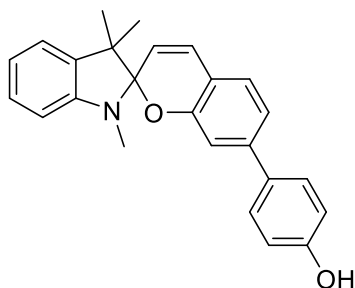
4.17b ^{1}H NMR (300 MHz,CDCl$_3$) δ 1.18 (3H, s), 1.34, (3H, s), 2.76 (3H, s), 5.66 – 5.70 (1H, d, *J* = 12 Hz), 6.52 – 6.55 (1H, d, *J* = 9 Hz), 7.82 – 7.86 (6H, m), 7.00 – 7.04 (1H, dd, *J* = 9 Hz, 3 Hz), 7.07 – 7.09 (2H, d, *J* = 6 Hz), 7.15 – 7.22 (1H, td, *J* = 6 Hz, 3 Hz), 7.39 – 7.43 (2H, dt, *J* = 9 Hz, 3 Hz). Yield 67 %

4.18b ^{1}H NMR (300 MHz,CDCl$_3$) δ 1.18 (3H, s), 1.34, (3H, s), 2.76 (3H, s), 5.69 – 5.72 (1H, d, *J* = 9 Hz), 6.52 – 6.55 (1H, d, *J* = 9 Hz), 6.75 – 6.79 (1H, ddd, 9 Hz, 3 Hz, 1.5 Hz), 6.82 – 6.91 (2H, m), 6.98 – 7.00 (2H, m), 7.04 – 7.12 (4H, m), 7.15 – 7.22 (1H, td, *J* = 9Hz, 3 Hz). 13C NMR (300 MHz, CDCl$_3$) δ 155.88, 154.76, 148.24, 142.12, 136.83,

129.92, 129.10, 127.65, 126.96, 121.55, 119.43, 119.36, 118.72, 118.13, 114.42, 113.76, 113.51, 106.88, 104.45, 51.80, 29.02, 25.86, 20.23. Yield = 81 %.

4.6.9   Synthesis of Tetrabutylammonium Hexatungstate **4.21**

Sodium tungstate dihydrate (33.0 g, 100.0 mmol), DMF (30 mL) and Ac_2O (40 mL) was heated at 100 ºC for 3 h. The suspension gradually became clouded and viscous. Once the reaction had cooled to room temperature, a solution of HCl (37 %, 18 mL) in AcO_2 (20 mL) and DMF (20 mL) was added in small portions, which resulted in the immediate precipitation of an off-white solid from the solution. The insoluble white precipitate was removed *via* filtration and the turbid yellow filtrate was taken and stirred with tertrabutylammonium bromide (15.0 g, 47.0 mmol) vigorously. A white crystalline precipitate formed and after 10 min stirring, the solid was isolated *via* filtration and washed with MeOH (20 mL) and Et_2O (50 mL). The white powder was recrystallized from the minimum amount of hot MeCN and isolated *via* filtration. The product was taken for the synthesis of **4.22**. Yield = 34 %

4.6.10 Synthesis of Mn-substituted Hexametalate Dimer, $[(MnW_5O_{18}H)_2](TBA)_6$ **4.22**

A 0.98 M solution of tertrabutylammonium hydroxide in MeOH (4.36 mL, 4.27 mmol) was added to a Schlenk flask under an atmosphere of Ar. The solvent was removed and the pale yellow oil was redissolved in dry MeCN (5 mL). The solvent was again removed, and this step was repeated two more times to ensure complete removal of MeOH. In a secondary flask under an atmosphere of Ar, $(TBA)_2[W_6O_{19}]$ **4.21** (2.02 g, 1.06 mmol) was suspended in dry MeCN (10 mL). TBA(OH) was redissolved in MeCN and delivered to the secondary flask *via* cannula. The reactants were allowed to stir at room temperature for 45 min, which resulted in a pale yellow, clouded solution. The reaction mixture was then transferred to another flask containing $Mn(NO_3).6H_2O$ (0.37 g, 1.28 mmol) *via* cannula. Upon addition, the reaction solution became intense yellow and a small amount of white precipitate formed.The reaction solution was allowed to stir at room temperature for 2 days, over which time the solution became purple in colour, suggestion oxidation of Mn(II) to Mn(III). The dark purple solution was evapourated to dryness then redissolved in the minimum amount of MeCN, and added to an excess of rapidly stirring EtOAc, which resulted in the precipitation of a fine purple powder. The product was obtained *via* filtration

and washed with Et_2O (3 x 15 mL). The powder was dried under vacuum to yield the purified product. Yield 89 %

FTIR (cm^{-1}) 2960 (m), 2953 (m), 2873 (m), 1645 (w), 1483 (s), 1379 (w), 1343 (w), 1153 (w), 940 (s), 885 (m), 841 (s), 700 (s), 684 (s), 576 (s), 528 (m).

4.6.11 General Synthesis of Pyridylspiropyran Polyoxometalate Complexes

In general, SpPy (50.0 mg, 0.14 mmol) and $[(MnW_5O_{18}H)_2](TBA)_6$ (280.8 mg, 0.07 mmol) was dissolved in MeCN (3 mL) and allowed to stir at room temperature for 2 h. Solvent was removed under reduced pressure and the viscous product was triturated with Et_2O to yield a powdered product.

4.15a FTIR (cm^{-1}) 2960 (m), 2951 (m), 2872 (m), 1611 (w), 1596 (w), 1482 (s), 940 (s), 788 (s), 761 (s), 573 (s)

4.16a FTIR (cm^{-1}) 2960 (m), 2951 (m), 2872 (m), 1648 (w), 1596 (m), 1482 (s), 1380 (m), 939 (s), 788 (s), 761 (s), 576 (m)

4.15b FTIR (cm^{-1}) 2959 (m), 2951 (m), 2871 (m), 1644 (w) 1596 (w), 938 (s), 1381 (m), 789 (s), 761 (s), 577 (m)

4.16b FTIR (cm^{-1}) 2961 (m), 2951 (m), 2872 (m), 1642 (w), 1607 (w), 1382 (m), 1022 (w), 939 (s), 788 (s), 785 (s), 727 (m), 757 (m)

*4.6.12   General Synthesis of Acrylated Spiropyran Compounds, SpA **4.23, 4.24a-c***

SpOH (369.5 mg, 1.0 mmol) was dissolved in dry THF (10mL) and cooled to 0 °C under an inert atmosphere. Dry triethylamine (0.09 mL, 1.20 mmol) was added dropwise to the solution before dropwise addition of acryloyl chloride (0.12 mL, 1.20 mmol). The reaction solution was allowed to warm to room temperature and left to react for 16 h. The resulting suspension was evapourated to dryness and redissolved in EtOAc (45 mL). The organic layer was washed with saturated sodium bicarbonate solution (50 mL) then brine (50 mL). The reaction solution was then dried over $MgSO_4$ before the solvent was removed under vacuum. All SpA products were retrieved as viscous gels.
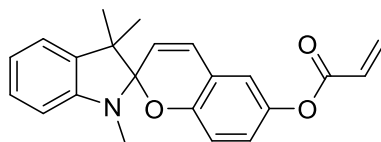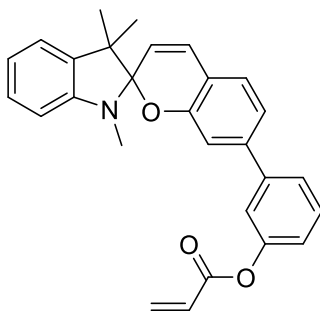
4.23 ^{1}H NMR (300 MHz, CDCl$_3$) δ 1.18 (3H, s), 1.33, (3H, s), 2.74 (3H, s), 5.71 – 5.75 (1H, d, J = 9 Hz), 5.98 – 6.02 (1H, dd, J = 12 Hz, 3Hz), 6.26 – 6.36 (1H, dd, J = 12 Hz, 9 Hz), 6.53 – 6.62 (2H, m), 6.70 – 6.73 (1H, d J = 9 Hz), 6.80 – 6.88 (4H, m), 7.08 – 7.10 (1H, d, J = 6 Hz), 7.16 – 7.22 (1H, td, J = 9 Hz, 3Hz). Yield 94 %
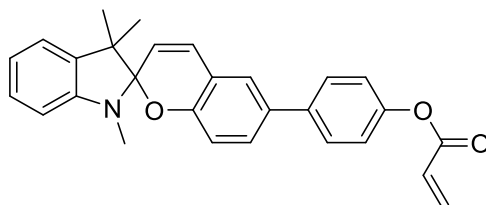
4.24a ^{1}H NMR (400 MHz, CDCl$_3$) δ 1.19 (3H, s), 1.34, (3H, s), 2.76 (3H, s), 5.72 – 5.75 (1H, d, J = 12 Hz), 6.01 – 6.04 (1H, d, J = 12 Hz), 6.31 – 6.38 (1H, dd, J = 16 Hz, 12 Hz), 6.53 – 6.55 (1H, d, J = 8 Hz), 6.60 – 6.65 (1H, d, J = 18 Hz), 6.77 – 6.79 (1H, d, J = 8 Hz), 6.83 – 6.85 (1H, t, J = 4 Hz), 6.90 – 6.92 (1H, d, J = 8 Hz), 7.08 – 7.25 (5H, m), 7.29 – 7.32 (1H, dd, J = 12 Hz, 4 Hz), 7.52 – 7.54 (2H, d, J = 8 Hz). Yield 91 %
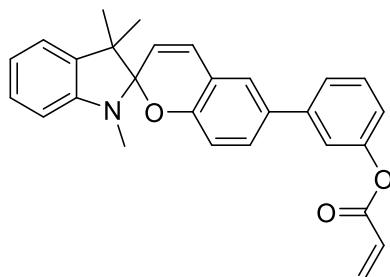
4.24b ^{1}H NMR (400 MHz, CDCl$_3$) δ 1.19 (3H, s), 1.33, (3H, s), 2.76 (3H, s), 5.72 – 5.75 (1H, d, J = 12 Hz), 6.01 – 6.04 (1H, d, J = 12 Hz), 6.31 – 6.38 (1H, dd, J = 16 Hz, 12 Hz), 6.53 – 6.55 (1H, d, J = 8 Hz), 6.60 – 6.65 (1H, d, J = 18 Hz), 6.77 – 6.79 (1H, d, J = 8 Hz), 6.83 – 6.85 (1H, t, J = 4 Hz), 6.90 – 6.92 (1H, d, J = 8 Hz), 7.06 – 7.10 (2H, m), 7.17 – 7.21 (1H, dd, J = 12 Hz, 4 Hz), 7.30 – 7.33 (2H, m), 7.41 – 7.41 (2H, m). Yield 89 %

4.24c ^{1}H NMR (300 MHz,CDCl$_3$) δ 1.18 (3H, s), 1.33, (3H, s), 2.7 (3H, s), 5.70 − 5.73 (1H, d, J = 12 Hz), 5.99 − 6.03 (1H, d, J = 12 Hz), 6.52 − 6.55 (1H, d, J = 9 Hz), 6.58 − 6.64 (1H, dd, J = 15 Hz, 3 Hz), 6.82 − 6.91 (2H, m), 7.05 − 7.09 (4H, m), 7.29 − 7.31 (1H, q, J = 1.5 Hz), 7.39 − 7.41 (2H, m). Yield 98 %

4.6.13   General Procedure for the Synthesis of SpA Hydrogels

NIPAM (200.0 mg, 1.77 mmol), MBIS (8.0 mg, 0.053 mmol), acrylic acid (6.0 mg, 0.089 mmol) and SpA (15.0 mg, 0.035 mmol) and Irgacure 290 (5 wt%) was dissolved in 1:4 water:dioxane (0.9 mL) and agitated until all solid was dissolved. 0.45 mL of the monomer solution was deposited onto a glass slide and the mixture was allowed to photopolymerise under UV-light (395 nm) for 10 min. The resulting hydrogel was washed with water then stored in a vile with fresh water (10 mL) and allowed to equilibrate in the dark.

144

4.7 References

[1] B. S. Lukyanov, M. B. Lukyanova, *Chem. Heterocycl. Compd.*, 2005, **41**, 281 – 311.

[2] H. Gorner, L. S. Atabekyan, A. K. Chibisov, *Chem. Phys. Let.*, 1996, **260**, 59 – 64.

[3] S. Bénard, P. Yu*, Adv. Mater.*, 2000, **12**, 48 - 50

[4] J. H. Day, *Chem. Rev.*, 1963, **63**, 65 - 80.

[5] a) T. A. Darwish, R. A. Evans, M. James, T. L. Hanley, *Chem. Eur. J.,* 2011, **17**, 11399 – 11404; b) T. Satoh, K. Sumaru, T. Takagi, K. Takai, T. Kanamori, *Phys. Chem. Chem. Phys.*, 2011, **13**, 7322 – 7329; c) M. Mandal, D. Banik, A. Karak, S. K. Manna, A. K. Mahapatra, *ACS Omega*, 2022, **7**, 36988 – 37007.

[6] L. Kortekaas, W. R. Browne, *Chem. Soc. Rev.*, 2019, **48**, 3406 – 3424.

[7] a) L. Cui, H. Zhang, Gu. Zhang, Y. Zhou, L. Fan, L. Shi, C. Zhang, S. Shuang, C. Dong, *Spectrochim. Acta A Mol. Biomol. Spectrosc.*, 2018, **202**, 13 – 17; b) E. I. Balmond, B. K. Tautges, An. L. Faulkner, V. W. Or, B. M. Hodur, J. T. Shaw, A. Y. Louie, *J. Org. Chem.*, 2016, **81**, 8744 – 8758.

[8] M. Irie, *Chem. Rev.*, 2000, **100**, 1683 – 1684.

[9] R. Heiligman-Rim, Y. Hieshbeeg, E. Fischeb, *J. Phys. Chem.*, 1962, **66**, 2470 - 2477.

[10] A. K. Chibisov, H. Görner, *Phys. Chem. A*, 1997, **24**, 4305–4312.

[11] A. Abdollahi, Z. Alinejad, A. R. Mahdavian, *J. Mater. Chem. C*, 2017, **5**, 6588 - 6600.

[12] R. Rosario, D. Gust, M. Hayes, J. Springer, A. A. Garcia, *Langmuir*, 2003, **19**, 8801 – 8806.

[13] E. Kim, Y. Kang, D. W. Kim, C. Lee, *Mol. Cryst. Liq. Cryst.,* 2003, **406**, 169 – 179.

[14] C. F. Koelsch, *J. Org. Chem.*, 1951, **9**, 1362 – 1370.

[15] B. Ziółkowski, L. Florea, J. Theobald, F. Benito-Lopez, D. Diamond, *Soft Matter*, 2013, **9**, 8754 - 8760.

[16] Y. Yang, Zhaohui Wang, H. Wu , Y. Li, Y Chen, L. Hu, W. Wu, *Mater. Chem. Front.,* 2022, 6, 1948 – 1955.

[17] M. Wang, G. Liu, H. Gao, C. Su, J. Gao, *Colloids Surf. A Physicochem. Eng. Asp.*, **659**, 130808 – 130908.

[18] O. Ivashenko, J. T. van Herpt, B. L. Feringa, P. Rudolf, Wesley R. Browne, *J. Phys. Chem. C*, 2013, **36**, 18567 – 18577.

[19] S. Zhang, Q. Zhang, B. Ye, X. Li, X. Zhang, Y. Deng, *J. Phys. Chem. B*, 2009, **17**, 6012 – 6019.

[20] Y. Liao, *Acc. Chem. Res.*, 2017, **50**, 1956 – 1964.

[21] J. H. Lee, E. S. Park, C. M. Yoon, *Tetrahedron Lett.*, 2001, **42**, 8311 - 8314.

[22] K. Wagner, M. Zanoni, A. B. S. Elliott, P. Wagner, R. Byrne, L. E. Florea, D. Diamond, K. C. Gordon, G. G. Wallace, D. L. Officer, *J. Mater. Chem. C*, 2013, **1**, 3913 – 3916.

[23] S. Bhattacharyya, M. Maity, A. Chowdhury, M. L. Saha, S. K. Panja, P. J. Stang, P. S. Mukherjee, *J. Inorg. Chem.*, 2020, **59**, 2083–2091.

[24] N. C. Bruno, N. Niljianskul, S. L. Buchwald, *J. Org. Chem.*, 2014, **79**, 4161−4166.

[25] C. A. Fleckenstein, H. Plenio, *Green Chem.*, 2007, **9**, 1287–1291.

[26] B. Diehl, in NMR Spectroscopy in *Pharmaceutical Analysis*, ed. U. Holzgrabe, I. Wawer, B. Diehl, Elsevier, Amsterdam, 1st edn, 2008, vol. 1, ch 1, pp 1 – 41.

[27] T. Halbritter, C. Kaiser, J. Wachtveitl, A. Heckel, *J. Org. Chem.*, 2017, **15**, 8040 – 8047.

[28] Z. Wu , Q. Wang , P. Li , B. Fang, M. Yin, *J. Mater. Chem. C*, 2021, **9**, 6290 – 6296.

[29] A. Saad, O. Oms, J. Marrot, A. Dolbecq, K. Hakouk, H. El Bekkachi, S. Jobic, P. Deniard, R. Dessapt, D. Garrot, K. Boukheddaden, R. Liu, G. Zhang, B. Keita, P. Mialane*, J. Mater. Chem. C*, 2014, **2**, 4748-4758.

[30] R. J. Errington, G. Harle, W. Clegg, R. W. Harrington, *Eur. J. Inorg. Chem.*, **1**, 2009, 5240–524

[31] D. Shiels, R. J. Errington, unpublished work.

[32] M. C. Kung, H. H. Kung, *Cat. Rev.*, 1985, **27**, 425 - 460.

Chapter 5 Conclusion

5.1 Summary of Work and Outlook

The work carried out in this thesis can be summarised in two parts: Chapters 2 and 3 where POM@polymer indicator materials were developed and tested in prototype TTI devices, respectively; and Chapter 4 where the chromatic properties of spiropyran compounds were explored. The development of light sensitive Sp-hydrogel valve materials was also attempted.

In Chapter 2, four different indicator materials were developed *via* immobilisation of [$PMo_{12}O_{40}$](TBA)$_3$ onto different polymer supports (Figure 5.1). The composites PMo_{12}@Vim:PEG400DA, PMo_{12}@Vim:PEG700DA, PMo_{12}@BuVimBr:PEG400DA and PMo_{12}@BuVimBr:PEG700DA were characterised by analytical techniques such as FTIR, CHN, TGA, solid state NMR and solid state UV-Vis. Unsurprisingly, it was found that the ionic polymers immobilised a greater amount of POM than the neutral polymer supports.
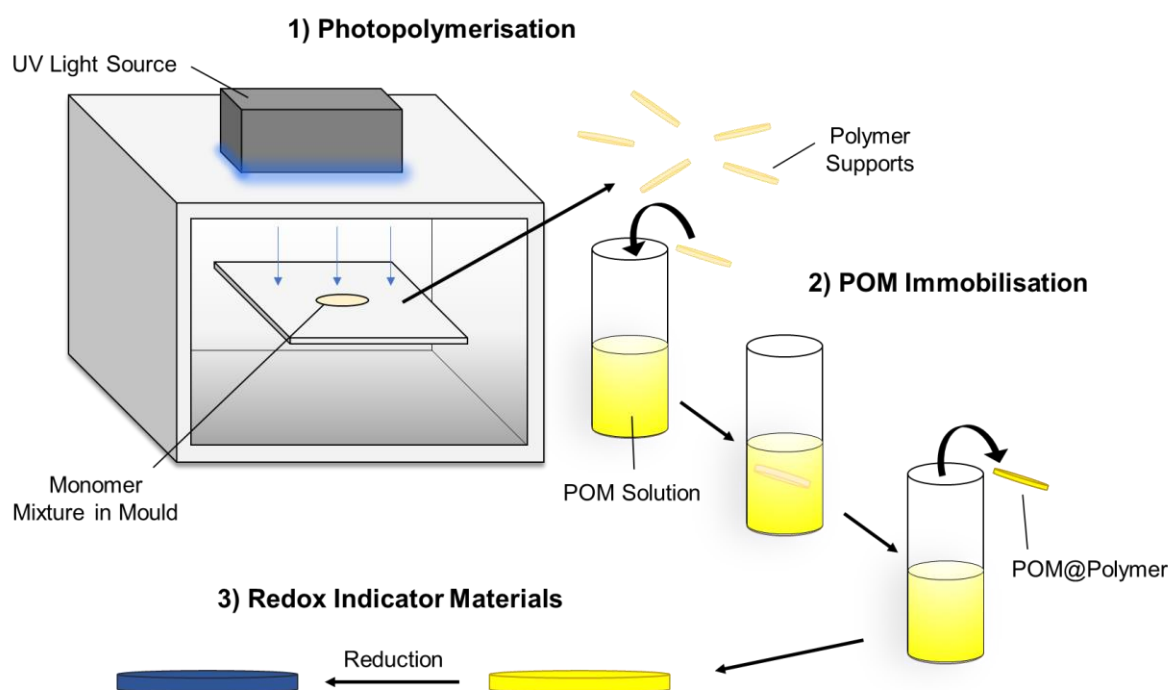
Figure 5.1: A schematic to summarise the synthesis of indicators in Chapter 2: 1) photopolymerisation of a monomer solution to a highly crosslinked, hydrogel-like material; 2) immobilisation of a polyoxometalate onto the polymer support *via* wet impregnation post-polymerisation; 3) reduction of the redox-active material in aqueous solution to induce a colour change.

PEG700DA-based composites were then taken forward in Chapter 3 for testing in prototype TTI devices. The effects of varying the indicator material, temperature, and ascorbic acid concentration on the time in which it took for colour change to occur was explored.

Overall, the findings in Chapters 2 and 3 partially satisfied the aims set out in Section 1.5.1. Although the materials show promise as redox-active indicators for use in TTI devices, much more work is needed to fully characterise the composites and establish commercial viability. Firstly, the loading of PMo_{12} onto each of the supports was not fully quantified. Controlling POM loading quantities would be of paramount importance for accuracy of any prospective TTI. The indicator composites also suffered from undesirable mechanical characteristics when handling (e.g., fracturing). Adjusting the polymer support formulae may address this issue (e.g., altering monomer:crosslinker ratios or introducing plasticisers). Although the prototype device experiments confirmed time-temperature dependency of the systems with respect to colour change, they also suffered from a lack of reproducibility.

In Chapter 4, spiropyran (Sp) derivatives were successfully accessed *via* Pd-catalysed Suzuki-cross coupling reactions between aryl boronic acids bromo-substituted Sp parent compounds. The phenol-substituted Sp derivatives (SpOH) were taken forward in an attempt to satisfy the last objective outlined in section 1.5.2, which was to incorporate Sp-derivatives into hydrogels for use as light-actuated valves. Unfortunately, this aim was not completely fulfilled in this work. Although Sp-acrylates were synthesised and polymerised into poly(*N*-isopropylacrylamide) based hydrogels, their response to visible light was not confirmed.

Overall, POM@polymer composites in this work show promise as viable indicator materials for TTI devices, albeit with the need for further development. Although the light-sensitivity of Sp-hydrogels was not seen in this work, a synthetic route to different Sp-acrylate derivatives was established.

Appendix

A1   Chapter 2

A1.1 FTIR Spectrum of [PMo$_{12}$O$_{40}$](TBA)$_3$ 2.1
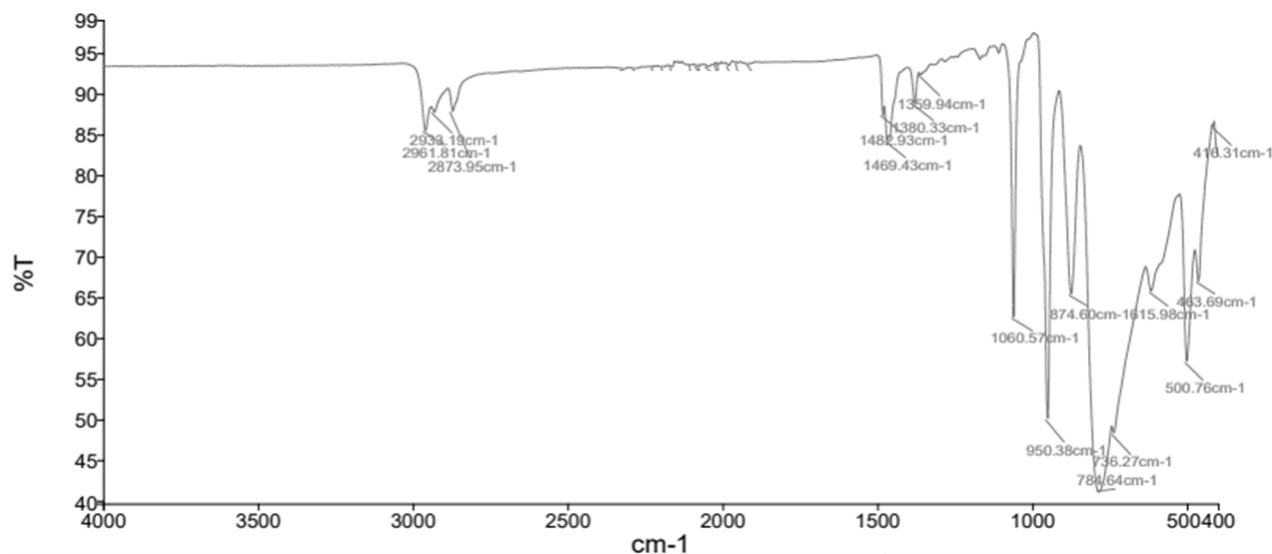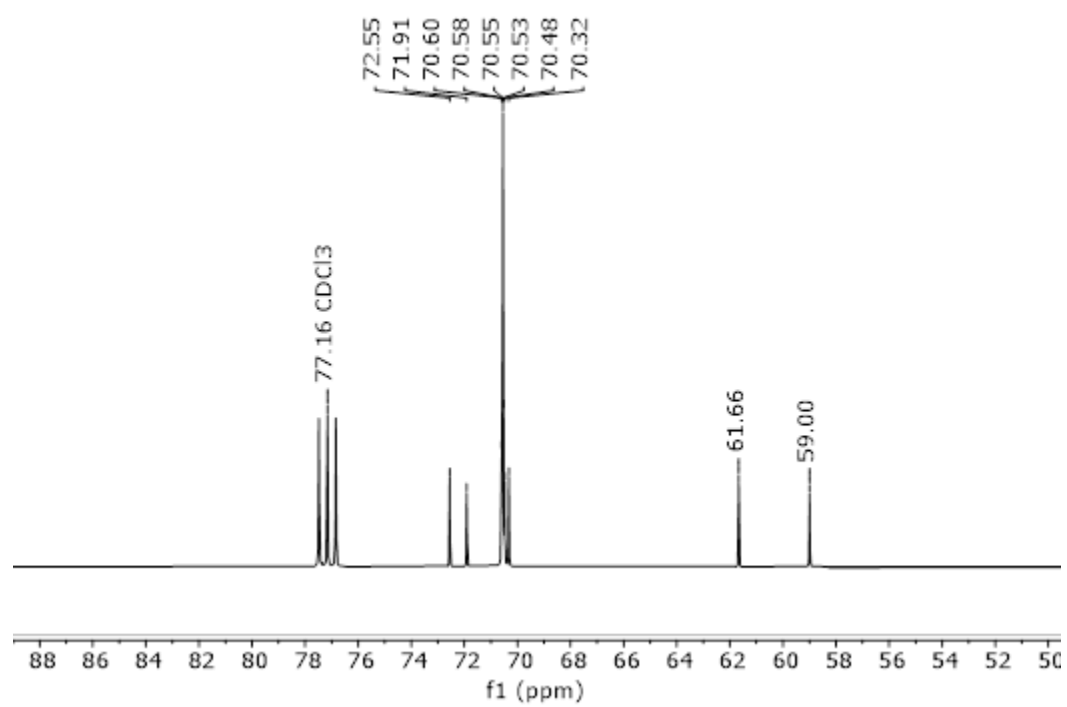

A1.2 FTIR Spectrum of [PW$_{12}$O$_{40}$](TBA)$_3$ 2.2

A1.3 FTIR Spectrum of [SiW₁₂O₄₀](TBA)₄ 2.3
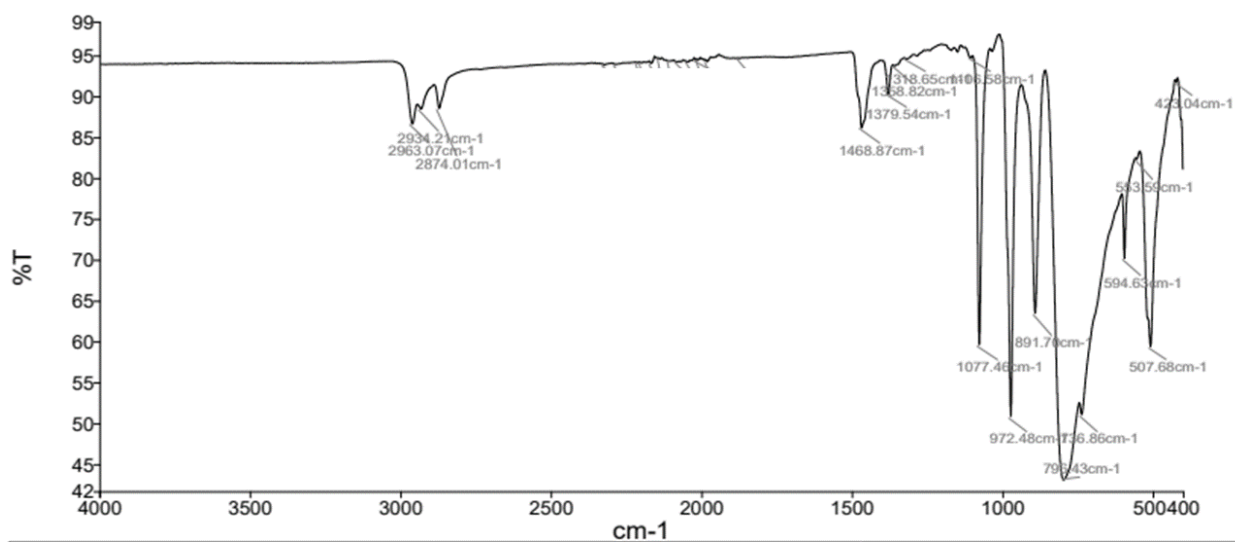
$A1.3\ FTIR\ Spectrum\ of\ [SiW_{12}O_{40}](TBA)_4\ 2.3$

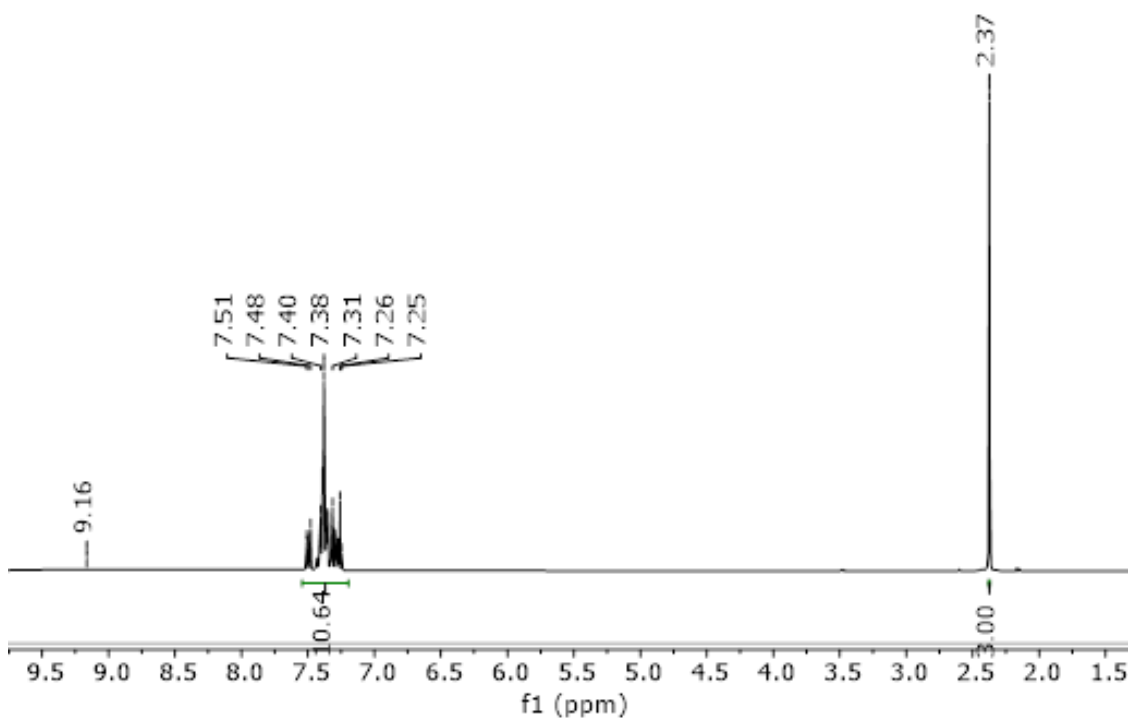*A1.4 ¹H NMR Spectrum of PEGCl 2.13*
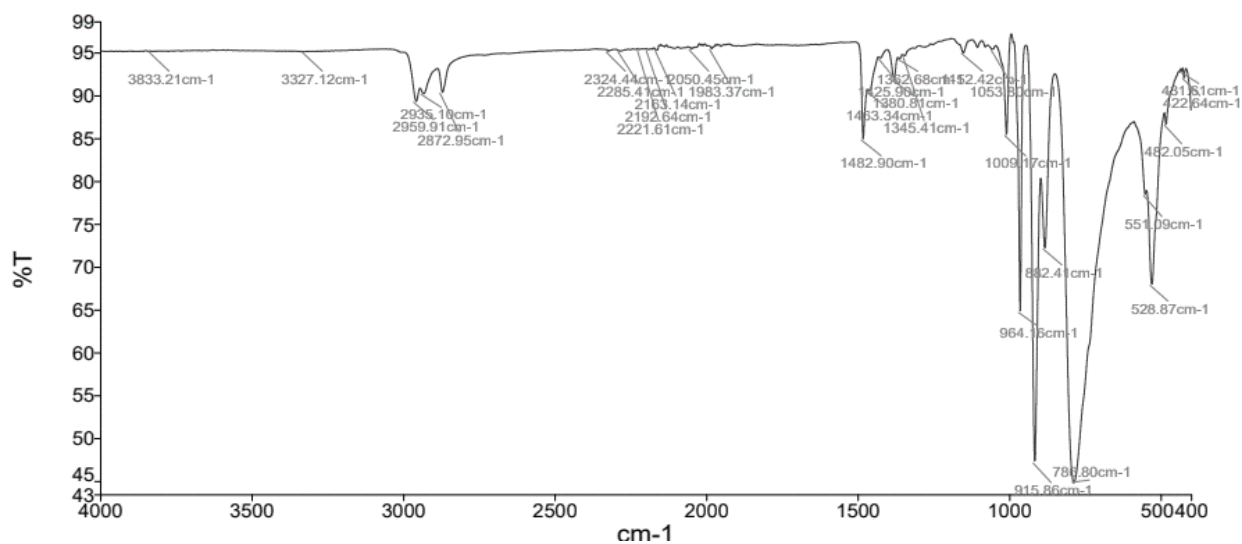
$A1.4\ ^1H\ NMR\ Spectrum\ of\ PEGCl\ 2.13$
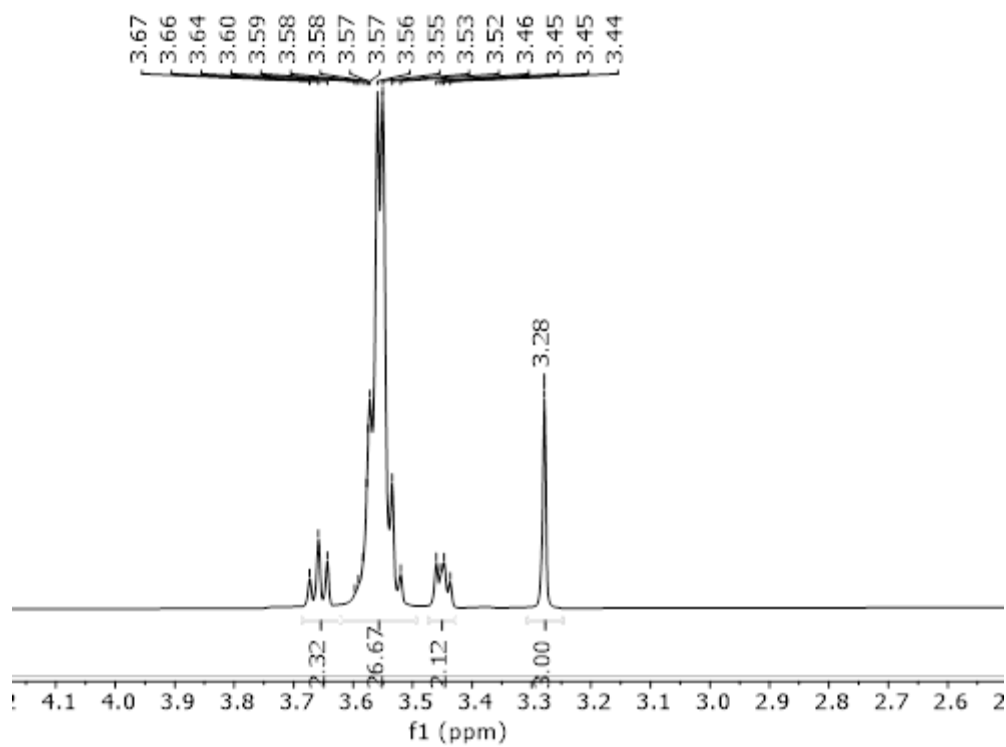
A1.5 ^{13}C NMR Spectrum of PEGCl 2.13

A2 Chapter 4

A2.1 ¹H NMR Spectrum of 2-amomoniumbiphenyl mesylate 4.5

A2.2 ¹H NMR Spectrum of μ-OMs dimeric Pd species 4.6
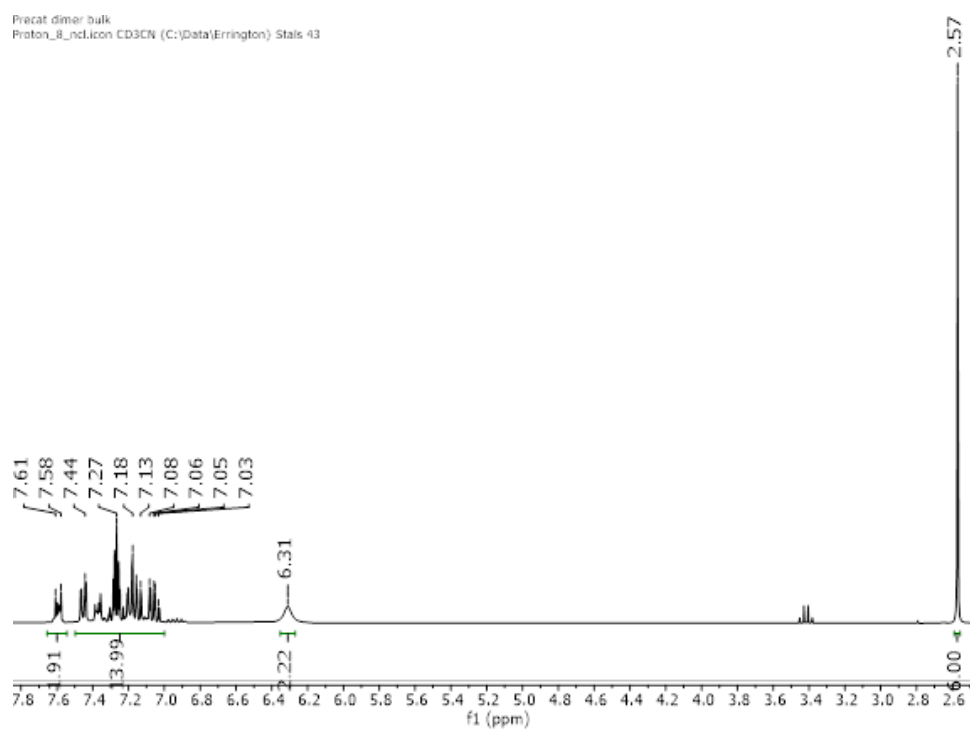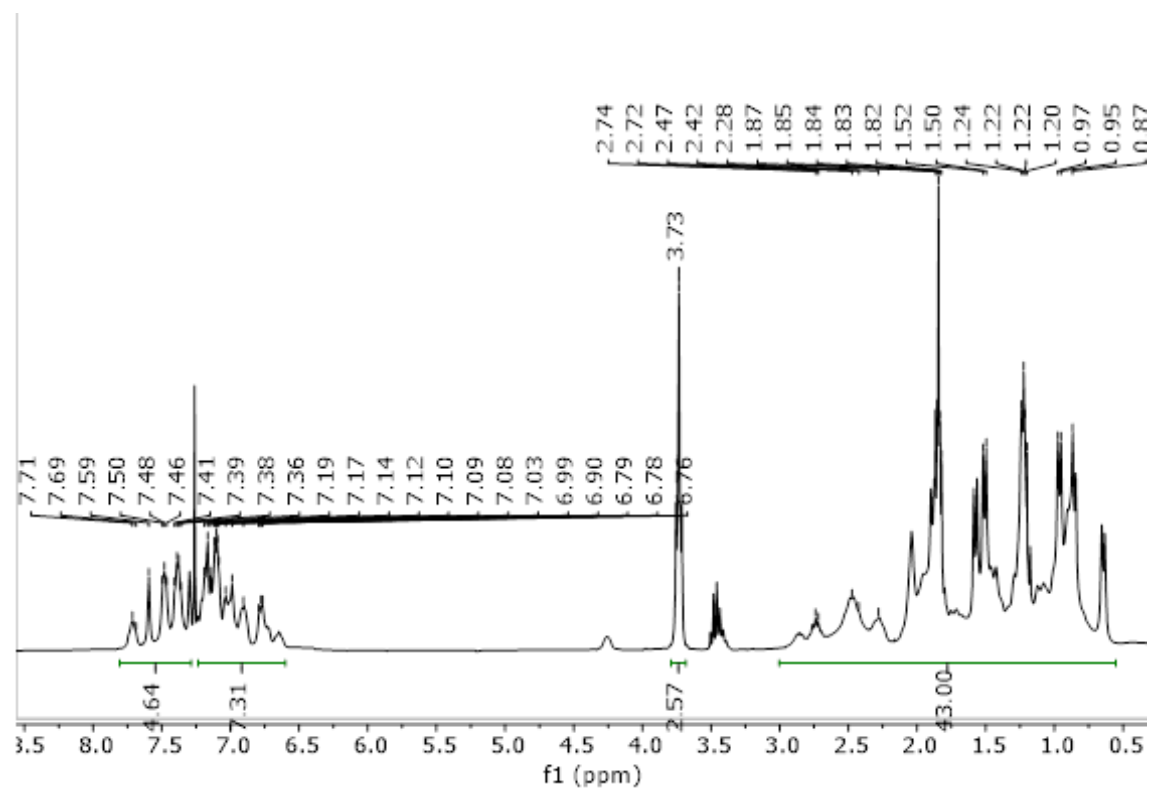
A2.4 ¹H NMR Spectrum of SpPy 4.15a
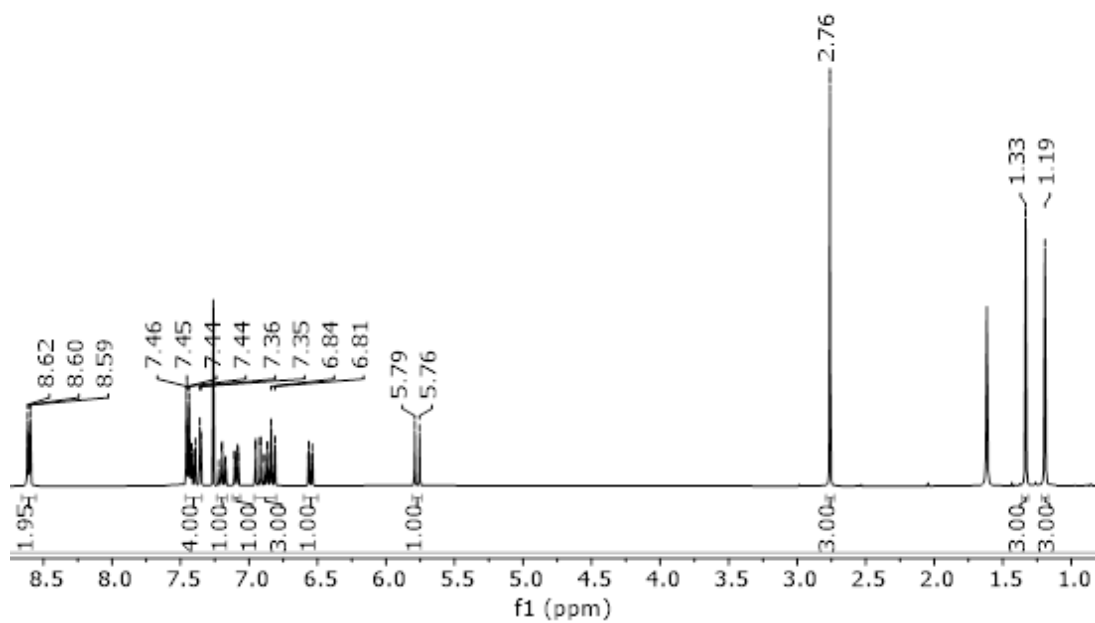
A2.5 ¹H NMR Spectrum of SpPy 4.15b
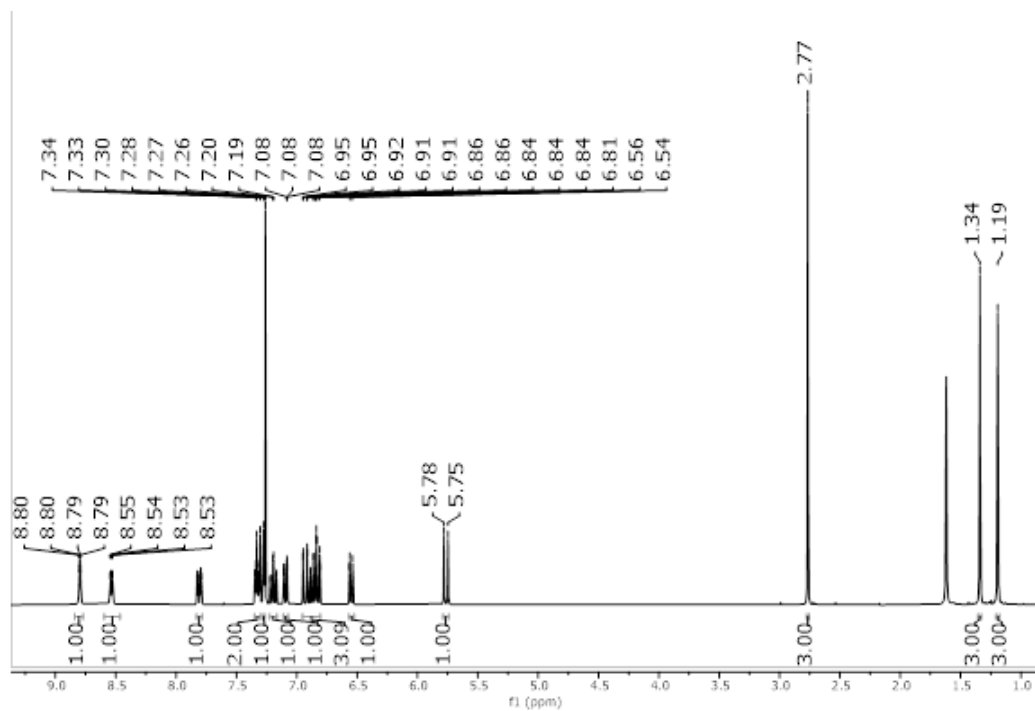
A2.7 ¹H NMR Spectrum of SpPy 4.16b
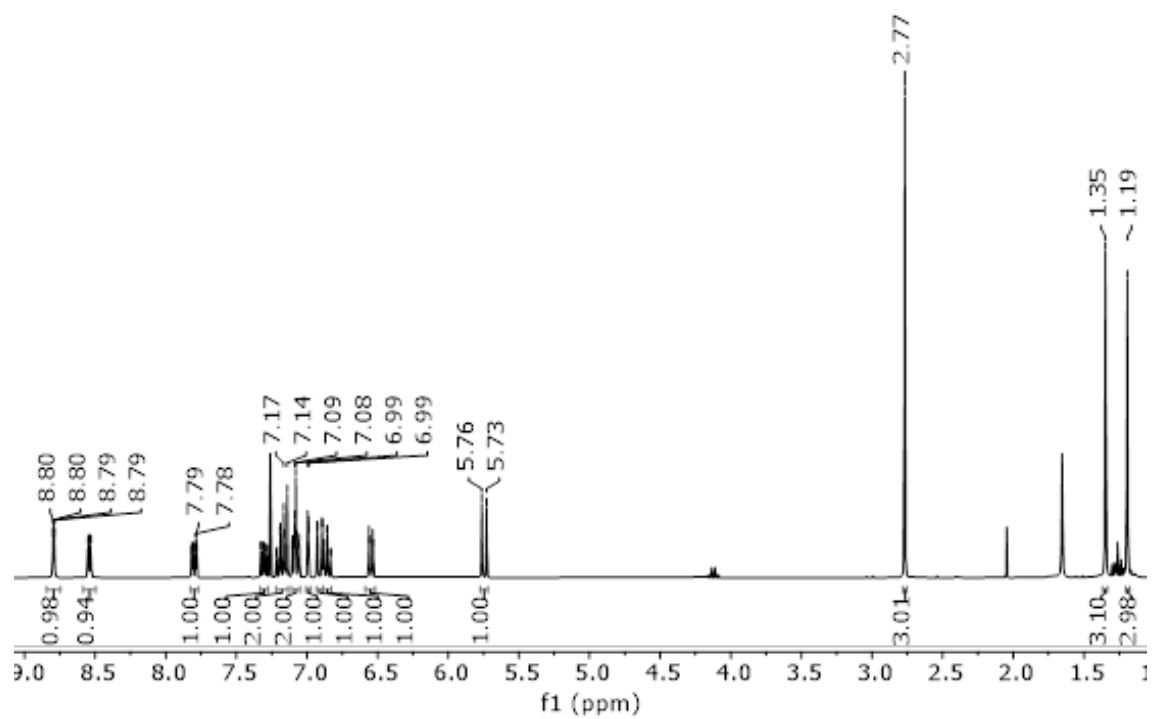
A2.8 ¹H NMR Spectrum of SpOH 4.17a
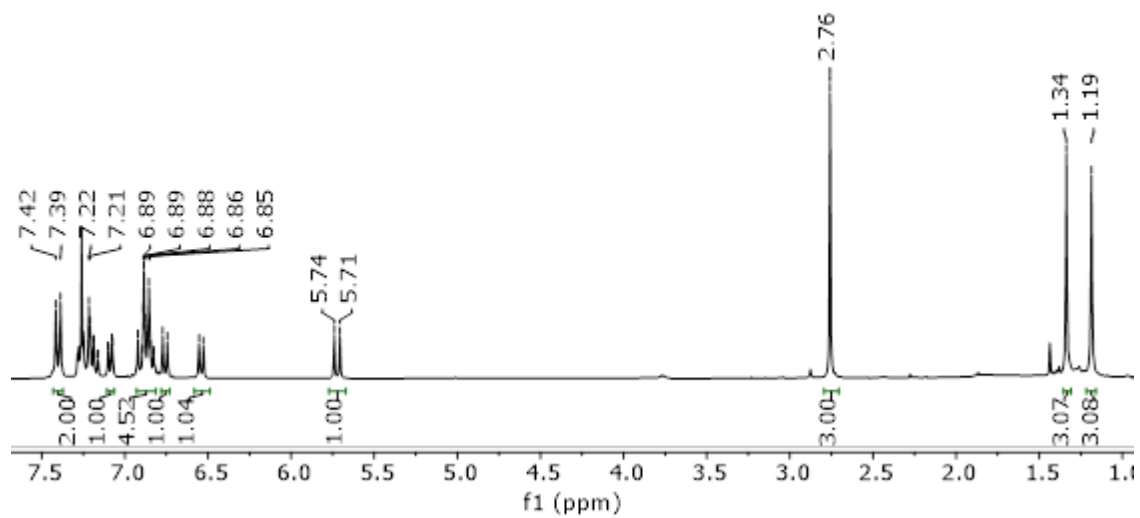
A2.9 ¹³C NMR Spectrum of SpOH 4.17a
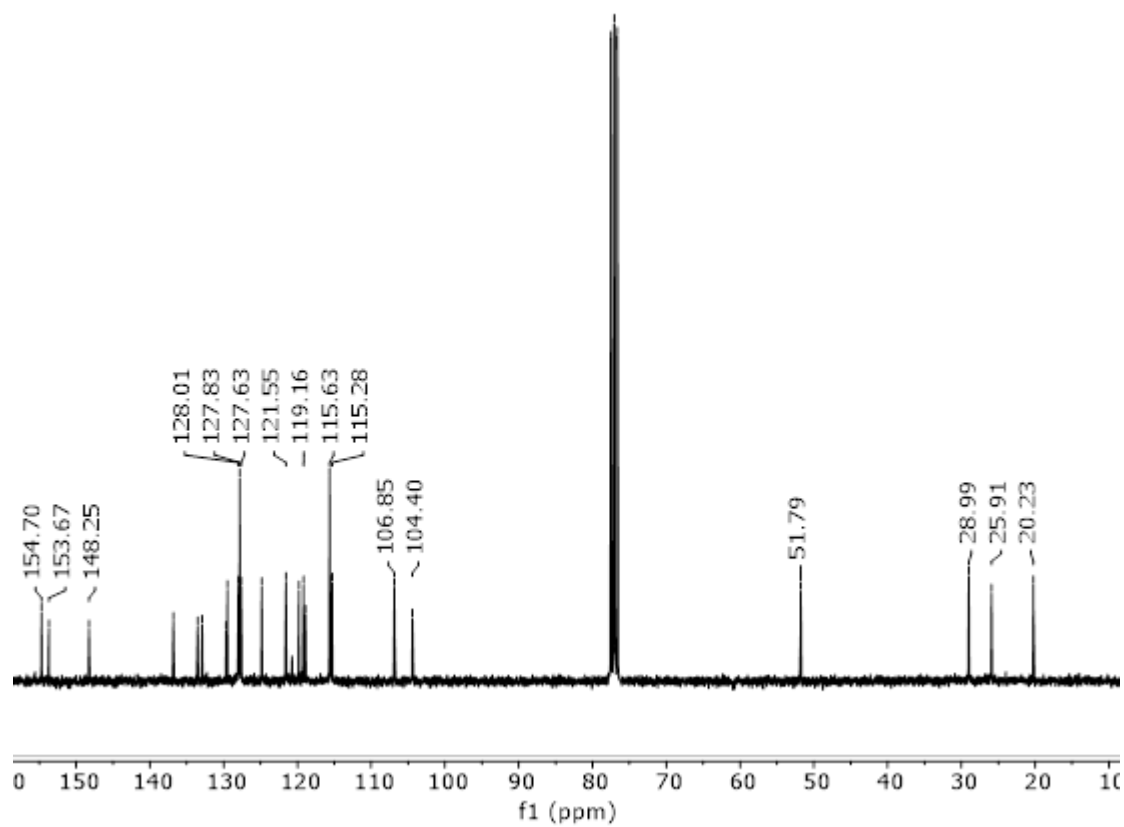
A2.10 ¹H NMR Spectrum of SpOH 4.17b
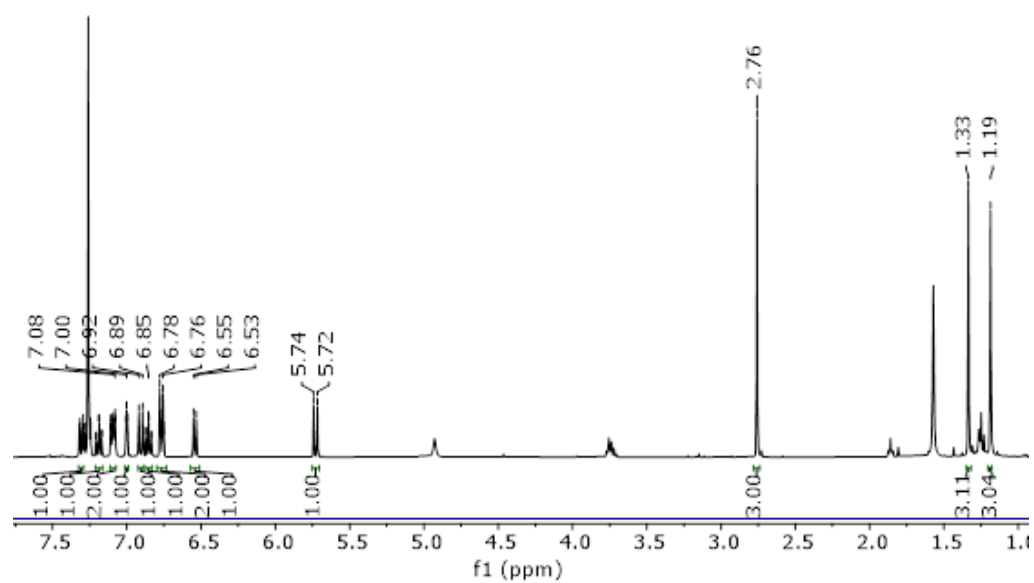
A2.11 ^{13}C NMR Spectrum of SpOH 4.17b
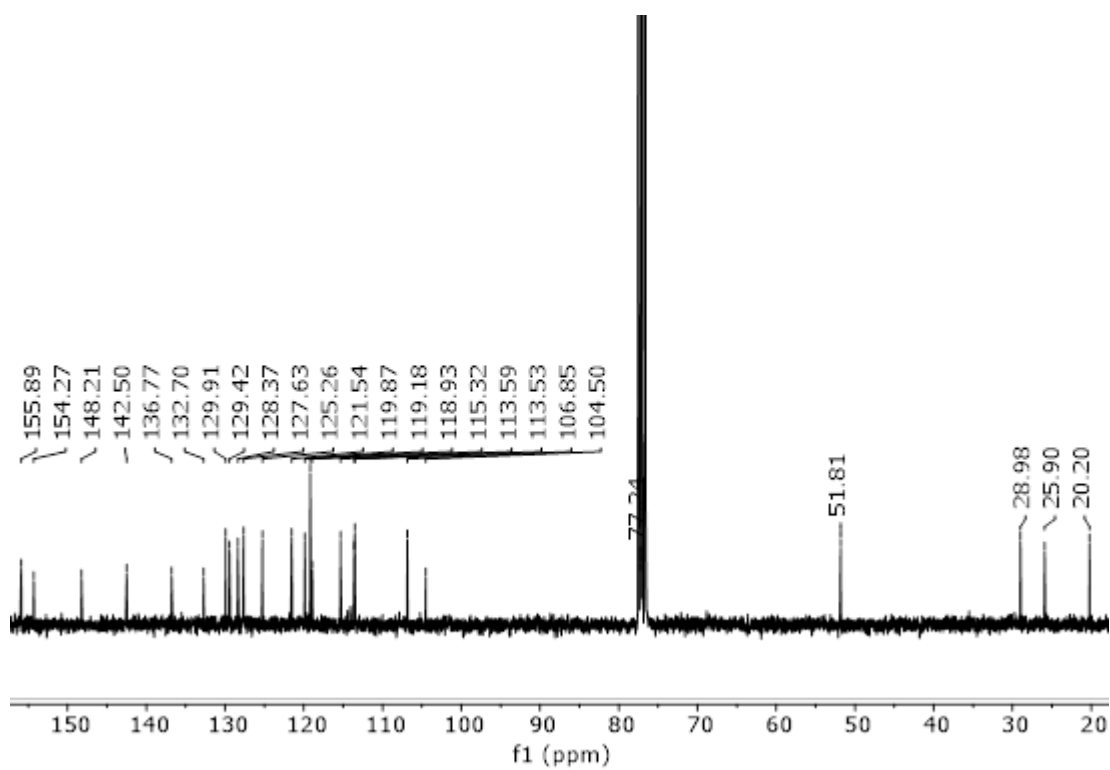
A2.12 ^{1}H NMR Spectrum of SpOH 4.18a
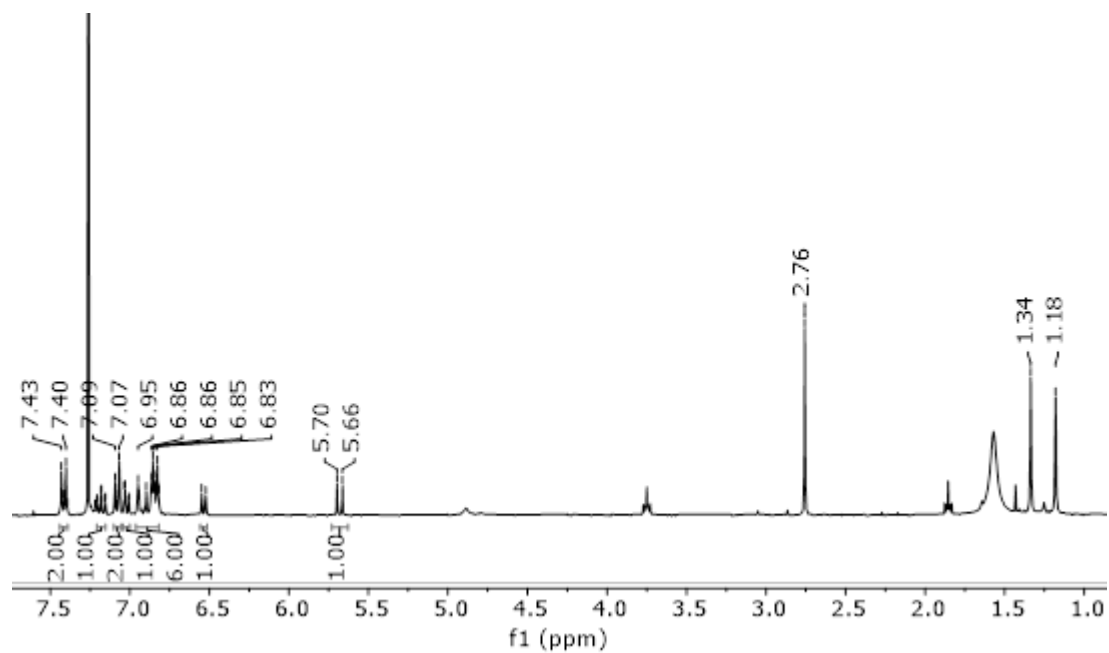
A2.13 ^{1}H NMR Spectrum of SpOH 4.18b
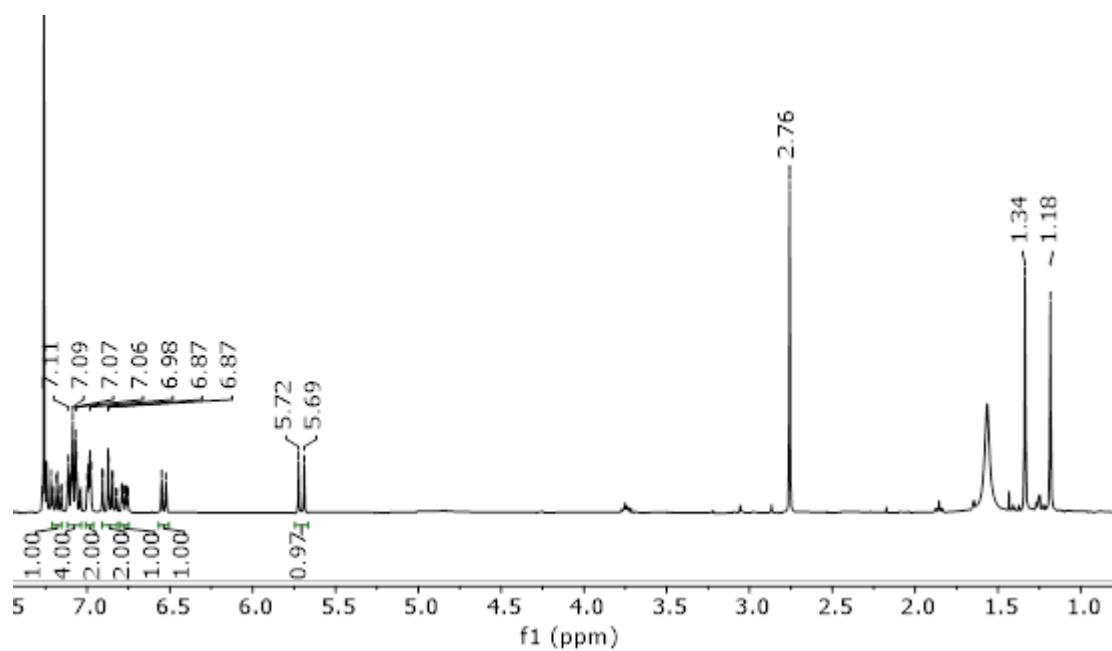
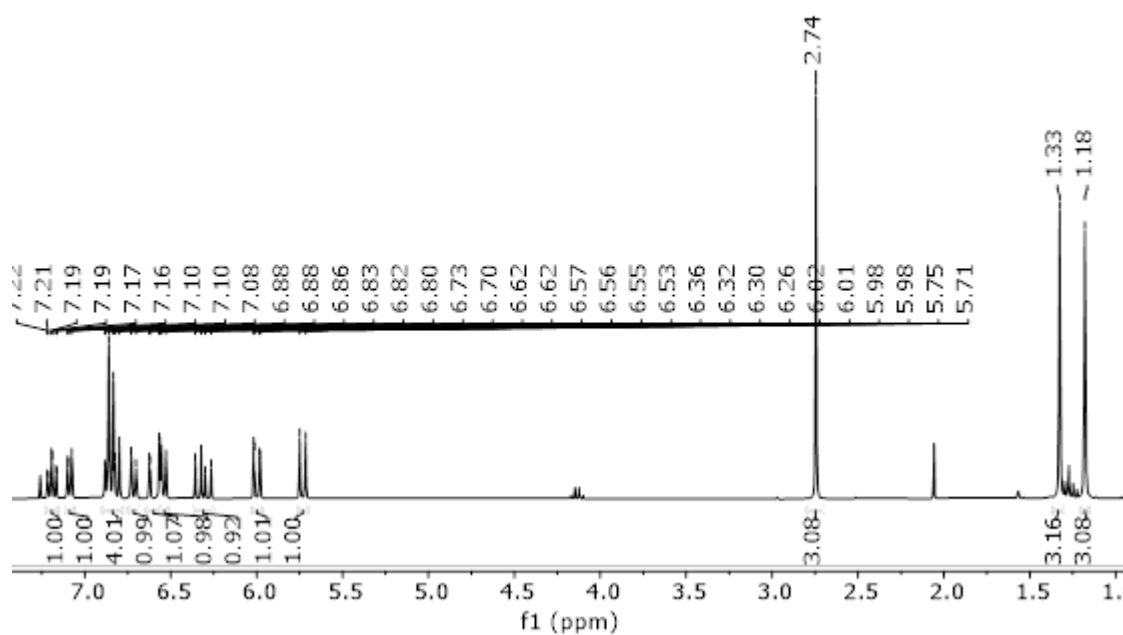*A2.14 ^{13}C NMR Spectrum of SpOH 4.18b*
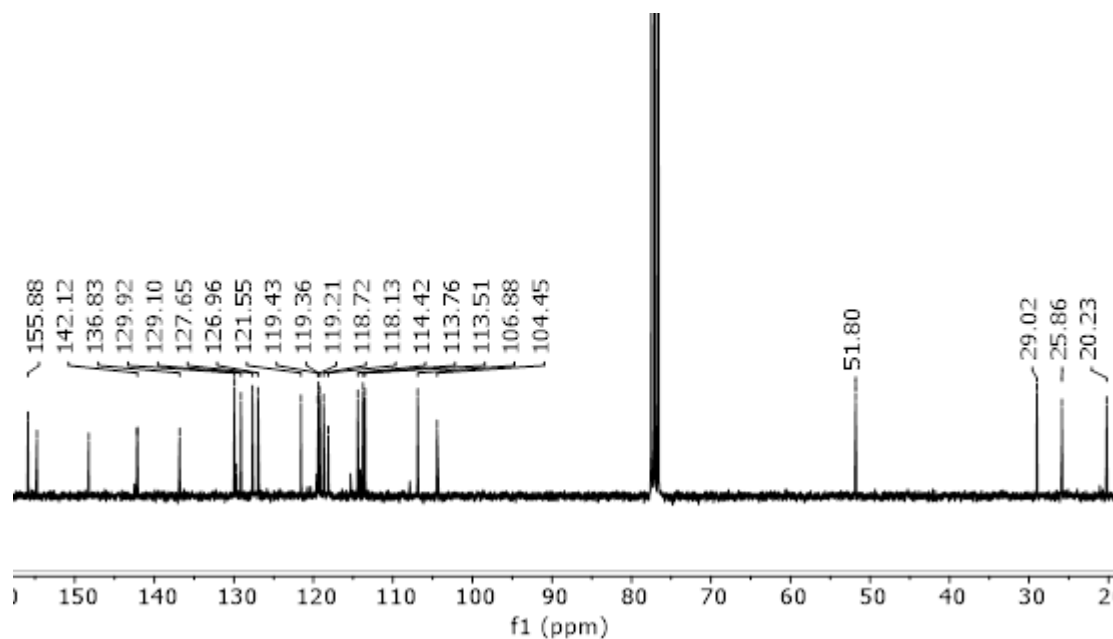
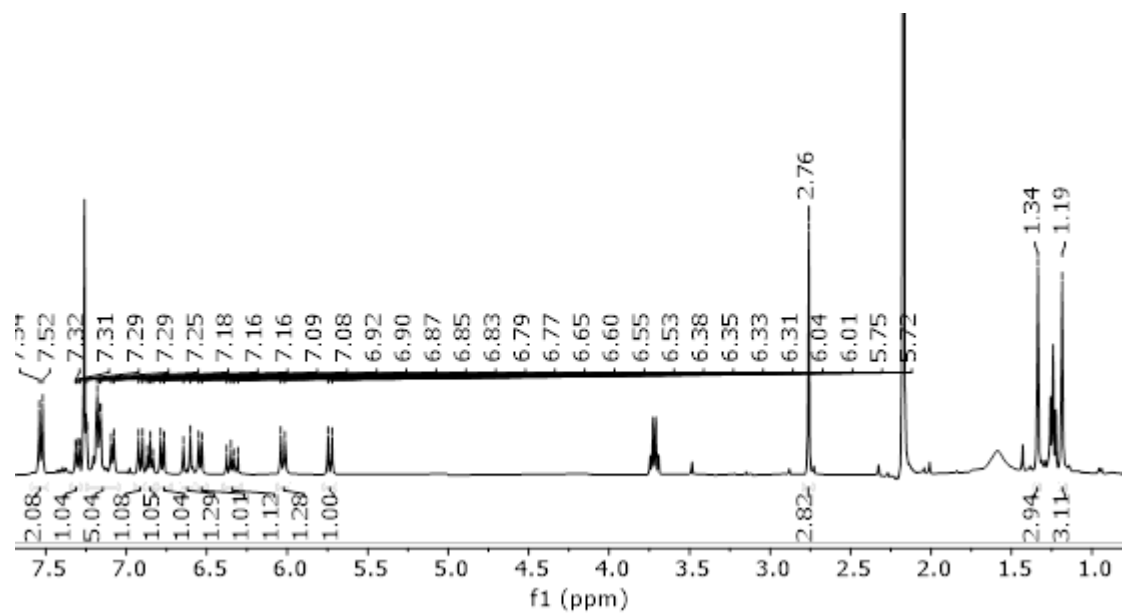*A2.15 ^{1}H NMR Spectrum of SpA 4.23*

SpA mod1

A2.16 ^{1}H NMR Spectrum of SpA 4.24a

A2.17 ^{1}H NMR Spectrum of SpA 4.24b